TUDelft

Delft University of Technology

Angles-only relative navigation in low earth orbit

Important note
To cite this publication, please use the final published version (if applicable).
Please check the document version above.

ANGLES-ONLY RELATIVE NAVIGATION IN LOW EARTH ORBIT

ANGLES-ONLY RELATIVE NAVIGATION IN LOW EARTH ORBIT

Dissertation

for the purpose of obtaining the degree of doctor
at Delft University of Technology,
by the authority of the Rector Magnificus prof. dr. ir. T.H.J.J. van der Hagen,
chair of the Board for Doctorates
to be defended publicly on
Wednesday, 2 September 2020 at 15:00 o'clock

by

Jean-Sébastien ARDAENS

Diplômé de l'École Centrale des Arts et Manufactures, Paris, France,
born in Lille, France

This dissertation has been approved by the promotors

promotor: Prof. dr. E.K.A. Gill
copromotor: Dr. ir. R. Fonod

Composition of the doctoral committee:

Rector Magnificus,	chairperson
Prof. dr. E.K.A. Gill,	Delft University of Technology, promotor
Dr. ir. R. Fonod,	Delft University of Technology, copromotor

Independent members:

Prof. dr. ir. P.P. Jonker	Delft University of Technology
Prof. dr. ir. M. Mulder	Delft University of Technology
Prof. dr. ir. P.N.A.M. Visser	Delft University of Technology
Prof. dr. A.K. Misra	McGill University, Canada
Dr. G.V.M. Gaias	Polytechnic University of Milan, Italy

TUDelft Delft University of Technology

CONTENTS

SUMMARY

Rendezvous in orbit has recently regained considerable attention, as it is required to enable on-orbit servicing or active debris removal activities. The pressing need for the realization of such missions falls within the more general societal attempt to make human activities more sustainable, avoiding wasting valuable resources and ensuring that the environment remains clean after exploitation. Despite the technical heritage of decades of experience, space rendezvous faces, with these new prospects, additional challenges due to the possible noncooperative nature of the target of the rendezvous. A successful and safe approach has to be ensured with limited relative navigation capabilities while reducing the overall mission costs. This quest for cost-effectiveness is indeed required to eventually reach an economically viable large-scale solution able to mitigate the threat posed by the evergrowing population of orbiting space debris.

This dissertation demonstrates that the first part of a rendezvous to a noncooperative object, starting from large separations of several tens of kilometers down to a few hundred meters, can be safely and reliably performed using line-of-sight navigation and solely relying on a single spaceborne camera. More specifically, this research shows that it is possible to use a simple, low-cost, computationally-light and autonomous camera-based embedded navigation system to perform the far-to mid-range approach, thus greatly reducing the necessary onboard equipment and the operational costs. In order to demonstrate this assertion, the dissertation is articulated around three Research Questions: How to design a reliable and accurate spaceborne real-time angles-only relative navigation system? How does it behave under real conditions? How can future angles-only relative navigation systems be improved?

In-flight experience plays a predominant role in this research. As a matter of fact, this dissertation mainly focuses on the validation of angles-only navigation systems in real conditions, and on the subsequent exploitation of data collected in orbit. Two experiments have been realized to support this research. The ARGON experiment, conducted in 2012 using the PRISMA formation-flying demonstration mission, demonstrated the ability to perform a ground-in-the-loop rendezvous from 30 km to 3 km intersatellite distance based on line-of-sight measurements. The AVANTI experiment, executed in 2016 on the BIROS satellite, aimed at demonstrating a more challenging objective: the ability to perform a fully autonomous far-to-mid range rendezvous with a noncooperative target by solely relying on angles-only navigation.

After a general presentation of the technical framework used to conduct these experiments, the dissertation introduces the mathematical and astrodynamical tools required to develop an angles-only navigation system. Following this introduction, an answer to the two first research questions is elaborated by describing and justifying the design of the onground and onboard angles-only relative navigation systems used during the AVANTI experiment, and by presenting key flight results. The on-ground relative orbit determination system is first described. This operational tool has primarily been used

as verification layer to support the AVANTI experiment. Its design inherits from the development done for the ARGON experiment and benefits from its lessons learned. In particular, a new target detection algorithm has been introduced for improved performance and robustness. In order to better highlight the specificities introduced by the orbit of a given mission, previous flight data from the ARGON experiment are reprocessed using this new design and serve as comparison for the discussion of the results. Together, both experimental data sets yield a unique description of the real navigation conditions encountered in low Earth orbits.

The embedded real-time angles-only relative navigation system that enabled the autonomous rendezvous performed during the AVANTI experiment is subsequently presented. Compared to a ground implementation, the algorithms and methods are tailored to cope with the real-time requirements and limited onboard resources. After a brief overview of the necessary adaptations and of the resulting system design, the in-orbit behavior and performance are presented. Overall, this dissertation shows that the autonomous angles-only rendezvous system outperformed the expectations, since it was ultimately employed to reach the boundaries of the close-range field, yielding unprecedented pictures in orbit of the picosatellite BEESAT-4 at a distance of only 50 m.

The conduction of the ARGON and AVANTI experiment resulted in a priceless mine of lessons learned and experience, which is finally exploited to answer the third research question. In order to simplify the interfaces and avoid the provision of external *a priori* information to initialize the navigation systems, a novel algorithm is proposed to solve the problem of Initial Relative Orbit Determination based on line-of-sight measurements. Finally, the relative orbit determination task is revisited to remedy some operational limitations encountered during the execution of the experiments. An innovative preprocessing stage is introduced to greatly improve the robustness of the orbit determination process in the presence of measurement errors and large perturbations of the relative motion. Overall, the proposed improvements make the navigation systems employed for AVANTI operationally more sound, paving the way for the widespread utilization of autonomous angles-only relative navigation systems to support upcoming challenging rendezvous missions.

SAMENVATTING

Rendez-vous in een baan om de aarde heeft recentelijk aandacht herwonnen omdat het een vereiste is voor onderhoud op locatie en voor actieve opruiming van ruimte-afval. De dringende behoefte aan realisatie van dergelijke missies valt binnen de meer algemene maatschappelijke beweging om menselijke activiteiten te verduurzamen, minder waardevolle middelen te verspillen en er zorg voor te dragen dat de omgeving schoon blijft na exploitatie. Ondanks het technische erfgoed van tientallen jaren aan ervaring leveren de nieuwe vooruitzichten extra uitdagingen vanwege het mogelijke niet-coöperatief karakter van het doelwit van de rendez-vous. Een succesvolle en een veilige aanpak moet worden gerealiseerd met beperkte relatieve navigatiemogelijkheden en een vermindering van de totale missiekosten. Deze zoektocht naar kosteneffectiviteit is vereist om uiteindelijk een economisch haalbare grootschalige oplossing te bereiken die de dreiging van de steeds groter wordende populatie van ruimteafval kan verminderen.

Dit proefschrift laat zien dat het eerste deel van een rendez-vous met een niet-coöperatief object, beginnend bij grote afstanden van enkele tientallen kilometers tot enkele honderd meters, veilig en betrouwbaar kan worden uitgevoerd met behulp van gezichts-lijnnavigatie en slechts afhankelijk van een enkele camera in de ruimte. Meer specifiek toont dit onderzoek aan dat het mogelijk is om aan boord een eenvoudig en goedkoop autonoom navigatiesysteem te gebruiken met beperkte rekenkracht voor toenadering met middel- tot ver bereik. Hiermee wordt de benodigde apparatuur aan boord en de operationele kosten verminderd. Om deze bewering aan te tonen, is het proefschrift gearticuleerd rond drie onderzoeksvragen: Hoe kan een betrouwbaar en nauwkeurig 'real-time' navigatiesysteem met alleen hoeken worden ontworpen voor de ruimte? Hoe gedraagt dit zich onder reële omstandigheden? Hoe kunnen in de toekomst navigatiesystemen met alleen hoeken worden verbeterd?

Vlucht ervaring speelt een overheersende rol in dit onderzoek. In feite richt dit proefschrift zich voornamelijk op de validatie van navigatiesystemen met alleen hoeken onder echte condities en op de daaropvolgende exploitatie van gegevens die in een baan om de aarde zijn verzameld. Twee experimenten zijn gerealiseerd om dit onderzoek te ondersteunen. Het ARGON-experiment, uitgevoerd in 2012 met behulp van de PRISMA demonstratie missie voor formatie vliegen, toonde het vermogen aan om met tussenkomst van de grond een rendez-vous uit te voeren van 30 km tot 3 km afstand tussen satellieten op basis van zichtlijnmetingen. Het AVANTI-experiment, uitgevoerd in 2016 op de BIROS-satelliet, richtte zich op het demonstreren van een meer uitdagende doelstelling: het vermogen om een volledig autonome rendez-vous van middel- tot ver bereik uit te voeren met een niet-coöperatief doel door uitsluitend te vertrouwen op navigatie met alleen hoeken.

Na een algemene presentatie van het technische kader dat werd gebruikt om deze experimenten uit te voeren, introduceert het proefschrift de benodigde wiskundige en astrodynamische hulpmiddelen om een navigatiesysteem met alleen hoeken te ontwik-

kelen. Na deze inleiding wordt een antwoord van de eerste twee onderzoeksvragen uitgewerkt door het ontwerp te beschrijven en te rechtvaardigen van de relatieve navigatiesystemen met alleen hoeken die op de grond en aan boord worden gebruikt tijdens de AVANTI-experiment en door de belangrijkste vluchtresultaten te presenteren. Het relatieve baanbepalingssysteem op de grond wordt eerst beschreven. Dit operationele hulpmiddel is voornamelijk gebruikt als verificatie-laag ter ondersteuning van het AVANTI-experiment. Het ontwerp is een erfenis van de ontwikkeling van het ARGON-experiment en profiteert van de geleerde lessen. In het bijzonder is een nieuw doeldetectie-algoritme geïntroduceerd voor verbeterde prestaties en robuustheid. Om de specificiteiten van de baan van een bepaalde missie betere toe te lichten worden eerdere vluchtgegevens van het ARGON-experiment opnieuw verwerkt, gebruikmakend van dit nieuwe ontwerp en dienend als vergelijking voor de bespreking van de resultaten. Beide experimentele datasets geven samen een unieke beschrijving van de echte navigatie omstandigheden die zich voordoen in lage banen om de aarde.

Het ingebedde 'real-time' relatieve navigatiesysteem met alleen hoeken, dat autonome rendez-vous mogelijk maakte tijdens het AVANTI-experiment, wordt vervolgens gepresenteerd. In vergelijking met een implementatie op de grond zijn de algoritmen en methoden op maat gemaakt om te voldoen aan de 'real-time' vereisten en beperkte middelen aan boord. Na een kort overzicht van de nodige aanpassingen en van het resulterende systeemontwerp, worden het baangedrag en prestaties gepresenteerd. Al met al laat dit proefschrift zien dat het autonome rendez-vous systeem met alleen hoeken de verwachtingen overtrof, omdat het uiteindelijk was gebruikt om de grenzen van het nabije veld te bereiken, wat ongekende foto's van de picosatelliet BEESAT-4 op een afstand van slechts 50 meter opleverde.

De uitvoering van het ARGON- en AVANTI-experiment resulteerde in een goudmijn van geleerde lessen en ervaring, die uiteindelijk wordt benut om de derde onderzoeksvraag te beantwoorden. Om de 'interfaces' te vereenvoudigen en het verstrekken van externe a priori informatie om de navigatiesystemen te initialiseren te voorkomen, wordt een nieuw algoritme voorgesteld om het probleem op te lossen van initiële relatieve baanbepaling op basis van zichtlijnmetingen. Tot slot wordt de relatieve baanbepalingstaak opnieuw bekeken om enkele operationele beperkingen te verhelpen die werden ondervonden tijdens de uitvoering van de experimenten. Een innovatief voorbereidingssysteem wordt geïntroduceerd om de robuustheid van de het baanbepalingsproces aanzienlijk te verbeteren in de aanwezigheid van meetfouten en grote storingen van de relatieve beweging. In algemene zin zijn de voorgestelde verbeteringen aan de navigatiesystemen werkzaam voor AVANTI operationeel beter verantwoord, waardoor de weg wordt vrijgemaakt voor een wijdverbreid gebruik van autonome relatieve navigatiesystemen met alleen hoeken om komende uitdagende rendez-vous missies te ondersteunen.

LIST OF SYMBOLS

A	Cross-sectional area
B	Ballistic coefficient
$\boldsymbol{B}$	Bezier curve or input matrix
C_{D}	Drag coefficient
$\mathscr{C}$	Camera frame
$\boldsymbol{C}$	Output matrix
F	Camera angular field of view
$\boldsymbol{F}$	Force acting on a satellite
$\boldsymbol{H}$	Partial derivatives of $\boldsymbol{h}$ with respect to the current state $\boldsymbol{x}(t)$
$\tilde{\boldsymbol{H}}$	Partial derivatives of $\boldsymbol{h}$ with respect to the initial state $\boldsymbol{x}(t_0)$
I	Brightness of an object $\mathscr{O}$
I_{ob}	Threshold for target detection based on obvious brightness
$\mathscr{I}$	Inertial Cartesian frame
J_2	Geopotential second-order zonal coefficient
$\boldsymbol{K}$	Kalman gain
L	Intersatellite distance
$\mathscr{L}$	Set of all luminous pixels in an image
M	Mean anomaly
$\mathscr{O}$	Orbital Cartesian frame or set of pixels constituting an imaged object
$\boldsymbol{P}$	Error covariance matrix
$\boldsymbol{P}_0^{\mathrm{apr}}$	*A priori* covariance information
$\boldsymbol{Q}$	Process noise matrix
R	Camera resolution
$R_{\oplus}$	Earth's radius
$\boldsymbol{R}_{\mathscr{I}}^{\mathscr{C}}$	Rotation matrix from inertial to camera frame
S	Search radius to select the possible candidates in the image
$\mathscr{T}$	Set of points representing a trajectory
$\mathscr{V}$	Frame of the virtual camera pointing in flight direction
a	Semi-major axis
b	Pixel brightness
$\square_{\mathrm{c}}$	Subscript indicating chaser spacecraft
$\boldsymbol{c}$	Pixel
d_{m}	Minimum distance in the plane perpendicular to the flight direction
e	Eccentricity
$\boldsymbol{e}_{\mathrm{R}},\boldsymbol{e}_{\mathrm{T}},\boldsymbol{e}_{\mathrm{N}}$	Unit vectors defining the orbital frame $\mathscr{O}$
$\boldsymbol{f}$	Generic nonlinear function or focal length of the camera
$\boldsymbol{g}$	Camera model

$\boldsymbol{h}$	Measurement model as function of the current state $\boldsymbol{x}(t)$
$\tilde{\boldsymbol{h}}$	Measurement model as function of the initial state $\boldsymbol{x}(t_0)$ and time t
i	Inclination
k	Lens distortion coefficient of the camera
m	Mass
n	Mean orbital motion or number of line-of-sight measurements
$n_{\min}$	Minimum number of points to form a dense region for the clustering algorithm
$\boldsymbol{p}$	Centroid of an object $\mathcal{O}$
$\hat{\boldsymbol{p}}$	Normalized position of an object $\mathcal{O}$
$\tilde{\boldsymbol{p}}$	Position of an object $\mathcal{O}$ as seen as seen in the virtual camera frame $\mathcal{V}$
$\tilde{\boldsymbol{p}}^{\mathrm{apr}}$	Expected position of the target as seen in the virtual camera frame $\mathcal{V}$
$\boldsymbol{r}$	Inertial position
r	radius of the near-circular orbit
s	Brightness of an object $\mathcal{O}$
$\square_{\mathrm{t}}$	Subscript indicating target spacecraft
t	Time
u	Mean argument of latitude
$\boldsymbol{u}$	Line-of-sight vector to the target
$\boldsymbol{u}^{\mathcal{C}}$	Line-of-sight vector to the target expressed in the camera frame $\mathcal{C}$
$\boldsymbol{v}$	Inertial velocity
v	Pixel brightness
$\boldsymbol{x}$	Generic state vector
x,y,z	Cartesian components of the relative position
$\boldsymbol{y}$	Inertial state (position and velocity) vector
$\boldsymbol{z}$	Measurement vector
$\Delta\boldsymbol{r}$	Relative position
$\Delta\boldsymbol{v}$	Relative velocity
$\Delta\boldsymbol{V}$	Velocity increment (*i.e.,* maneuver)
Δt	Time elapsed since reference epoch t_0
$\Delta\boldsymbol{y}$	Relative inertial state vector
$\boldsymbol{\Lambda}$	Information matrix
Ω	Right ascension of the ascending node
$\boldsymbol{\Phi}$	State transition matrix
α	Right-ascension angle
$\hat{\alpha}$	Azimuth angle
$\boldsymbol{\alpha}$	Classical absolute orbital elements
β	Approximation of the angular distance traveled by the target between two pictures
δ	Declination angle
$\hat{\delta}$	Azimuth angle
$\delta\boldsymbol{\alpha}$	Relative orbital elements
δa	Relative semi-major axis
$\delta\boldsymbol{e}$	Relative eccentricity vector

$\delta \boldsymbol{i}$	Relative inclination vector
$\delta \lambda$	Relative mean longitude
ϵ	Distance between two points for the clustering algorithm
γ	Intrinsic camera parameters
τ	Parameter of the Bezier curve
$\boldsymbol{\xi}$	Principal point coordinates of the camera
ω	Argument of perigee
μ	Scaling factor for the solution describing the relative motion
$\mu_{\oplus}$	Gravitational coefficient of the Earth
σ	Measurement noise
$\boldsymbol{\sigma}$	Standard deviation of the least-squares solution
$\boldsymbol{\sigma}_{\Delta r}^{RTN}$	Standard deviation of the position mapped in the RTN frame
σ_B	Standard deviation of the fitting residuals of a Bezier curve
$\sigma_{B,max}$	Acceptance threshold for Bezier fitting residuals
σ_c	Value of the image background noise
Ξ	Control point of the Bezier curve

ACRONYMS

AOCS   Attitude and Orbit Control System
AOK   Autonomous Orbit Keeping
ARGON   Advanced Rendezvous demonstration using GPS and Optical Navigation
AVANTI   Autonomous Vision Approach Navigation and Target Identification
BIROS   Bispectral InfraRed Optical System
CCD   Charge-Coupled Device
CNES   Centre National d'Etudes Spatiales
DBSCAN   Density-Based Spatial Clustering of Applications with Noise
DLR   Deutsches Zentrum für Luft-und Raumfahrt
DTU   Danmarks Tekniske Universitet
EKF   Extended Kalman Filter
EPOS   European Proximity Operations Simulator
FFRF   Formation Flying Radio Frequency
GNC   Guidance Navigation and Control
GNSS   Global Navigation Satellite System
HCW   Hill-Clohessy-Wiltshire
IROD   Initial Relative Orbit Determination
LEO   Low Earth Orbit
LoS   Line-of-Sight
LVLH   Local Vertical Local Horizontal
MSS   Multi-Satellite Simulator
PRISMA   Prototype Research Instruments and Space Mission Technology Advancement
R&D   Research and Development
ROI   Region of Interest
RQ   Research Question
RTN   Radial-Tangential-Normal
SAFE   Spaceborne Autonomous Formation Flying Experiment
TIRA   Tracking and Imaging Radar
TLE   Two-Line Elements
TRL   Technology Readiness Level
VBS   Vision-Based Sensor

1

INTRODUCTION

1.1. NEW PROSPECTS FOR SPACE RENDEZVOUS

The ability to send artificial objects in space has opened up new doors for humankind, paving the way for space exploration but also providing unprecedented services and applications, such as telecommunication or outstanding scientific instrumentation. Since the launch of Sputnik 1, the first artificial satellite in 1957, about 9,000 spacecraft have been placed into orbit [1]. Meanwhile, many of them have become inactive but did not return to Earth. According to the United Nations Office for Outer Space Affairs, about 5000 satellites (active or inactive) are currently orbiting the Earth [1]. The conquest of space is a difficult and risky endeavor. Numerous spacecraft have suffered from unrecoverable failure before their nominal end of life and, even worse, about 500 unfortunate events such as explosions or collisions resulted in spacecraft fragmentation [2]. As a result, the space surrounding the Earth is nowadays populated with a large number of inactive and uncontrolled objects. Recent estimations indicate that about 34,000 objects larger than 10 cm and 900,000 smaller parts between 1 cm and 10 cm are now orbiting the Earth [2].

It has early been recognized that the increasing number of space debris could become a major threat to the space sector. Kessler already warned in 1978 that collisions between large spacecraft could create fragments which, in turn, could hit other spacecraft, resulting in a dramatic collisional cascading between space debris and satellites [3]. In order to limit the probability of experiencing such a horrific scenario, some studies recommend removing at least the largest inactive objects or placing them on less populated graveyard orbits [4]. Most of the envisioned solutions for the so-called active debris removal activities are based on a physical capture of disabled spacecraft [5], thus requiring a rendezvous in space.

Space rendezvous is not a new topic. It was already studied and exercised in the 60's during the first human spaceflight programs [6]. Nowadays, this activity is still frequently performed, for example to resupply the International Space Station. The more recent need for active space debris removal gives a second youth to this field. As explained in more detail in the next sections, dealing with passive and tumbling space

objects poses new challenges compared to a rendezvous with an active and stabilized spacecraft. Furthermore, reliable and affordable technology is required to safely rendezvous with a debris at economically viable cost, in order to make active space debris removal a reality. In fact, large-scale space cleaning remains unlikely if removing an object has a non-negligible probability of creating more debris or if the associated costs remain prohibitive. Some of the solutions adopted so far for space rendezvous can be reused, but many technological bricks still need to be developed or refined to reach the desired level of cost-efficiency and reliability.

Active space debris removal faces several challenges culminating with the safe capture of a tumbling object. This research intends to advance the technical solution needed to realize the first chronological step towards capture: how to safely navigate to an inactive object during a rendezvous using simple and low-cost technology. Note that, even if active debris removal was primarily the main motivation for this research, other space applications such as on-orbit servicing, sample return or even asteroid exploration might also benefit from this work.

1.2. Relative Navigation to a Noncooperative Object

Space rendezvous requires the ability to accurately determine the relative motion, that is, the motion of the object which is being approached with respect to the spacecraft performing the rendezvous. In the general case, the subject of the rendezvous can either be passive or active. Passive, in this context, means that the object is not exerting any force to control its motion. This research only focuses on passive noncooperative objects. In this thesis, the passive object is called target and the active spacecraft is named chaser. During a rendezvous, the absolute motions of the chaser and target, which are expressed relative to an external reference system, are of little interest compared to the relative motion. In fact, the absolute motion is relevant, for example, for ground communication or to ensure proper illumination conditions. Thus, the absolute orbits can be determined with poor accuracy (position estimation errors at kilometer level are still acceptable for the two above-mentioned examples). Instead, the relative motion has to be precisely known to avoid collision and to ensure successful rendezvous and capture. The required relative navigation accuracy greatly depends on the phases of the rendezvous. When initiating the approach at far-range (more than 10 km distance between the satellites), relative position errors of a few hundred meters might be acceptable, but not anymore when capturing the target. In this case, the required relative navigation accuracy can drop to the centimeter level if it is, for example, necessary to grasp a specific part of the target with a robotic arm.

The set of physical variables required to fully determine and predict the future motion of a spacecraft is named state of the dynamical system. In what follows, the relative state will be used to describe the relative motion of the target with respect to the chaser. The determination of the (relative) state is performed by a so-called (relative) navigation system, comprising a set of sensors and dedicated algorithms to further process the measurements delivered by the sensors. These additional processing algorithms, such as the model of the dynamics of the problem, are often justified by the necessity to gain further information not provided by the sensors or to enable new functionalities. For example, if a sensor only provides position measurements, it is possible to derive velocity informa-

tion by considering a set of position observations over time. Or it might be desirable to fuse different sensor measurements to reach a better estimate of a physical quantity by combining the specific advantages brought by different sensors. Generally, it is simply desired to smooth the noisy data delivered by the sensors and to predict the value of the state in the absence of measurements. In case that none of these additional functionalities is needed, a navigation system can be, in its simplest form, only composed of one single sensor.

Several criteria influence the design of a navigation system. Among them, two important aspects need to be introduced. First, it has to be distinguished whether the state estimation, performed as part of the navigation task, has to be done in real-time (for example to feed a controller) or whether it can be done *a posteriori* with relaxed time constraints. Usually, real-time requirements are often associated to onboard applications, where it is necessary to quickly react, while subsequent data processing done on-ground can afford some time lag. In this thesis, both relative state estimation strategies are, respectively, called onboard real-time navigation and on-ground orbit determination to ease the distinction. When dealing with rendezvous in space, another important aspect will also drive the design of the relative navigation system: the ability of an object to provide any information about its state and characteristics to a rendezvousing spacecraft. An object which does not have this capability or feature is called noncooperative.

When dealing with cooperative spacecraft, there exists a large variety of sensors to support the relative navigation task. For most spacecraft in low Earth orbits (LEOs), a GNSS (Global Navigation Satellite System) receiver represents the best sensor choice for absolute and relative navigation, because it combines low mass, limited power consumption, a high technology readiness level (TRL), and accurate measurements. It nominally provides absolute position information at meter level but, depending on the mission needs, advanced processing techniques can extend its capabilities to provide absolute and relative position information respectively at centimeter and millimeter levels [7]. If an intersatellite link is available to exchange data between the satellites, it becomes possible to design GNSS-based embedded real-time navigation systems, which can be used to autonomously control a formation of several cooperative spacecraft as demonstrated with the TanDEM-X [8, 9] or PRISMA [10, 11] missions. These capabilities and flexibilities make a GNSS receiver a well rounded sensor which is the first choice for absolute and relative navigation of many space projects.

However, there exist cases in which such a receiver cannot be used: missions flying far beyond the GNSS constellations (*e.g.*, deep-space projects or formations flying on high elliptic orbits such as Proba-3 [12]), missions requiring specific performance unreachable with GNSS technology (*e.g.*, determination of the intersatellite range rate within 1 μm/s for the GRACE formation [13]), or missions requiring ultimate availability and reliability of the sensors (*e.g.*, when docking to the International Space Station, it is highly probable but not guaranteed that GNSS constellations will always be properly functioning. Standalone optical sensors are thus preferred). To satisfy such needs, dedicated sensor systems (self-contained Formation Flying Radio Frequency metrology [14], optical metrology [15], microwave ranging system [16], etc.) have to be installed. All of them require dedicated hardware on each spacecraft (sender, transponder, reflectors, etc.), thus requiring a certain level of cooperation between the spacecraft. Note that

in case of rendezvous, the cooperation is not necessarily actively done in orbit but can be made at a design level by introducing passive elements (such as reflectors or special markers) to ease the collection of measurements. In this case, the target object is semi-cooperative.

For the specific case of rendezvous with a noncooperative object, any sensor requiring the smallest level of cooperation (for example the use of passive elements) is, however, excluded, posing severe constraints to the relative navigation task. In fact, the sensing methods which can be employed are reduced to only two options: either actively producing electromagnetic radiation which will be reflected by the target and measured by the chaser spacecraft, or passively observing the radiation naturally emitted or reflected by the object. The first approach encompasses sensors like radar, lidar, time-of-flight cameras, while the second option relies on cameras (monocular, stereo, in the visible or infrared domains, etc.).

Apart from the technical or physical feasibility of the sensing method, several criteria have also to be considered when designing a navigation system, such as mass, cost, power consumption, complexity. The active sensors present, for example, the drawback of high power requirements if the noncooperative object is far from the chaser satellite. On the contrary, it was early recognized that passive imagery could play a predominant role in the sensor assembly required for the relative navigation to a noncooperative target [17]. A camera can be a simple, cheap, small, low-mass and low-power consumption device presenting a high technology readiness level. These characteristics are arguably not shared by all space cameras. Dedicated scientific cameras (such as used for the space telescope Hubble [18] or for Earth observation satellites like Sentinel-2 [19]) are expensive and complex devices. In fact, a large variety of parameters affects the design of a camera, such as quality of the optics, optical resolution, type of imaging sensor chip, spectral utilization, thermal stability. The Advanced Camera for Surveys [20] on Hubble comprises, for example, three cameras with a resolution better than 0.05 arcsec/pixel, has a mass of 397 kg and costs more than US$ 80 millions. The camera performance requirement for space rendezvous are, however, not so stringent. In fact, as seen later in this thesis, a resolution of about 1 arcmin/pixel in the visible spectrum is sufficient. Numerous suitable space cameras are now available, driven by the wide adoption of star trackers and the emergence of low-cost imaging technology for picosatellites. Among them, the star-tracker from the Technical University of Denmark (DTU) [21] is a radiation-hardened device based on a Charge-Coupled Device (CCD) sensor of 752×580 pixels and offers a resolution of 80 arcsec/pixel. It can act as a standard camera by offering the possibility to transmit the images processed by the star tracker functionality. The 5MP space camera from Space Micro [22] provides a radiation tolerant design, a sensor of 2560×2160 pixels and several possible configurations for the fields of view (29°, 39°, 80°). The C3D camera from XCAM [23] is a flight-proven device based on Commercial-off-the-Shelf components with 1280 x 1024 pixels and also offers different possible field-of-view configurations. From the specifications of these three examples, it can be concluded that a typical space camera belonging to this category has a mass of less than 1 kg, a power consumption of a few Watts, and a resolution of about 1 arcmin/pixel.

The aforementioned characteristics make a camera often well suited to support the relative navigation task, delivering line-of-sight measurements (*i.e,* the direction to the

target) at far-range when the shape of the target cannot be distinguished and allowing for advanced shape-matching techniques at close-range. These appealing sensing capabilities come, however, at the cost of additional difficulties. First, the image of an object strongly depends on the illumination conditions. Second, the sensor does not provide direct measurements. The measurements have to be first extracted from the image. In other words, it is, compared to other sensors requiring for example precise time synchronization or fine pointing, easy to make an image of the environment. However, additional advanced processing techniques have to be subsequently introduced to reliably find and extract the measurements from the pictures and accurately estimate the relative state. At far-range, the difficulty rather lies in distinguishing the target from other celestial objects. At close-range, retrieving the full pose (relative position and attitude) of the target constitutes the main challenge. Still, in view of its aforementioned qualities, a camera remains nonetheless a first-choice sensor to navigate to a noncooperative spacecraft and was thus selected as the fundamental sensor for this work.

The scope of the research has intentionally been restricted to the far- to mid-range domain, where only line-of-sight observations can be exploited, thus focusing on angles-only relative navigation. This choice is driven by the fact that an autonomous rendezvous with a noncooperative target in space is a delicate task (in view of the risk of collision and of the difficulty to achieve reliable real-time close-range navigation with image processing techniques) whose complexity has to be mastered step-by-step. Before reaching close proximity, it is first necessary to demonstrate the ability to initiate an approach from a separation distance between the chaser and the target of several tens of kilometers (the far-range field) and the capability to safely navigate to the target up to an intersatellite distance of a few hundred meters. This frontier with the close-range domain (below hundred meters) constitutes the boundaries of this research. At smaller separations, specific methods and sensors will have to take over the relative navigation task, in order to much more precisely measure the state and attitude of an object based on its visible shape or relying on other sensing technology.

1.3. STATE OF THE ART

1.3.1. LINE-OF-SIGHT NAVIGATION

Line-of-sight navigation itself is an ancient technique (see Section 3.1) which has already extensively been addressed in the literature. In fact, such a method is used in many domains, such as in naval applications [24] or for the orbit determination of asteroids or artificial satellites from the Earth's surface [25]. More recently, it has been recognized that angles-only measurements might as well help navigating in space. Chari [26] and Woffinden [27] have both provided major contributions to this field by investigating the usage of angles-only navigation for autonomous orbital rendezvous. Most of the research done in this field deals with the problem of weak observability and proposes solutions to improve it by altering the natural dynamics [28, 29, 30, 31], introducing a camera offset [32, 33] or improving the measurement and dynamical models [34, 35, 29, 33]. Several authors have more specifically focused on algorithms and methods to solve the initial relative orbit determination problem using solely angular measurements [36, 37, 35, 38, 39, 40]. A deeper insight into the state of the art concerning these particular

research topics is provided in Section 6.1.2. Note that the availability of a set of bearing observations is usually taken for granted by the authors. In reality, the extraction of the measurements from the images is sometimes not obvious in the presence of undesired additional artificial objects in the field of view, showing room for further investigations.

1.3.2. SIMULATION CAPABILITIES

It has to be emphasized that the research activities presented in the previous Section remain fairly theoretical. Numerical simulations were sometimes used to support the investigations, but no author could afford building a testbed in space for realistic behavior and performance analysis. In real conditions, the angles-only relative navigation problem becomes more arduous. First, because some perturbations of the relative motion of spacecraft can hardly be simulated with high fidelity. The distribution of observations over time and the measurement errors are also extremely difficult to be faithfully modeled as they intricately depend on the orbit, on the target object and on the chaser spacecraft and operations. In order to better investigate these aspects, several research groups have recognized the need for highly realistic simulation and test environments able to include real hardware sensors in the loop. The robotic facilities, widely used to test and verify close-range navigation algorithms and sensors, are not adapted to cover the far-range field because of the limited size of the buildings hosting the hardware-in-the-loop facilities. Thus, the only way to include a far-range sensor in the loop is to simulate the environment sensed by the hardware device. This is the approach retained by DTU when developing their Optical Stimulator for Vision-Based Sensors (VBS). This system relies on a monitor viewed by a sensor through corrective optics [41]. The Space Rendezvous Laboratory at Stanford University has also developed high-fidelity simulation tools for vision-based sensors. Among them, a far-range stimulator has been created based on similar principles. In order to achieve physically sound simulations, considerable efforts have been spent in understanding and quantifying the radiometric budget and optical distortions [42]. Even if these hardware-in-the-loop facilities are precious assets to develop and test vision-based systems, the underlying simulations are often too limited to realistically assess the achievable performance and the robustness of the line-of-sight navigation. This opens up gaps in the body of knowledge which this thesis tries to cover.

1.3.3. IN-ORBIT EXPERIENCE

In fact, the real in-orbit expertise in angles-only relative navigation is very limited. It is generally admitted that the first relevant experience in this field has been collected in 2007 in the frame of Orbital Express, a technology demonstration mission for on-orbit servicing from the American Defense Advanced Research Projects Agency (DARPA) [43]. Among the different activities conducted during the mission lifetime, a noncooperative autonomous approach mainly based on passive imagery has been conducted. However, the detailed outcome of the mission remained confidential, making it difficult to assess what precisely has been done and achieved. The Prototype Research Instruments and Space Mission Technology Advancement (PRISMA) formation-flying demonstration mission [44], conducted by the Swedish Space Corporation (SSC), constituted the second major gain of flight experience. Among others, it offered the possibility to image a target

satellite using a dedicated VBS composed of two different cameras (far- and close-range) [45]. Thanks to dedicated algorithms located in its data processing unit, the far-range sensor was able to extract line-of-sight measurements of the luminous objects which were not included in its star catalog. Several vision-based rendezvous activities were conducted by the different partners of the mission. The Autonomous Rendezvous experiment (ARV) on PRISMA led by the former Swedish Space Corporation could exercise angles-only navigation using the line-of-sight observations delivered in real-time by the VBS [46]. The French and German space research centers (respectively CNES and DLR) also performed their own investigations on angles-only navigation. While the CNES experiment relied on the measurements extracted by the sensor [47], the DLR activities were instead designed to work directly with the pictures output by the camera and culminated with the ARGON (Advanced Rendezvous demonstration using GPS and Optical Navigation) experiment [48], which demonstrated the ability to perform a ground-in-the-loop approach from 30 km to 3 km to a noncooperative target using solely line-of-sight measurements. The ARGON experiment constituted the starting point of this research.

Despite the substantial achievements of the PRISMA mission, the aforementioned experiments could benefit from the optimal visibility conditions offered by the dawn-dusk orbit of the mission and from the safety guaranteed by the onboard formation monitoring system based on differential GPS. Thus, they were not fully representative of the conditions encountered when rendezvousing with an object flying on an arbitrary orbit. This has been identified as additional gap in the body of knowledge. This research aims at demonstrating that angles-only relative navigation can in fact be reliably employed in more challenging conditions and intends to shed light on the aspects which are too often ignored or omitted in the theoretical research but are crucial to successfully use this technology in real missions: reliable target detection, data screening, operational friendliness and robustness, real-time implementation with limited resources and realistic performance assessment.

1.4. OBJECTIVES AND RESEARCH QUESTIONS

The objective of this work is to demonstrate the ability to reliably and safely reach the close-proximity domain, paving the way for further research and development activities. Such a safe and reliable rendezvous is often guaranteed at the expense of multiple costly and redundant sensors combined with intensive ground support. This research aims at demonstrating that it is instead possible to use a simple, low-cost, computationally-light and autonomous camera-based navigation system to perform far-and mid-range approach, thus greatly reducing the necessary onboard equipment and the operational costs. It has to be noted that autonomy may not only contribute to a cost reduction but might be a mission requirement to ensure enough reactivity if the mesh of ground stations is not dense enough to provide full satellite coverage.

The focus of this research lies in the design and implementation of a spaceborne autonomous angles-only relative navigation system, and in the analysis of its behavior under real conditions. As this thesis focuses on an end-to-end engineering application, only limited theoretical advances are addressed. Any of the employed methods belong to the standard mathematical and astrodynamical toolboxes. The backbone of this re-

search instead consists of the design and engineering of a real system able to perform in orbit, in order to collect meaningful flight data which will constitute a priceless mine of lessons learned and experience.

The desire to build such an autonomous system raises several Research Questions (RQs) which constitute the core of this thesis:

- **RQ1: How to design a reliable and accurate spaceborne real-time angles-only relative navigation system?**

  Onboard autonomy raises the need for reliability and real-time capability. Even if the theoretical foundations for angles-only navigation are already available, the question of how to design and implement a reliable relative navigation system able to operate on a spacecraft with limited resources remains open. In particular, the reliable extraction of line-of sight measurements from pictures and the choice of accurate but computationally-light estimation concepts have to be addressed. In order to monitor the proper functioning of the system, the addition of a ground-based verification layer is of advantage, raising the question of whether more robust and accurate estimation concepts can be used when more resources and less time constraints are available.

- **RQ2: How does an angles-only relative navigation system behave under real conditions?**

  The main achievement of this research will consist in the experience collected in orbit from real missions. This allows addressing the fundamental question of robustness of the data processing algorithms and of the validity of the underlying assumptions and models. In particular, this research question aims at investigating how do the orbit perturbations and system uncertainties affect the navigation behavior, what is the impact of the visibility conditions and how robust is the navigation system in the presence of outliers.

- **RQ3: How can future angles-only relative navigation systems be improved?**

  Answering RQ2 will allow questioning some of the design choices made when responding to RQ1. In particular, RQ3 intends to investigate what can be improved to make the relative navigation task more robust, faster and simpler.

1.5. RESEARCH METHODOLOGY

This research has been conducted using a stepwise iterative approach, putting emphasis on collecting real flight data and subsequently improving the algorithms and methods based on the lessons learned. As already stated, the origin of this work dates back to 2011. At that time, a unique opportunity arose to collect images of another spacecraft in orbit using the PRISMA formation-flying demonstrator, which had been launched one year before. As described in more detail in Chapter 2, the PRISMA mission was composed of two cooperative spacecraft (called Mango and Tango) and aimed at demonstrating and qualifying key technology and methods for formation-flying. The main spacecraft (Mango) was equipped with several relative navigation sensors (among which a far-range camera) and could rely on a propulsion system to build a close formation

with Tango. Both satellites carried a GPS receiver. Since the spacecraft were flying on a similar orbit, it was possible to gather images of Tango using the onboard camera of Mango with reduced operational effort. In fact, it was enough to point the camera in the flight direction to image the target spacecraft at several kilometer distance. The first few images of the target at far-range were collected for DLR at the end of the PRISMA extended mission phase in August 2011, initiating the Research and Development (R&D) activities on angles-only navigation.
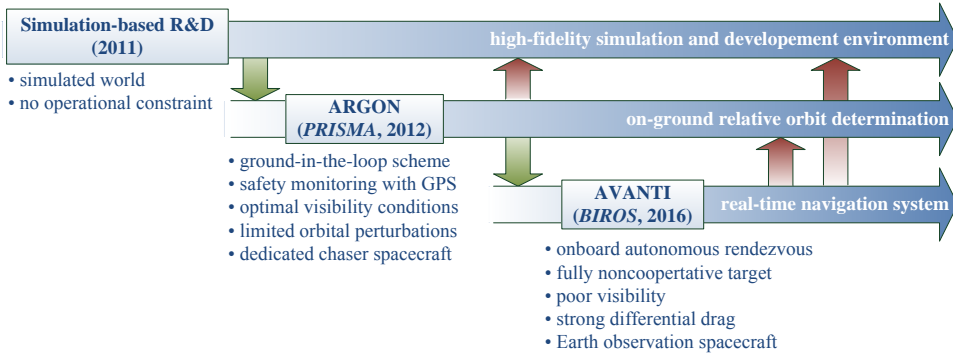

Figure 1.1: Research roadmap. The blue arrows depict the high-level systems used to conduct the research. The green ones represent the transfer of expertise needed to initiate the development of a more complex system. The red arrows correspond to the feedback experience used to improve the processes.

This triggered the development and conduction of the dedicated ARGON experiment in 2012, aiming at demonstrating the ability to rendezvous with a noncooperative spacecraft based only on line-of-sight navigation [48]. In order to reduce the complexity of this task, the experiment had been designed in a ground-in-the-loop scheme: the images were acquired in orbit but processed *post-facto* on-ground, and the resulting guidance profile for the rendezvous was uploaded to the chaser spacecraft at the following ground contact.

The fruitful experience gained with the PRISMA satellites served as baseline to design and implement the more complex AVANTI (Autonomous Vision Approach Navigation and Target Identification) experiment [49]. This technological demonstration was conducted in autumn 2016 using the BIROS Earth observation satellite [50] and could successfully show in orbit the ability to fully autonomously approach a passive object in a safe and propellant-efficient way using only line-of-sight measurements provided by a single camera. As sketched in Fig. 1.1 and explained in more detail in Chapter 2, AVANTI was way more complex than ARGON, due to the quest for autonomy but also to some additional constraints posed by the satellite and orbital environment.

In view of the complexity and experimental status of the AVANTI onboard software, it early appeared obvious that a ground-based verification layer would be needed to support the characterization and validation of the onboard algorithms, giving the birth to the ground facility for precise vision-based relative orbit determination. Compared to the onboard real-time navigation, the ground-based orbit determination benefits from larger computational power (allowing thus for more advanced and accurate algorithms),

1

from much more relaxed time constraints, and from the critical eye of the human operator, able to better assess the plausibility of the solution. As a consequence, the resulting reconstructed relative trajectory becomes the best possible post-facto knowledge of the state of the formation. This can serve as reference to characterize the performance of the onboard algorithms and, of course, to monitor from ground the safety of the formation during close approaches. This facility was an evolution of the version built to support the ARGON experiment and benefited from the experience gained at that time. For clarity, this thesis will only present the most mature version used for the AVANTI experiment. Data from ARGON has retroactively been processed to support the analyses.

Conducting such an endeavor would not have been possible without a realistic simulation environment for the design, implementation, validation and test of the algorithms. This environment had to mature in parallel to the progress of the experiment preparation. Different assumptions had been made concerning the orbit perturbations, sensor behavior and visibility of the target. The experience gained in orbit indicated that some of the assumptions were not fully correct, opening new doors for further improvements. Furthermore, some of the adopted technical solutions also showed the need for enhancement. As a consequence, in a final movement, the thesis revisits the algorithms and methods, looking for what could have been done better by extracting lessons learned from past applications which can be used for future missions.

1.6. THESIS OUTLINE

The thesis closely follows the historical roadmap of the research. Chapter 2 and 3 introduce the problem of angles-only relative navigation in detail as well as the experimental framework used to validate the algorithms and to gain relevant flight experience. Chapter 4 tackles the problem of on-ground relative orbit determination. As already stated, in order to better highlight the specifics of each mission, flight data coming from the AR-GON and AVANTI experiments are analyzed together. Chapter 5 focuses on the design of a spaceborne relative navigation system. In view of the limitations posed by onboard implementation, dedicated design choices had to be made in order to ensure a real-time utilization. The experience coming from the AVANTI experiment is used to support the discussion. Chapters 6 and 7 summarize the further research activities that have been carried out since the AVANTI experiment was conducted. They aim at answering RQ3 by investigating what could have been improved in order to make the relative orbit determination task operationally more sound. Chapter 6 focuses on the problem of initial orbit determination, demonstrating that it would have been possible to make the relative navigation algorithms fully standalone. Chapter 7 concludes the investigations by introducing new methods to improve the robustness of the navigation in the presence of outliers and enhance the realism of the expected navigation errors. Chapter 8 summarizes the achievements and lessons learned and concludes with open issues and recommendations.

2

MISSIONS AND TOOLS

This chapter provides an overview of the framework used to develop and conduct the in-orbit experiments. After the description of the PRISMA and FireBird missions, which respectively hosted the ARGON and AVANTI experiments in 2012 and 2016, the model-based development and simulation environment is presented. This tool set was employed to support the design, implementation, testing and validation of AVANTI's spaceborne angles-only autonomous rendezvous system.

2

2.1. IN-ORBIT DEMONSTRATION MISSIONS

2.1.1. THE PRISMA FORMATION

The PRISMA satellites [54] constitute one of the most ever sophisticated and successful formation-flying missions. This technology demonstration was led by the Swedish Space Corporation (now OHB-Sweden) and launched in 2010. Its objective was to advance and validate key technology (sensors, actuators, methods, algorithms) for formation flight [44]. As already mentioned in the introduction, several international partners were involved in the mission: the French space agency (CNES), the Technical University of Denmark (DTU) and the German Aerospace Center (DLR). Two small satellites have been injected in a near-circular, Sun-synchronous dawn-dusk orbit at about 750 km altitude to create the PRISMA formation depicted in Fig. 2.1: Mango, equipped with a propulsion system and bedecked with different formation-flying sensors, actively chasing Tango, a simpler satellite without orbit maneuvering capability.

Figure 2.1: The PRISMA formation: Mango (left) chasing Tango (right) (image credit: OHB-Sweden).

Mango was a three-axis stabilized satellite with 3D maneuver capability. Its precise attitude control relied on reactions wheels and star trackers. In addition to the equipment required for attitude and orbit control, Mango embarked dedicated sensors for formation-flying: a Formation Flying Radio Frequency (FFRF) system contributed by CNES [14], a Vision-Based System (VBS) constituted of far- and close-range cameras together with a processing unit provided by DTU [45], and a spaceborne real-time GPS-based navigation system delivered by DLR [55]. Tango was instead simpler, featuring a coarse three-axis attitude stabilization based on magnetometers and torquers. Despite its simplicity, Tango was equipped with sensors enabling precise formation-flying: a GPS receiver delivering in real-time raw measurements to the Mango spacecraft via an intersatellite link, as well as additional equipment to support the FFRF and VBS systems. Table 2.1 summarizes the main mission and spacecraft characteristics. Note that, in Table 2.1, the nominal cross-sectional area A (*i.e.*, normal to the spacecraft velocity) has been used to compute the ballistic coefficient $B = C_D A / m$, where $= C_D$ and m stand for drag coefficient and mass. For a dawn-dusk orbit, the normal to the solar panels is oriented towards the orbit angular momentum, so that the cross-sectional areas for Mango and Tango respectively amounted to 80x80 and 80x30 cm^2. An identical drag coefficient $C_D = 2.3$ has been assumed for both spacecraft in order to compute their ballistic coefficients.

Table 2.1: Relevant characteristics of the PRISMA mission.

	Item	Value	Unit
Formation	semi-major axis	7130	km
	eccentricity	0.004	-
	inclination	98	deg
	local time of ascending node	06:00	hour
	argument of perigee	178	deg
Mango	mass (wet)	145	kg
	dimensions	$80 \times 80 \times 130$	cm^3
	ballistic coefficient	10.2×10^{-3}	m^{2}kg^{-1}
Tango	mass	40	kg
	dimensions	$80 \times 80 \times 30$	cm^3
	ballistic coefficient	13.8×10^{-3}	m^{2}kg^{-1}

The GPS-based navigation system was composed of single-frequency GPS-receivers developed by DLR [56], of two antennas per spacecraft (to ensure full sky coverage) and of an onboard navigation filter implemented on the Mango spacecraft able to process the GPS raw measurements of both spacecraft, in order to deliver real-time absolute and relative navigation with unprecedented accuracy (at meter and centimeter levels respectively). This system served as backbone to continuously monitor the safety of the formation and to perform precise GPS-based formation control. The onboard navigation system was complemented with an on-ground verification layer, which could deliver even more precise relative positioning products accurate at sub-centimeter level [11]. These products served as reference to calibrate and cross-validate all the other relative navigation sensors during the mission.

During the mission experiment timeline, numerous advanced formation-flying activities were conducted by the different partners [54]. In addition to the delivery of the GPS system, the contribution of DLR consisted in the conduction of the SAFE (Spaceborne Autonomous Formation Flying Experiment) formation keeping [57, 10] as well as the AOK (Autonomous Orbit Keeping) [58] experimental campaigns. This latter experiment was set up to show how formation-flying techniques could also be exploited to accomplish autonomous control for a single satellite to maintain its ground track close to a reference trajectory. In the framework of the SAFE experiment, several autonomous formation acquisition and control experiments based on

Figure 2.2: Cooperative close-proximity operations (distance of about 15 m) during the PRISMA mission (image credit: OHB-Sweden).

the impulsive control and relative orbital elements frameworks (described in Section 3.2.4) were conducted, demonstrating close rendezvous up to a few tens of meters [57]. Other experimenters of the PRISMA project focused on continuous control applications and could even demonstrate closer approaches such as depicted in Fig. 2.2. In fact, being specifically designed for precise formation-flying in low Earth orbit, the PRISMA testbed offered the possibility to demonstrate what could ultimately be done using two cooperative spacecraft.

2.1.2. The ARGON Experiment

After the successful completion of its primary mission goal, namely of the demonstration of precise GPS-based formation-flying, it became tempting for DLR to use the PRISMA testbed to simulate rendezvous with noncooperative targets. In this context, *noncooperative* means that the target spacecraft does not transmit any information anymore (position, velocity, etc.) to the chaser. This triggered the conduction of two camera-based experiments. In order to get familiarized with this topic, images of the target spacecraft have been first collected during the time in which the mission was operated by DLR [59]. Based on this precursory experience, the ARGON (Advanced Rendezvous demonstration using GPS and Optical Navigation) experiment has been designed and executed between April 22nd and 27th, 2012 [48]. The objective was to demonstrate the ability to conduct a ground-in-the-loop vision-based rendezvous to a noncooperative target from 30 km to 3 km intersatellite separation. Mango played the role of the chaser spacecraft in charge of the approach. Tango, which had been considered noncooperative for the sake of the experiment, took the role of the target. In view of the reduced experimental time slot, only one approach could be exercised.

This on-orbit demonstration could benefit from the technological wealth offered by a formation-flying testbed: 3D maneuver capability, precise attitude control and dedicated far-range tracking camera on the chaser side. Because the target was considered noncooperative, the GPS-based relative navigation system was not directly used during the experiment but was in the background always active for formation safety monitoring, such that valuable accurate measurements of the formation at any time could be stored for further investigations. The existence of precise relative positioning products derived *post-facto* using the raw (code and carrier phase) GPS data [11] constitutes in fact a precious asset for the precise analysis of the navigation and control errors, but also for the characterization and validation of the sensor and image processing performance.

The VBS far-range sensor used to track the target object was a modified version on the fully autonomous miniaturized μASC star-tracker [21], whose main characteristics are summarized in Table 2.3a. The same sensor would be later used for AVANTI, allowing for extensive transfer of experience between both experiments. As already explained in the introduction, compared to the traditional star-tracker, the VBS introduces an electronic shutter control for improved dynamic range and dedicated algorithms located in the digital processing unit to automatically detect non-stellar objects [45]. During the ARGON experiment, it has been preferred to directly process the raw images (*i.e.,* to detect and extract the non-stellar objects from the pictures) instead of relying on the additional built-in feature provided by the VBS system to do this task.

In order to cope with the limited data budget of the Mango satellite, a special feature

| Items	Value	Unit
field of view	18.3×13.7	deg
resolution	752×580	pixel
focal length	20	mm
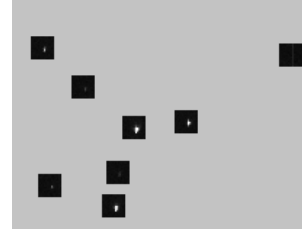
(a) Key camera parameters.

(b) Delivery of Regions of Interest.

Figure 2.3: Some relevant characteristics of the μASC star tracker.

of the camera allowed sending only the most important information of the image, by automatically selecting Regions of Interest (16x16 pixels) around the luminous objects detected in the image as depicted in Fig. 2.3b. This compression format allows for a substantial reduction of the picture size. In fact, the size of a typical image comprising 60 objects is decreased from 436 kB to only 15 kB.

2.1.3. The FireBIRD Mission

The second experimental opportunity for this research was given by the FireBIRD mission, which is primarily a small-scale Earth observation mission for the detection and quantitative analysis of High Temperature Events like wildfires and volcanoes [50]. FireBIRD consists of a constellation of two similar satellites: TET-1 (*Technologie-Erprobungsträger 1,* launched in 2012) and BIROS (*Bispectral InfraRed Optical System,* launched in 2016) which are both equipped with a bispectral infrared sensor and a camera recording in the visible and near-infrared ranges. Together, the satellites constitute an experimental platform for early fire detection with high spatial resolution. Both spacecraft inherit from the technological expertise gained with the precursor satellite BIRD (*Bispectral InfraRed Detection,* launched in 2001) and fly on near-circular low-altitude high-inclination orbits typical for Earth observation missions (*c.f.,* Table 2.2) .
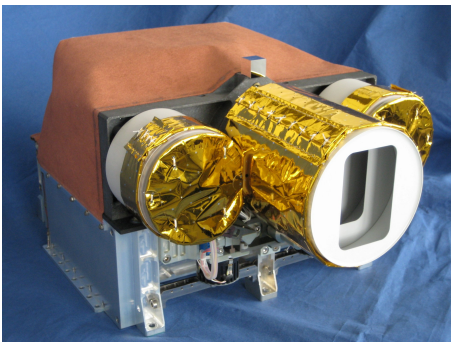
(a) The main payload of TET-1/BIROS.
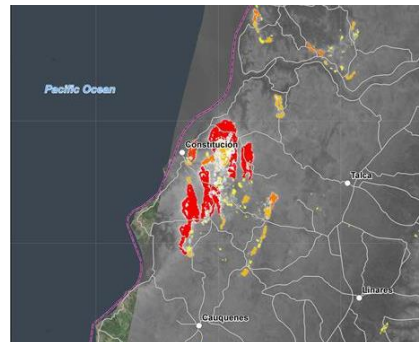
(b) Fire detection made by TET-1 in Chile (2017).

Figure 2.4: Fire detection payload and product (image credit: DLR-OS).

TET-1 and BIROS share the same satellite bus and are thus similar in shape. Both spacecraft belong to the class of small satellites with a wet mass of less than 150 kg and are three-axis stabilized thanks to the use of reaction wheels and star trackers (the same μASC star-trackers [21] as for PRISMA). Despite their similarity, TET-1 and BIROS embark different secondary experimental payloads. Two of them are of special relevance for this research. First, a single-direction cold-gas propulsion system has been introduced for BIROS, allowing for minor orbit corrections. Second, BIROS has been designed to embark a third-party picosatellite built by the Technical University of Berlin (named BEESAT-4 [60]) to be released in-orbit by means of a picosatellite launcher [61].

Table 2.2: Relevant characteristics of the AVANTI formation.

	Item	Value	Unit
Formation	semi-major axis	6880	km
	eccentricity	0.001	-
	inclination	97	deg
	local time of ascending node	21:30	hour
	argument of perigee	246	deg
BIROS	mass (wet)	140	kg
	dimensions	$58 \times 88 \times 68$	cm^3
	ballistic coefficient	8×10^{-3}	m^{2}kg^{-1}
BEESAT	mass	1	kg
	dimensions	$10 \times 10 \times 10$	cm^3
	ballistic coefficient	23×10^{-3}	m^{2}kg^{-1}

This latter feature has been motivated by the desire to gain experience in the design of small distributed Earth observation satellite systems, for which a child spacecraft flies well in advance in front of a mother satellite to coarsely detect events of interest, letting time to the mother spacecraft to subsequently orient its accurate payload towards the location of this event. The ejection of a Cubesat in space was a unique opportunity for this research, since it could serve as noncooperative target for the sake of a rendezvous experiment without the need of spending a large amount of propellant to navigate to an existing space object. The resulting formation (depicted in Fig. 2.5) has been used as experimental platform to conduct the AVANTI experiment in autumn 2016, which aimed at demonstrating spaceborne vision-based autonomous approach to a noncooperative target [49].
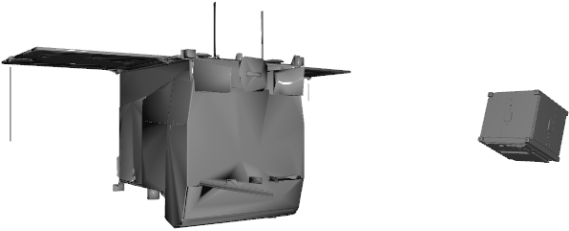

Figure 2.5: The AVANTI formation: BIROS (left) chasing BEESAT-4 (right).

2.1.4. The AVANTI Experiment

The major advance of the AVANTI (Autonomous Vision Approach Navigation and Target Identification) experiment is summarized in the first letter of the name: *autonomy*. Many tasks had to be autonomously executed onboard: image processing and target detection, relative navigation, creation of safe and propellant-optimal orbit guidance plan, execution of maneuvers, switch between different attitude modes, and formation safety monitoring [49]. The ground activities were limited to the choice of the final formation configuration to be reached by the onboard autonomous system, and to some additional monitoring and validation activities. In view of the required level of onboard autonomy, the core algorithms have been implemented as additional guidance navigation and control (GNC) modes directly interfaced to the Attitude and Orbit Control System (AOCS) of the chaser spacecraft [62], implying that the onboard AVANTI software module had full translational and rotational control of the chaser satellite during the experiment lifetime.
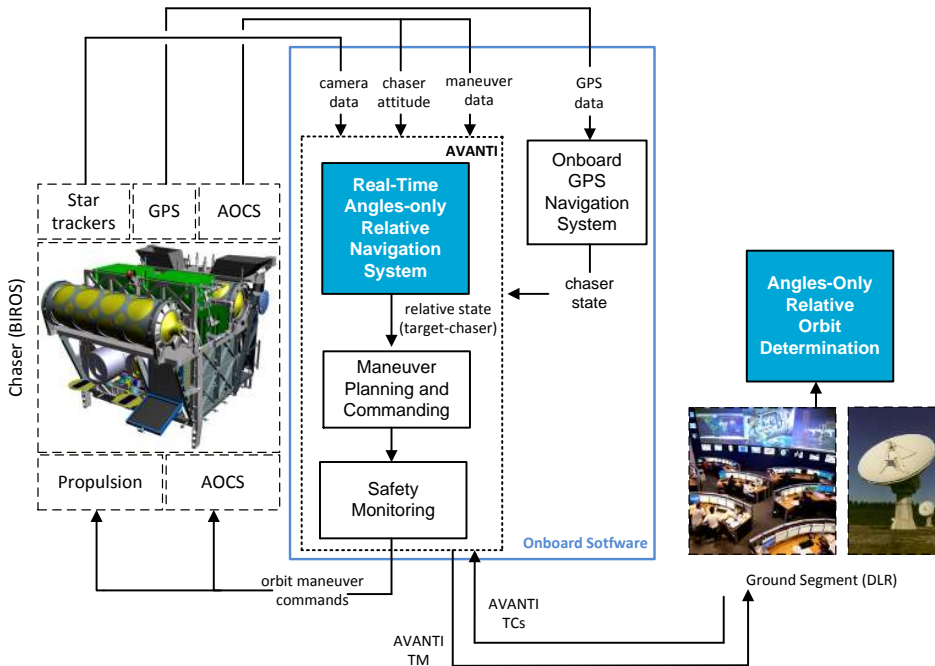
Figure 2.6: Architecture of the AVANTI experiment.

In fact, AVANTI is a complete self-contained GNC experiment, as depicted in Fig. 2.6. The real-time angles-only relative navigation system and the facility for angles-only relative orbit determination, main topics of the thesis and highlighted in blue, are only parts of the whole system. As shown in the figure, the onboard relative navigation system is in charge of processing the images collected by the camera and, together with the knowledge of the maneuvers which have been executed, is able to derive in real-time a relative navigation solution which feeds the onboard controller. A safety monitoring module ultimately validates the onboard autonomously generated guidance plan before sending

the maneuver commands to the AOCS. The AVANTI flight software is written in C++ and runs under the RODOS operating system [63]. More details on the experiment design can be found in [49].

As already sketched in Fig. 1.1, this peculiar experimental framework induced some additional difficulties compared to the ARGON experiment, making AVANTI a much more challenging scenario in terms of angles-only rendezvous in orbit [64]. Four additional difficulties can be in fact identified. First, contrary to the ARGON experiment which, thanks to the dawn-dusk orbit of the PRISMA satellites, benefited from optimal illumination conditions, AVANTI is meant for approaching target objects flying on any kind of low Earth orbits. As depicted in Fig. 2.7, this has dramatic impacts in terms of visibility of the target with respect to the chaser, since the target object is eclipsed during a large part of the orbit (blue part of the relative elliptical motion) and the camera becomes blinded by the Sun during another large part of the orbit (corresponding to the portion of the relative motion represented in orange). As shown in the figure, the camera is blinded during a large period of time. This is due to the fact that, at far-range, the exposure time of the camera is set to a high value (0.25 s) in order to track the faint objects (up to a visual magnitude of 6-7). Even if the camera is not directly pointing to the Sun, multiple reflections of light within its baffle might be enough to blind it. A Sun-exclusion angle of 70°(according to the constructor) has thus to be kept to ensure the proper functioning of the camera. As a result, only a small portion (about 10 %) of the relative motion can be observed, weakening thus the observability property. Note that, during most of the experiment time, the camera was used as standard star-tracker with a fixed exposure time, but the device also offers the possibility to activate automatic shutter control if needed. This function was used during the experiment when entering the close-range domain (typically for intersatellite distances smaller than 1 km).
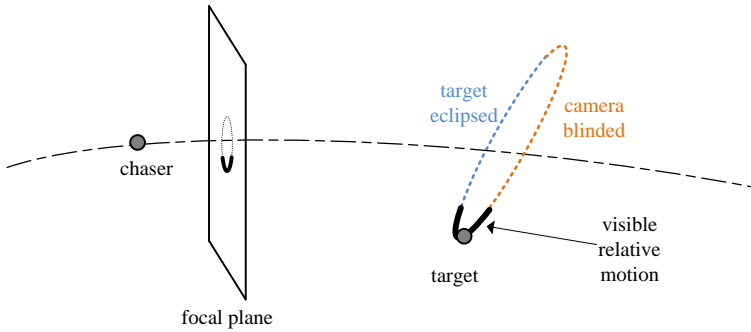
Figure 2.7: Limited visible relative motion in low Earth orbits. The part of the trajectory which is not visible is represented by a dashed line.

The second major difference with respect to ARGON is due to the low altitude of the BIROS orbit. Combined with the fact that BIROS and BEESAT-4 greatly differ in shape and mass, thus featuring a very different ballistic coefficient (*c.f.*, Table 2.2), this induces a strong unknown differential drag which has to be estimated as part of the relative navigation process.

The third difference comes with the limited onboard resources and the constraints

posed by the satellite. In particular, it had been chosen to make use of one of the existing star cameras as shown in Fig. 2.6 to follow the picosatellite instead of using a dedicated tracking camera like in PRISMA, resulting in a non-nominal attitude profile which, in turn, conflicted with the power and thermal requirements. As a result, dedicated phases were necessary to cool down the satellite during which the target was not anymore in the field of view. Furthermore, BIROS was equipped with a single-direction thruster, so that dedicated slews of the satellites were necessary to execute maneuvers, reducing further the time allotted to observe the target. Last but not least, the frequency of observations was limited to one image every 30 seconds to cope with the limited data bandwidth and computational power of the onboard computer. In fact, the star tracker was interfaced to the onboard computer with a serial link, requiring 10-15 s to transfer a single image comprising 60 Regions of Interest. The onboard computer was based on an industrial Power PC 823e processor without floating point support and clocked at 48 MHz, yielding a computational speed of 66 MIPS [65]. In view of this limited power, several seconds were necessary to perform the image processing activities. As highlighted in the following chapters, these constraints (poor visibility and spacecraft limitations) contributed to a very limited amount of measurements.

The final major difficulty of AVANTI lies in the lack of any external reference for cross-validation. Contrary to ARGON, no differential GPS could support the experiment, making the monitoring of the formation safety and the subsequent analysis of the system performance much more difficult. As already explained, the results of the precise orbit determination done on ground are the best possible *post facto* knowledge of the state of the formation. This optimistic statement should not hide the fact that in such conditions (degraded visibility conditions and strong orbit perturbations), angles-only relative orbit determination in low Earth orbit remains a delicate task. As a result, collecting valuable in-orbit experience regarding the system behavior and the achievable performance was also part of the experiment. In order to obtain a unique independent assessment of the accuracy of the relative trajectory reconstruction, a short ground-based radar tracking campaign has been carried out during the commissioning of AVANTI using the German TIRA (Tracking and Imaging Radar) ground station of the Fraunhofer-Institut für Hochfrequenzphysik und Radartechnik (Institute for High Frequency Physics and Radar Techniques).

More than two months in orbit were necessary for the successful completion of the experiment, most of the time being dedicated to a thorough commissioning of the spacecraft. Dealing with spaceborne autonomous close-proximity formation-flight, it was indeed necessary to ensure that all subsystems involved in the experiment were working properly before starting an autonomous approach. As depicted in Fig. 2.8, following the ejection of BEESAT-4 on 9 September 2016, several rendezvous and recede activities with different levels of autonomy could be already exercised during the commissioning phase, generating a valuable collection of images at different ranges. Once the satellite was commissioned, the full featured experiment (called *autonomous rendezvous* in Fig. 2.8) could start on 19 November 2016, during which two autonomous approaches were performed, first from 13 km to 1 km, then from 3 km to 50 m [62].

The problem of angles-only navigation presents different flavors depending on the intersatellite distance. Since the complete AVANTI experiment (including the commis-
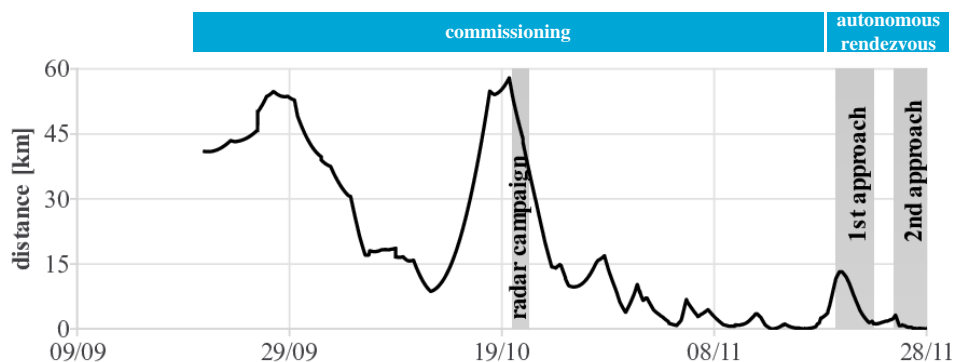
Figure 2.8: Intersatellite distance during the AVANTI campaign in 2016.

sioning phase) covered the full range between 50 km to 50 m, the following scenarios could be investigated during the experiment:

- **Far-range field** (during the commissioning phase: 21 September to 6 October and 15 to 23 October). This corresponds to the first contact with the target object at far-range, typically for separations of a few tens of kilometers. The main difficulty here is to be able to distinguish the target and to perform a meaningful orbit determination given the hardly observable variations of relative motion at this distance.

- **Far to mid-range approach** (during the commissioning phase: 7 to 14 October and 24 October to 18 November; autonomously: 19 to 23 November). This range covers the main objective of the AVANTI experiment, namely the ability to autonomously navigate towards a desired hold point at a few hundred meters distance, far enough to guarantee homogeneous visibility and brightness conditions throughout the entire approach.

- **Close-range field** (autonomously: 25 to 28 November). When decreasing further the distance, the increasing brightness and target size greatly degrade the accuracy of the line-of-sight measurements, posing new challenges to the relative navigation.

The peculiarities encountered at different distances will be described more in details in Sections 4.4 and 5.4.

2.2. DEVELOPMENT, SIMULATION AND TEST ENVIRONMENTS

The scarcity of real space missions makes a flight opportunity an exceptional occasion for every research team and a unique chance which should not be missed. However, it can be challenging to design a system able to perform in orbit if the resources and time allotted to the development are limited. The design, implementation and operations of the AVANTI experiment were made by a small team of two people within a limited time span of about four years. A few engineering solutions have been identified during the de-

velopment of AVANTI which have undoubtedly contributed to its successful realization. They are summarized in what follows.

2.2.1. Model-Based Multi-Satellite Simulator

The more complex a system, the more acute the need for a comprehensive and highly realistic simulation environment. In the case of AVANTI, it early became obvious that such a tool would be needed in view of the numerous challenging and sometimes conflicting interactions posed by the experiment (see [66] for further details). In order to simultaneously address all this issues, an advanced simulation environment is required to properly model the perturbations acting on the system, understand the interactions between the different spacecraft components, assess the impact of the error sources, define and verify the behavior in case of contingencies, etc. Understanding the main factors impacting the navigation performance in the AVANTI experiment allows deriving the following requirements in terms of level of realism:

- The simulator shall create realistic pictures of the sky, affected by image distortion and comprising additional random non-stellar objects. Rationale: in low Earth orbit, the probability to image other debris is non negligible, which might impact the target detection performance.

- The simulator shall allow for translational control during the execution of a scenario, shall simulate the typical maneuver execution errors and shall offer the possibility to simulate failures of the thruster system. Rationale: as described later in Chapter 3, angles-only relative navigation suffers from weak observability, requiring the execution of maneuvers to solve the ambiguity in the range determination. These maneuvers are part of a rendezvous guidance profile, which has to be done safely, and which has to be autonomously computed onboard. Maneuver execution errors affect the relative navigation and guidance performance.

- The simulator shall allow for rotational control during a scenario and shall simulate the time required to slew. Rationale: since BIROS does not have 3D maneuvering capability, the spacecraft needs to rotate to execute an orbit maneuver, in which case the target spacecraft might exit the field of view of the camera. The same happens if the communication antennas need to be directed to the ground stations.

- The simulator shall realistically model the target visibility. Rationale: eclipses and camera blinding due to the Sun greatly affect the target visibility and relative navigation performance.

- The simulator shall include attitude-dependent power and thermal models. Rationale: the camera has to be directed towards the target picosatellite, resulting in a non-nominal attitude profile, which impacts the power and thermal budget of the chaser spacecraft.

- The simulator shall realistically model the orbit perturbations. Rationale: the high differential drag encountered at low altitude (500 km) greatly disturbs the relative navigation and control algorithms.

The design of the AVANTI experiment could fortunately rely on DLR's in-house Multi-Satellite Simulator (MSS) [67], which had already been used in the past to design advanced autonomous embedded formation-flying systems like the TanDEM-X Autonomous Formation Flying System [9] or the SAFE experiment with PRISMA [57]. MSS is based on the C++ libraries provided in [68] and comprises a collection of aerospace components to accurately model the environment (gravity field, orbital perturbations, position of the celestial objects, reference frames) as well as key sensors and actuators. This simulation environment originally focused on GNSS-based formation navigation and control. Therefore new developments were necessary to cover the problem of camera-based navigation. Still, the majority of the models were already existing and validated, resulting in a significant gain of time during the development phase of the simulation tools. Two models needed to be added to support the experiment:

- **A camera model**, able to create representative images. Here, some trade-off were necessary, because the simulation of high-fidelity images is an extremely difficult task. However, dealing with line-of-sight navigation, most of the difficulties could be avoided: all objects imaged by the camera (stars, planets, artificial satellites) can be approximated by a Gaussian point spread function, whose shape only depends on the object magnitude. Still, the model has to account for typical error sources in order to faithfully model the reality: background noise, optical distortion, aberration, hot spots (pixels which are constantly bright), presence of other satellites, non-visibility during eclipse and blinding due to the Sun. The execution of ARGON prior to AVANTI was of great help, because the camera model could be calibrated using real images [57].

- **A specific spacecraft model**, able to mimic the relevant characteristics of the satellite (time necessary to slew, thermal and power behavior, maneuver execution and attitude guidance errors).

Despite the considerable efforts devoted to the realization of a high-fidelity simulation environment, it is always wise to have in mind that a model might have some deficiencies. For AVANTI, the most difficult modeling aspect was the visibility prediction. Dealing with a very small target whose apparent magnitude at several tens of kilometers reaches the sensitivity limit of the camera (magnitude 6-7), the maximal distance at which the spacecraft could be imaged was not precisely known. Similarly, the time during which the camera was blinded by the Sun was also extremely difficult to model, because of the multiple reflections of the stray lights with the spacecraft structure which might affect the camera.

Being written in C++, the MSS framework can support a large variety of missions. For the past research activities, a MATLAB/Simulink® wrapper had been created by the means of so-called S-Functions. For AVANTI, it appeared more convenient to embed the models within a proprietary graphical interface (shown in Fig. 2.9) able to offer more flexibility (such as to display in real-time simulated images) and able to integrate custom tools (creation of procedures, control of an external optical simulator).
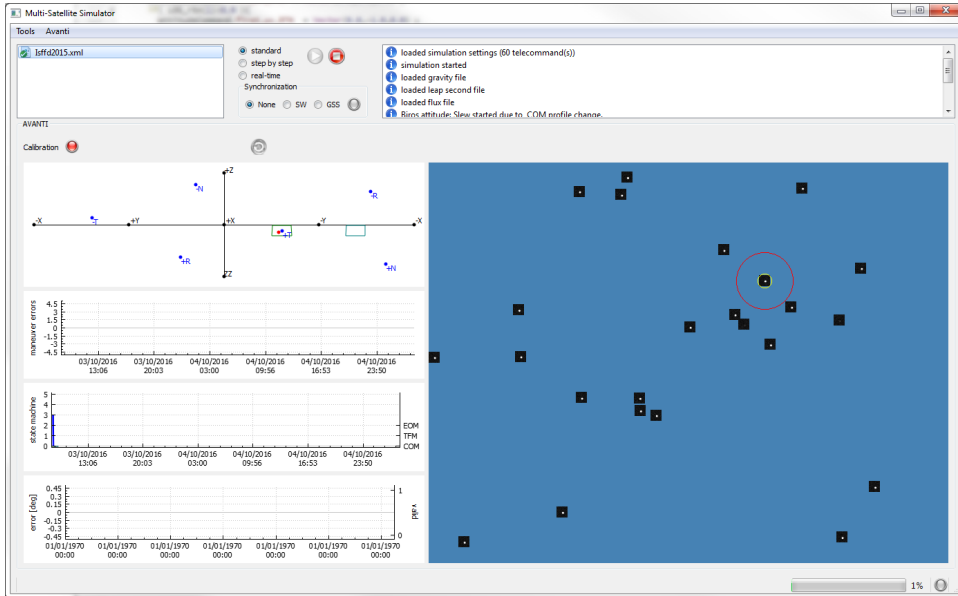
Figure 2.9: MSS simulator used to simulate the AVANTI experiment.

2.2.2. Rapid Software Prototyping

During the development of the flight software, two aspects greatly reduced the implementation efforts.

1. **Interfacing from the very beginning the flight software with an existing simulation environment**. In order to speed up the development process, it is tempting to begin with the implementation of the flight software at a very early stage, while the underlying core algorithms are still under investigation and development. This approach presents the advantage of providing well in advance relevant system information (telemetry budget, interface definition, system behavior, etc.). On the other hand, the development of novel complex GNC algorithms might require the use of an already existing and validated external high-fidelity simulation environment, as described in the previous section. This poses severe constraints in terms of software design since, having been developed and validated prior to the start of the project, this simulation environment is not necessarily compatible with the software environment required by the flight software (featuring, for example, a different operating system or programming language).

   The solution to this issue consists in creating a separated container where the experiment flight-software is running and where the key functionalities of the on-board operating system are implemented. This container can take the form of an external computer, of a virtual machine, or simply of a dynamic library running on the simulation computer, which is then called by the different functions and models composing the simulation.
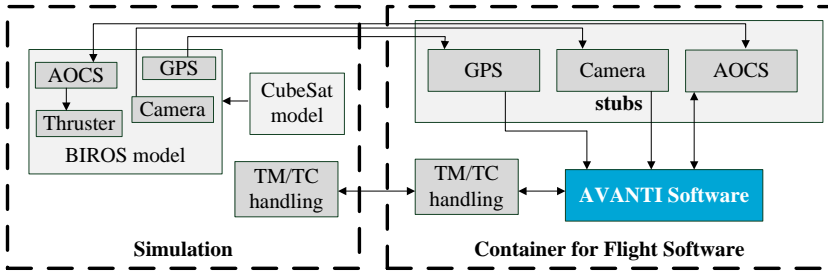
2

Figure 2.10: Interfacing an existing validated simulation environment with the flight software.

Figure 2.10 provides a graphical representation of this approach. The flight software is implemented in the container using the target programming language and relies on the libraries provided by the target operating system (access the other devices of the satellites bus, timing and threading functions, handling of telemetry and telecommands, etc.). The main advantage of this approach is that the flight software does not need to be adapted for the sake of the simulation. In fact, it uses the same objects and methods as the ones available on the satellite bus, so that the blue component in Fig. 2.10 is identical to the flight version. As a result, there is no need to keep several versions of the software for different purposes: the flight version is directly used during the early investigations of the GNC algorithms and grows in maturity as the developments mature.

Inside the container, some software stubs need to be implemented as gateways to the simulation models (and are thus totally different from their equivalent flight version). For example, a model of a GPS receiver computes a simulated GPS navigation fix in the simulation environment, which is sent to the stub of the object instance interfacing the GPS receiver. The stub, which is fed with simulation data, provides this simulated navigation fix when requested by the flight software as if data from real hardware components were read. Of course, it is also needed to modify the handling of time within the container, so that the algorithms can run in accelerated time (the operating system is nominally designed to work in real-time, which is not suited to the design of the GNC algorithms). Note that there is no general recipe for such a low-level modification which is specific to the operating system. For AVANTI, this has been done by replacing the RODOS timing functions (which controls the thread scheduling) with a modified version which is externally triggered by the simulation environment.

2. **Interface definition as meta data**. Interfaces are one of the most important aspects for the successful integration of a subsystem into a complex system. As a result, special care must be taken to precisely define the interfaces in the very early phases of the project. The interfaces definition is however subject to frequent updates throughout the development process. Automation can be of great help to reduce the efforts needed to reflect the interface changes in the documentation and software. It has been found useful to rely on a central database serving as backbone for the development and documentation tools. A dedicated library

has been developed in form of a C++ class for this purpose, comprising several methods to generate different products (documents, code) once the database has been loaded. Some of these functions are illustrated with a yellow background in Fig. 2.11. The library takes advantages of the Object Linking and Embedding (OLE) automation offered by Microsoft ActiveX to access and write inside documents from an external application [69].
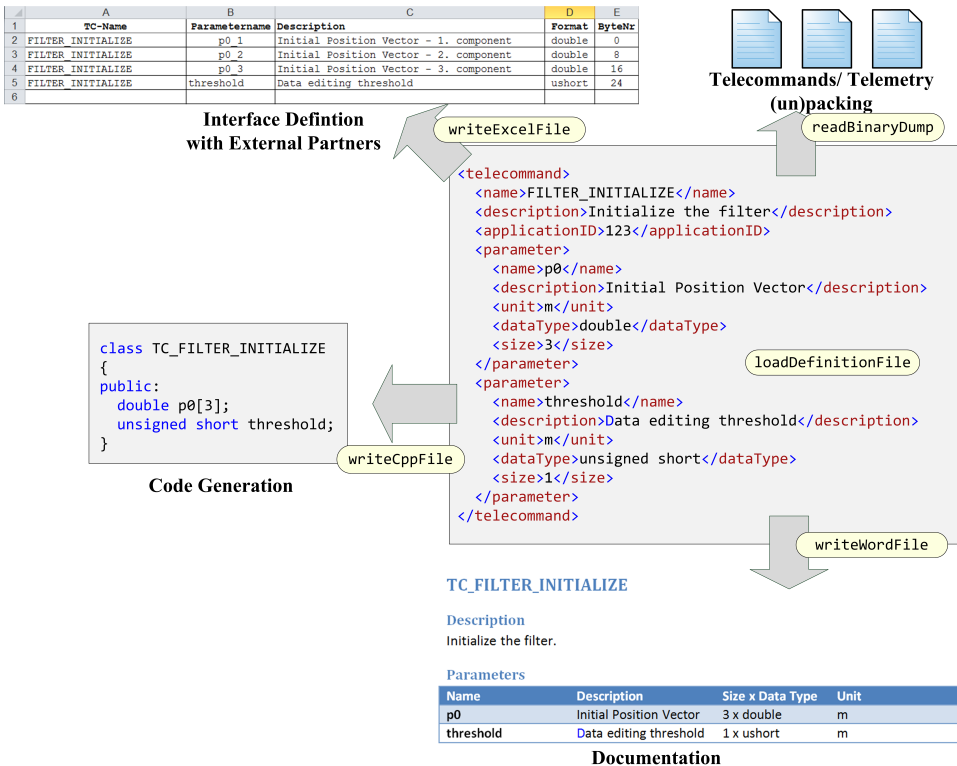
Figure 2.11: Centralized interface database as backbone for several interfacing tasks.

The database contains:

- The inputs/outputs of each component of the GNC system (such as filter, guidance, safety monitoring, or image processing modules).

- The telecommands, comprising Application ID, description, and list of parameters, etc.

- The telemetry packets, comprising Application ID, description and content, which is made of a selection of the outputs of the GNC components.

As depicted in Fig. 2.11, the centralization of all interface information into a unique database allows for a rapid update of the documentation and software, and ensures the overall consistency of the interfaces. In particular, the update process takes care of:

- Generating the C++ objects describing the inputs and outputs of every GNC component.

- Generating the C++ functions to generate telemetry packets by assembling the outputs of the GNC components and to read the content of a packet.

- Updating the Interface Control Document and filling the interface database of the external partners (such as Ground Segment).

Overall, this approach based on a centralized database presents many advantages, which are only tempered by two small drawbacks. First, this requires the development and maintenance of additional tools to support the aforedescribed automation (note that this effort is greatly reduced once the tools already exist). Second, this might result in a lack of flexibility during the definition of the interfaces if, for example, non-standard data types have to be introduced but are not supported by the database.

2.2.3. HARDWARE-IN-THE-LOOP CAPABILITY

Last but not least, the ability to include the real sensor hardware in the simulation environment greatly improves the validation and test activities. Here again, the construction of such testbeds can require considerable resources. The basic underlying idea consists in physically simulating the environment sensed by the camera. This can be realized by building a model of the target spacecraft and illuminating it in a realistic way (as done with the DLR's European Proximity Operations Simulator facility (EPOS 2.0) [70]), or by actively stimulating the sensor with electromagnetic radiations generated by a dedicated device. This latter approach is much more flexible and more adapted to far-range navigation, and was thus retained to support the AVANTI experiment. However, reproducing the reality in this way can be extremely challenging, even for simple line-of-sight navigation. If the objective of the hardware-in-the-loop facility consists in assessing the sensor performance, dedicated efforts have to be made in the realistic modeling of the quantity of light emitted by the different objects of the imaged scene and in compensating the possible optical distortions. Such realistic test facilities are used for the development of star trackers and could unfortunately not be used for AVANTI because they do not foresee the possibility to simulate in real-time a moving artificial satellite.

As a result of the needs and constraints, a simple solution was preferred. In view of the difficulty of simulating realistic images, it has been decided to restrict the scope of the hardware-in-the-loop facility to a functional verification tool. In fact, performance analyses could already be conducted to a large extent using the flight-data collected during the ARGON experiment. For AVANTI, only additional functional tests were needed to verify the proper interfacing of the camera with the flight software, to perform software profiling activities using the target computer and to conduct end-to-end tests during the integration of the satellite.

A minimalistic approach was shown to be enough to satisfy these basic functional needs. In fact, a star camera often recognizes the celestial objects based on the geometry of the star pattern, and the μASC is no exception. Thus, the luminosity of the stars does not need to be modeled to ensure proper recognition of the spacecraft attitude. In addition, a star camera tolerates some angular errors (typically up to a few arcminutes

[71]) to compensate for its own optical distortion, making the introduction of complex and expensive compensation optics unnecessary.
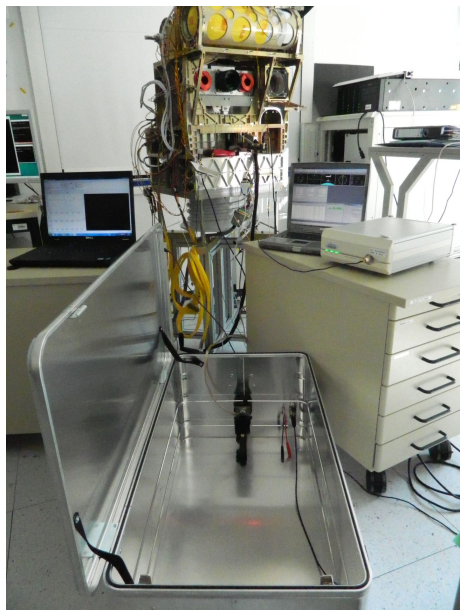
(a) Integration tests in the clean room.
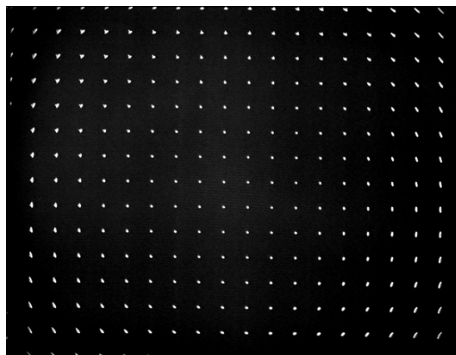
(b) Test image using a grid of pixels.
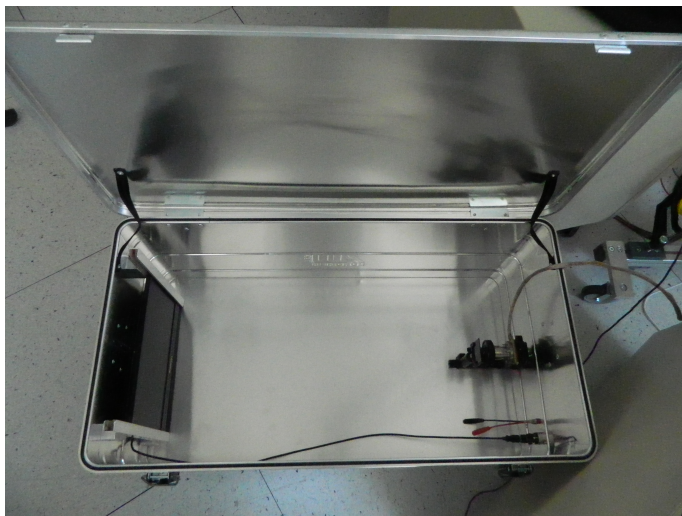
(c) Content of the box. The LCD display is on the left.

Figure 2.12: Minimalistic optical simulator built to support the development and testing of the AVANTI experiment.

As shown in Fig. 2.12, the design adopted for the AVANTI experiment simply consists

in a 90 cm long box, in which a LCD display is fixed at one side and an engineering model of the star tracker is located at the other side. Because the star tracker expects rays of light coming from a source located at infinity, a collimation has to be introduced. This is realized with a simple convex lens with a focal length of 70 cm. The stars are simulated by activating single pixels of the display. As shown in Fig 2.12b, the images taken by the star tracker are affected by distortion, induced by its own optics and by the use of a simple convex lens. However, in the center of image, the quality is good enough to derive attitude information and simulate a moving target object. This non-stellar moving object was simulated in the same way as the stars, by activating a single pixel on the screen and updating in real-time its position based on a model of the relative dynamics.

Despite its simplicity and poor simulation performance, this basic testbed revealed itself incredibly useful during the tests, showing that simple engineering solutions might often be as suited as much more complex and expensive alternatives.

2.2.4. SOFTWARE VERIFICATION AND VALIDATION

The afore-presented tools are in fact part of a larger integrated methodology employed for the verification and validation of the AVANTI autonomous embedded system, which is depicted in Fig. 2.13 and is commonly known as V-diagram. According to the diagram, the development of the flight software is the result of a top-down cascade of activities. Starting from the definition of the top level needs (what shall the system do?), the system requirements are derived, followed by the architectural and detailed design. Finally, the system components are implemented during the coding phase.
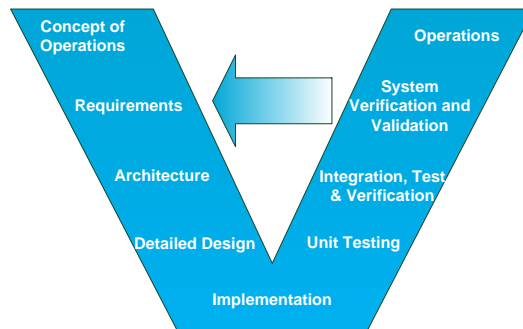
Figure 2.13: Graphical representation of the Verification and Validation process, inspired from Reference [72].

On the contrary, the verification and validation activities are done in a bottom up approach. The proper implementation of the components is verified by the means of unit tests. This process is entirely automated and runs at every change of the flight software. Unit testing plays a fundamental role during the development, since it accompanies all the components from their very early phase up to their most mature version. Numerous software errors and flaws could be successfully detected using this method during the development of AVANTI.

The verification of the interactions between the different components constitutes the second step. This is first performed using the simulation environment and then using

the real sensor in the loop during integration tests.

Finally the system behavior and performance are validated using the simulation environment during the development phase and then during commissioning activities following the launch. Here again, it has been found extremely useful to early define reference scenarios which are well understood and allow for an immediate comprehension of the advantages and drawbacks induced by every further modification of the algorithms.

At a later stage, the experience gained during operations provides relevant feedback on how the system could be improved, paving the way for the next generation of product.

It has to be mentioned that this verification and validation flow represents a desired and idealized process. In reality, vicissitudes of life (lack of communication, inexperience, unexpected problems) make this process nonlinear and highly iterative. In view of the experimental nature of the system, it is not uncommon that new requirements arise at a very late stage of the testing process (or even during the commissioning phase), or that components flaws are detected during operations, thus requiring software patch. During the AVANTI experiment, it was for example first discovered in orbit that the special spacecraft attitude profile required to follow the target with the camera resulted in an overheating of the spacecraft, which had not been properly simulated before launch. Therefore, a new functionality was introduced in the AVANTI software (the so-called *cool-down* mode, see Fig. 4.18) to automatically orient the radiators away from the Sun every time the spacecraft temperature reached a certain threshold.

Still, the adopted validation and verification approach revealed itself to be a fundamental tool to ensure the quality of a complex system.

3

ANGLES-ONLY RELATIVE NAVIGATION

This chapter describes the core principles of relative navigation using line-of-sight measurements and addresses the problem of observability. Relevant mathematical and astrodynamical concepts are also introduced to ease the comprehension of the following chapters.

3.1. Overview

The principles of line-of-sight navigation are straightforward and can easily be recalled using a two-dimensional representation. As depicted in Fig. 3.1a, two bearing angles $\{\alpha_A, \alpha_B\}$ to a static object located at position C and measured at known positions A and B are enough to determine in the plane spanned by A, B, and C the unknown position C. This method is called triangulation and has been known since thousands of years: it was, for example, already used by Hero of Alexandria [73] for the design of its dioptra, an ancient astronomical and surveying instrument. If the object is moving, the two observations have to be simultaneously taken from two different observers at time t to determine the position $C(t)$. Alternatively, if the motion of the object can be modeled, one single observer can determine the resulting trajectory by taking measurements at different epochs (Fig. 3.1b). Since the motion model relies on the initial position $C(t_0)$ and velocity $\dot{C}(t_0)$ of the object, at least four observations are necessary to solve the problem in the two-dimensional space.

Such a case is, however, rarely encountered: most of the time, the motion of an unknown moving object (car, airplane, animal, etc.) cannot be modeled nor predicted because the object is actively controlling its trajectory, and this control action is unknown to the observer. On the contrary, if no action is exerted by the moving object to alter its trajectory, the motion obeys the laws of dynamics and can be modeled, provided that the natural forces acting on the object are known and can be mathematically described. This favorable case can be advantageously exploited in astrodynamics, where the physical forces are well understood and where most of the objects are passive (except for some artificial satellites). The main drawback of this method lies in the possible singularity which might appear if identical measurement profiles exist for different initial conditions. An example is shown in Fig. 3.1c. In this case, two state vectors at initial time t_0 can result in different trajectories $C(t)$ and $D(t)$ yielding exactly the same set of measurements: the state determination suffers from range ambiguity. Thus the value of the initial state cannot be determined from the system output (*i.e*, the line-of-sight measurements) and the system is said unobservable. Note that this issue would be immediately solved if only one single distance measurement were available.

(a) Triangulation.   (b) Trajectory determination   (c) Unobservable motion.
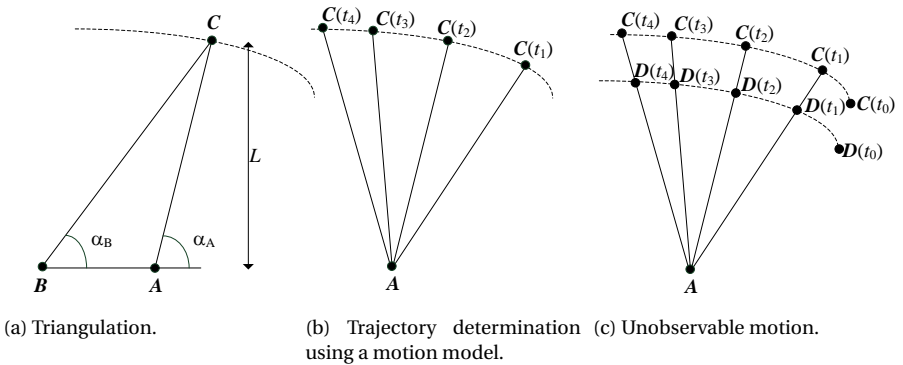   using a motion model.

Figure 3.1: Determination of a position or trajectory using line-of-sight measurements.

The use of angles-only observations has early been adopted in astrodynamics in order to determine the trajectory of asteroids. In this case, the problem is three-dimensional and the observations are direction vectors which can be parameterized by two angles. In view of the large distance to the asteroid, a simple triangulation method would not work in a real application because the baseline $\overline{AB}$ between two observers on Earth would be too small to yield enough observability (*i.e.*, A and B would be almost confounded in Fig. 3.1a). Fortunately, the motion of objects in space can be modeled with great precision, so that a trajectory determination as represented in Fig. 3.1b becomes possible, with the difference that at least three independent observations are now required to fully determine the motion: three pairs of angles to solve the six unknown components of the initial state vector. Different methods have been developed to solve this problem, the oldest one dating back to more than 200 years (Laplace and Gauss, respectively, developed their own algorithms in 1780 and 1809 [74]).

Estimating the relative state of a target satellite during a rendezvous in orbit is very similar to the orbit determination of asteroids, except that the observations are taken by a chaser satellite instead of a station on the Earth. This difference has a dramatic consequence: the system becomes unobservable (in reality it is only weakly observable, as described in Section 3.3.2). This property can be intuitively understood using Fig. 3.2. Before initiating a rendezvous, the orbit of the chaser is first altered relying on ground-based absolute navigation to coarsely match the target orbit. Thus the chaser is ultimately co-moving with the target along a common orbital path. This configuration greatly differs from an observer which would be fixed in space. Fig. 3.2 depicts the case for which the chaser and target are flying on similar orbits with identical semi-major axis. As seen later in this chapter, this configuration results in an elliptical relative motion with a fixed mean separation between the satellites. The projection of the relative motion on the focal plane of the chaser camera can be well measured, but not the inter-satellite separation: an infinity of configurations corresponds to one given measurement profile.
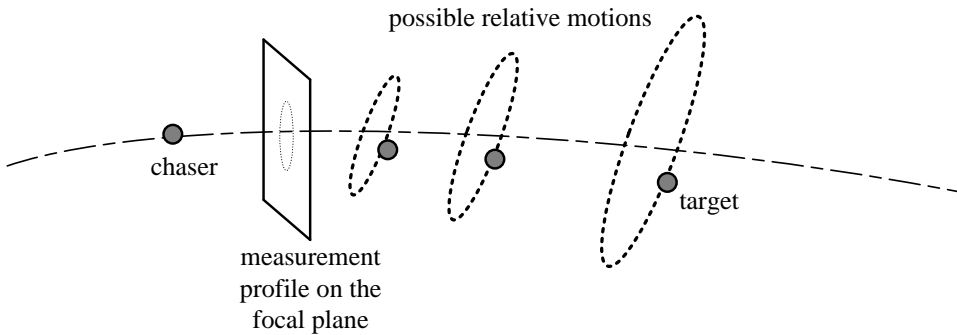

Figure 3.2: Range ambiguity in the determination of the relative motion: several solutions match the same measurement profile.

This limitation constitutes a severe difficulty when estimating the relative motion using a single observer but, unfortunately, no other affordable alternative exists when

dealing with noncooperative objects at far-range. As explained in the introduction, the use of active ranging devices would result in high power consumption. The method of triangulation could also solve the range ambiguity but would require the use of two different cameras separated by a very large baseline. The exact computation of the distance L estimated by measuring two angles α_A and α_B as shown in Fig. 3.1a is:

$$L = \overline{AB} \frac{\sin\alpha_A \sin\alpha_B}{\sin\alpha_A + \sin\alpha_B}. \tag{3.1}$$

Without entering into a cumbersome variance analysis of this triangulation equation, a rough order of magnitude of the offset required to yield exploitable measurements can be obtained by considering the angle subtended by a camera offset $\overline{AB}$ seen from a distance $L = 50$ km. This angle is smaller than the typical sensor noise $\epsilon = 40$" if the baseline $\overline{AB}$ is smaller than 10 m. Thus, a baseline of several times this value would be needed to discriminate the measurements from the sensor noise and solve the range ambiguity. Alternatively, this could also be done using two chaser satellites simultaneously observing the same target, but this would dramatically increase the cost and system complexity. Thus, the single-observer strategy is the most suitable method for far- to mid-range angles-only relative navigation. When reaching the close-range field, the shape of the object becomes visible. Thus, other optical methods become possible to directly estimate the distance between the spacecraft, such a stereo vision using two cameras or pose estimation by measuring the shape of the model and comparing it to a known model [75].

3.2. RELATIVE MOTION MODELS

3.2.1. INTEGRATING THE EQUATIONS OF MOTIONS

It is now assumed that a rendezvous in orbit is initiated. For this purpose, the orbit of a chaser spacecraft has been beforehand modified to match the orbit of the desired target satellite, and the distance between the satellites has been reduced to less than 50 km. The fact that both spacecraft are co-moving in close vicinity makes a description of the relative motion more simple and convenient. It is assumed that the absolute chaser state $\boldsymbol{y}_c^T = (\boldsymbol{r}_c^T, \boldsymbol{v}_c^T)$ expressed in an inertial frame $\mathscr{I}$ is known. Here, $\boldsymbol{r}_c$ and $\boldsymbol{v}_c$ stand for inertial position and velocity of the chaser satellite. In low Earth orbit, this is easily achieved by equipping the chaser with a GNSS receiver. The inertial target state $\boldsymbol{y}_t^T = (\boldsymbol{r}_t^T, \boldsymbol{v}_t^T)$ is instead unknown. If $\Delta\boldsymbol{r}(t) = \boldsymbol{r}_t(t) - \boldsymbol{r}_c(t)$ denotes the inertial relative position at time t, the most general approach to describe the relative motion consists in integrating Newton's second law of motion:

$$\Delta\ddot{\boldsymbol{r}}(t) = \frac{\boldsymbol{F}_t(t)}{m_t} - \frac{\boldsymbol{F}_c(t)}{m_c}, \tag{3.2}$$

where m and $\boldsymbol{F}(t)$, respectively, denote the mass and force acting on the spacecraft. Here, the subscript c and t are introduced to denote quantities related to the chaser and target.

The main advantages of this approach are the flexibility and achievable model accuracy, because $\boldsymbol{F}_i(t)$ can be described with high precision and complexity. This is not true anymore if the target is actively performing unknown orbit maneuvers, but this case is not considered in this research. This strategy comes, however, at the cost of high computational efforts because the integration has to be numerically done as there exists no

analytical solution for such a general problem. However, if the motion is Keplerian (*i.e.*, the gravity field created by the Earth is approximated as a mass point and is the only force acting on the satellites), a simple solution exists, provided that the absolute motion is parameterized in terms of orbital elements:

$$\boldsymbol{\alpha}(t)^T = (a, e, i, \Omega, \omega, M(t)). \tag{3.3}$$

Here, the components of the vector respectively denote the semi-major axis, eccentricity, inclination, right ascension of the ascending node, argument of perigee and mean anomaly of the orbit. Note that the mean argument of latitude

$$u = \omega + M \tag{3.4}$$

can also equivalently be used in the place of *M*). In this case, the time evolution of the absolute satellite state is trivial [68]:

$$\dot{\boldsymbol{\alpha}}(t)^T = (0, 0, 0, 0, 0, n), \tag{3.5}$$

where $n = \sqrt{\mu_\oplus/a^3}$ stands for the orbit mean motion, $\mu_\oplus$ being the gravitational coefficient of the Earth. Despite this simplicity, the Cartesian relative state corresponding to this model (called nonperturbed relative motion) is not as trivial, because a nonlinear transformation $\boldsymbol{f}$ is needed to convert the orbital elements into their Cartesian representation:

$$\Delta \boldsymbol{y}(t) = \boldsymbol{y}_t(t) - \boldsymbol{y}_c(t) = \boldsymbol{f}(\boldsymbol{\alpha}_t(t)) - \boldsymbol{f}(\boldsymbol{\alpha}_c(t)). \tag{3.6}$$

3.2.2. HILL-CLOHESSY-WILTSHIRE MODEL
In view of these limitations (computational complexity of the general formulation or nonlinearity of the nonperturbed relative motion), considerable research efforts have been dedicated in the last decades to derive analytical models able to describe the relative motion in a more simple way. The first and most famous one is represented by the Hill-Clohessy-Wiltshire equations (referred as HCW in what follows), developed to study the rendezvous problem. This model describes the relative motion in the rotating Cartesian Hill frame $\mathcal{O}$ [76] whose origin is located at the center of mass of the reference satellite (chosen to be the chaser in the thesis). The axes of this local co-moving frame (also called orbital frame) are defined based on the inertial state of the reference spacecraft. The *x*-axis is along the radius vector, the *y*-axis is in the orbit plane in the direction of the motion, and the *z*-axis is perpendicular to the orbit plane. This frame is called Local Vertical Local Horizontal (LVLH) or RSW [77] in the literature. Note that this latter convention is named after the unit vectors $\boldsymbol{R}, \boldsymbol{S}, \boldsymbol{W}$ defining the local orbital frame in [77] and oriented, respectively, in radial, along-track and cross-track directions. This work uses a different but equivalent naming convention, where the *x*, *y*, *z* directions are called Radial-Tangential-Normal (or R-T-N) as depicted in Fig. 3.3. Mathematically, the unit vectors of the orbital frame $\mathcal{O}$ with respect to the inertial frame are defined as follows:

$$\boldsymbol{e}_R = \frac{\boldsymbol{r}_c}{\|\boldsymbol{r}_c\|}, \quad \boldsymbol{e}_N = \frac{\boldsymbol{r}_c \times \boldsymbol{v}_c}{\|\boldsymbol{r}_c \times \boldsymbol{v}_c\|}, \quad \boldsymbol{e}_T = \boldsymbol{e}_N \times \boldsymbol{e}_R. \tag{3.7}$$
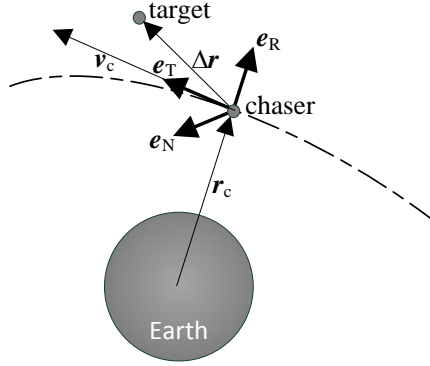
Figure 3.3: Definition of the R-T-N local orbital frame.

Note that the y direction is named tangential because this work focuses on near-circular orbits. The relative state $\boldsymbol{x}^T = (x, y, z, \dot{x}, \dot{y}, \dot{z})$ between both spacecraft is expressed in the frame $\mathscr{O}$. Three assumptions are made to derive the HCW equations: the chaser orbit is circular (*i.e.*, $e = 0$), the Earth is a point mass (*i.e.*, the motion is Keplerian), and the distance between the spacecraft is small compared to the radius of the chaser orbit (*i.e.*, $\|\Delta \boldsymbol{r}\| \ll \|\boldsymbol{r}_c\|$). Based on these assumptions, the linearized equations of motion become [78]:

$$\ddot{x} - 2n\dot{y} - 3n^2 x = 0, \tag{3.8a}$$

$$\ddot{y} + 2n\dot{x} = 0, \tag{3.8b}$$

$$\ddot{z} + n^2 \dot{z} = 0. \tag{3.8c}$$

This system of first order ordinary differential equations is analytically integrable, yielding the following solution of the initial value problem:

$$x(t) = 2\left(2x_0 + \frac{\dot{y}_0}{n}\right) - \left(3x_0 + 2\frac{\dot{y}_0}{n}\right)\cos n\Delta t + \frac{\dot{x}_0}{n}\sin n\Delta t, \tag{3.9a}$$

$$y(t) = y_0 - 2\frac{\dot{x}_0}{n} - 3\left(2x_0 + \frac{\dot{y}_0}{n}\right)n\Delta t + \frac{2\dot{x}_0}{n}\cos n\Delta t + 2\left(3x_0 + 2\frac{\dot{y}_0}{n}\right)\sin n\Delta t, \tag{3.9b}$$

$$z(t) = z_0 \cos n\Delta t + \frac{\dot{z}_0}{n}\sin n\Delta t, \tag{3.9c}$$

$$\dot{x}(t) = 3x_0 n \sin n\Delta t + \dot{x}_0 \cos n\Delta t + 2\dot{y}_0 \sin n\Delta t, \tag{3.9d}$$

$$\dot{y}(t) = 6x_0 n \left(\cos n\Delta t - 1\right) - 2\dot{x}_0 \sin n\Delta t + \dot{y}_0 \left(4\cos n\Delta t - 3\right), \tag{3.9e}$$

$$\dot{z}(t) = -n z_0 \sin n\Delta t + \dot{z}_0 \cos n\Delta t, \tag{3.9f}$$

where the subscript $\square_0$ denotes the initial value taken at reference epoch t_0, and introducing $\Delta t = (t - t_0)$. Equations 3.9a to 3.9f show that the relative motion is coupled with the absolute motion of the formation by the term

$$n\Delta t = u(t) - u_0. \tag{3.10}$$

The general solution of the HCW homogeneous linear ordinary differential equations is conveniently expressed using a fundamental matrix $\mathbf{\Phi}$ such as

$$\boldsymbol{x}(t) = \mathbf{\Phi}(t, t_0)\boldsymbol{x}(t_0), \tag{3.11}$$

$\mathbf{\Phi}$ is called state transition matrix and directly relates the state at different times. This formulation is of great relevance since it allows taking benefit from the powerful linear theory, widely used for state estimation and control. The state transition matrix can be finally derived using Equations 3.9a to 3.9f:

$$\mathbf{\Phi}(t, t_0) =$$

$$\begin{pmatrix} 4-3\cos n\Delta t & 0 & 0 & \frac{1}{n}\sin n\Delta t & \frac{2}{n}(1-\cos n\Delta t) & 0 \\ 6(\sin n\Delta t - n\Delta t) & 1 & 0 & \frac{2}{n}(\cos n\Delta t - 1) & \frac{1}{n}(4\sin n\Delta t - 3n\Delta t) & 0 \\ 0 & 0 & \cos n\Delta t & 0 & 0 & \frac{1}{n}\sin n\Delta t \\ 3n\sin n\Delta t & 0 & 0 & \cos n\Delta t & 2\sin n\Delta t & 0 \\ 6n(\cos n\Delta t - 1) & 0 & 0 & -2\sin n\Delta t & 4\cos n\Delta t - 3 & 0 \\ 0 & 0 & -n\sin n\Delta t & 0 & 0 & \cos n\Delta t \end{pmatrix}.$$

$$\tag{3.12}$$

3.2.3. ALTERNATIVE MODELS

Simplicity and linearity are the two major strengths of the HCW model, which also explains its popularity. However, it is only valid under the following assumptions:

1. small intersatellite distances (*i.e.*, $\|\Delta\boldsymbol{r}\| \ll \|\boldsymbol{r}_c\|$)

2. circular orbits

3. Keplerian motion

These limitations can easily be explained by the fact that the HCW equations were mainly derived to support the spacecraft close-proximity and docking applications in the 60's, thus assuming small separation and limited duration of the rendezvous. Since then, new applications in the field of navigation, guidance, control and maintenance of formations of satellites have arisen, shedding light to the deficiencies of this simple model. In the last decades, numerous research activities were conducted to remedy these issues.

In particular, Assumption #1 is due to the fact that the motion parameterization in the orbital frame $\mathcal{O}$ does not take the curvature of the orbit path into account. The resulting errors are not negligible anymore for separations reaching several tens of kilometers, which is clearly a problem when addressing far-range rendezvous. This issue can be mitigated using a curvilinear system [79] or using a parameterization based on relative orbital elements [80, 81].

Assumption #2 constitutes a problem if the chaser orbit is elliptical (which is not the case for this research). Tschauner-Hempel [82] and Yamanaka-Ankersen [83] have both derived models able to deal with elliptical relative motion. Here again, a parameterization based on orbital elements such as provided in [81] is also well adapted to take the eccentricity of the reference orbit into account.

Finally, Assumption #3 is a real problem in LEO, where for example the Earth's oblateness strongly influences the orbital motion, causing secular and periodic variations of the orbital elements, and where atmospheric drag might also have a strong impact, depending on the spacecraft altitude and on the difference in the ballistic coefficients of the two satellites. In the presence of a non-spherical gravity field, the orbital elements corresponding to a given Cartesian state vector are named *osculating*. If the motion were Keplerian, they would stay constant. Instead, they vary over time because of the variations of the gravitational potential. The usual approach to deal with the nonhomogeneous mass distribution of the Earth consists in computing the *mean* orbital elements (*i.e.*, by removing the short- and long-term periodic oscillations) to isolate their slowly varying secular variation [84, 85]. The contribution of this secular effect is then introduced to improve the modeling of the relative dynamics. The conversion between osculating and mean orbital elements is performed using averaging techniques applied to analytical orbital theories [84, 85]. The geopotential perturbation depends on the position of the satellite with respect to the Earth and is therefore almost identical for two spatially close spacecraft. Thus, in a first approximation, the mean and osculating relative orbital elements might be considered identical if such an approximation is compliant with the required accuracy. This is illustrated in Table 3.1, where a formation of two spacecraft flying on almost identical orbits and separated by 5 km is defined. At this distance, the simple difference of osculating elements $\boldsymbol{\alpha}$ and mean elements $\bar{\boldsymbol{\alpha}}$ yield similar results (especially for the relative inclination and relative right ascension of the ascending node), but notable differences for the other relative orbital elements already appear. Thus, approximating relative mean and osculating elements might be a problem when designing control laws based on relative orbital elements. This is the case, for example, if a fine control (at meter level) of the intersatellite distance is required. According to Eq. 3.15 (introduced later in this chapter), a relative semi-major axis error of about 8 m resulting from such approximation would translate into along-track errors of about $3\pi \times 8\text{m} \approx 75$ m after one orbit.

Table 3.1: Example of relative orbital elements for a close formation with 5 km intersatellite distance. $\boldsymbol{y}_c$ and $\boldsymbol{y}_t$ are the absolute inertial state vectors of the chaser and target at a given epoch.

$\boldsymbol{y}_c$ [m,m/s]	(2220310	633762	-6815160	7015.79	-1138.41	2170.52)
$\boldsymbol{y}_t$ [m,m/s]	(2224938	633095	-6813904	7014.08	-1138.53	2175.32)
$\boldsymbol{\alpha}_t - \boldsymbol{\alpha}_c$ [m,-]	(-2.29	1.96×10^{-5}	-4.24×10^{-6}	4.22×10^{-5}	-0.0055	0.0062)
$\bar{\boldsymbol{\alpha}}_t - \bar{\boldsymbol{\alpha}}_c$ [m,-]	(-10.00	1.63×10^{-5}	-4.17×10^{-6}	4.21×10^{-5}	-0.0126	0.0133)

Consequently, a careful distinction between mean and osculating quantities is often necessary. The non-homogeneous mass distribution of the Earth generates a gravity field that can be modeled through a potential function comprising zonal, tesseral, and sectorial terms [86]. With respect to the uniform mass distribution, the main perturbation effect is produced by the second order zonal contribution (called J_2). Among the relative motion models that include the secular effect produced by J_2, one may mention the contributions done by Sedwick-Schweighart [87], by Gim-Alfriend [81], and the model described by [88] and presented in detail in the next section. These models are based on the propagation of mean relative orbital elements. Thus, if the relative state in a Cartesian frame needs to be retrieved out of these relative motion models, it is first

required to convert the mean relative orbital elements into osculating quantities, which are finally used to compute the Cartesian relative position and velocity.

This section does not pretend to provide a comprehensive and comparative overview of all the existing models. Such a survey can be found in [89]. Instead, it aims at indicating that, currently, several models exists, based on different possible parameterizations and offering distinct benefits, depending on the specific application case [90]. The model retained for this research also belongs to the class of J_2-perturbed relative motion models relying on relative orbital elements [10]. The following section will show that this model has been selected based on its operational friendliness, long-term accuracy, ability to also take the mean effect of the atmosphere into account but also on the fact that a special parameterization of the motion is adopted which is particularly suited for angles-only navigation. This model is however only valid for near-circular orbits in its current formulation. This is, however, not a limitation for this research, since all demonstration missions were flying in near-circular orbits. Note that the accuracy of several models is also later discussed in Section 3.3.3.

3.2.4. Analytical Model for the J_2-Perturbed Relative Motion
In order to address and solve the angles-only relative navigation problem, a model is needed to faithfully represent and predict the relative motion with a precision equivalent or better than the measurement noise (40") over a time span of several days. For this research, it was also required to have a computationally-light solution able to enable an onboard real-time implementation. Dealing with real demonstration missions, it was finally highly desirable to have a model able to ease the operations. The model presented in this section fulfills these requirements. It makes use of a special parameterization of the relative motion based on relative orbital elements. It has been intensively used at the German Aerospace Center (DLR) to support the formation flying activities conducted in the last 15 years [52]. Compared to other J_2-perturbed models, the main advantage of this formulation lies in its operational friendliness, since it provides an easy insight into the geometry of the relative motion and a simple criterion to guarantee the safety of the formation [91].

The relative state vector $\delta\boldsymbol{\alpha}$ is composed of relative orbital elements defined as follows:

$$\delta\boldsymbol{\alpha} = \begin{pmatrix} \delta a & \delta\lambda & \delta e_x & \delta e_y & \delta i_x & \delta i_y \end{pmatrix}^T, \tag{3.13}$$

where δa is the relative semi-major axis, $\delta\lambda$ stands for the relative mean longitude and $\delta\boldsymbol{e} = \left(\delta e_x, \delta e_y\right)^T$ and $\delta\boldsymbol{i} = \left(\delta i_x, \delta i_y\right)^T$ are respectively called relative eccentricity and inclination vectors. According to [10], the relative orbital elements are derived from the classical Keplerian elements defined in Eq. 3.3:

$$\delta a = (a_t - a_c)/a_c, \tag{3.14a}$$

$$\delta\lambda = u_t - u_c + (\Omega_t - \Omega_c)\cos i_c, \tag{3.14b}$$

$$\delta\boldsymbol{e} = (e_t\cos\omega_t - e_c\cos\omega_c, e_t\sin\omega_t - e_c\sin\omega_c)^T, \tag{3.14c}$$

$$\delta\boldsymbol{i} = (i_t - i_c, (\Omega_t - \Omega_c)\cos i_c)^T. \tag{3.14d}$$

This set of relative orbital elements is used to describe the state of the formation at any time and can, if needed, be translated into a Cartesian representation. Fig. 3.4

depicts for example the relative motion in the orbital frame $\mathcal{O}$. Note that $\delta\boldsymbol{\alpha}$ is adimensional. In order to retrieve the geometrical dimension of the relative motion, the vector components have to be scaled by the semi-major axis $a = a_c$.
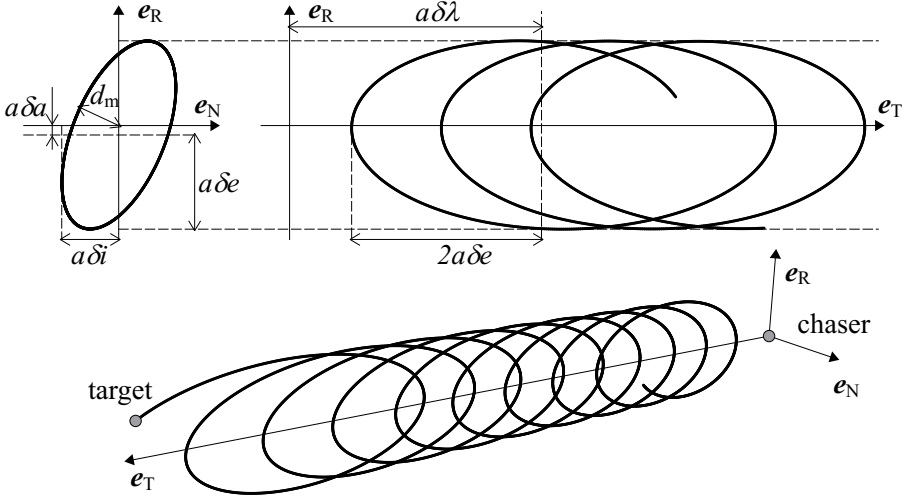

Figure 3.4: Relative motion parameterized with relative eccentricity/inclination vectors.

Figure 3.4 shows that the in-plane relative motion (RT plane in the upper right part) is described by δa, δe and $\delta\lambda$ whereas δi is responsible for the cross-track motion (RN plane in the upper left part). By using a proper phasing of the relative eccentricity and inclination vectors (parallel or anti-parallel configuration) and under the assumption of a small relative semi-major axis δa, it can be ensured that the intersatellite distance in the plane perpendicular to the flight direction (RN plane) will never drop below a certain value d_m which depends on δa, δe and δi [10]. This allows for the design of relative orbits which are passively safe. When conducting a rendezvous in space, the introduction of a nonzero relative semi-major axis creates a spiraling approach (Fig. 3.4, bottom) that guarantees that the formation will stay safe even in the presence of unexpected events (except for specific failures of the thruster system resulting in undesired random orbit maneuvering). Note that some care has to be taken during the drifting phase if δa is large, since this can lead to a dramatic reduction of d_m [66].

The convenience of this formulation becomes obvious when considering the strong anisotropy exhibited by angles-only navigation. Because of the absence of range measurements, the achievable lateral accuracy (that is, perpendicular to the line-of-sight) is always much better than the longitudinal accuracy. In terms of relative orbital elements, this means simply that, at far- to mid-range, $\delta\lambda$ is less observable and its estimation will be affected by larger errors, while δa, δe and δi will be estimated much more accurately, which is exactly what is needed to assess the safety of the formation. Note that this statement applies only to the type of formations considered for a rendezvous, where the along-track component of the relative motion is predominant. Under this assumption, the lateral directions correspond to the radial ($\boldsymbol{e}_R$) and cross-track ($\boldsymbol{e}_N$) unit vectors,

while the longitudinal one is almost aligned with $\boldsymbol{e}_\mathrm{T}$. In Fig. 3.4, this means that the lateral accuracy relates to the plane R-N (top left). Later in this section, Eq. 3.23 will show that the R-N components of the relative position $\Delta \boldsymbol{r}(t)$ depend in a first approximation on all the relative orbital elements except $\delta\lambda$.

Dealing with orbital elements, one additional major benefit of this parameterization is the ability to predict the state $\delta\boldsymbol{\alpha}(t)$ knowing the initial value $\delta\boldsymbol{\alpha}(t_0)$. This property derives from the fact that, compared to a Cartesian state vector, the underlying absolute orbital elements are slowly varying according to Eq. 3.5. In fact, for the nonperturbed motion, the state transition matrix takes this simple form (which is equivalent to the HCW state transition matrix expressed in terms of relative orbit elements [88]):

$$\boldsymbol{\Phi}(t,t_0) = \boldsymbol{\Phi}_\mathrm{HCW}(t,t_0) = \begin{pmatrix} 1 & 0 & 0 & 0 & 0 & 0 \\ -\frac{3}{2}n\Delta t & 1 & 0 & 0 & 0 & 0 \\ 0 & 0 & 1 & 0 & 0 & 0 \\ 0 & 0 & 0 & 1 & 0 & 0 \\ 0 & 0 & 0 & 0 & 1 & 0 \\ 0 & 0 & 0 & 0 & 0 & 1 \end{pmatrix}. \tag{3.15}$$

In a J_2-perturbed environment, within the assumption of near-circular problem and first-order relative dynamics, the state transition matrix is complemented with an additional contribution:

$$\boldsymbol{\Phi}(t,t_0) = \boldsymbol{\Phi}_\mathrm{HCW}(t,t_0) + \boldsymbol{\Phi}_\mathrm{J2}(t,t_0). \tag{3.16}$$

This additional term is described in detail in [88] and recalled here for convenience:

$$\boldsymbol{\Phi}_\mathrm{J2}(t,t_0) = n\Delta t \begin{pmatrix} 0 & 0 & 0 & 0 & 0 & 0 \\ -\frac{21}{4}\gamma H(\eta+1) & 0 & 0 & 0 & -\frac{3}{2}\gamma\sin(2i)(3\eta+4) & 0 \\ 0 & 0 & 0 & -\varphi' & 0 & 0 \\ 0 & 0 & \varphi' & 0 & 0 & 0 \\ 0 & 0 & 0 & 0 & 0 & 0 \\ \frac{21}{4}\gamma\sin(2i) & 0 & 0 & 0 & 3\gamma\sin^2 i & 0 \end{pmatrix} \tag{3.17}$$

where the auxiliary quantities are defined as follows ($R_\oplus$ being the Earth radius and J_2 the geopotential second-order zonal coefficient):

$$\begin{aligned} \eta &= \sqrt{1-e_\mathrm{c}^2}, & \gamma &= \frac{J_2}{2}\frac{R_\oplus^2}{a_\mathrm{c}^2\eta^4}, & H &= (3\cos^2 i_\mathrm{c} - 1) \\ K &= (5\cos^2 i_\mathrm{c} - 1), & \varphi' &= (3/2)\gamma K. \end{aligned} \tag{3.18}$$

During the design of the AVANTI experiment, it has also been recognized that, at low altitude, the differential drag needs to be accounted for. Unfortunately, the mathematical derivation of the impact of this perturbation on the relative elements would require the introduction of a model of the atmospheric density and additional parameters to take into account the geometry of the spacecraft. Moreover, the resulting linearized dynamics would be a complicated linear time-variant system, not solvable in closed-form. Consequently, in order to obtain a compact state transition matrix independent from any density model, it has been decided to use a semi-empirical method. This consists in

introducing the following additional parameters: the mean time derivative of δa and δe due to the differential drag, which are able to reproduce the effects of this perturbation on the relative orbital elements. Accordingly, the state $\delta\boldsymbol{\alpha}$ is augmented to form the new state [88]:

$$\boldsymbol{\xi} = \begin{pmatrix} \delta\boldsymbol{\alpha}^T & \delta\dot{a} & \delta\dot{e}_x & \delta\dot{e}_y \end{pmatrix}^T \tag{3.19}$$

and the associated state transition matrix becomes:

$$\boldsymbol{\Phi}_\xi(t,t_0) = \begin{pmatrix} \boldsymbol{\Phi}_{\text{HCW}}(t,t_0) + \boldsymbol{\Phi}_{\text{J2}}(t,t_0) & \boldsymbol{\Phi}_{\text{drag}}(t,t_0) \\ \mathbf{0}_{3\times 6} & \mathbf{I}_{3\times 3} \end{pmatrix}, \tag{3.20}$$

where

$$\boldsymbol{\Phi}_{\text{drag}}(t,t_0) = \begin{pmatrix} \Delta t & 0 & 0 \\ -(\frac{21}{8}\gamma H(\eta+1) + \frac{3}{4})n(\Delta t)^2 & 0 & -3\Delta t \\ 0 & \Delta t & 0 \\ 1/n & 0 & \Delta t \\ 0 & 0 & 0 \\ \frac{21}{8}\gamma\sin(2i)n(\Delta t)^2 & 0 & 0 \end{pmatrix}. \tag{3.21}$$

Note that [88] also includes some additional small periodic variations of the relative orbital elements which have been neglected (because their effect on the apparent relative motion is much smaller than the measurement noise). The coupling effect of J_2 and differential drag (the terms proportional to γ) has been instead retained.

Finally, the impact of the execution of maneuvers from the chaser, such as arising from thrusters, needs to be described to provide a complete model for the relative motion able to support formation control and guidance activities. This can for example be found in [10], which describes the instantaneous change of relative orbital elements $\Delta\delta\boldsymbol{\alpha}$ due to an impulsive maneuver with velocity increment $\Delta\boldsymbol{V}$ expressed in the orbital frame $\mathcal{O}$ and executed at argument of latitude u_{M}:

$$\Delta\delta\boldsymbol{\alpha} = -\frac{1}{na}\begin{pmatrix} 0 & 2 & 0 \\ -2 & 0 & 0 \\ \sin u_{\text{M}} & 2\cos u_{\text{M}} & 0 \\ -\cos u_{\text{M}} & 2\sin u_{\text{M}} & 0 \\ 0 & 0 & \cos u_{\text{M}} \\ 0 & 0 & \sin u_{\text{M}} \end{pmatrix}\Delta\boldsymbol{V} = \boldsymbol{B}(u_{\text{M}})\Delta\boldsymbol{V}. \tag{3.22}$$

It has to be again emphasized that the relative orbital elements constitute the framework of the relative motion model. If other quantities need to be retrieved (for example, the relative position), additional transformations are needed, which could lead to a performance degradation. This is the case for instance if a linear mapping is required to provide the Cartesian relative state in the frame $\mathcal{O}$. This transformation is provided in [10]:

$$\Delta\boldsymbol{r}(t) = a\begin{pmatrix} 1 & 0 & -\cos u(t) & -\sin u(t) & 0 & 0 \\ 0 & 1 & 2\sin u(t) & -2\cos u(t) & 0 & 0 \\ 0 & 0 & 0 & 0 & \sin u(t) & -\cos u(t) \end{pmatrix}\delta\boldsymbol{\alpha}(t)$$
$$= \boldsymbol{C}(u(t))\delta\boldsymbol{\alpha}(t). \tag{3.23}$$

As shown later in Section 3.3.3, the accuracy of this transformation is however not enough for the need of this research, because the curvature of the orbital path is not modeled and this has a large impact on the radial component at far-range (see Section 3.3.3 for more detail). Consequently, a nonlinear transformation is used in this work to model the Cartesian position from the formation state parameterized with relative orbital elements. This complex transformation is composed of several nonlinear transformations which are summarized in Fig. 3.5

Note that the aforedescribed model is only valid for near-circular orbits. Recent research activities have shown that the state transition matrix can also be reformulated to account for an arbitrary eccentricity [92, 90].
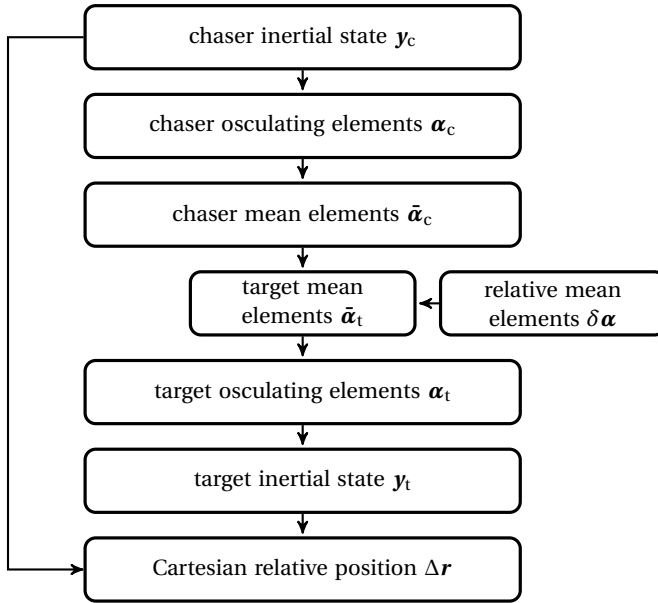

Figure 3.5: Process flow of nonlinear transformations to properly compute the Cartesian relative position from the relative state.

3.3. ESTIMATING THE RELATIVE MOTION

3.3.1. LINE-OF-SIGHT OBSERVATIONS

The angles-only relative navigation task consists in finding the relative state $x(t)$ between a target and a chaser spacecraft corresponding to a given set of n line-of-sight measurements $\{u_i\}$ taken at times $t_i, i \in [1, n]$, and collected by a camera mounted on the chaser spacecraft. To that end, a model $h(t)$ of the measurement taken at time t is needed to relate the observations with the relative state. If $r_{cam}(t)$ denotes the inertial absolute position of the camera optical center, the line-of-sight vector to the center of

mass of the target is given by:

$$\boldsymbol{h}(t) = \frac{\boldsymbol{r}_{\mathrm{t}}(t) - \boldsymbol{r}_{\mathrm{cam}}(t)}{\|\boldsymbol{r}_{\mathrm{t}}(t) - \boldsymbol{r}_{\mathrm{cam}}(t)\|}. \tag{3.24}$$

Note that, practically, the line-of-sight to the center of mass of the target cannot be re-trieved in case of a noncooperative target. What is measured by the optical sensor is the center of the target image seen by the camera. At far-range, this can be approximated by the target center of mass, but this is no more valid as the distance decreases, resulting in increasing line-of-sight errors (see for example Fig. 4.9). This research focuses on the far- to mid-range domain, where the intersatellite distance varies between several tens of kilometers and a few hundred meters. The camera offset with respect to the chaser center of mass does typically not exceed one meter on a small satellite. Thus, this offset is considered negligible in what follows, simplifying Eq. 3.24 to:

$$\boldsymbol{h}(t) \approx \frac{\boldsymbol{r}_{\mathrm{t}}(t) - \boldsymbol{r}_{\mathrm{c}}(t)}{\|\boldsymbol{r}_{\mathrm{t}}(t) - \boldsymbol{r}_{\mathrm{c}}(t)\|} = \frac{\Delta\boldsymbol{r}(t)}{\|\Delta\boldsymbol{r}(t)\|}. \tag{3.25}$$

The line-of-sight is a three dimensional vector but, because it is normalized, some infor-mation is lost (*i.e.*, only bearing angles are provided). In fact, only two angular variables are enough to fully describe $\boldsymbol{h}$ (note that the parameter t has been omitted for clarity):

$$\boldsymbol{h} = \begin{pmatrix} \cos\alpha\cos\delta \\ \sin\alpha\cos\delta \\ \sin\delta \end{pmatrix}. \tag{3.26}$$

Thus it is possible to reduce the line-of-sight $\boldsymbol{h}$ to an equivalent two-dimensional mea-surement vector $\boldsymbol{h}^{\dagger}$:

$$\boldsymbol{h}^{\dagger} = \begin{pmatrix} \alpha \\ \delta \end{pmatrix} = \begin{pmatrix} \arctan\frac{h_2}{h_1} \\ \arcsin h_3 \end{pmatrix}, \tag{3.27}$$

where the subscript $\square_i$ corresponds to the ith component of the vector $\boldsymbol{h}$;. If $\boldsymbol{h}^{\dagger}$ is de-scribed in the inertial frame, α and δ are called right-ascension and declination. If it is instead expressed in a Cartesian frame linked to the camera frame (in this case, one axis is conveniently chosen to be aligned with the camera boresight), the angles are called azimuth and elevation. A third parameterization is also possible using the slope of the unit vector $\boldsymbol{h}^{\ddagger} = (h_1/h_3, h_2/h_3)^T$.

From now on, the model of the measurement will simply be noted $\boldsymbol{h}$, disregarding which parameterization has been chosen.

3.3.2. The Problem of Observability

The combination of both relative motion and measurements models enables the estima-tion of the state vector from a set of observations. However, the previous section shows that, disregarding the choice of parameterization, the measurement model is nonlinear with respect to the Cartesian relative position. This is at the first glance a major limita-tion, which makes the characterization of the system observability much more difficult, preventing the use of tools from the linear theory. By linearizing a nonlinear system

around a particular state, powerful analyses can be made using the Gramian matrix as done, for example, in [93]. This matrix can be used as measure for observability, where large eigenvalues indicate good observability in the directions corresponding to those eigenvalues. These analyses are often justified by the fact that the nonlinearities are very small. However, it has to be kept in mind that linear observability analyses for a particular state may not necessarily be globally valid. It has early been recognized that it is still possible to reach a linear measurement relation, able to provide some global insight into the observability of the problem. Hammel and Aidala [94] showed that it is possible to reformulate Eq. 3.27 to create a linear measurement relation of the form $H\Delta r = 0$. Similarly, Woffinden [95] also derived an alternative linear measurement relation to elegantly demonstrate that, under the assumption of a homogeneous linear relative motion with a linear model of the Cartesian relative position, the relative motion is simply not observable. The demonstration is quickly recalled here for completeness. Let $x(t)$ denote the relative state at time t (either in a Cartesian frame or parameterized with relative orbital elements). A linear relative motion model implies that

$$x(t) = \Phi(t, t_0)x(t_0),\tag{3.28}$$

where $\Phi(t, t_0)$ is the state transition matrix. Let us assume that the relative position $\Delta r(t)$ has a linear dependency to the state vector $x(t)$ (which is trivial if x is formulated in the Cartesian frame but is not necessarily the case if relative orbital elements are employed, cf. Section 3.2.4):

$$\Delta r(t) = C(t)x(t).\tag{3.29}$$

Since the line-of-sight measurements are assumed to be directed to the center of mass of the target, they are aligned with the relative position vector Δr, assuming that the optical center of the camera is located at the chaser center of mass. Thus, in the absence of measurement noise, each line-of-sight observation u_i from a given set of measurements satisfies:

$$u_i \times \Delta r(t_i) = 0, i \in [1, n].\tag{3.30}$$

Substituting Eq. 3.28 and Eq. 3.29 into Eq. 3.30 yields:

$$u_i \times (C(t_i)\Phi(t_i, t_0)x(t_0)) = 0, i \in [1, n].\tag{3.31}$$

It can clearly be recognized that, if $x(t_0) = x_0$ is a solution of Eq. 3.31, the scaled solution μx_0 is also a solution, leading to an infinity of solutions matching a given measurement profile. This result is known as Woffinden's dilemma [27].

   The nonobservability is however only strictly valid under the aforementioned assumptions. By relaxing some of them, it is in reality however possible to reach a weak observability. This is described in more detail in Chapter 6. Still, the most obvious and simple way to improve the observability consists in executing maneuvers, so that the relative motion is no more homogeneous (i.e., $x(t) \neq \Phi(t, t_0)x(t_0)$). This corresponds to the classical approach to mitigate the observability problem posed by angles-only navigation. This strategy has been used during the two in-orbit experiments ARGON and AVANTI, in order to reach observability. It has to be noted that this is not a real limitation, because maneuvers are anyway needed to perform a rendezvous.

3.3.3. Suitable Relative Motion Models

The objective of this section is to select relative motion models suitable for the angles-only relative navigation task. This selection is done based on the achievable accuracy of the models: as rule of thumb, the line-of-sight errors coming from the model deficiencies should be smaller than or at least at the same order of magnitude as the typical measurement noise (40"). Among the different possibilities presented in Section 3.2, only 10 candidates have been retained (it is not intended here to make an exhaustive comparison of all existing models). Their characteristics are summarized in Table 3.2, where the last column indicates how the modeled relative position is related to the model state.

Table 3.2: Models retained for the following investigations.

Model	Type	Perturbations	Modeled Δr
M1	numerical propagation	all	linear ($\Delta r = \Delta y_{1-3}$)
M2	numerical propagation	20x20 gravity field and drag	linear
M3	numerical propagation	J_2 and drag	linear
M4	two Keplerian motions	-	nonlinear (Eq. 3.6)
M5	HCW model	-	linear
M6	curvilinear HCW model	-	nonlinear
M7	analytical (Section 3.2.4)	J_2	linear (Eq. 3.23)
M8	analytical	J_2	nonlinear (Fig. 3.5)
M9	analytical	J_2 and drag effect ($\delta \dot{a}, \delta \dot{e}$)	nonlinear
M10	analytical	J_2 and restricted drag ($\delta \dot{a}$)	nonlinear

The investigations are conducted as follows: the accuracy of Model 1 is first verified using real flight data. This model subsequently serves as reference to simulate different cases for which flight data might not exist. The model fitting accuracy is investigated, meaning that, given a 3D reference trajectory, the initial conditions of the relative state vector referring to a specific model are adjusted to best fit the trajectory over a given time interval. The resulting fitting errors are an indication of the model deficiencies. A model will be considered suited for the navigation task if the fitting residuals are below the typical measurement noise of 40". Note that this process does not exactly correspond to the angles-only navigation task, where only direction vectors are fitted instead of 3D positions.

Model 1 consists in a numerical propagation using a 20x20 gravity field and including the perturbations due to the drag, solar radiation pressure and luni-solar perturbations. The drag is modeled using a simple cannon-ball model, empirically-measured ballistic coefficients and an atmospheric density described by a simple Harris-Priester model [96]. Model 1 is validated against flight data coming from the PRISMA mission (during a 10-hour-long maneuver-free phase where the spacecraft were separated by 30 km). During this data arc, both satellites of the formation were following their nominal attitude profile, resulting in a constant differential drag. This reference relative trajectory has been determined using differential GPS and is accurate at subcentimeter level [11]. Figue 3.6 shows that Model 1 matches the reality with a precision of a few decimeters over 10 hours. Note that this reference model is not state-of-the-art (the differential drag could be better described using more advanced models) but is fully sufficient for the following analyses.

The same procedure is now applied for Models 2-10 with respect to Model 1. In order
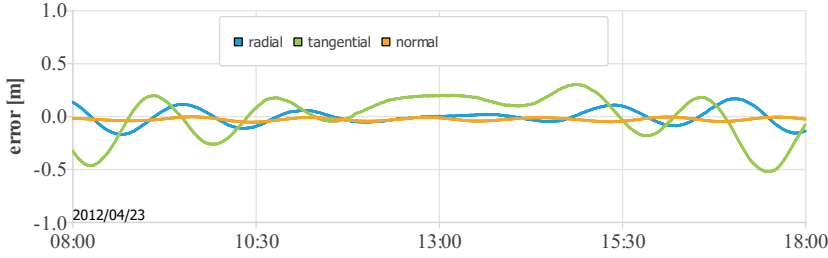
Figure 3.6: Fitting errors of Model 1 with respect to GPS-based flight data from the PRISMA mission.

3

to better relate the model deficiencies with the measurement noise, the model errors are from now on translated into line-of-sight (LoS) errors. This is done by computing the modeled relative position $\Delta \boldsymbol{r}(t)$ at time t and evaluating the angular deviation ρ with respect to the reference $\Delta \boldsymbol{r}^{\text{ref}}(t)$ as follows:

$$\rho(t) = \cos^{-1}\left(\frac{\Delta \boldsymbol{r}(t)\Delta \boldsymbol{r}^{\text{ref}}(t)}{\|\Delta \boldsymbol{r}(t)\| \, \|\Delta \boldsymbol{r}^{\text{ref}}(t)\|}\right). \tag{3.32}$$

Two representative cases are investigated:

1. 4-day-long arc without differential drag (similar to the ARGON experiment)
2. 4-day-long arc with differential drag (similar to the AVANTI experiment)

Both cases are simulated using a near-circular orbit. A high value for the differential drag is selected for the Case 2 to match the experimental conditions offered by the AVANTI experiment (*c.f.*, Chapter 2). This is done by setting very different ballistic coefficients B to the chaser and target spacecraft and by assigning a low altitude to the orbit (500 km). The simulation parameters used for the investigation are summarized in Table 3.3.

Table 3.3: Simulation parameters used to produce Cases 1 and 2. Note that the modeling of the drag is deactivated for Case 1.

$\boldsymbol{\alpha}^T$	$(6877 \times 10^3, 0.001, 1.7, 5.0, 5.5, 0)$ [m,-]
$a\delta\boldsymbol{\alpha}^T$	$(0, 30000, 0, 400, 0, 600)$ m
B_c	$10.0 \times 10^{-3}\,\text{m}^2\text{kg}^{-1}$
B_t	$20.0 \times 10^{-3}\,\text{m}^2\text{kg}^{-1}$

Comparing all models together could rapidly become confusing. For this reason, the focus is first given on some models which are obviously not adapted. Figure 3.7 depicts the fitting errors for Models 4 to 7 using the drag-free case.

A few conclusions can already been drawn. By neglecting the curvature of the orbit path, Models 5 and 7 exhibit a similar large offset of about 500". As depicted in Fig. 3.8, this corresponds to the contribution of the orbit curvature at an intersatellite distance L=30 km.

According to Fig 3.8 (left), if r denotes the radius of the near-circular orbit (*i.e.*, $r \approx a$), an error $\epsilon = \sqrt{r^2 + L^2} - r$ is introduced when using a rectilinear frame instead of a curvi-
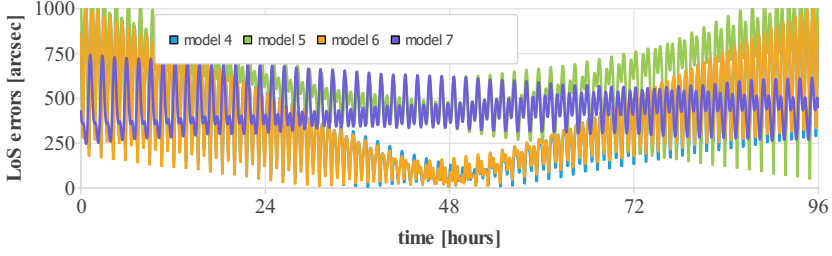
Figure 3.7: Models obviously not suited for far-range angles-only relative navigation (Case 1).

linear one. This error is depicted in Fig 3.8 (right) after division by the intersatellite distance, in order to provide an angular line-of-sight error. Models 4 and 6 are not suffering from this limitation and are thus clearly more accurate.

Interestingly enough, the error patterns of Model 4 and 6 are similar, meaning that the linearization of the Keplerian relative motion using a curvilinear frame is very accurate in the particular case described by Table 3.3 (where the eccentricity is small and the relative motion mainly consists in an along-track separation). Alas, Models 4 and 6 do not take the contribution of J_2 into consideration, and this deficiency is responsible for large fitting errors. In fact, a clear long-term difference is observable between Models 4-6 and Model 7, which includes the secular effect of J_2 and thus reaches a more balanced error pattern. The short-term variations affecting all the models are instead due to the unmodeled periodic contributions of J_2. In view of the large errors exhibited by these four models, and having in mind a typical sensor noise of about half-a-pixel or 40" (c.f. Chapter 2), Models 4 to 7 can already be declared not suited for far-range angles-only navigation, leading to the following conclusion: an appropriate relative motion model needs to take both effects of J_2 and orbit curvature into account.

Figure 3.9 depicts the model fitting errors using numerical propagations (Models 2 and 3) and analytical model (Model 8) in the drag-free case. Here again, several interesting conclusions can immediately be drawn. The model deficiencies are now of the same order of magnitude as the measurement noise. These errors correspond to the small perturbations which have not been modeled (third-body, solar radiation pressure,
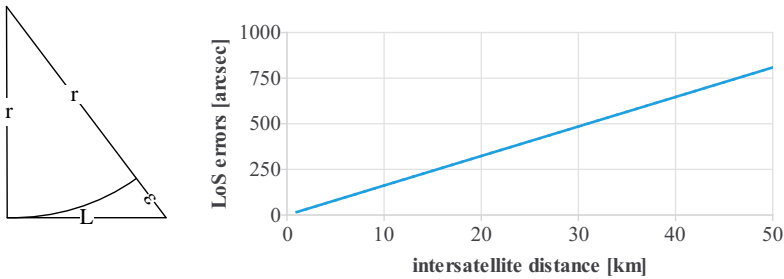

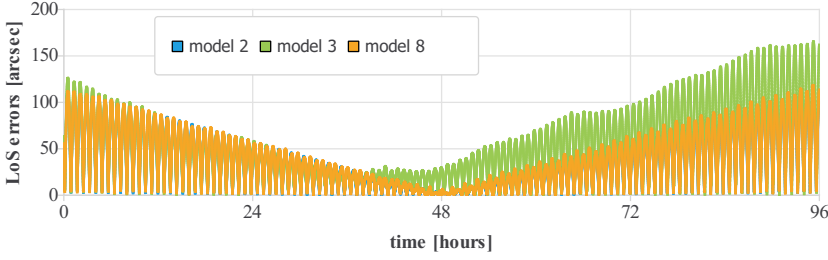Figure 3.8: Line-of-sight errors introduced by the orbit curvature.

Figure 3.9: Numerical vs. analytical models without differential drag (Case 1). Note that the LoS errors of Models 2 and 8 are almost confounded.

higher gravity orders etc.) and become visible when using an extended propagation arc of several days (they would be hidden by the sensor noise if the time span were reduced to a single day). Interestingly, the analytical model which only considers the effect of J_2 (Model 8) behaves slightly better than the numerical propagation using only J_2 (Model 3). This is due to the numerical integration errors affecting Model 3 which accumulate over a long propagation time.

Figure 3.9 shows that, in spite of minor differences, Models 2, 3, and 8 are more or less equivalent for our needs. Thus, the perturbation due to the higher orders and degrees of the gravity field can be neglected to describe the relative motion similar to Case 1. On the contrary, the effect of the differential drag has to be taken in account at low altitude. Based on Case 2, Fig. 3.10 shows that neglecting this perturbation (as done with Model 8) is unacceptable at 500 km altitude.
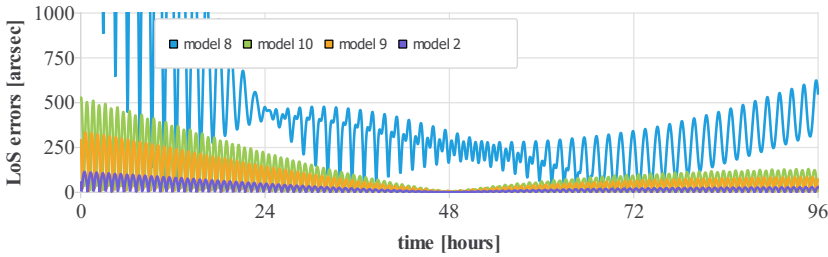

Figure 3.10: Numerical vs. analytical models in the presence of differential drag (Case 2).

The error pattern exhibited by Fig. 3.10 might be surprising. Intuitively, one would expect the errors to be symmetrical with respect to the center of the data arc like in Fig. 3.7. The reason for this behavior lies in the specific method adopted to assess the quality of the models: a least-squares adjustment is done to best fit a trajectory predicted by a given model with a reference trajectory. In the presence of differential drag, however, a rapid drift of the relative motion will appear, even when initializing the simulation with vanishing relative semi-major axis. As a consequence, the trajectory to be fitted corresponds to a drifting formation. Using the simulation parameters described in Table 3.3, the mean along-track separation amounts to 30 km at initial epoch and grows up to 120 km after 4 days. The least-squares process will try to minimize the 3D position

residuals between modeled and reference trajectories over the whole data arc. Thus the minimum residual values are expected in the middle of the arc and are symmetrically increasing towards the boundaries of the arc, as seen for the previous cases. Figure 3.10, however, does not depict these residuals but the line-of-sight errors, which mainly correspond to the lateral position residuals divided by the intersatellite distance. Thus, they decrease as this distance increases, making the error pattern unsymmetrical.

When dealing with a noncooperative satellite, the major challenge is that the differential drag is unknown. As a result, this effect will need to be estimated as part of the relative navigation task. Here, the numerical method (Model 2) is more advantageous compared to the analytical model (Models 9 and 10) for two reasons. First, Fig. 3.10 shows that the numerical propagation (which properly models the drag acceleration using an atmospheric model and a ballistic coefficient) is slightly more accurate than the analytical model including the empirical mean effect of the drag. Second, the analytical model (Model 9) requires the estimation of three parameters ($\delta \dot{a}$, $\delta \dot{e}$), while the numerical model will simply adjust the differential ballistic coefficient. Thus, an estimation based on the numerical model is likely to be more robust, because less parameters are used to describe the same phenomenon. Practically, the weakness of the analytical model is mitigated by estimating only $\delta \dot{a}$ and setting $\delta \dot{e} = 0$, which however results in further performance degradation (Model 10). Being several orders of magnitude faster than the numerical propagation, the analytical solution still represents a judicious choice in some cases such as onboard implementation (*c.f.*, Chapter 5).

Table 3.4: Models used for the on-orbit demonstrations.

Experiment	On-ground orbit determination	Onboard real-time navigation
ARGON	**M8**: analytical model without drag	-
AVANTI	**M1**: numerical model with all perturbations	**M10**: analytical model with restricted drag

As summarized in Table 3.4, during the ARGON experiment, the analytical solution has also been retained for on-ground relative orbit determination because the differential drag was negligible [29, 57]. For AVANTI, it has instead been chosen to rely on the numerical propagation for the onground relative orbit determination to reach ultimate accuracy (*c.f.*, Chapter 4). This design choice comes however at the expense of high computational load and will be critically reviewed in Chapter 7.

3.4. ESTIMATION TECHNIQUES

A state observer is finally required to fulfill the navigation task, in order to determine the relative state of the formation from a set of line-of-sight measurements. Several well-established techniques are available to realize this objective. This work is based on two different methods which are recalled in the sequel for completeness: the nonlinear batch least-squares process and the extended Kalman filter. The former method estimates a state vector at a given initial epoch to best fit a set of observations over a given data arc. As described in the next section, it requires several iterations to converge. This technique is well adapted to estimate the state vector *a posteriori*, once a set of measurements is

available. Thus, it has been employed to perform the on-ground relative orbit deter-
mination task during the ARGON and AVANTI experiments. For real-time application,
the extended Kalman filter is more appropriate, because it processes the observations
sequentially. Consequently, this estimation concept has been preferred to design the
onboard real-time navigation filter of the AVANTI experiment.

3.4.1. NONLINEAR BATCH LEAST-SQUARES

As described in Section 3.3.1, the angles-only estimation problem is nonlinear due to the
nature of the measurements. In its general form, the measurement model is a function
of the time t and of the initial relative state $\boldsymbol{x}(t_0) = \boldsymbol{x}_0$. In order to better reflect this
dependency, the measurement model of Section 3.3.1 is reformulated as:

$$\boldsymbol{h}(\boldsymbol{x}(t)) = \tilde{\boldsymbol{h}}(t, \boldsymbol{x}_0). \tag{3.33}$$

The estimation problem consists in finding $\boldsymbol{x}_0$ matching the n noisy observations:

$$\boldsymbol{z}_1 = \tilde{\boldsymbol{h}}(t_1, \boldsymbol{x}_0) + \boldsymbol{\epsilon}_1,$$
$$\vdots \tag{3.34}$$
$$\boldsymbol{z}_n = \tilde{\boldsymbol{h}}(t_n, \boldsymbol{x}_0) + \boldsymbol{\epsilon}_n.$$

Here the generic observation $\boldsymbol{z}$ has been introduced, and $\boldsymbol{\epsilon}_i$ stands for the measurement
noise. Depending on the chosen parameterization, $\boldsymbol{z}$ corresponds to the line-of-sight
vector (*i.e.*, $\boldsymbol{z} = \boldsymbol{u}$) or to a set of two angles. If the measurement model were linear (*i.e.*,
$\boldsymbol{h}(t, \boldsymbol{x_0}) = \boldsymbol{H}(t)\boldsymbol{x_0}$), the problem could be easily reformulated as:

$$\begin{pmatrix} \boldsymbol{z}_1 \\ \vdots \\ \boldsymbol{z}_n \end{pmatrix} = \begin{pmatrix} \boldsymbol{H}(t_1) \\ \vdots \\ \boldsymbol{H}(t_n) \end{pmatrix} \boldsymbol{x}_0 + \begin{pmatrix} \boldsymbol{\epsilon}_1 \\ \vdots \\ \boldsymbol{\epsilon}_n \end{pmatrix} \tag{3.35}$$

corresponding to the classical linear system $\boldsymbol{Ax}_0 = \boldsymbol{b}$. In this case, three independent
observations would be enough to retrieve the six-dimensional initial state $\boldsymbol{x}_0$, provided
that $\boldsymbol{A}$ can inverted. If more observations are available, the problem is overdetermined
and the solution which minimizes the sum of the squared residuals $J = \|\boldsymbol{b} - \boldsymbol{Ax}\|^2$ would
be given by

$$\boldsymbol{x}_0 = (\boldsymbol{A}^T \boldsymbol{A})^{-1} \boldsymbol{A}^T \boldsymbol{b} = \boldsymbol{A}^+ \boldsymbol{b} \tag{3.36}$$

where $\boldsymbol{A}^+ = (\boldsymbol{A}^T \boldsymbol{A})^{-1} \boldsymbol{A}^T$ is called Moore–Penrose pseudoinverse. Alas, the nonlinearity
of the problem makes the derivation of such a direct solution impossible. The classical
approach to solve this problem consists in employing a nonlinear least-squares method.
This is done by linearizing the measurement model around a reference *a priori* solution
$\boldsymbol{x}_0^{\text{apr}}$, which has to be guessed

$$\tilde{\boldsymbol{h}}(t, \boldsymbol{x}_0) = \tilde{\boldsymbol{h}}(t, \boldsymbol{x}_0^{\text{apr}}) + \left. \frac{\partial \tilde{\boldsymbol{h}}(t)}{\partial \boldsymbol{x}_0} \right|_{\boldsymbol{x}_0 = \boldsymbol{x}_0^{\text{apr}}} (\boldsymbol{x}_0 - \boldsymbol{x}_0^{\text{apr}}). \tag{3.37}$$

In this case, Eq. 3.34 becomes

$$
\boldsymbol{z}_1 - \tilde{\boldsymbol{h}}(t_1, \boldsymbol{x}_0^{\text{apr}}) = \frac{\partial \tilde{\boldsymbol{h}}(t_i)}{\partial \boldsymbol{x}_0}\bigg|_{\boldsymbol{x}_0 = \boldsymbol{x}_0^{\text{apr}}} (\boldsymbol{x}_0 - \boldsymbol{x}_0^{\text{apr}}),
$$

$$
\vdots \tag{3.38}
$$

$$
\boldsymbol{z}_n - \tilde{\boldsymbol{h}}(t_n, \boldsymbol{x}_0^{\text{apr}}) = \frac{\partial \tilde{\boldsymbol{h}}(t_n)}{\partial \boldsymbol{x}_0}\bigg|_{\boldsymbol{x}_0 = \boldsymbol{x}_0^{\text{apr}}} (\boldsymbol{x}_0 - \boldsymbol{x}_0^{\text{apr}}).
$$

3

This can equivalently be simplified using a linear formulation:

$$
\Delta \boldsymbol{z} = \tilde{\boldsymbol{H}} \Delta \boldsymbol{x_0}, \tag{3.39}
$$

where $\Delta \boldsymbol{z}$ is the column vector corresponding to the left part of Eq. 3.38. Eq. 3.39 can finally be solved using the least-squares solution given by Eq. 3.36. In this case, $\tilde{\boldsymbol{H}}$ is the Jacobian matrix and $\Delta \boldsymbol{x_0} = \boldsymbol{x}_0 - \boldsymbol{x}_0^{\text{apr}}$ is the correction of the *a priori* reference solution. Until now, all the measurements have been treated equally. In order to account for the individual contributions of the noise, a weighting matrix $\boldsymbol{W}$ is introduced. Assuming a Gaussian noise distribution of the noise $\boldsymbol{\epsilon}_i$ with standard deviation $\boldsymbol{\sigma} = (\sigma_{i,1}, \cdots, \sigma_{i,m})^T$, m being the dimension of the measurement vector $\boldsymbol{h}$, the weighting matrix takes the form:

$$
\boldsymbol{W} = \text{diag}(\sigma_{1,1}^{-2}, \cdots, \sigma_{1,m}^{-2}, \cdots \sigma_{n,1}^{-2}, \cdots, \sigma_{n,m}^{-2}). \tag{3.40}
$$

This yields the following solution [68]:

$$
\Delta \boldsymbol{x}_0 = (\tilde{\boldsymbol{H}}^T \boldsymbol{W} \tilde{\boldsymbol{H}})^{-1} (\tilde{\boldsymbol{H}}^T \boldsymbol{W} \Delta \boldsymbol{z}). \tag{3.41}
$$

The covariance of the solution is finally given by [68]:

$$
\boldsymbol{P} = (\tilde{\boldsymbol{H}}^T \boldsymbol{W} \tilde{\boldsymbol{H}})^{-1}. \tag{3.42}
$$

In case of weak observability, it might be useful to avoid the singularities by also introducing *a priori* covariance information in the form of the matrix $\boldsymbol{P}_0^{\text{apr}}$. In this case, the solution depends on the so-called information matrix $\boldsymbol{\Lambda} = (\boldsymbol{P}_0^{\text{apr}})^{-1}$ to become [68]:

$$
\Delta \boldsymbol{x}_0 = (\boldsymbol{\Lambda} + \tilde{\boldsymbol{H}}^T \boldsymbol{W} \tilde{\boldsymbol{H}})^{-1} (\boldsymbol{\Lambda} \Delta \boldsymbol{x_0}^{\text{apr}} + \tilde{\boldsymbol{H}}^T \boldsymbol{W} \Delta \boldsymbol{z}). \tag{3.43}
$$

More details on the batch least-squares approach can be found in Reference [68]. It has to be noted that, compared to a linear approach, this method has several limitations:

- an *a priori* reference solution is required;
- several iterations are needed to converge to the solution;
- there is no guaranty that the method will converge to the global optimum;
- the method is prone to divergence if the problem is not linear enough.

3.4.2. EXTENDED KALMAN FILTER

The fact that the batch least-squares method takes the complete set of n measurements into consideration is desirable in terms of robustness, because the whole history of observations is used to derive the solution. This makes this technique well adapted for on-ground orbit determination. However, limited onboard computational resources make it not suited for real-time embedded space applications. In this case, a sequential approach is often preferred. The Kalman filter has been developed for this purpose [97]. This section briefly summarizes the principles of its extension for nonlinear problem, called Extended Kalman Filter or EKF. The main advantage of the filter is that the estimate of the current state only depends on the previous state and on the current observation. Thus, it is not needed to store and process the whole history of observations. The state of the filter is represented by the *a posteriori* state estimate x_i at time t_i and the *a posteriori* covariance matrix P_i. The estimation is done in two steps (prediction and update), making the distinction between the results of these two steps necessary. Classically, the notation $\square_{n|m}$ is used, describing the state at time t_n given all the observations collected up to the time t_m. The prediction step propagates the previous state and covariance to the current time

$$
\begin{aligned}
x_{i|i-1} &= f(t_i, x_{i-1|i-1}), \\
P_{i|i-1} &= \Phi(t_i, t_{i-1})P_{i-1|i-1}\Phi(t_i, t_{i-1})^T,
\end{aligned}
\tag{3.44}
$$

while the update step uses the current observation to improve the knowledge of the state:

$$
\begin{aligned}
x_{i|i} &= x_{i|i-1} + K_i(z_i - h(x_{i|i-1})), \\
P_{i|i} &= (I - K_i H_i)P_{i|i-1}.
\end{aligned}
\tag{3.45}
$$

Here, $H_i = \frac{\partial h}{\partial x}\big|_{x=x_{i|i-1}}$ and K_i is called Kalman gain and computed as:

$$
K_i = P_{i|i-1}H_i^T(R_i^{-1} + H_i P_{i|i-1} H_i^T)^{-1},
\tag{3.46}
$$

where R_i is the noise covariance matrix. The danger of this formulation lies in the fact that, if the covariance matrix becomes too small, the filter becomes insensitive to new observations, eventually leading to a filter divergence. This issue can be mitigated by introducing the covariance matrix of the process noise $Q(t_i, t_{i-1})$ in the estimation process, in order to cope with the model deficiencies. In this case, the propagation of the covariance (Eq. 3.44) becomes

$$
P_{i|i-1} = \Phi(t_i, t_{i-1})P_{i-1|i-1}\Phi(t_i, t_{i-1})^T + Q(t_i, t_{i-1}).
\tag{3.47}
$$

Introducing process noise is a powerful technique which also allows obtaining more realistic covariance predictions through a proper balancing of measurement and process noise [68]. However, this comes at the cost of additional efforts when tuning the filter. As seen later in this thesis, it is, in fact, not always trivial to derive the proper filter settings.

This tuning difficulty is a major drawback of the EKF compared to the batch least-squares approach, especially if one does not know exactly what to expect in terms of model deficiencies and measurement errors. In addition, the sequential processing is also prone to instability in case of outliers. In fact, by considering the whole history of

observations and using several iterations, the batch processing is more capable to detect the bad observations by comparing their residuals with the overall residual pattern of the whole data arc. Similarly, fitting the complete history of measurements with a given model will better highlight the model deficiencies and the systematic errors, whereas these errors are likely to be hidden by the process noise in a sequential approach. In view of its intrinsic robustness, the least-squares method has thus been preferred whenever time and computational resources are sufficient (*i.e.*, for on-ground relative orbit determination), while the EKF has been limited to onboard real-time utilization.

3.4.3. A PRIORI SOLUTION FOR THE INITIAL STATE

The main difficulty posed by the afore-presented estimation techniques lies in the necessity to provide an *a priori* solution around which the measurement model is linearized. Due to the nonlinear nature of the estimation problem, a reference solution deviating too much from reality can rapidly lead to a divergence. Finding a suitable guess is not trivial and belongs to the field of initial relative orbit determination. This aspect will be specifically treated in Chapter 6. Without going too much into the details, it can simply be stated that exploiting the nonlinearities of the measurement model allows solving for the range ambiguity. This is especially true for large separations, where the major nonlinear contribution is represented by the orbit curvature (as already shown in Fig. 3.8).

For simplicity, it has been decided in the early phases of this research to rely on Two-Line Elements (TLE) to derive the initial *a priori* relative state vector. This was not considered a limitation because the target of a noncooperative rendezvous is never totally unknown. Despite this external aiding, Chapter 4 shows that it is still not always obvious to derive an appropriate *a priori* solution, especially because of the unknown differential drag which might heavily degrade this guessed reference. Chapter 7 will revisit this peculiar problem, improving the precision of the guessed solution once the rendezvous has been initiated.

3.4.4. ADVANCED FILTERING CONCEPTS

The batch least-squares adjustment and the extended Kalman filter present the undeniable advantage of simplicity, which explains their popularity in the engineering community. However, the linearization around a reference solution done to cope with the nonlinear nature of the estimation problem is questionable. This supposes that the problem is still linear enough to ensure the convergence. The fact that the nonlinearity of the measurement equation brings observability suggests that dedicated nonlinear filtering techniques might be more suited for angles-only navigation. Among them, the unscented Kalman filter or cubature Kalman filter are natural candidates. The use of an unscented Kalman filter was for example investigated in [38], demonstrating that the observability and filter performance can be improved when the nonlinearities of the measurement model are taken into account.

An important additional assumption for both least-squares method and extended Kalman filter is that the distribution of the measurement noise is Gaussian. If this is not the case, different estimation techniques have to be used, such as particle filter [98].

This research does not pretend to reach the ultimate estimation concept. As already stated in the introduction, the primary objective is to build a system able to perform in

real conditions, in order to collect valuable in-orbit experience. Investigating the benefits and drawbacks presented by alternative estimation algorithms is of great scientific interest but is not part of the Research Questions formulated for this thesis. As a result, it has been decided to only make use of batch least-squares adjustment and extended Kalman filter to conduct this research. This leaves room for further possible investigations about advanced filtering for future research activities.

3

4

ON-GROUND RELATIVE ORBIT DETERMINATION

This chapter describes the on-ground angles-only precise relative orbit determination system employed to support the AVANTI experiment. This operational tool has primarily been used as verification layer during the conduction of this challenging in-orbit demonstration. The system performance and behavior is analyzed using the experience gained during two months of operations. In order to highlight the specificities introduced by the orbit of a given mission, previous flight data from the ARGON experiment are reprocessed in the same way and serve as comparison.

4.1. OVERVIEW

The angles-only precise relative orbit determination process can be functionally divided in three modules which are depicted in Fig. 4.1. As mentioned in the introduction, the apparent simplicity offered by passive imagery comes at the cost of additional processing difficulties. Before making use of line-of-sight measurements, it is first necessary to extract them from the raw images. This is the task of the target identification module which is in charge of providing a set of observations to the relative state estimation.
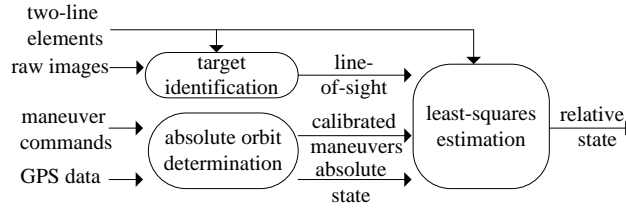

Figure 4.1: Functional view of the relative orbit determination task performed onground.

The reliable extraction of line-of-sight observations from pictures is a fundamental task. However, this aspect has not been deeply investigated in the literature, probably because the large majority of authors does not deal with real flight data. The built-in target detection software [99] of the VBS flown with PRISMA (see Section 2.1.1) constitutes one of the few available references. Being directly implemented in the camera system, the algorithm is able to run at a high frequency of 2 Hz and detects non-stellar objects based on their expected inertial angular velocity. The sensor internally keeps track of all the detected objects and delivers only the best candidate, based on the luminosity and the number of sequential detections. During PRISMA operations, false detections were however sometimes reported [46, 47]. Delpech et al. conducted three 16-hour-long approaches from 4 km to about 100 m intersatellite distance and reported less than 10 wrong measurements [47] during each rendezvous. Considering the full visibility of the relative motion and the high frequency of the VBS, it is estimated that about 10^5 measurements have been collected during each rendezvous. It has to be noted that the strategy implemented by the VBS appeared more difficult to implement considering the low image rate of one image every 30 seconds used during AVANTI. During the ARGON experiment, a target detection algorithm based on the linking of bright connected sets of pixels over sequences of images had been used [100]. However, the algorithm was also subject to some misdetections [48]. As a result, a novel and more robust algorithm has been developed to support the AVANTI experiment, based on the kinematic detection of target trajectories. This algorithm is described in detail in Section 4.2.

The precise estimation of the relative trajectory is done *a posteriori* on ground and is thus subject to very few restrictions concerning the computational and data storage resources. As a result, in view of the sparse observations and the weak observability of the relative motion, a batch least-squares estimation is preferred to a sequential filtering to improve the overall robustness of the solution. By considering long observations arcs, it is indeed possible to observe the long-term effects of perturbations, such as differential drag, which are otherwise difficult to be properly estimated. Furthermore, the

resulting iterative refinement of the solution is well adapted to remove possible outliers of the observations which could degrade the accuracy. As described in Section 3.4.1, the nonlinear least-squares adjustment requires a reference solution around which the state is linearized. It has been chosen to make use of TLEs to derive an approximate initial value of the relative state, which can easily be justified by the fact that almost all orbiting objects larger than 10 cm are catalogized as part of the space awareness activities, so that any rendezvous in low Earth orbit with a noncooperative satellite can rely on TLEs for initial target acquisition. Moreover, as described later in this chapter, the TLEs ideally complement angles-only navigation at far-range: while the latter is extremely precise in lateral positioning, but has trouble in properly estimating the intersatellite separation, the former provides a valuable estimate of the relative separation in along-track. The position error of the TLEs is typically comprised between hundreds of meters up to a few kilometers, which only corresponds to a few percent of error when starting the approach at 50 km distance.

In the adopted design, the least-squares method adjusts a numerically propagated relative trajectory to best fit the available line-of-sight measurements. As described in Section 3.3.2, the execution of maneuvers during the rendezvous will improve the observability. In order to reduce the errors of the dynamical model, the maneuvers executed by the chaser are calibrated prior to the relative orbit determination. This calibration is done using GPS data collected onboard as part of a GPS-based absolute orbit determination combining code and low-noise carrier phase measurements to reconstruct the absolute trajectory of the chaser with a precision at submeter level [101]. The resulting calibration errors are believed to be reduced to 0.1 mm/s. Note that this specific external module is not part of this research work and thus will not be described in the thesis.

4.2. Target Identification

Reliably detecting the target is an easy task at mid- and close-range, where the luminosity of the object allows for an unambiguous recognition. However this is challenging at far-range, where it is impossible to immediately recognize whether a luminous spot in the image represents a faint star, a hot pixel or a satellite. The use of a star catalog is of great help to distinguish the target from celestial objects. However, this approach is not sufficient to discriminate between all the objects present in the image, because some stars might not be included in the catalog or simply because additional non-stellar objects might be simultaneously visible.

As already stated, most of the time additional *a priori* information is available by the means of TLEs. However, the poor accuracy of the TLEs [102] makes them inappropriate for direct target recognition at intersatellite distances smaller than 50 km. At 10 km separation, for example, a cross-track error of 500 m translates into an error of about 3°. Considering the typical field of view of the camera (18° x 14° in our case, *cf.* Table 2.3a), this results in a large search domain which could lead to numerous false detections. In view of the measurement sparsity encountered during the AVANTI experiment, it is however important to ensure that all the line-of-sight measurements refer to the same target, otherwise the additional outliers could prevent the convergence of the solution. The strategy retained in this work to ensure a robust and reliable target detection consists in

combining a kinematic and a dynamic approach, described in the sequel. In this context, the kinematic approach means a detection that is only based on the observation of the apparent motion of the target, without considering the forces acting on it.

4.2.1. KINEMATIC DETECTION

The first step relies on the fact that, flying on a similar orbit, the apparent motion of the target seen by the chaser is very different from the motion of a star or from the motion of a satellite flying on a different orbit. Imagine a camera pointing in the direction of flight, seeking for a satellite flying ahead (or behind) on almost the same orbit. Once the stars have been identified using a catalog, a few objects might remain unknown, so that additional intelligence is needed to select the desired target. As depicted in Fig. 4.2, when superimposing a sequence of images, some trajectories can be recognized, greatly helping the discrimination.
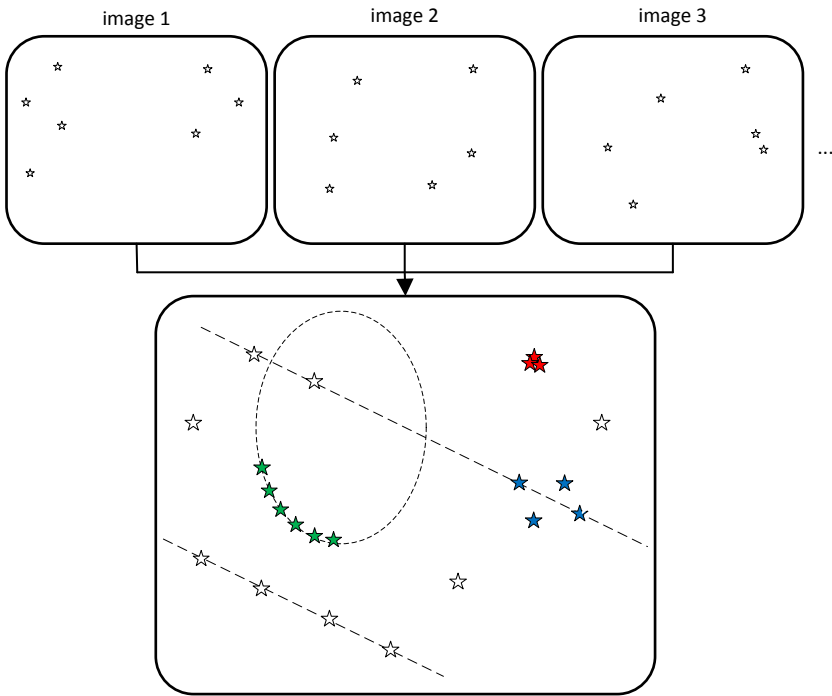

Figure 4.2: Density-based clustering of the non-recognized objects (the elliptical relative motion of the target is depicted by a dashed ellipse).

Of course, this is valid only if the camera pointing is fixed in the local orbital frame, which might not be the case, if the orientation of the camera follows the target or in case of large attitude control errors. As a result, it is necessary to consider the history of the non-recognized objects as viewed by a virtual camera which is fixed in the local orbital frame. Once this is done, the points belonging to the same trajectory are grouped using a clustering algorithm. The Density-Based Spatial Clustering of Applications with

Noise (DBSCAN) [103] has been found extremely convenient for this purpose, since it allows grouping the points whose interdistance is below a certain threshold considering the other ones as noise. Since the angular distance traveled by the target object between two images is much smaller than the traveled distance of a non-recognized star or of a satellite flying on a different orbit, this clustering algorithm automatically selects the set of points which are likely to belong to the same trajectory and groups them in clusters (green, blue and red groups of stars in Fig. 4.2).

DBSCAN requires only two parameters: the angular distance threshold ϵ between the points and the minimum number of points $n_{\min}$ required to form a dense region. Some care has to be taken for the definition of ϵ, which should correspond to the distance traveled by the satellite between two consecutive images, and which depends on the unknown target orbit. Several strategies are possible to set the proper value of ϵ:

- Based on simple considerations, a coarse value able to capture a trajectory and to reject the non-recognized stellar objects is manually set. Given the orbital period of the chaser satellite (about 90 minutes) and the time interval between two images (30 seconds), an inertially fixed celestial object would travel an angular distance of about 1.9° between two images which corresponds to about 80 pixels for the camera. Instead, a target object exhibiting a two-kilometer-large elliptical relative motion (*cf.* Fig. 3.4) seen from 20 km would travel only 3-4 pixels between two images. As a result, a conservative value of ϵ = 10 pixels should ensure the detection of the target (note that this is at this stage very similar to the detection based on the inertial angular velocity of the VBS sensor [99], except that the orbital frame is used as reference frame to analyze the relative motion). However, it has to be emphasized that this approach is only valid if the coarse assumptions about the target relative motion are correct. In addition, the average distance traveled by the target between two images might vary a lot at mid- and close-range, so that some adaptations of the threshold might be required throughout the complete approach. This simple strategy has been adopted for the on-ground data processing, for which frequent setting modification is not an issue.
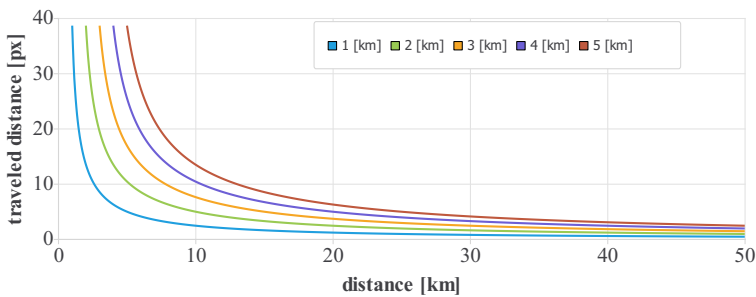

Figure 4.3: Approximated traveled angular distance between two images for different sizes (represented by different colors) of the relative motion.

A coarse approximation of the apparent angular distance traveled by the target between two images will be given in the next chapter in Eq. 5.2. Based on this formula, Fig. 4.3 depicts this distance in pixels for different sizes of the relative motion at different intersatellite separations. It can be recognized that a threshold

$\epsilon = 10$ pixels can be used to detect large elliptical relative motions up to 5 km down to an intersatellite distance of 15 km. However, this maximal working distance decreases to 3 km if the size of the motion is reduced to 1 km during the rendezvous. Since the objective of a passively safe approach is to reach a final relative motion size of a few hundred meters, or even tens of meters, the same value of threshold $\epsilon = 10$ pixels can be employed during a large part of the rendezvous.

- Since the orbit determination process requires anyway a reference target trajectory, the value of ϵ can also be derived from this *a priori* knowledge of the relative orbit, based on the same considerations as before. In view of the numbers derived above, a coarse value based on the size of the relative motion and the intersatellite distance should be enough (the exact apparent distance traveled between two images is the projection of a 3D elliptical motion on the focal plane of the camera and is difficult to compute). This solution based on Eq. 5.2 has been retained for the onboard real-time processing (for which frequent setting modification using telecommands would be tedious) and is described in detail in Section 5.2.1.

- A more elegant solution could be to derive the mean distance between the objects by analyzing the image without *a priori* information, as a human eye would do. This would be useful for example for a survey of space debris or asteroids which could be discovered for the first time. However, this induces more complexity and is not required for a target whose orbit is not unknown.

The DBSCAN algorithm yields clusters forming dense regions. In order to distinguish a trajectory (green cluster in Fig. 4.2) from a conjunction of random non-recognized objects (blue cluster in Fig. 4.2), the target identification algorithm relies on the fact that the relative motion of the spacecraft obeys the laws of orbital dynamics. The projection of its elliptic trajectory on the focal plane can thus be easily recognized as a curve. This concept is illustrated in Fig. 4.4. The algorithm attempts to identify this trajectory by fitting each cluster with a second order Bezier curve (represented by a blue line in Fig. 4.4) and by retaining the clusters which could be successfully fitted, based on the fitting residuals σ_B. The only limitation here is that a second-order Bezier curve can only describe a portion of a trajectory, so that a sliding sequence of only 20 images (corresponding to 10 minutes) is used to piece-wise recognize the trajectory. Considering typical centroiding errors of less than half a pixel and the fact that the Bezier curve is only an approximation of the real trajectory, the algorithm considers a fit successful if $\sigma_B < \sigma_{B,max} = 1$ pixel.
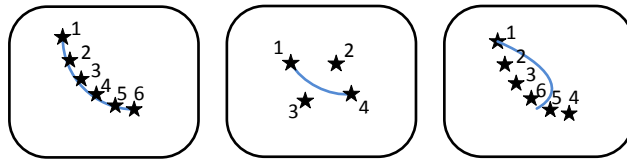

Figure 4.4: Bezier fits: success (left) and failures (middle and right). The Bezier curve is represented in blue. Small fitting residuals σ_B are only achieved in the first case.

As depicted in Fig. 4.4, this simple strategy allows detecting trajectories among the clusters provided by the DBSCAN algorithm. The beauty of this approach is that, if the

superimposition of images provides an apparent trajectory but the order of the points composing the trajectory is wrong (right case in Fig. 4.4), the algorithm will fail fitting a Bezier curve, since the parameter of the curve is chosen to be the time stamp of the images. This kinematic approach is appealing, since it requires little a priori knowledge about the orbit the target, but might however fail in rare cases:

- if a hot pixel appears, an object will be recognized as being fixed in the orbital frame (red cluster in Fig. 4.2), which could in principle correspond to a satellite seen at very large distance (the image of a 500-meter-large relative elliptical orbit seen at 100 km would also be almost a fixed pixel) or a pure along-track (also called V-bar in the literature) approach. Similarly, if a conjunction of random nonrecognized objects appears with very small interdistance, a Bezier curve with $\sigma_B < \sigma_{B,max}$ could be found by fitting the cluster.

- if another satellite is visible on a similar orbit (for example, a spacecraft launched with the same rocket), several trajectories can be simultaneously visible.

The occurrence of such events is impossible to precisely quantify, since it directly depends on the mission characteristics. The apparition of hot pixels is related to the aging of the camera and to the time at which the rendezvous is performed. During the ARGON experiment, three hot pixels were identified, while no hot pixel was encountered during the AVANTI experiment. This is probably due to the fact that ARGON has been conducted after two years in orbit, while AVANTI started a few months after the launch of the BIROS spacecraft. Furthermore, if a hot pixel is detected before initiating a rendezvous, it is possible to provide the flight software with such information to mitigate its effect. Therefore, this event becomes problematic only if a hot pixel suddenly appears during the few days of a rendezvous. On the contrary, the presence of other satellites flying on similar orbits was an issue, mainly during the first days of the commissioning of the AVANTI experiment. In view of the early conduction of the experiment in the mission timeline, it is assumed that a satellite launched together with BIROS was visible at that time. However, no further identification attempt has been done to confirm this assumption.

The consequence of these events is that, in some cases, the algorithm will find several possible plausible trajectories. In other cases, it will provide a single wrong trajectory, if a parasite target is visible instead of the desired one. Consequently, additional validation of the target detection has to be performed, before delivering the angles-only observations to the relative orbit determination process. This data screening is described in Section 4.3.2 but, before addressing it, the above-described ideas are first formalized in the next section.

4.2.2. ALGORITHM DESCRIPTION

Fig. 4.5 depicts the different steps involved in the target detection. In what follows, all objects imaged by the camera are considered as n point sources, whose centroids $\boldsymbol{p}_i$ have first to be determined. This task is a basic star tracker functionality and recalled here for completeness. In a first step, all pixels $\boldsymbol{c}$ whose brightness $b(\boldsymbol{c})$ is greater than the background noise σ_c are selected, forming a set $\mathscr{L}$ of luminous pixels which are
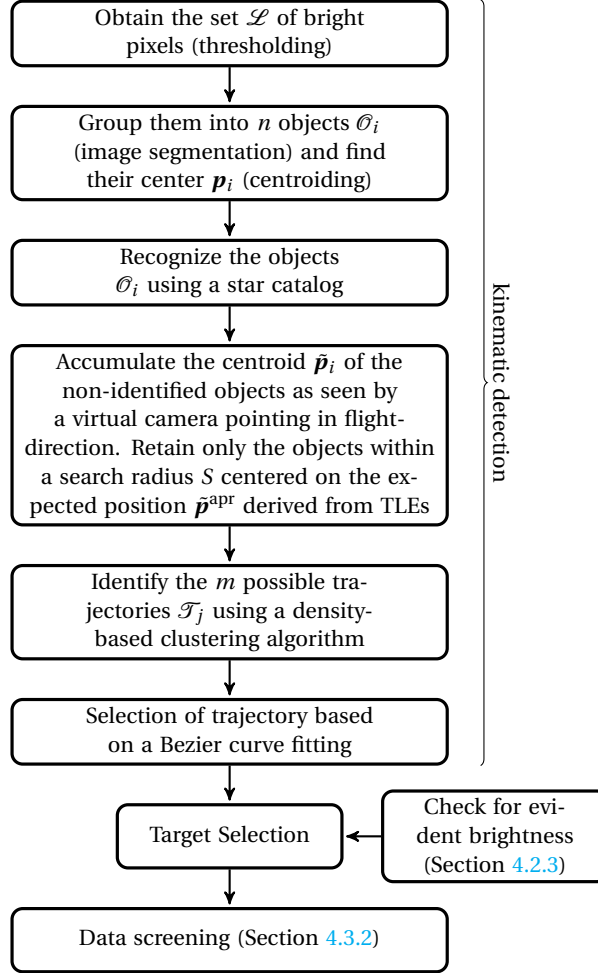
```
┌─────────────────────────────────┐
│   Obtain the set 𝓛 of bright    │
│     pixels (thresholding)       │
└─────────────────────────────────┘
                │
┌─────────────────────────────────┐
│  Group them into n objects 𝒪ᵢ   │
│  (image segmentation) and find  │
│  their center pᵢ (centroiding)  │
└─────────────────────────────────┘
                │
┌─────────────────────────────────┐
│      Recognize the objects      │
│    𝒪ᵢ using a star catalog      │
└─────────────────────────────────┘
                │
┌─────────────────────────────────┐
│ Accumulate the centroid p̃ᵢ of the│
│   non-identified objects as seen by│
│   a virtual camera pointing in flight-│
│  direction. Retain only the objects within│
│  a search radius S centered on the ex-│
│  pected position p̃ᵃᵖʳ derived from TLEs│
└─────────────────────────────────┘
                │
┌─────────────────────────────────┐
│   Identify the m possible tra-  │
│  jectories 𝒯ⱼ using a density-  │
│   based clustering algorithm    │
└─────────────────────────────────┘
                │
┌─────────────────────────────────┐
│  Selection of trajectory based  │
│     on a Bezier curve fitting   │
└─────────────────────────────────┘
```

Figure 4.5: Functional view of the target detection algorithm.

distributed over the whole image:

$$\mathscr{L} = \{\boldsymbol{c} : b(\boldsymbol{c}) > \sigma_{\mathrm{c}}\}. \tag{4.1}$$

The pixels referring to the same object have to be grouped in n clusters $\{\mathscr{O}_i\}$. For this purpose, several methods exist. The DBSCAN algorithm can be for simplicity advantageously reused (for example with $\epsilon = 2$ and $n_{\mathrm{min}} = 2$, so that any group of more than 2 pixels will be considered as an object $\mathscr{O}$). Once the objects are formed, their centroiding can be computed using a simple arithmetic mean:

$$\boldsymbol{p}_i = \sum_{\boldsymbol{c} \in \mathscr{O}_i} b(\boldsymbol{c}) \boldsymbol{c} \frac{1}{\sum_{\boldsymbol{c} \in \mathscr{O}_i} b(\boldsymbol{c})} = \sum_{\boldsymbol{c} \in \mathscr{O}_i} b(\boldsymbol{c}) \boldsymbol{c} \frac{1}{I_i}, \tag{4.2}$$

where I_i can be taken as a measure of the brightness of the object. The pixel position $\boldsymbol{p}_i$
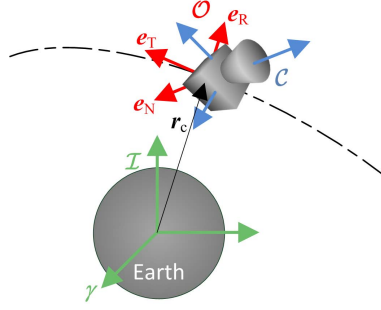
Figure 4.6: References frames used in this work: the inertial frame $\mathcal{I}$ is centered on the Earth, with x-axis aligned with the mean equinox γ and z-axis aligned with the Earth's spin axis. The local orbital frame $\mathcal{O}$ is defined according to the spacecraft position and velocity. The camera frame $\mathcal{C}$ is assumed to have its origin at the spacecraft center of mass and can be oriented in any direction.

is then transformed in a line-of-sight measurement $\boldsymbol{u}_i^{\mathcal{C}}$ (expressed in the camera frame $\mathcal{C}$, as depicted in Fig. 4.6.) to the object $\mathcal{O}_i$ after taking the intrinsic camera parameters γ into account (comprising focal length, principal points, skew coefficient and distortion):

$$\boldsymbol{u}_i^{\mathcal{C}} = \boldsymbol{g}^{-1}(\boldsymbol{p}_i, \gamma). \tag{4.3}$$

For this work, a simplified camera model $\boldsymbol{g}$ (mapping a unit vector into a pixel position) considering a pinhole camera accompanied with lens distortion has been found sufficient. This model is provided by Bouguet [104] and directly derived from the model proposed by Heikkila and Silven [105]. In this model, the pixel position $\boldsymbol{p}$ depends on the normalized position $\hat{\boldsymbol{p}}(\boldsymbol{u}) = \left(u_1/u_3, u_2/u_3\right)^T$

$$\boldsymbol{p} = \begin{pmatrix} f_1 & 0 & \xi_1 \\ 0 & f_2 & \xi_2 \end{pmatrix} \begin{pmatrix} (1 + k\|\hat{\boldsymbol{p}}\|^2)\hat{\boldsymbol{p}} \\ 1 \end{pmatrix}, \tag{4.4}$$

where $\boldsymbol{f} = \left(f_1, f_2\right)^T$ is the focal length in pixels, $\boldsymbol{\xi} = \left(\xi_1, \xi_2\right)^T$ is the camera principal point coordinates in pixels and k the main radial distortion coefficient. Note that no skew coefficient has been introduced because its contribution to the modeled pixel position was judged negligible by the constructor of the camera.

The knowledge of the line-of-sight $\boldsymbol{u}^{\mathcal{C}}$ of the objects present in the image allows the identification of the celestial objects. This can be done either using a lost-in-space approach, in which the stars are identified without any *a priori* information, or using the onboard knowledge of spacecraft attitude together with the mounting information of the camera. Once the stars are identified, the extrinsic camera parameters (that is, the orientation of the camera $\boldsymbol{R}_{\mathcal{I}}^{\mathcal{C}}$ in the inertial frame $\mathcal{I}$) can be derived, for example using the q-method [106].

At this stage, a set of still unidentified objects $\{\mathcal{O}_i\}$ remains. The next step is to recreate their virtual image $\tilde{\boldsymbol{p}}_i$ as seen in the frame $\mathcal{V}$ of a virtual camera perfectly pointing in the flight-direction

$$\tilde{\boldsymbol{p}}_i = \boldsymbol{g}\left(\boldsymbol{R}_{\mathcal{I}}^{\mathcal{V}} \boldsymbol{R}_{\mathcal{C}}^{\mathcal{I}} \boldsymbol{g}^{-1}(\boldsymbol{p}_i, \gamma)\right). \tag{4.5}$$

Once this is done, the DBSCAN algorithm can be run on the set of unrecognized objects $\tilde{\boldsymbol{p}}_i$. In order to reduce the number of possible candidates for the target, it is at this stage advised to accumulate only those unrecognized objects which are compatible with the coarse *a priori* image position $\tilde{\boldsymbol{p}}^{\text{apr}}$ provided by the TLEs. Their poor cross-track accuracy will, however, result in a large search area S. Thus, this feature is more helpful if a better *a priori* solution is available, resulting for example from a previous iteration. In this case, a candidate $\mathcal{O}_i$ is selected if $\|\tilde{\boldsymbol{p}}_i - \tilde{\boldsymbol{p}}^{\text{apr}}\| < S$. The output of the clustering algorithm is a set of m clusters $\{\mathcal{T}_j\}$ representing all possible trajectories. The next step is to fit the clusters $\{\mathcal{T}_j\}$ with a second order Bezier curve $\boldsymbol{B}(\tau)$, parameterized by the variable τ and defined by a set of three control points Ξ_0, Ξ_1 and Ξ_2

$$\boldsymbol{B}(\tau) = (1 - \tau)^2 \Xi_0 + 2\tau \Xi_1 + \tau^2 \Xi_2, \tau \in [0, 1]. \tag{4.6}$$

Three control points are at least required to describe a curve in the plane (two control points describe a straight line). It has been chosen to restrict the order of the Bezier curve to its minimum value to improve the robustness of the data fitting and avoid overfitting. In view of the simple expression of the Bezier curve, fitting the data is trivial and can be done using a least-squares approach. Here the parameter τ has to capture the fact that the trajectory is a time-dependent suite of points. This can be achieved by considering the timestamp t_k of the points $\tilde{\boldsymbol{p}}_k$ composing a cluster $\mathcal{T}$. If $t_{\min}$ and $t_{\max}$ denote respectively the oldest and newest timestamp of the set of points composing $\mathcal{T}$, the parameter τ_k associated to the point $\tilde{\boldsymbol{p}}_k$ can be defined as

$$\tau_k = \frac{t_k - t_{\min}}{t_{\max} - t_{\min}} \tag{4.7}$$

so that the oldest point will be associated with $\tau = 0$ and the newest point with $\tau = 1$.

4.2.3. EXPLOITING BRIGHTNESS INFORMATION

Until now, the brightness of the target has never been used. This is due to the fact that, at far-range, the brightness information can hardly be used in a reliable way. In fact, the quantity of light reflected by the target spacecraft depends on its surface properties and on its attitude which is unknown, since we are dealing with noncooperative targets. Fig. 4.7 depicts for instance the variation of brightness that has been observed during the ARGON experiment, when the spacecraft were separated by 28 km.

At mid and close-range instead, the object becomes so bright that an obvious detection based on this criterion becomes possible. The measure I of brightness as defined in Eq. 4.2 can be used for this purpose. Here, some calibration is required to get an idea on the specific values obtained with a given sensor and the chosen exposure time. Fig. 4.8a depicts for instance the brightness of 10000 stars measured during the ARGON experiment and ordered according to their magnitude.

Figure 4.7: Variation of brightness during one orbit at 28 km (ARGON experiment).
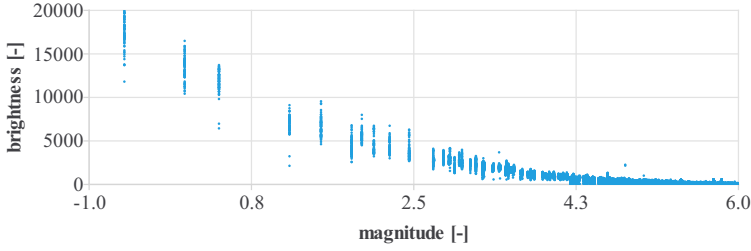
(a) Star brightness (exposure time = 0.5 s).
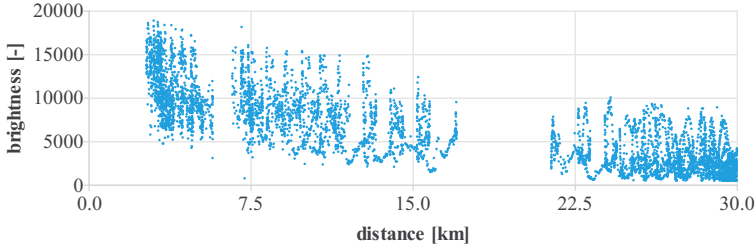
(b) Brightness of the Tango spacecraft (adaptive exposure time below 10 km).

Figure 4.8: Brightness measured using the μASC camera during the ARGON experiment.

The brightness of the target depends in addition on the object itself (size and surface) and will vary if the electronic shutter is used at mid- to close-range. As a consequence, some care has to be taken while defining a brightness detection threshold. Fig. 4.8b depicts the brightness of the target measured during the ARGON approach. A few data gaps are visible, due to the limited onboard storage capability during the ARGON experiment which made it necessary to discard some data [48]. Fig. 4.8b shows that an obvious detection threshold of $I_{ob} = 5000$ would capture the few stars with magnitude below 2.5 (which are anyway included in any star catalog and can easily be recognized) and the target at a distance smaller than about 7 km. Note that the knowledge of the planets should be also available to avoid false detections, because they can be as bright as the most luminous stars. The advantage here is that this additional detection based on the brightness will work only at small separations, which corresponds exactly to the domain where the kinematic detection will experience a performance degradation, due to possible wrong settings for ϵ and increasing centroiding errors.

This latter effect can be better understood by inspecting Fig. 4.9. The centroiding function will provide a measure of the center of the satellite based on the centroid of the flare which might greatly differ from the center of mass. Of course, at far-range this does not matter, since one pixel is larger than the size of the object. However, at mid- and close-range, this is not true anymore. The kinematic detection fits the target trajectory with a Bezier curve, which
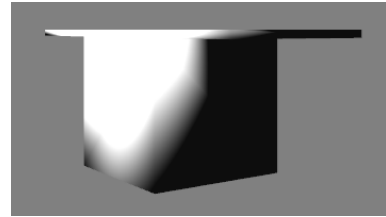

Figure 4.9: Example of unfavorable target illumination: the measured centroid will be far from the center of mass.

might fail in the presence of large centroiding errors. A detection based on the brightness can help mitigating this loss of performance.

4.3. BATCH-LEAST SQUARES ADJUSTMENT

4.3.1. SYSTEM DESIGN AND SETTINGS

The reconstruction of the relative orbit is done by means of a nonlinear batch least-squares adjustment as introduced in Section 3.4.1. A numerical propagation has been preferred to model the relative motion, in order to reach the best possible accuracy. This design choice will be critically revisited in Chapter 7. In this case, the relative trajectory is described in the form of a differential equation associated with an initial value $\boldsymbol{x}_0$ at time t_0

$$\dot{\boldsymbol{x}} = \boldsymbol{f}(\boldsymbol{x}, \boldsymbol{y}_\mathrm{c}(t), t), \tag{4.8}$$

where $\boldsymbol{f}$ describes the relative motion model and is a time-dependent function of the relative state vector $\boldsymbol{x}$ and of the absolute state of the chaser $\boldsymbol{y}_\mathrm{c}$. As explained in Section 3.3.3, this model must at least include the perturbation due to the Earth-oblateness (J_2) and to the differential drag. The relative state vector $\boldsymbol{x}$ is composed of the inertial relative position $\Delta\boldsymbol{r}$ and inertial relative velocity $\Delta\boldsymbol{v}$ of the target object with respect to the chaser. In order to estimate the relative drag as part of the orbit determination process, the state vector is augmented with the drag coefficient of the chaser spacecraft C_D (keeping the drag coefficient of the target constant):

$$\boldsymbol{x} = \begin{pmatrix} \Delta\boldsymbol{r}^T & \Delta\boldsymbol{v}^T & C_D \end{pmatrix}^T. \tag{4.9}$$

Note that this choice has been preferred over the estimation of the relative drag coefficient to better reflect the underlying physics: the target of AVANTI is a Cubesat with symmetrical shape resulting in a constant C_D, while BIROS undergoes frequent changes of attitude (as seen later), resulting in large variations of its drag coefficient. In view of the weak observability and the sparse measurements, it has been chosen to restrict the maximum number of estimated parameters. As a direct consequence, the maneuvers execution errors are, for example, not estimated. Instead, they are independently externally estimated using GPS data (*cf.* Section 4.1). Following Section 3.3.1, it has been chosen to parameterize the inertial line-of-sight vector using right-ascension (α) and declination (δ) angles (*c.f.*, Eq. 3.27) to form the measurement vector $\boldsymbol{h}$:

$$\boldsymbol{u} = \frac{\Delta\boldsymbol{r}}{\|\Delta\boldsymbol{r}\|} = \begin{pmatrix} \cos\alpha\cos\delta \\ \sin\alpha\cos\delta \\ \sin\delta \end{pmatrix} \tag{4.10a}$$

$$\boldsymbol{h} = \begin{pmatrix} \alpha \\ \delta \end{pmatrix} = \begin{pmatrix} \arctan\left(\frac{u_2}{u_1}\right) \\ \arcsin(u_3) \end{pmatrix}. \tag{4.10b}$$

The derivation of the Jacobian matrix is done using Eq. 4.10a and Eq. 4.10b:

$$\tilde{H} = \frac{\partial h}{\partial \Delta r}\frac{\partial \Delta r}{\partial x_0} = \begin{pmatrix} -\frac{r_2}{r_1^2+r_2^2} & \frac{1}{\frac{r_2^2}{r_1}+r_1} & 0 \\ -\frac{r_1 r_3}{r^2+\sqrt{1-\frac{r_3^2}{r}}} & -\frac{r_2 r_3}{r^2+\sqrt{1-\frac{r_3^2}{r}}} & \frac{\frac{1}{r}-\frac{r_3^2}{r^3}}{\sqrt{1-\frac{r_3^2}{r}}} \end{pmatrix} \frac{\partial \Delta r}{\partial x_0}. \tag{4.11}$$

For clarity, the notation r_i has been chosen to represent the ith component of Δr. The quantity $\partial \Delta r/\partial x_0$ is numerically evaluated as part of the numerical integration of the relative motion. The derivation of the least-squares solution is provided in Section 3.4.1. The force model used to represent the relative motion is summarized in Table 4.1. The covariance matrix P is of great interest in what follows. The first reason is that the introduction of the *a priori* P_0^{apr} covariance helps the convergence of the nonlinear least-squares solution in case of weak observability. The second reason is that the diagonal elements yield the vector σ of standard deviations of the components of the solution, which provides a measure of the achievable accuracy. In view of the strong anisotropy of the problem and in order to ease the following discussions, it is more convenient to map this vector in the Radial-Tangential-Normal frame and to restrict it to its first three components, corresponding to the relative position. As a result, the variable $\sigma_{\Delta r}^{\text{RTN}}$ will often be used in the sequel as measure of achievable accuracy for Δr_0.

Table 4.1: Relative motion model used for the numerical propagation.

Items	Value
Gravity model	JGM3 20x20
Atmospheric density model	Harris-Priester
Solar radiation pressure	applied
Luni solar perturbations	applied
Satellite area	cannonball model

Table 4.2 finally summarizes the key settings adopted for target detection and relative orbit determination during the AVANTI experiment. Note that P_0^{apr} was only used when divergence problems were encountered (*i.e.*, mostly at far-range because of the weak observability).

Table 4.2: Settings adopted during the AVANTI experiment.

Parameters	Value	Unit
ϵ	10	pixel
n_{min}	5	-
S	50	pixel
$\sigma_{\text{B,max}}$	1.0	pixel
I_{ob}	5000	-
σ	40	arcsec
P_0^{apr}	diag($5000^2,5000^2,5000^2,5^2,5^2,5^2,1$)	(m^2,m^2/s^2,-)

The values of the parameters are derived from simple considerations and flight experience. The proper setting for ϵ was already discussed in Section 4.2.1. It has been chosen to collect at least $n_{\min} = 5$ nonrecognized objects to form a cluster, in order to discard most of the unfortunate random conjunctions of nonrecognized objects. The size of the search radius S is derived from the accuracy of the TLEs, assuming a lateral error of 1 km at 50 km. The threshold $\sigma_{B,\max}$ to consider a curve fitting successful is based on the typical centroiding performance at subpixel level. The threshold I_{ob} was derived during the commissioning phase by measuring the brightness as depicted in Fig 4.8. The measurement noise σ assumes centroiding performance of half a pixel. The covariance $\boldsymbol{P}_0^{\mathrm{apr}}$ assumes larger TLEs errors up to 5 km to cope with possible large along-track errors. The nonlinear batch least-squares estimator relies on the provision of a reference trajectory derived from TLEs. In order to simplify the interfaces, it is appealing to compute this *a priori* solution using only line-of-sight measurements. This process is called angles-only Initial Relative Orbit Determination (IROD) in the literature and will be investigated in Chapter 6 as part of the research activities conducted after the collection of flight data. For simplicity, a derivation of the reference trajectory based on TLEs has been preferred during the AVANTI experiment.

4.3.2. DATA SCREENING AND REFERENCE TRAJECTORY

The kinematic target detection might sporadically deliver wrong trajectories corresponding to parasite objects, which need to be filtered out before the least-squares adjustment. In fact, if another object flying on a similar trajectory is also visible (for example a spacecraft that has been launched together with the target), the target detection algorithm will deliver two plausible trajectories. In rare cases, a random conjunction of nonrecognized objects might also be recognized as a trajectory. One might wonder why this additional data screening is required. Since the probability of such events is small, the healthy observations will greatly outnumber the misdetections so that, notwithstanding the outliers, a proper estimate of the trajectory can be derived. This is of course correct in case of continuous observations like ARGON. However for AVANTI, the problem is much more delicate. In this case, in view of the weak observability and sparse measurements, a few large outliers could prevent the convergence of the least-squares process. This is also due to the fact that a line-of-sight error of several degrees (corresponding to a wrong target detection in the search area S delimited by the TLEs) is several orders of magnitude larger than the expected measurement noise and can thus quickly endanger the integrity of the least-squares solution.

In order to mitigate this problem, the relative orbit determination process can rely on one fundamental advantage compared to a real-time sequential implementation (such as described in Chapter 5): the possibility to consider the whole history of measurements, in order to select the object which statistically more frequently appears. In this case, one can
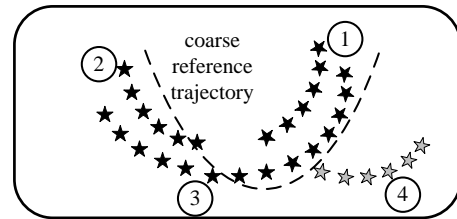

Figure 4.10: Statistical discriminations of wrong trajectories.

consider the entire collection of pieces of trajectories detected in the virtual frame and recognize the few trajectories which obviously do not belong to the same relative orbit based on the statistical distribution, as a human eye would do. This idea is depicted in Fig. 4.10: four pieces of trajectories have been found, but the gray one obviously corresponds to another spacecraft. The practical implementation is, however, not trivial. A clustering algorithm could help treating this problem by grouping the observations which form a dense region and rejecting the outliers. However, this approach has been found difficult to implement in a reliable way because the distance between the observations considerably varies during the entire approach, making the formation of clusters difficult. In fact, at this point, the problem is no more treatable solely based on a kinematic approach. Some information on the dynamics is needed to help the discrimination.

In view of the aforementioned difficulty, a simpler approach has been retained during the conduction of the AVANTI experiment, consisting in a basic data screening against the reference solution. The drawback of this strategy is that long data arcs are often needed to improve the observability. Starting from a reasonable guess reference trajectory, the pattern of line-of-sight errors is likely to grow exponentially when propagating over the complete data arc. Fig. 4.11 illustrates this phenomenon by depicting the line-of-sight errors between the measurements provided by the target detection and a reference solution using the flight data of the ARGON experiment. Even if the *a priori* solution is not bad at the beginning, small uncertainties regarding the initial conditions have a dramatic impact after several days. As a result, it might be difficult to automatically detect outliers based on simple thresholding. Here again, a clustering algorithm like DBSCAN is of help to discard the isolated points which are too far from the main error pattern. The advantage of such a strategy is shown in Fig. 4.11, where the red crosses correspond to the measurements which have been rejected after analyzing the error pattern with DBSCAN.
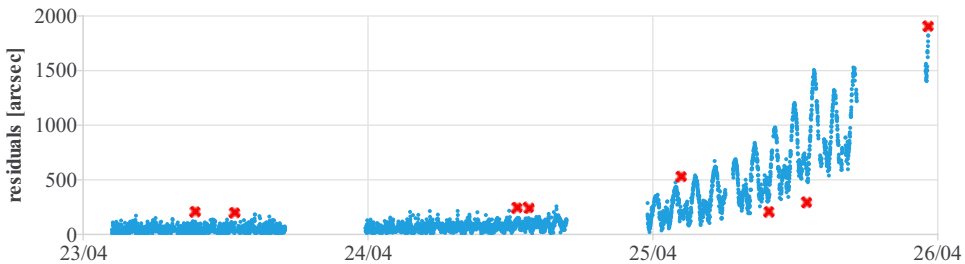

Figure 4.11: Line-of-sight errors (in blue) over a long data arc starting from a coarse reference trajectory (ARGON experiment). The red crosses correspond to outliers detected by the data screening.

Still, as summarized in the lessons learned concluding this chapter, this simple strategy was not always performing well, raising the need for an improved method. Thus, a more advanced data screening approach has been developed after the conduction of the experiment as part of the post-processing activities and will be presented in Chapter 7.

4.4. FLIGHT RESULTS

4.4.1. OPERATIONAL DIFFICULTIES

Overall, the facility for angles-only relative orbit determination successfully fulfilled its primary objective since it could support all the phases of the experiment with precise relative trajectory reconstruction. However, the proper selection of healthy measurements was the most difficult task. In fact, in view of the sparsity of the observations and of the nonlinear nature of the estimation problem, a few large outliers can endanger the integrity of the relative orbit determination. A wrong observation, off by a few degrees, introduces a considerable error which is one or two orders of magnitude larger than the measurement noise. The adopted approach to select the healthy data consists in delimiting a search area S around a reference solution but was shown to be sometimes not well adapted. A small search area of a few pixels will obviously exclude any fatal outliers. However, this is incompatible with the cross-track errors exhibited by the TLEs. Even if a very good reference solution is available at initial epoch t_0 (resulting for example from a successful previous estimation), the success of the subsequent relative orbit determination is never guaranteed, because of the unknown differential drag which might render the value of the previously estimated drag effect obsolete. In this case, as depicted in Fig. 4.11, the line-of-sight residuals with respect to the reference solution might rapidly grow, so that a small search area S will lead to the exclusion of a large part of the data comprised in the selected arc.

During the experiment, this major flaw has been mitigated using intensive manual labor, consisting in altering the duration of the data arc, refining the reference solution and modifying the value of the search area. This resulted in a large number of iterations which, combined with the fact that a numerical propagation had been chosen, made the orbit determination a very time-consuming task. Despite this difficulty, relative orbit determination products could always be derived. The key results are summarized in what follows.

4.4.2. THE FAR-RANGE FIELD

This analysis tackles the problem of approaching for the first time a noncooperative object at far-range. In this scenario, it is assumed that a coarse orbit phasing has already been performed by the ground segment based on the available TLEs of the target. A more general definition of orbit phasing is meant here, consisting in matching the target orbital plane and the in-plane properties of its elliptical motion, so that target and chaser are flying on identical orbits and separated by a few tens of kilometers. In view of the poor accuracy of the TLEs, no passive safety can be enforced at this stage, since the values of the relative eccentricity and inclination vectors cannot be determined accurately enough using TLEs. As a result, a safe separation of several tens of kilometers is kept during the orbit phasing.

The strategy for a successful target detection at far-range is to keep the camera pointing in flight direction, hoping that the target will become visible at some point. If the orbit phasing has been correctly done, the large separation ensures that the apparent relative motion is entirely contained in the field of view of the camera. At this safe distance, the longitudinal direction is difficult to be accurately estimated, since only large

and costly maneuvers would induce a perceptible change of relative motion. However, this matters little. In fact, it is much more judicious to exploit the complementarity between the TLEs and the line-of-sight measurements in order to focus on the motion perpendicular to the flight direction (*i.e.*, in the RN plane).

The power of this strategy can be demonstrated using a simple example from the ARGON experiment. Let us observe the Tango satellite on 23 April 2012 during only two orbits (between 18:00 and 21:00), when the spacecraft are separated by 30 km. The orbits are chosen to be maneuver-free resulting in a weak observability. Let us now consider that we have little information about the target orbit, thus assuming a pure along-track separation of 25 km. In view of the weak observability and the limited observation time, the least-squares adjustment is likely to diverge. If we now constrain the problem by introducing the *a priori* covariance P_0^{apr} corresponding to the accuracy of a coarse orbit phasing based on TLEs (errors of 5 km for the position and 5 m/s for the velocity), the process is able to converge to provide an estimate x_0 at epoch t_0=2012/4/23 18:00:00 UTC.

Table 4.12a summarizes the orbit determination results. Since this section focuses mainly on formation safety based on geometrical considerations, the state vectors are translated into dimensional relative orbital elements $a\delta\boldsymbol{\alpha}$ for simplicity and the drag coefficient is omitted. The reference relative state is derived from the GPS-based relative orbit determination products. It can be observed that, without the need of executing any maneuver, the relative orbit determination is already able to estimate $a\delta a$ accurately to a few meters. This is of great importance, since $a\delta a$ directly drives the drift rate during the rendezvous, so that its accurate knowledge ensures a smooth approach. Passive

(a) Relative orbit determination results.

a priori	$a\delta\boldsymbol{\alpha}_0^{\mathrm{apr}}$	= (0	-25000	0	0	0	0) m
estimated	$a\delta\boldsymbol{\alpha}_0$	= (2	-33500	-83	-417	1	246) m
reference	$a\delta\boldsymbol{\alpha}_0^{\mathrm{ref}}$	= (-6	-30000	-80	-370	3	220) m
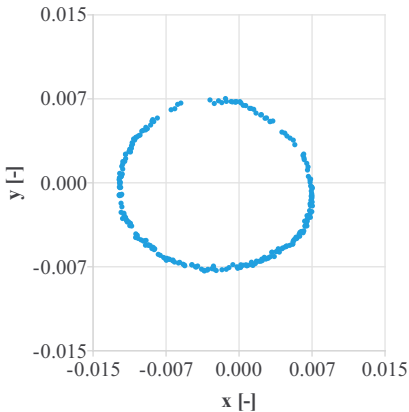
(b) Normalized coordinates $\hat{\boldsymbol{p}}$ of the target measured in the virtual frame $\mathcal{V}$.
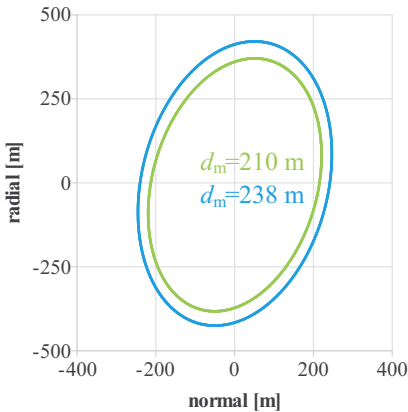
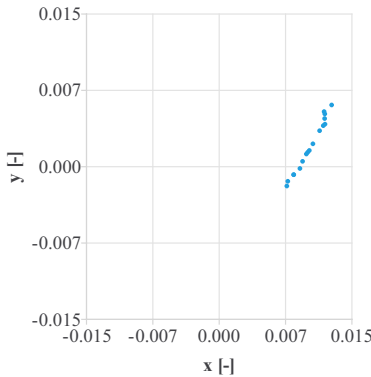(c) Estimated (blue) vs. true (green) relative motion in the RN plane.

Figure 4.12: Relative orbit determination with *a priori* covariance at far-range (ARGON).

safety is established by ensuring that the relative inclination and eccentricity vectors are collinear. The error of the estimated vectors $a\delta e$ and $a\delta i$ amounts to about 10% of their size, allowing already at that stage for the design of passively safe relative orbits. Note that this discussion is done using an external reference instead of the covariance of the solution. The reason is that, due to the adopted parameterization of the state vector (a Cartesian inertial relative state) in the onground orbit determination process, the covariance is not helpful to understand the accuracy of the estimated relative orbital elements. This is an important lesson learned for the design of a relative orbit determination system: the parameterization of the state vector using relative orbit elements, as seen in the next chapters, is operationally more convenient for the evaluation of the system performance. Figure 4.12c graphically depicts the estimated and true relative motion in the RN plane, showing that the shape of the orbit has properly been reconstituted but its size has been overestimated by about 10% (because the distance has been as well overestimated by 10%), leading to a too optimistic minimum distance $d_{\min}$.

In the following, a similar exercise is performed using the data collected during the AVANTI experiment. This is done by selecting a four-hour-long data arc on 24 September 2016, when the spacecraft are separated by 45.6 km, according to TLEs. Here again, the relative orbit determination is aided by the covariance matrix $\boldsymbol{P}_0^{\mathrm{apr}}$ and the *a priori* reference trajectory assumes a pure along-track separation of 45 km. As shown in Fig. 4.13b, the visible relative motion is dramatically reduced. Here again, it is challenging to perform a successful orbit determination without constraining the problem with the covariance matrix. However, the interesting outcome is that, despite the small amount of observations, it is also possible to estimate the shape of the relative motion at this distance. In the absence of external reference during the AVANTI experiment and because of the difficulty to exploiting the covariance, it is not easy to assess the accuracy of the solution. The standard deviation of the estimated relative position in the local frame is

(a) Relative orbit determination results.

a priori	$a\delta\boldsymbol{\alpha}_0^{\mathrm{apr}}$	= (0	45000	0	0	0	0) m
estimated	$a\delta\boldsymbol{\alpha}_0$	= (-30	48500	- 534	670	4	852) m

(b) Normalized coordinates $\hat{\boldsymbol{p}}$ of the target measured in the virtual frame $\mathcal{V}$
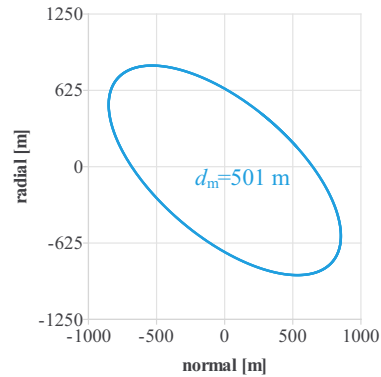
(c) Estimated relative motion in the RN plane.

Figure 4.13: Relative orbit determination with *a priori* covariance at far-range (AVANTI).

$\boldsymbol{\sigma}_{\Delta r}^{\text{RTN}}$ = (26, 4968, 56) m. Thus, it can be concluded that the estimated lateral apparent motion (the "shape" of the relative orbit) is accurate to a few tens of meters, while the range uncertainty has not yet been solved due to the weak observability and is still affected by the error of 5 km specified by $\boldsymbol{P}_0^{\text{apr}}$. Consequently, the "size" of the relative orbit will also be affected by an error of approximately 10%. Note that this discussion will later be resumed in Section 5.4.2, where the parameterization of the state vector with relative orbital elements offers a better framework for such analyses.

One interesting comparison consists in estimating the relative motion this time without any *a priori* covariance information. The main problem for this exercise is that, in order to greatly improve the observability and enable the convergence of the least-squares filter, one would need to considerably alter the relative motion, which is usually not the preferred approach. In order to keep a reasonable propellant budget, an alternative strategy consists in executing small maneuvers and observing the resulting effect over a longer time interval. This idea was retained in AVANTI, where a single 1.2 cm/s maneuver has been executed on 23 September. Small maneuvers will only slightly improve the observability, thus requiring a longer observation arc (typically several days) to ensure the convergence of the least-squares process. However, this comes at the cost of a degradation of the dynamical model over the considered arc, because the mismodeling errors will become predominant. To illustrate this idea, a sensitivity analysis with respect to the data arc is performed by running two orbit determinations with different data arcs lengths of, respectively, five and seven days.

The results are summarized in Table 4.3. The range estimate between the two runs differs by about 20%, which is worse than the accuracy of the TLEs. This example has been chosen to highlight the difficulty to choose the proper length of the data arc. By selecting five days of observations, the standard deviation of the least-squares solution indicates a large uncertainty in the along-track direction (7 km). It is thus tempting to increase the data arc in order to reduce the standard deviation, but then the data fitting degrades.

Table 4.3: Orbit determination without *a priori* covariance with different data arcs.

data arc	2016/9/21 - 2016/9/26	2016/9/21 - 2016/9/28
observations	346	444
residuals (α, δ)	$0 \pm 33'', 0 \pm 35''$	$0 \pm 38'', 0 \pm 42''$
$a\delta\boldsymbol{\alpha}_0$	(4 47227 -724 555 2 875) m	(13 57261 -860 691 2 1041) m
C_D	2.39	1.91
$\boldsymbol{\sigma}_{\Delta r}^{\text{RTN}}$	$\begin{pmatrix} 164 & 7269 & 133 \end{pmatrix}$ m	$\begin{pmatrix} 101 & 4205 & 76 \end{pmatrix}$ m

A closer look on the residuals pattern in Fig. 4.14 can help assessing the quality of the orbit determination. The residuals in the order of 30" correspond to measurement noise of less than half a pixel, with one pixel corresponding to 80". Some data gaps can be observed. They correspond to time intervals where the chaser had to interrupt the observation due to thermal problems on the BIROS satellite.

Figure 4.14b shows that the residuals of the 7-day solution (especially of the declination) slightly increase and cannot be considered as white noise anymore, indicating that the quality of the orbit determination is probably not as good as the one done with
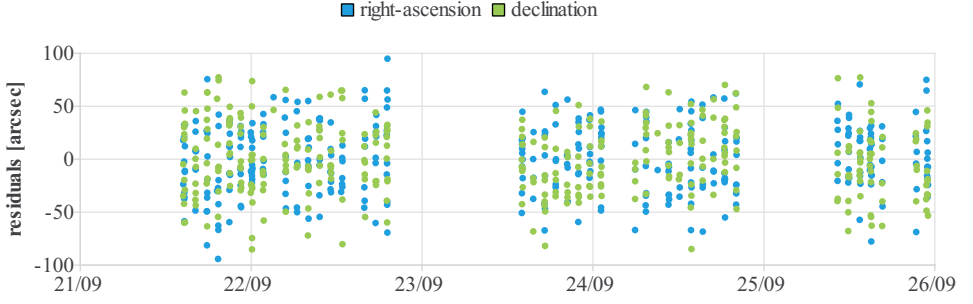
(a) 5 days.
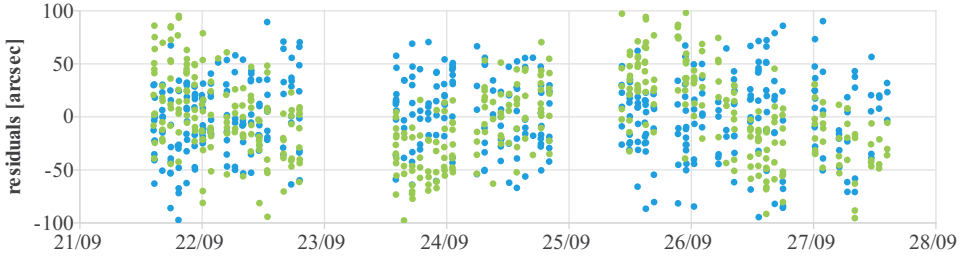
(b) 7 days.

Figure 4.14: Relative orbit determination residuals without *a priori* covariance at far-range (AVANTI).

the 5-day-long arc, because the dynamical model is not adequate anymore. At far-range, some dexterity is thus required to select the best compromise between observability and validity of the dynamical model, as well as to judge the quality of the products.

These are however subtle considerations, since the accuracy of the relative orbit determination will anyway improve with decreasing distance and since, despite the difficulty in estimating properly the range, the different orbit determinations already provide a very good estimate of the geometry of the relative motion. Figure 4.15 depicts for instance the difference between the relative motion in the RN plane estimated using orbit determinations performed with and without *a priori* covariance. As expected after the analysis of the residuals, the 5-day solution shows a good match with the solution computed using the *a priori* covariance.
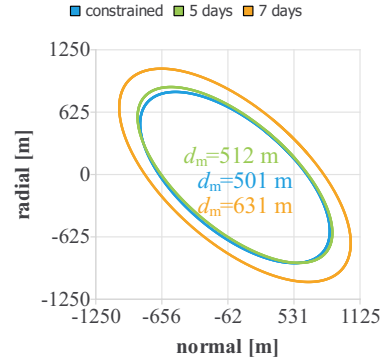
Figure 4.15: Estimated relative motion in the RN plane on 24 September 2016 12:00 UTC by performing a relative orbit determination with *a priori* covariance (in blue), complemented by two orbit determination runs without *a priori* covariance over 5 days in green and over 7 days in orange (AVANTI).

4.4.3. FAR- TO MID-RANGE REGIME

As soon as larger variations of the apparent relative motion can be observed in far- to mid-range regimes, the difficulties described in the previous section disappear. The orbit determination rapidly converges and consistent results are observed between consecutive data arcs. Here again, the skill of the user is required to select the most appropriate data arc, long enough to ensure observability and short enough to minimize the impact of the errors of the relative motion model. The first analyses are done with the good experimental conditions offered by the ARGON experiment. For this purpose, the pictures collected with the PRISMA satellites have been reprocessed over a 4-day-long data arc.
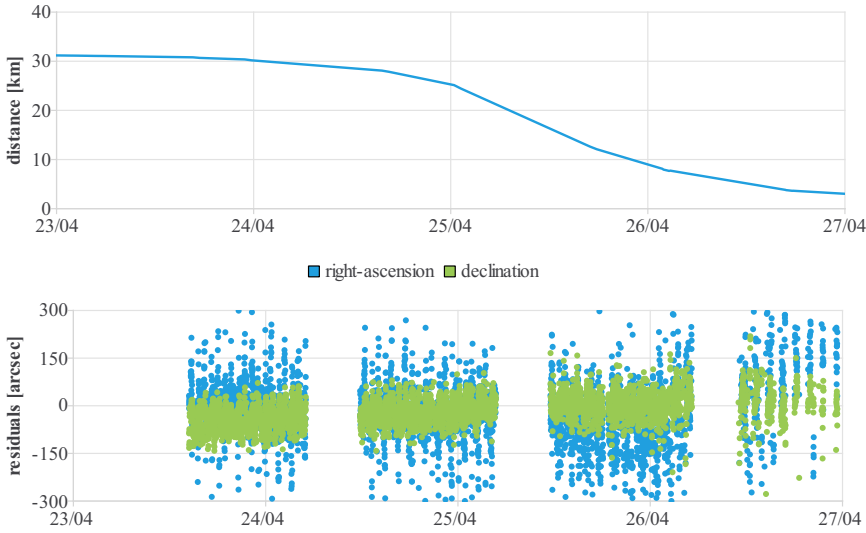
Figure 4.16: Intersatellite distance and residuals during the ARGON experiment (2012).

Figure 4.16 depicts the variation of distance during ARGON and the line-of-sight residuals after least-squares adjustment. At close distance, the target becomes so bright that the stars in the background are not visible anymore. This problem will be described in detail in the next section.

It has been decided to simply reject all the images if less than 6 stars are visible since, in this case, no precise estimation of the orientation of the camera can be done. This explains why the number of observations decreases when approaching. In view of the rapid change of relative motion from 30 km to 3 km over 5 days, the system is well observable, so that a good accuracy of the relative orbit determination can be achieved. Figure 4.17 depicts the orbit determination errors with respect to the GPS-based relative positioning products which are at meter level for all the components except for $a\delta\lambda$ which exhibits an error up to a few hundred meters, consistent with the results formerly obtained with ARGON [48].

It is interesting to focus on the remaining error sources. Obviously, the systematic centroiding errors due to the truncation of information in the Regions of Interests, as

documented in [48], plays a role in the overall error budget. The second obvious source of errors lies in the relative motion model and in particular in the errors due to the maneuvers. The fact that the least-squares process considers the entire data arc constitutes at the same time its force (to improve the observability) and its weakness, since the mismodeling are summed up over the complete arc. During the 4-day-long data arc, 26 maneuvers have been executed. Therefore, many maneuver execution errors are introduced in the relative motion model. Since the PRISMA satellites were fully cooperative, it is tempting to *a posteriori* recalibrate the maneuvers using differential GPS [107], to investigate the influence of maneuver execution errors. The least-squares solution obtained with the fine calibration of the maneuvers is depicted for comparison in red in Fig. 4.17. A clear improvement can be seen. Note this additional analysis based on fine maneuver calibration is only done for the sake of completeness in this thesis. In the general case, it is impossible to calibrate maneuvers using differential GPS with a noncooperative target. Once the error due the maneuvers is well reduced, the remaining perturbation of the relative motion model is mainly due to the differential drag. It can be seen that the filter is not able to precisely estimate the time variation of $a\delta a$ due to the differential drag, whose cumulative effect in 4 days amounts to about 3 m. This translates into an error of a few hundreds meters in $a\delta\lambda$. The orbit determination results using both fine and coarse maneuver calibration are summarized in Table 4.4.

During the AVANTI experiment, these difficulties are exacerbated by the fact that considerably less measurements are available and that the perturbation of the differential drag is much stronger. In addition, this perturbation is far from being constant.
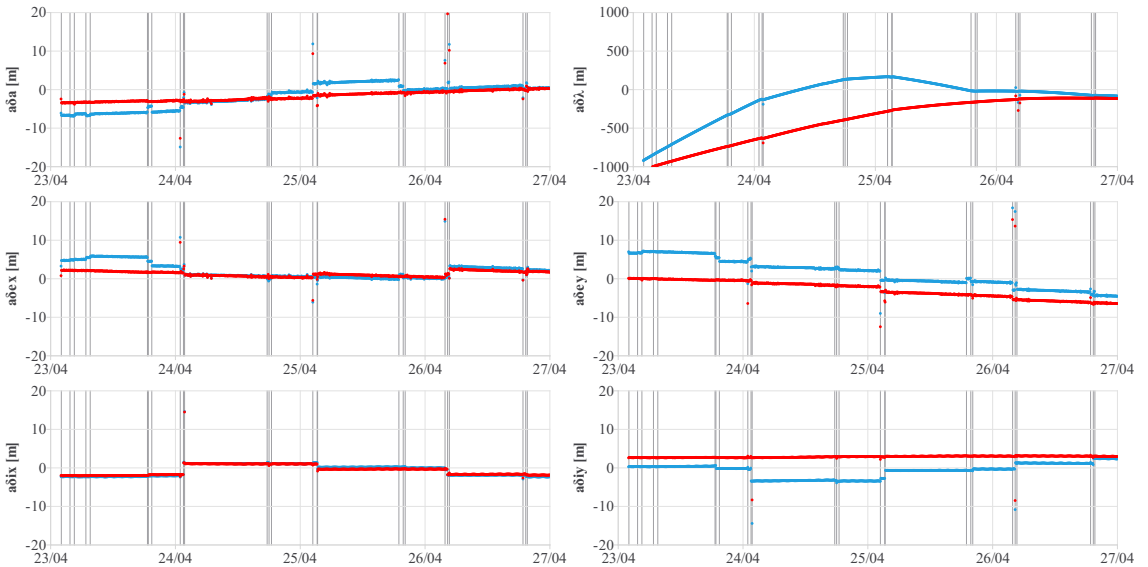

Figure 4.17: Error of the estimated relative orbital elements for both angles-only orbit determinations, using coarse (blue) and fine (red) maneuver calibration. The maneuvers are represented by gray vertical lines (AR-GON).

Table 4.4: Relative orbit determination results using coarse and fine maneuver calibration (ARGON).

Maneuver	coarse calibration	fine calibration
Data arc	2012/4/23 - 2012/4/27	2012/4/23 - 2012/4/27
Observations	4461	4499
Residuals (α, δ)	$19 \pm 90'', 11 \pm 49''$	$17 \pm 90'', 17 \pm 45''$
$a\delta\boldsymbol{\alpha}_0$	(-7 -30038 -83 -390 -4 202)m	(-3 -31151 -85 -397 -3 204)m
C_D	3.85	3.78
$\boldsymbol{\sigma}^{\mathrm{RTN}}_{\Delta r}$	$\begin{pmatrix}0.2 & 27.8 & 0.1\end{pmatrix}$ m	$\begin{pmatrix}0.2 & 27.4 & 0.1\end{pmatrix}$m

In the current design of the relative orbit determination facility, a constant value for the drag coefficient C_D is estimated over the whole data arc. In reality, the constraints posed by the chaser satellite during AVANTI resulted in frequent changes of attitude profiles to satisfy the mission requirements, inducing large variations of the cross-sectional area of the chaser. Fig. 4.18 depicts for example the area subject to the differential drag in different attitude modes: Earth-pointing (in order to orient the communication antennas to the ground), Target-pointing (when tracking the target with the star tracker), and cool-down mode (when the spacecraft needed to be actively cooled).

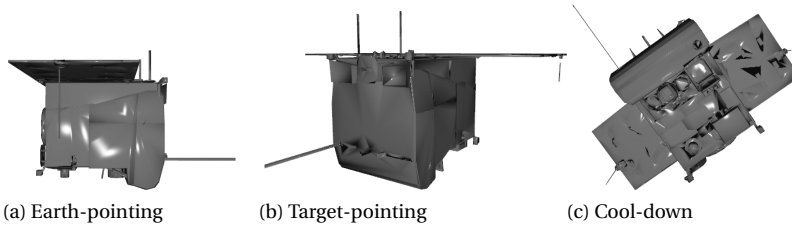(a) Earth-pointing   (b) Target-pointing   (c) Cool-down

Figure 4.18: Variation of cross-sectional area for different attitude profiles (AVANTI).

These difficulties have to be kept in mind but do not prevent the completion of the relative orbit determination task. Figure 4.19 depicts for instance more than one month of relative orbit determination, covering a large part of the commissioning phase as well as the first autonomous approach (19 to 23 November). Figures 4.19a and 4.19b show, respectively, the estimated relative semi-major axis and mean along-track separation. Figure 4.19c and 4.19d depicts the residuals and standard deviation (derived from the covariance) of the solution of each data arc. The gray zones correspond to different arcs for the relative orbit determination. The 154 maneuvers executed during this period have not been represented for clarity. Note at the boundaries how accurately the different solutions match with respect to each other. Small discrepancies can be sometimes recognized (for example between the first and second data arc for $a\delta a$) but the errors are limited to a few percent of the estimated values. In fact, only a closer look to the standard deviation of the solution in Fig. 4.19d can provide us with a better insight into the achieved accuracy.

A clear correlation between the intersatellite distance and the performance of the orbit determination can be recognized. Starting with a fairly large along-track error of about 1 km at 40 km (*cf.* previous section), the accuracy improves when the distance be-
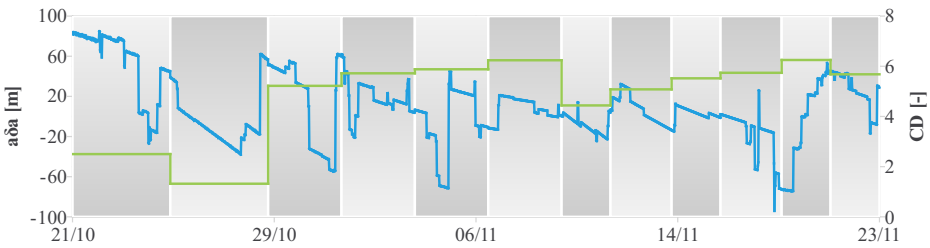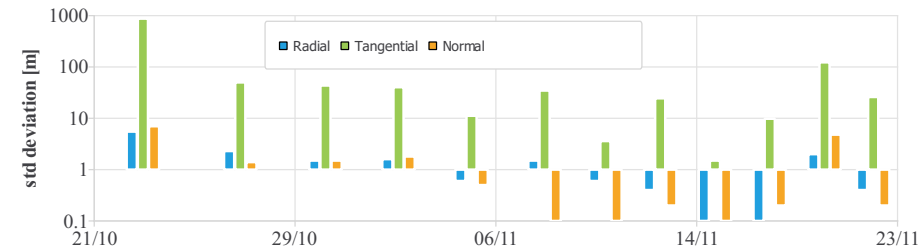
(a) Estimated relative semi-major axis (in blue) and chaser drag coefficient (in green).
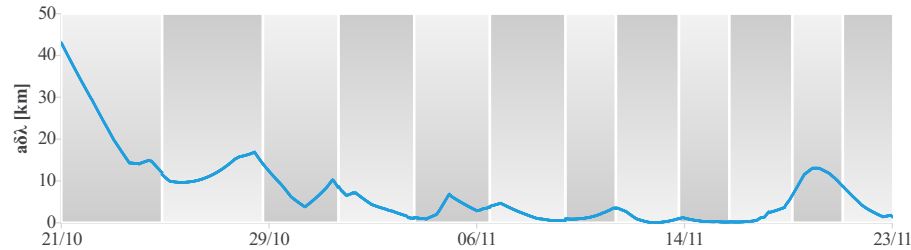
(b) Estimated mean along-track separation.
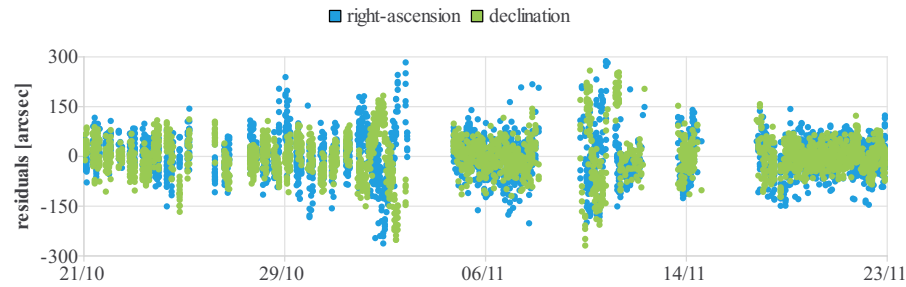
(c) Line-of-sight residuals.

(d) Standard deviation of the position, derived from the covariance of the solution at initial epoch of each data arc.

Figure 4.19: One month of relative orbit determination during the AVANTI campaign.

tween the satellites decreases, reaching relative positioning performance at meter level when the separation drops below 1 km (for example on 16 November). This feature makes angles-only navigation well adapted for space rendezvous, where more accurate knowledge of the relative motion is required when the separation decreases, in order to reduce the risk of collision. The estimated drag coefficient C_D of the chaser spacecraft is also represented for each orbit determination arc (green lines in the Fig. 4.19a associated to the right y-axis). Obviously, unrealistic values are obtained such as below zero or above six. They correspond to the fact that the orbit determination tends to capture the mean effect of the differential drag over the whole arc by adjusting C_D while keeping the area of the spacecraft constant. It can also be that the adopted model of the atmospheric drag (Harris-Priester) is too inaccurate. Further improvements are obviously needed to better model this perturbation.

Regarding the image processing, it seems that the assumptions done in Section 4.2 in terms of centroiding errors and target brightness were fully justified. Fig. 4.20 shows the Bezier curve fitting residuals and measured brightness for the tracked objects. In both experiments, the fitting residuals are similar, indicating that the centroiding performance is almost the same for Tango and BEESAT-4. The chosen limit $\sigma_{B,max} = 1$ pixel is adequate for the whole approach. The brightness is instead fairly different. This was expected considering the difference of size of the objects, 10x10 cm for BEESAT-4 against 30x30 cm for Tango. It can been observed that the intensity of Tango is limited. This is due to the fact that an automatic electronic shutter had been used during the conduction of the ARGON experiment, while this functionality was not yet activated during the considered data arc for AVANTI (*cf.* next section).
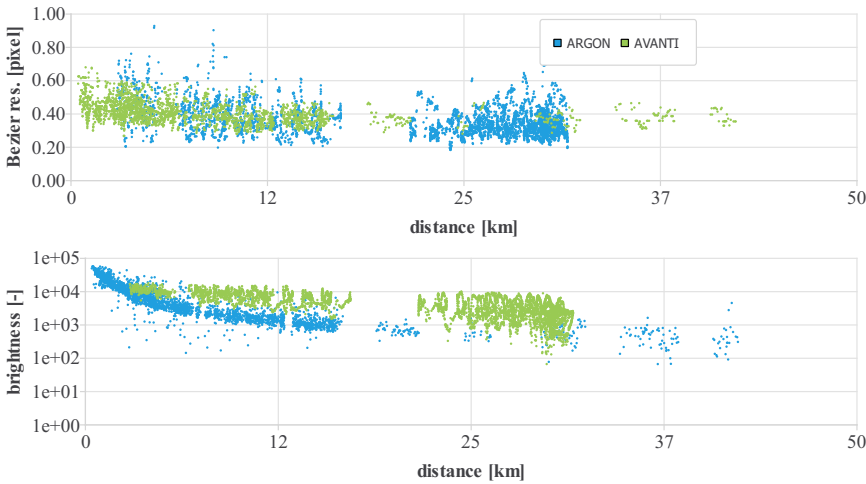

Figure 4.20: Output of the image processing for the ARGON and AVANTI experiments.

In the absence of other external references, it is still possible to get some insight into the navigation performance by analyzing, for example, the covariance of the solution. This provides a measure of the achieved orbit determination accuracy in terms of statistical errors. However, this measure "is often found to be too optimistic in the presence

of systematic force and measurement model error" [68]. This statement is easily illustrated by the discrepancies observed for ARGON between the orbit determination errors (Fig. 4.17), which indicates lateral and longitudinal navigation errors of a few meters and a few hundred meters, while the standard deviation (Table 4.4) indicates lateral errors below one meter and longitudinal errors of a few tens of meters. Still, this does not mean that this value cannot be exploited, rather that it has to be considered with care.

In order to assess the validity of the assumptions used for relative orbit determination, a radar campaign has been conducted as independent means of verification using the German TIRA system. The radar on ground suffers, however, from the difficulty to discriminate the signals reflected by the chaser and target satellites if the intersatellite distance is too small. Consequently, it has been decided to conduct this campaign when the satellites were far away (more than 40 km distance). Three radar passes have been scheduled on 20-21 October 2016, following the recommendations of the in-house expertise already available in this domain [108]. The resulting radar-based orbit determination is expected to be affected by an error of about 2 m in the radial direction and 20 m in the other directions [108]. For the angles-only orbit determination, a data arc spanning 5 days (18 to 22 October) has been selected for relative orbit determination, where a controlled approach had been initiated from ground to bring the formation back to 15 km separation.

Fig. 4.21 depicts the relative orbit determination errors compared to the radar-based solution in the local orbital frame. As expected, at this distance the longitudinal error is much larger (two orders of magnitude) than the lateral error. The covariance of the solution at epoch t_0=2016/10/20 20:00 UTC for the relative orbit determination indicates an error of [5.5 873.8 7.3] m in the RTN frame, which is consistent with the observed errors. Interestingly, the error predicted by the covariance is in line with the measured errors of the solution. This is due to the fact, at far-range, the systematic measurement errors are negligible and the assumption of Gaussian noise distribution is valid to a large extent. On the contrary, the already mentioned discrepancy between covariance and measured errors observed during the PRISMA experiment is due to the fact that systematic measurement errors are more pronounced at mid-range (below 10 km).
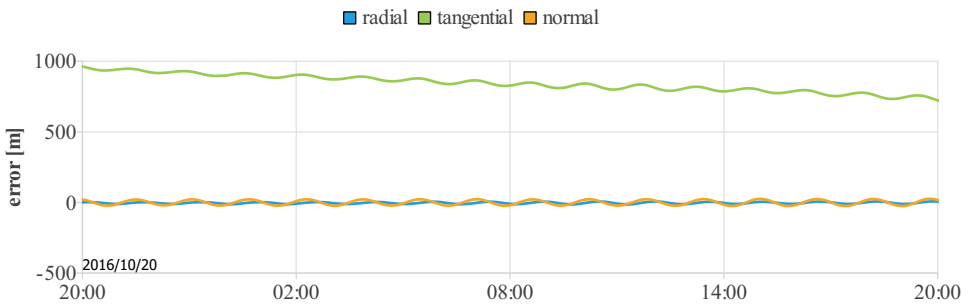

Figure 4.21: Orbit determination errors: angles-only vs. radar-based solution (AVANTI).

The lateral relative navigation performance is already at meter level at this distance (see radial and normal components in Fig. 4.21). This performance is needed in the early phase of a rendezvous to smoothly control the drift rate of the approach and to

establish a safe relative orbit. On the contrary, the exact knowledge of the intersatellite separation (which is in our case anyway accurately estimated to 2%) is not required at far-range to ensure safe operations. This discussion is better supported using relative orbital elements. Figure 4.22 depicts the estimated relative semi-major axis and mean along-track separation estimated during the TIRA campaign. Already at this distance, the relative semi-major axis is accurately estimated at meter level. Its decay due to the differential drag is also well estimated. Note that a large discontinuity is visible on 19 October 11:16 UTC. This corresponds to a 2.3 cm/s maneuver commanded from ground as part of the commissioning activities to rapidly decrease the intersatellite separation by creating a large relative semi-major axis.
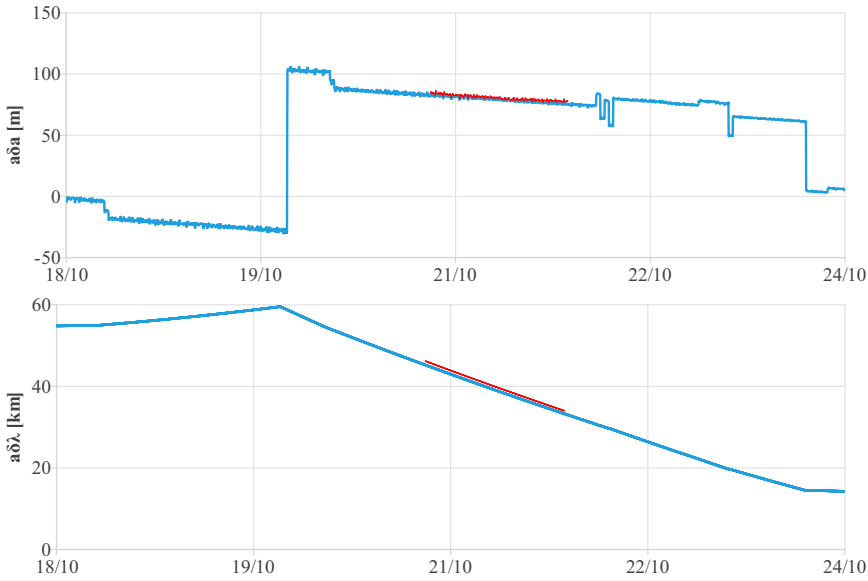

Figure 4.22: Angles-only (in blue) vs. radar-based (in red) solutions (AVANTI).

The lateral relative orbit determination performance is important from an operational point of view as this is needed to assess the risk of collision. The concept of passive safety adopted for both ARGON and AVANTI experiments requires a good knowledge of the Radial-Normal components of the relative motion, in order to accurately estimate the minimum intersatellite distance d_{m} perpendicular to the flight direction (cf. Section 3.2.4). It has to be emphasized that the risk of collision might become relevant at mid-to-close range, if systematic model and measurement errors degrade the lateral relative navigation accuracy while d_{m} is gradually decreased by the rendezvous guidance strategy. As a result, some safety margin (typically 10 m) should be applied when monitoring the minimum intersatellite distance d_{m}. As part of the post-analysis activities, Chapter 7 will perform a detailed covariance analysis, with the goal to understand the contribution of the different error sources (maneuver execution errors, improper drag modeling, measurement bias) and aiming at building a more realistic covariance, able to serve as reliable measure for the error of the solution.

4.4.4. CLOSE-RANGE CHARACTERISTICS

Angles-only navigation appears as method of choice to support far-to-mid range rendezvous. In this case, the target spacecraft is imaged as a point whose centroid accurately matches the actual center of mass, and the stars visible in the background ensure a precise knowledge of the orientation of the camera. All these aspects contribute to provide line-of-sight measurements accurate at the subpixel level and allow for accurate relative orbit determination throughout the entire rendezvous.
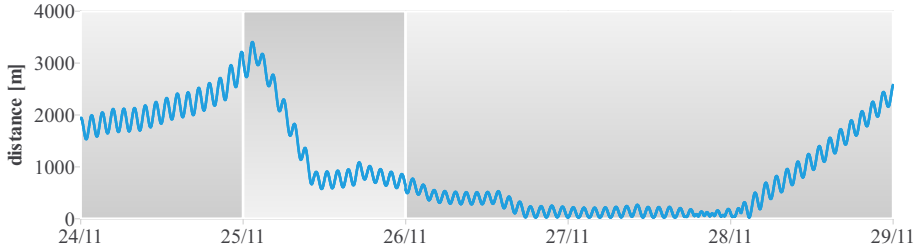
(a) Estimated instantaneous intersatellite separation. The data arcs are represented by different gray areas.
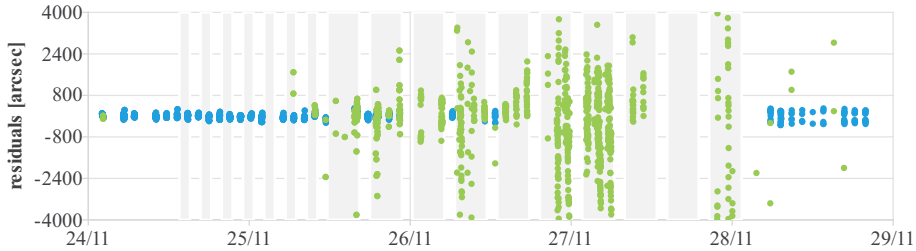
(b) Line of sight residuals with precise (blue) and coarse (green) knowledge of camera orientation. The vertical gray areas represent the time intervals during which the automatic shutter was activated.
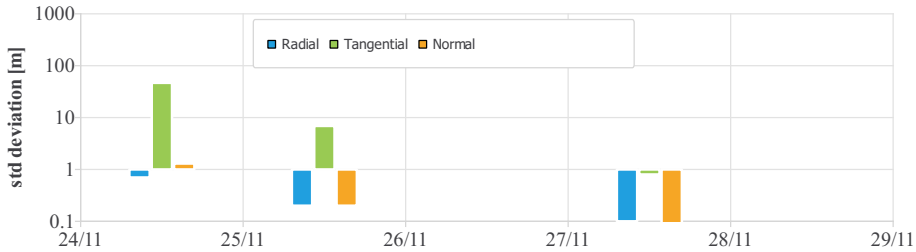
(c) Standard deviation of the position, derived from the covariance of the solution at initial epoch of each data arc.

Figure 4.23: Orbit determination results during the close approach (AVANTI).

In view of the satisfying performance obtained during the far-to-mid range approach, it was tempting to also investigate the behavior at closer distance. Can angles-only navigation also be used to bridge the mid-range gap, that is, to bring the target in the working range of close-proximity sensors?

The major difficulty during a close approach lies in treatment of the increasing brightness of the spacecraft, making the regulation of the exposure time mandatory. However, when reducing the exposure time, the stars in background will not be visible anymore and it becomes impossible to precisely derive the orientation of the camera. Another important limitation is due to the image of the target itself, which cannot be considered anymore as a point aligned with the center of mass (cf. Fig. 4.9). These two sources of error greatly contribute to a degraded accuracy of the line-of-sight measurements. However, since the problem very much depends on the distance, these uncertainties can still be acceptable for small separations. In fact, one degree measurement error corresponds to less than 1 m error at 50 m distance but translates into 174 m error at 10 km.

Two close approaches have been conducted during AVANTI, the first time (11-18 November, cf. Fig. 4.19) with a strong support from the ground as part of the commissioning phase, the second time fully autonomously. This section will only focus on the fully autonomous approach (24 to 27 November). Figure 4.23a depicts the estimated instantaneous intersatellite distance (not the mean along-track separation $a\delta\lambda$) during the approach. In Fig. 4.23b, the measurement residuals are represented with different colors, depending on the accuracy of the estimation of the camera orientation. The residuals in blue refer to angles-only observations which have been derived using the stars in the background to estimate the orientation of the camera. The residuals in green are instead computed when the onboard estimate of the attitude of the camera is used. For clarity, both right-ascension and declination measurements are indifferently represented with the same color, the color information being only used to distinguish if the knowledge of the camera orientation was precisely known or not.

When the electronic shutter is used, it becomes necessary to make use of the onboard at-
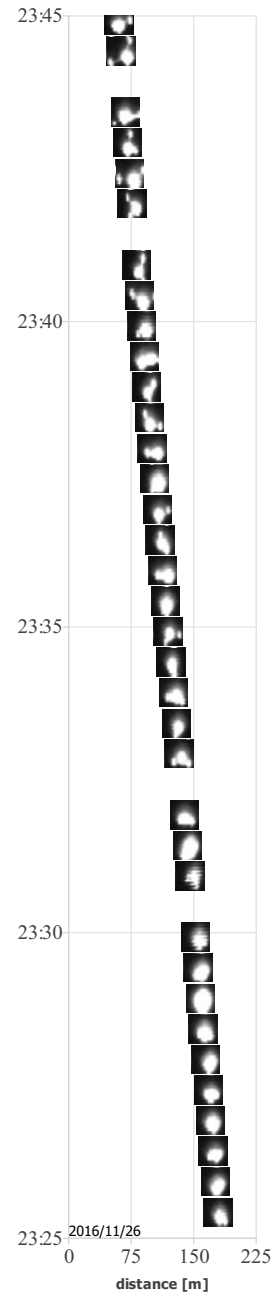

Figure 4.24: BEESAT-4 imaged a close range: coarse spacecraft features become observable at about 100 m (AVANTI).

titude to compute the inertial line-of-sight observations. In the case of AVANTI, since one of the star cameras was used to follow the target, it was unfortunately not possible to always keep a camera head pointed to deep space, so that the onboard attitude was sometimes affected by errors up to one degree. In view of this performance degradation, two different strategies have been investigated during the close approach. During some orbits, the sharpness of the target image has been sacrificed (by deactivating the electronic shutter) to obtain a more accurate line-of-sight observation thanks to a better attitude knowledge of the camera. Note that, for AVANTI, this strategy is also helped by the limited and symmetrical shape of the target: the centroid of the imaged object is close to the true projected position of the center of mass.. During the rest of the time, the electronic shutter was activated (depicted by gray areas in Fig. 4.23b), yielding accurate images but inaccurate angles-only observations. Fig. 4.24 shows the resulting target image at decreasing distance (the shutter was always activated during this sequence.). Starting from an unrecognizable blob, specific features can be detected (rectangular shape and presence of two antennas).

Some adaptation of the measurement noise in the least-squares process is needed when including the observations derived with the coarse onboard attitude. During the AVANTI experiment, two different values (80" and 3600") were used depending on the presence of stars in the background. Note that the poor performance of the onboard attitude encountered during AVANTI is specific to the minimalistic design of the experiment [62]. If additional star trackers are available to measure precisely the spacecraft attitude, the reconstructed orientation of the camera is more precise. Fig. 4.25 depicts, for instance, the line-of-sight residuals obtained with ARGON, already depicted in Fig. 4.16, but this time complemented with observations derived from the onboard attitude. The errors are clearly much smaller.

Anyway, with this settings a precise reconstruction of the relative trajectory becomes possible even with degraded observations. According to the covariance of the solution, relative positioning accuracy at sub-meter level is achieved at close range. In view of the discussions done before, the real accuracy should be however probably at meter level.
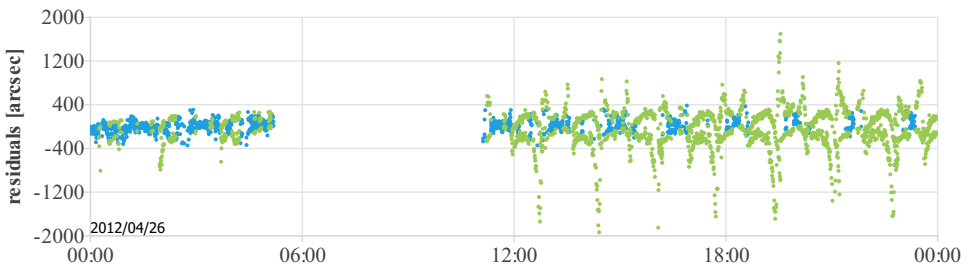

Figure 4.25: line-of-sight errors using the stars (blue) and onboard attitude (green) to estimate the orientation of the camera (ARGON).

4.5. Conclusion and Lessons Learned

During more than two months, angles-only relative orbit determination has been continuously performed to support the AVANTI experiment, covering intersatellite separations from 50 km down to 50 m. The resulting experience collected in orbit remarkably complements the legacy left by the precursor ARGON experiment, thus constituting a valuable collection of flight data and expertise. Despite the fact that both in-orbit demonstrations have been conducted in low Earth orbit and used the same camera to track the target object, substantial differences in terms of visibility and performance could be observed. These disparities are due to the choice of the orbit: while the ARGON experiment benefited from the optimal visibility conditions offered by a dawn-dusk configuration, AVANTI had to cope with eclipses and camera blinding, dramatically reducing the amount of observations. In addition, flying at lower altitude, AVANTI had to face much stronger orbital perturbations due to the differential drag. The design of the chaser also considerably impacts the flight results: ARGON could rely on the ideal experimental conditions offered by a dedicated formation-flying testbed, whereas AVANTI had to cope with numerous additional constraints such as single-direction maneuver capability or absence of dedicated tracking camera. The complementarity of both experiments is however of great interest: ARGON presents easier conditions for navigation and can also benefit from a precise reference based on differential GPS for performance validation. AVANTI instead explores the limits in terms of angles-only navigation and demonstrates that relative trajectory reconstruction can still be successfully performed under these difficult conditions.

Overall, angles-only navigation has been found to be a powerful method to be used as navigation method to approach a noncooperative target. AVANTI demonstrated that even a single-unit CubeSat can be visible at a distance up to 50 km. At far-range, angles-only relative orbit determination exhibits large along-track errors up to a few hundred meters but is able to accurately estimate the shape of the elliptical relative motion, thus supporting a smooth and safe rendezvous at this stage. The weak observability at very large separations (several tens of kilometers) might however prevent a convergence of the solution. In this case, constraining the least-squares solution around the relative orbit derived from TLEs is sufficient to mitigate this problem. At mid-range and in the presence of large variations of the relative motion, this latter difficulty disappears, so that the relative trajectory can be successfully determined during all the approaches exercised during the AVANTI experiment. The achievable accuracy is shown to continuously improve throughout the entire rendezvous, promising relative navigation performance at meter level at close-range according to the covariance of the solution.

Despite this achievement, numerous difficulties have been actually encountered during the data processing, indicating that the facility for relative orbit determination did not reach an acceptable operational maturity during the conduction of the experiment. Chapter 7 will revisit this particular weakness, showing that the use of the linear theory is of great help to mitigate this issue.

A second weakness, related to the prediction of the error of the solution, has also been identified. The results from the ARGON experiment clearly show that the relative orbital determination covariance is too optimistic, which could be operationally dangerous. Here again, Chapter 7 will investigate how this issue can be mitigated.

Finally, it also appeared desirable to avoid the assistance from TLEs, in order to simplify the interfaces. Chapter 6 will specifically address this topic, demonstrating that, at far-range, it is possible to derive a good initial estimate of the relative state of the formation only relying on angular measurements.

4

5

SPACEBORNE REAL-TIME RELATIVE NAVIGATION

This chapter describes the embedded real-time angles-only relative navigation system that enabled the autonomous rendezvous performed during the AVANTI experiment. Compared to a ground implementation, the algorithms and methods are tailored to cope with the real-time requirements and limited onboard resources. After a brief overview of the necessary adaptations and of the resulting system design, the key flight results are presented.

5.1. OVERVIEW

Dealing with a collection of already existing images, Chapter 4 might lead to the impression that the in-orbit acquisition of pictures is a simple process within the angles-only relative navigation task. This is partly the case at far- to mid-range, where it is sufficient to point the camera in along-track direction to entirely observe the relative motion, provided that the coarse orbit phasing prior to the rendezvous has been correctly done. Since the field of view of the camera is limited, this is unfortunately not true anymore during a passively safe rendezvous at short-range distances, for which a minimum intersatellite distance perpendicular to the flight direction is ensured at any time. In this case, the camera has to actively follow in real-time the direction to the target based on the onboard estimate of the relative state. Note that a pure V-bar approach would make the camera pointing easier but is unsafe and thus not advised. Obviously the realization of this task requires a high level of onboard autonomy.

The vision-based relative navigation system presented in this chapter is designed to be used by a chaser spacecraft to autonomously track and rendezvous with a known noncooperative target object from a distance of several tens of kilometers down to a few hundred meters. It is assumed that the orbit of the target is coarsely known (for example using ground-based radar tracking) and that the chaser is flying on a similar orbit. The onboard relative navigation task consists in continuously providing an estimate of the relative motion of the formation in real-time to the other onboard applications (guidance, control, attitude pointing). The system is assumed to only rely on a far-range camera to observe the target. Thus the estimation of the relative state is derived from line-of-sight measurements which first have to be extracted from the images taken by the camera. In view of the desired working range, all the objects imaged by the camera are considered as point sources.

As a matter of fact, the relative navigation task is very similar to what is needed for the angles-only relative orbit determination presented in the previous chapter, except that the algorithms have to be suited for real-time implementation with limited onboard resources. Figure 5.1 depicts the task flow of the onboard vision-based navigation system. The first four blocks are part of a minimalistic image processing, aiming at providing the line-of-sight measurements to the unrecognized objects of one image. This task, already described in Chapter 4, is computationally-light and thus very well adapted for a real-time implementation. The main steps are recalled here for completeness: a raw image is first processed to extract a collection of luminous spots after a threshold-filtering of the background noise (image segmentation). Once this is done, the centers of the spots are estimated by computing the arithmetic mean of the pixels (centroiding). At this stage, the raw image has been simplified to a list of so-called centroids, the majority of them corresponding to stellar objects. The next step consists in identifying these stellar objects (star identification) in order to derive the precise orientation of the camera. In principle, this could be done without any external help using a lost-in-space algorithm to recognize the stars. Such algorithms are typically implemented in star trackers. For simplicity, it has been decided to rely instead on the onboard knowledge of the spacecraft attitude (accurate to a few arcminutes) to first identify the stellar objects. In a second step, the knowledge of the orientation of the camera is refined (reaching an accuracy of a few arcseconds) using the q-method [106] (attitude estimation).
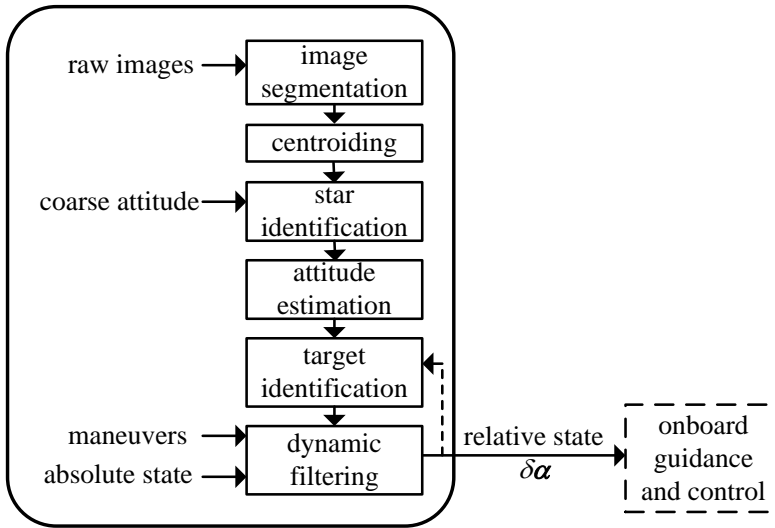
Figure 5.1: Functional view of the onboard vision-based relative navigation system.

The next step consists in detecting the noncooperative object. The kinematic target identification algorithm presented in Chapter 4 is also well adapted for an onboard implementation thanks to its sequential nature. In fact, the trajectory recognition is done based on a small portion of the relative elliptical motion, so that only a few processed images (typically 20, *cf.* Section 4.2.1) have to be stored onboard. Here, the major difference compared to the onground target detection is that advanced data screening techniques based on the complete history of measurements are no more possible. In order to mitigate this problem, the onboard relative state estimate is also used for the detection of the target after the convergence of the estimation process. This feature is represented by a dashed arrow in Fig. 5.1 and is named dynamic target detection.

Once the target has been recognized, the navigation filter processes these observations and, thanks to the knowledge (provided externally) of the absolute state and maneuvers executed by the chaser spacecraft (*i.e*, BIROS), estimates the relative state. Two major differences with respect to the on-ground relative orbit determination appear at this stage. First, a calibration of the maneuvers is no more possible, because it requires the subsequent accumulation and processing of GPS data over a long time, typically one orbit, in order to precisely estimate their effect on the relative motion. As a result, the *a priori* knowledge of the maneuvers is instead used, introducing additional errors in the relative state estimation. Second, a nonlinear batch least-squares approach relying on several iterations, taking the history of measurements into account and based on the numerical integration of the relative dynamics is also no more possible because of the required computational efforts. Thus, the approach that has been retained consists in implementing a sequential extended Kalman filter as described in Section 3.4.2 based on the computational-light analytical model for the relative motion introduced in Section 3.2.4.

5.2. ROBUST TARGET IDENTIFICATION

5.2.1. KINEMATIC TARGET DETECTION

As already mentioned, one of the main challenges faced by an autonomous vision-based navigation system is the ability to provide reliable line-of-sight measurements to the navigation filter. To do this, the measurements have to be extracted from the pictures, requiring the capability to identify the target object among all the luminous spots present in the image. As depicted in Fig. 5.2, it is from far-range not possible to distinguish at one glance the target satellite from the other objects imaged by the camera.
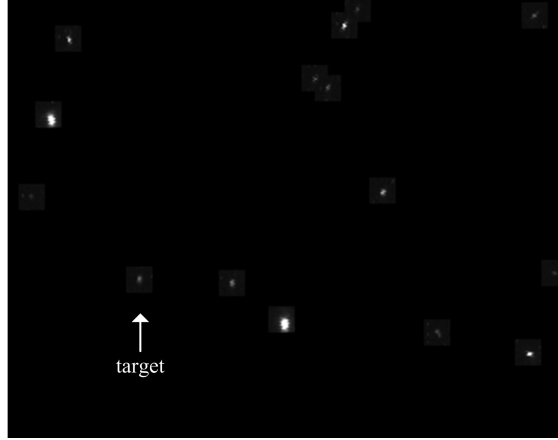

Figure 5.2: On the difficulty to recognize a target satellite at 30 km distance (image from the ARGON experiment).

Most of the celestial objects can be identified using a star catalog during the previous star identification process. Still, it cannot be excluded that several non-identified luminous spots remain, as already explained in Section 4.2.1. In order to select the target satellite among several candidates which are not recognized as stellar objects, additional knowledge about the target satellite is required. To that end, it is tempting to use the current onboard relative state estimate. However, this approach is considered not robust because the uncertainty on the relative state estimate is large before the filter has converged. Similarly, the apparent magnitude of the object provides valuable additional information at small separations but cannot be exploited at far-range, because it strongly depends on the unknown attitude of the target satellite, on its surface properties, and on the illumination conditions (*cf.* Fig. 4.7).

In view of the poor reliability of these two strategies, it has been decided to implement the pure kinematic approach presented in Section 4.2.1 as core algorithm to identify the possible targets, and to make use of additional information to aid the target detection only in case of difficulties. As described in Section 4.2.1, in spite of its simplicity, some (very) coarse *a priori* knowledge on the target relative orbit is needed to tune the parameter ϵ of the underlying DBSCAN algorithm. The angular distance traveled by the target between two consecutive pictures depends on the size of the relative elliptic motion and on the distance to the target. If the parameter ϵ is set too small, it

would result in the target trajectory being discarded as noise in the DBSCAN algorithm, while setting it too big would include unnecessary unrecognized objects to the target trajectory. For the on-ground relative orbit determination, it was chosen to use a default value which could be manually changed, if necessary. In order to improve the autonomy level of the onboard system, it has instead been decided to estimate this value based on the coarse reference solution provided to the system. In fact this information is anyway needed to initialize the dynamical filter after the target identification. As rule of thumb, it is enough to consider that the target travels the size of the relative elliptic motion in half-an-orbit, so that the expected angular displacement can be roughly estimated as follows. Considering the chaser mean motion n, the distance to the target spacecraft L, the cross-sectional size h of the relative elliptic motion (cf. Fig. 5.3) and the time interval T between two pictures, a very coarse approximation of the angular distance β traveled by the target between two pictures is

$$\beta = \tan\left(\frac{h}{L}\right) \cdot \frac{n}{\pi} T \tag{5.1}$$

which can be translated into a distance ϵ in pixels using the camera field of view F and resolution R:

$$\epsilon = \beta \cdot \frac{R}{F}. \tag{5.2}$$

Since all quantities are rough approximations, one may use a multiple of ϵ (for example 2ϵ or 3ϵ) to be on the safe side.
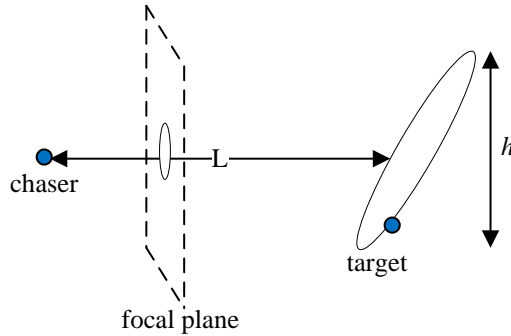

Figure 5.3: Relative elliptic motion and its projection.

The search area S described in Section 4.2.2 is another important parameter which needs to be adapted every time that the error affecting the *a priori* solution changes. In order to improve the level of autonomy, this parameter is also derived based on the co-variance of the relative state estimate. In principle, the search area corresponds to the projection of the covariance envelop on the focal plane. Its exact mathematical formu-lation would be tedious to derive but, because this search area only serves as boundaries to apply the target detection algorithm, a very coarse approximation is sufficient. Since the longitudinal accuracy of the relative state does not greatly impact the shape of the

imaged relative motion, a simple value for S can be computed using the standard deviation σ_i of all orbital elements except $\delta\lambda$:

$$S = \frac{a}{d}\sqrt{\sigma_{\delta a}^2 + \sigma_{\delta e_x}^2 + \sigma_{\delta e_y}^2 + \sigma_{\delta i_x}^2 + \sigma_{\delta i_y}^2} \cdot \frac{R}{F}. \tag{5.3}$$

This value is derived by approximating the lateral motion as a linear combination of all relative orbit elements except $\delta\lambda$ and by assuming that they are uncorrelated. Obviously, this approximation is rough. However, it is sufficient to provide an order of magnitude for S. Here again, a multiple of this value can be used to cope with the approximations (for example $3S$). Note that S serves at the same time as parameter for the target detection but also as data editing threshold for the subsequent dynamical filtering: only those measurements which satisfy the relative dynamics are included in the filter measurement update. Thus, if a more restrictive measurement editing is needed, the *a priori* covariance matrix provided to the filter has to be reduced.

Apart from these two adaptive parameters, the kinematic target detection algorithm and settings are identical to what has been presented in Chapter 4.

5.2.2. Final Integrity Check and Aided Target Selection

The strategy described above works well to find the candidate trajectories and to reject clusters made of the conjunction of random unrecognized objects, but might however fail, typically in less than 1% of the cases, if the cluster elements are too close to each other to allow for an obvious discrimination based only on the curve fitting residuals. This situation can, for example, occur in the case of hot spots, which are always located at same position with small variations due to the centroiding errors. Hot spots are pixels with abnormally high dark current. They represent a threat for the robustness of the target identification algorithm because they can hardly be distinguished from the target object at far-range. It has to be emphasized that hot spots should be catalogized as part of the calibration phase. However, the target identification algorithm needs to be robust to undetected hot spots during the calibration phase or to new hot spots appearing on-orbit.

Such outliers are more easily detected when considering the whole history of observations and relying on several iterations. Alas, this is not possible for an onboard real-time implementation. Consequently countermeasures, depicted in Fig. 5.4, have been introduced in the onboard software to help mitigate this issue and thus improve the robustness of the target detection. The most evident criteria to select the target trajectory in case of doubt is to use the object luminosity, since a hot spot affects only one pixel and the target image is spread over many pixels (at least 2 or 3 pixels at far-range). This is due to the fact that the optics of the camera is slightly defocused for better centroiding performance so that even an object of low visual magnitude is composed of several pixels. Thus, the centroiding function is designed to deliver (in addition to the estimated center) the luminosity I of the centroid, as defined by Eq. 4.2 (note that, in Fig. 5.4, $I(\mathcal{T})$ denotes the intensity of the most recent object $\mathcal{O}$ of a candidate trajectory $\mathcal{T}$). The camera retained for AVANTI encodes the pixels using a single Byte, so that its value is comprised between 0 and 255. Accordingly, it can be assumed that the intensity of a hot spot will be much smaller than $I_{\min} = 1000$ (in fact 255 should be enough, but some neighboring pixels might sometimes contribute to increase the measured brightness of the hotspot).
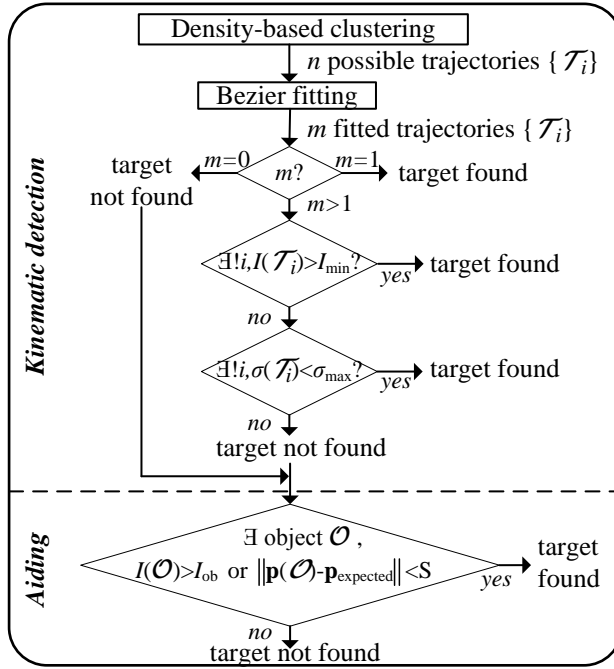
Figure 5.4: Functional view of the onboard target detection algorithm.

However, at far-range, it might be that the target satellite also occupies very few pixels, so that its luminosity is very close to that of a hot spot. In this case, it is helpful to remember that the distribution of the elements comprising a candidate trajectory obeys the space dynamics while the elements of the hot spots are randomly distributed, so that a small but observable difference in terms of fitting residuals will still be observable. At far-range, the advantage is that the centroiding errors are particularly small (approximately 0.2-0.3 pixel) since the object can be considered as a point source at this distance. Consequently, the fitting residuals of the target trajectory will also be particularly small, while the fitting residuals of a cluster of hot spots will be slightly larger due to the random distribution of the hot spots over time. Thus, if $\sigma_{\mathrm{B}}(\mathcal{T}_i)$ denotes the standard deviation of the Bezier fitting residuals of a candidate trajectory $\mathcal{T}_i$, a last discrimination can be done by retaining only the trajectories whose fitting residuals are below a given fine threshold $\sigma_{\mathrm{B,fine}}$ chosen to be very small (for example $\sigma_{\mathrm{B,fine}}=0.3$ pixel).

Figure 5.5 shows as examples two Bezier curve fittings, corresponding to the target trajectory and a randomly distributed collection of centroids corresponding to a single hot spot over a sequence of images. The axis coordinates of Fig. 5.5 correspond to the position in pixels in the focal plane and the number k close to the points indicates their index in the sequence of N images ($k = 0$ corresponds to the oldest image and $k = N - 1$ to the most recent one). Since the parameter τ of the Bezier curve is chosen to follow the picture index (*i.e.*, $\tau_k = k/(N-1)$), a series of points which are not properly ordered will be more difficult to fit (*cf.* Fig. 5.5b) . It has to be noted that this strategy excludes

(a) Target trajectory ($\sigma_{\rm B}$=0.21 pixel)
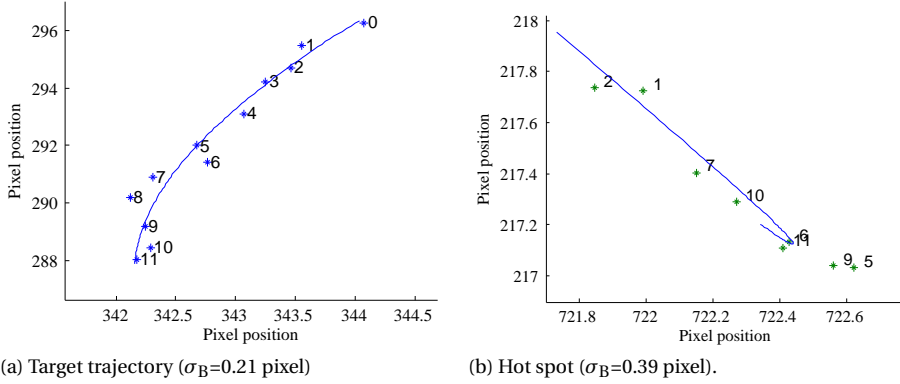
(b) Hot spot ($\sigma_{\rm B}$=0.39 pixel).

Figure 5.5: Examples of Bezier fitting (from the PRISMA mission during the ARGON experiment).

the possibility for the camera to actively follow the target spacecraft at far-range, oth-
erwise both the target and hot spot describe a similar apparent motion and cannot be
distinguished from their luminosity. This problem disappears at mid- and close-range
because the target becomes more luminous. Note that this strategy is no longer valid at
mid-range because the distribution of the pixels composing the target image cannot be
considered as a point spread function anymore, resulting in higher centroiding errors.
Figure 5.14 later provides an example of the target image at different separations. In this
case, the increasing centroid errors impact the curve fitting residuals, but this is not a
problem since the target luminosity can then be used to discriminate the candidates.

The kinematic target detection is best suited for initiating the approach at far-range
when coarse knowledge about the relative orbit is available. Once the filter has con-
verged, the dynamical solution can advantageously be used to support this task. In this
case, a predicted target position in the image can be derived from the filter relative state.
If a non-identified centroid is sufficiently close to the modeled position (within a toler-
ance derived from the covariance matrix), the centroid is identified as target. Similarly, at
close-range, the considerable brightness of the target allows for an unambiguous detec-
tion. Both criteria are summarized in Fig. 5.4: if the kinematic detection fails, the target
detection can be aided by scanning all the objects $\mathcal{O}$ in the image and checking if the lu-
minosity of a non-recognized object is greater than an obvious luminosity threshold $I_{\rm ob}$
or if its expected position $\boldsymbol{p}$ in the picture is close enough (less than a user-defined search
radius S) to the image position $\boldsymbol{p}_{\rm expected}$ predicted by the filter navigation solution. $I_{\rm ob}$
is empirically set to 10000, which corresponds to a square of 6x6 saturated pixels. This
value is also in line with what has been measured during the ARGON experiment (*c.f.*
Fig. 4.8b). This value has been derived considering the hardware specifications of the
camera employed for AVANTI. At far-range, when the exposure time of the camera is set
to 0.25 s, this value corresponds to the brightness of a star of magnitude 1. At mid- to
close-range, the electronic shutter of the camera adjusts the exposure time to keep the
image of an object into a Region of Interest (*i.e.*, a 16x16 pixel large area as explained
in Section 2.1.2). In this case, $I_{\rm ob}$ corresponds to a bright object occupying 15% of the
region (see Fig. 5.14 for some examples of Regions of Interest at close-range).

Note that, in spite of all the efforts to improve the robustness, the target detection might fail in some cases: if only a hot spot is visible (the target being for example eclipsed), if a set of hot spots exhibit particularly small fitting residuals or is very bright, if a non-recognized object is inside the search area delimited by the variable S, etc. In fact, it has to be kept in mind that a never-failing target detection is out of reach. The above-depicted strategy only intends to reduce the probability of misdetection. Operationally, the only countermeasure to limit at maximum the apparition of outliers is to reduce at maximum the search area S, but this requires a very good initialization of the filter, which is in turn incompatible with the accuracy of the TLEs.

5.3. DYNAMICAL FILTERING

5.3.1. FILTER DESIGN

Once the line-of-sight measurements are extracted from the images, the relative state of the formation can be estimated using a dynamical filter. As already stated, in view of the real-time requirements, an extended Kalman filter has been chosen as an estimator. The onboard filter is based on the parameterization of the relative motion described in Section 3.2.4 and relies on the related analytical model which includes the effect of J_2 and differential drag. For historical reasons, the adopted set of relative orbital elements $\delta\boldsymbol{\alpha}$ slightly differs from the convention adopted in Section 3.2.4 (which is more recent and thus better reflects the current state of the art at DLR) in the sense that the relative mean longitude $\delta\lambda$ is equivalently replaced by the relative argument of latitude $\delta u = \delta\lambda - \delta i_y/\tan(i)$ and occupies the 6th component of $\delta\boldsymbol{\alpha}$ instead of the 2nd. For consistency and historical fidelity, it has been chosen to describe the exact implementation of the algorithms used to conduct the experiment instead of adapting them with the newest convention. In order to avoid confusion, this old convention and the associated equations are described with the hat symbol:

$$\delta\hat{\boldsymbol{\alpha}} = \begin{pmatrix} \delta a & \delta e_x & \delta e_y & \delta i_x & \delta i_y & \delta u \end{pmatrix}^T. \tag{5.4}$$

As already stated, for embedded onboard systems, the major advantage of this parameterization lies in the associated analytical dynamical model, which provides an accurate and computationally-light prediction of the relative motion thanks to the inclusion of the perturbation due J_2. As explained in Section 3.2.4, the formation used for the AVANTI experiment undergoes a much stronger differential drag due to its low altitude and to the very different ballistic coefficients of BIROS and BEESAT-4 (see Table 2.2), so that the relative motion model needed to be revisited during the design of the AVANTI experiment to refine the modeling of the disturbance due to J_2 and to include the mean effects of the differential drag by the means of three additional parameters $(\delta\dot{a}, \delta\dot{e}_x, \delta\dot{e}_y)$.

The autonomy of the system would however suffer from the external manual input of these additional parameters. They have thus to be estimated onboard. However the weak observability of the state makes it less robust to estimate too many additional parameters. As a result, it has been decided to estimate only $\delta\dot{a}$, thus neglecting the impact of the differential drag on $\delta\boldsymbol{e}$ (which is smaller than the effect on δa).

Thus the state vector describing the formation which has to be estimated onboard

5

can be written as:

$$\boldsymbol{x} = \begin{pmatrix} \delta\hat{\boldsymbol{\alpha}}^T & \delta\dot{a} \end{pmatrix}^T, \tag{5.5}$$

and according to Section 3.2.4, the associated state transition matrix $\hat{\boldsymbol{\Phi}}$ becomes (after some minor adaptations due to the different convention chosen for $\delta\hat{\boldsymbol{\alpha}}$):

$\hat{\boldsymbol{\Phi}}(t, t_0) =$

$$\begin{pmatrix}
1 & 0 & 0 & 0 & 0 & 0 & \Delta t \\
0 & 1 & -n\varphi'\Delta t & 0 & 0 & 0 & 0 \\
0 & n\varphi'\Delta t & 1 & 0 & 0 & 0 & 0 \\
0 & 0 & 0 & 1 & 0 & 0 & 0 \\
\frac{21}{4}\gamma\sin(2i)n\Delta t & 0 & 0 & 3\gamma(\sin^2 i)n\Delta t & 1 & 0 & \frac{21}{8}\gamma\sin(2i)n\Delta t^2 \\
-\frac{3}{2}n\Delta t & 0 & 0 & -\frac{3}{2}\gamma\sin(2i)(5+3\eta)n\Delta t & 0 & 1 & -(3/4)n\Delta t^2 \\
-\frac{21}{4}\gamma(K+H\eta)n\Delta t & 0 & 0 & 0 & 0 & 0 & -\frac{21}{8}\gamma H(\eta+1)n\Delta t^2 \\
0 & 0 & 0 & 0 & 0 & 0 & 1
\end{pmatrix} \tag{5.6}$$

where $\Delta t = t - t_0$. The variables γ, K, H, φ', and η are described in Eq. 3.18. Note that the effect of J_2 is visible in the matrix terms comprising the variables γ and φ'. The linear mapping providing the Cartesian relative position $\Delta\boldsymbol{r}^{\mathcal{O}}$ in the orbital frame $\mathcal{O}$ (Eq. 3.23) is also slightly affected by the change of variable to become:

$$\Delta\boldsymbol{r}^{\mathcal{O}} = a \begin{pmatrix} 1 & -\cos u & -\sin u & 0 & 0 & 0 \\ 0 & 2\sin u & -2\cos u & 0 & \cot i & 1 \\ 0 & 0 & 0 & \sin u & -\cos u & 0 \end{pmatrix} \delta\hat{\boldsymbol{\alpha}} = \hat{\boldsymbol{C}}\delta\hat{\boldsymbol{\alpha}}. \tag{5.7}$$

The time update at each new epoch t is done using the state transition matrix of Eq. 5.6. The maneuvers executed by the chaser are crucial to improve the observability. In the filter design, they are considered impulsive and are included as part of the time update process according to Eq. 3.22. Here again, the equation relating the change $\Delta\delta\hat{\boldsymbol{\alpha}}$ of relative orbital elements due to a maneuver $\Delta\boldsymbol{V}$ executed at argument of latitude u_M has to be slightly modified to cope with the different convention adopted for $\delta\hat{\boldsymbol{\alpha}}$:

$$\Delta\delta\hat{\boldsymbol{\alpha}} = -\frac{1}{na} \begin{pmatrix} 0 & 2 & 0 \\ \sin u_M & 2\cos u_M & 0 \\ -\cos u_M & 2\sin u_M & 0 \\ 0 & 0 & \cos u_M \\ 0 & 0 & \sin u_M \\ -2 & 0 & -\sin u_M \cot i \end{pmatrix} \Delta\boldsymbol{V}. \tag{5.8}$$

The filter measurement update is done using the line-of-sight measurement $\boldsymbol{u}^{\mathcal{C}}$ to the target object expressed in the camera frame. Since the target detection provides a pixel position $\boldsymbol{p}$ corresponding to the center of mass of the target, it is first necessary to convert it into a line-of-sight measurement using a camera model (see Eq. 4.3). The line-of-sight can be written using the relative position in the camera frame $\Delta\boldsymbol{r}^{\mathcal{C}}$:

$$\boldsymbol{u}_{\mathcal{C}} = \frac{\Delta\boldsymbol{r}^{\mathcal{C}}}{\|\Delta\boldsymbol{r}^{\mathcal{C}}\|} = \frac{\boldsymbol{R}_{\mathcal{O}}^{\mathcal{C}}\Delta\boldsymbol{r}^{\mathcal{O}}}{\|\Delta\boldsymbol{r}^{\mathcal{O}}\|}. \tag{5.9}$$

Here $\boldsymbol{R}_{\mathcal{C}}^{\mathcal{O}}$ denotes the orthonormal rotation matrix from the frame camera frame $\mathcal{C}$ to the orbital frame $\mathcal{O}$ and is delivered by the image processing task (as part of the precise

star-based estimation of the orientation of the camera, cf. Fig. 5.1). As explained in Section 3.2.4, the nonlinear transformation described by Fig. 3.5 is needed to compute $\Delta r^{\mathcal{O}}$ from $\delta\hat{\alpha}$ with sufficient accuracy. During the design of the onboard software, it has been chosen to parameterize the line-of-sight vector $u^{\mathcal{C}}$ with a set of two angles $\hat{\alpha}$ and $\hat{\delta}$, respectively corresponding to the azimuth and elevation in the camera frame (the hat symbol is used here to better distinguish from the previously defined right-ascension and declination):

$$u^{\mathcal{C}} = \begin{pmatrix} \cos(\hat{\delta})\sin(\hat{\alpha}) \\ \sin(\hat{\delta}) \\ \cos(\hat{\delta})\cos(\hat{\alpha}) \end{pmatrix}. \tag{5.10}$$

These two angles are used to build the measurement vector $h = \begin{pmatrix} \hat{\alpha} & \hat{\delta} \end{pmatrix}^T$ used for the measurement update. The related Jacobian matrix H is computed considering the different frames used to derive the equations:

$$H = \frac{\partial h}{\partial x} = \frac{\partial h}{\partial \Delta r^{\mathcal{C}}} \cdot \frac{\partial \Delta r^{\mathcal{C}}}{\partial \Delta r^{\mathcal{O}}} \cdot \frac{\partial \Delta r^{\mathcal{O}}}{\partial x} = \frac{\partial h}{\partial \Delta r^{\mathcal{C}}} \cdot R_{\mathcal{O}}^{\mathcal{C}} \cdot \frac{\partial \Delta r^{\mathcal{O}}}{\partial x}. \tag{5.11}$$

Note that the partial derivatives have to be evaluated at the value of the state predicted by the filter time update (*cf.*, Eq. 3.44). In the formulation of the Jacobian, $\partial \Delta r^{\mathcal{O}}/\partial x$ is computed according to the simplified linear mapping provided by Eq. 5.7, and noting that the relative position does not depend on $\delta\dot{a}$:

$$\frac{\partial \Delta r^{\mathcal{O}}}{\partial x} = \begin{pmatrix} \hat{C} \mid 0_{3x1} \end{pmatrix}, \tag{5.12}$$

where $\hat{C}$ is the matrix defined in Eq. 5.7. The partial derivatives of the measurements with respect to the relative position in the camera frame are finally given by:

$$\frac{\partial \hat{\alpha}}{\partial \Delta r^{\mathcal{C}}} = \frac{1}{\Delta r \cos^2(\hat{\delta})} \cdot \begin{pmatrix} \cos\hat{\alpha}\cos\hat{\delta} & 0 & -\cos\hat{\delta}\sin\hat{\alpha} \end{pmatrix}, \tag{5.13a}$$

$$\frac{\partial \hat{\delta}}{\partial \Delta r^{\mathcal{C}}} = \frac{1}{\Delta r} \cdot \begin{pmatrix} -\sin\hat{\delta}\sin\hat{\alpha} & \cos\hat{\delta} & -\sin\hat{\delta}\cos\hat{\alpha} \end{pmatrix}. \tag{5.13b}$$

5.3.2. TUNING DIFFICULTIES

Compared to other estimation techniques (for instance least-squares adjustment), the Kalman filter offers the advantage of using process noise to cope with the errors of the dynamical model. This is of great importance since, in addition to the errors due to the differential drag, the filter has to cope with maneuver execution errors. On the other hand, the improvement of observability is obtained by considering the effect of maneuvers over time, requiring thus some filter memory, which fades quickly when introducing too much process noise. A tradeoff needs to be found between these contradictory settings.

The poor observability and the unknown perturbations of the relative dynamics make the proper tuning of the filter not trivial. In principle, dedicated process noise should be introduced when executing the maneuvers, corresponding to the execution errors.

However, numerical simulations have shown that this strategy weakens the observability, preventing the filter convergence. It has been found more robust to consider a global constant value for the process noise, reflecting the average uncertainties of the relative dynamics. In order to evaluate this value, an order of magnitude for the contribution of the unknown differential drag is derived considering an atmospheric density of 5 g/km^3 (computed using the Harris-Priester density model) at about 500 km altitude, yielding a relative acceleration of about 200 nm/s^2 for a differential ballistic coefficient of 0.015 m^2/kg. Since the sampling time of the filter is chosen according to the frequency of measurements, i.e. 0.033 Hz or 1 image every 30 s, this perturbation corresponds to a tangential velocity increment of 6 μm/s over 30 seconds. The overall contribution of the maneuver execution errors can be coarsely assessed by allocating a total error of 10 mm/s spread over one day (considering an average of 5 maneuvers affected by 2 mm/s errors), contributing to an average of 3 μm/s over 30 s.

According to Eq. 5.8, this total unknown ΔV of 9 μm/s translates into 1-2 cm error depending on the direction and location of the velocity increment. It has also to be noted that the influence of the drag on the relative eccentricity vector δe has been neglected in the relative motion model while the mean effect of this perturbation on δa is estimated by the filter, thus reducing the errors of the dynamics for this particular component. Consequently, it has been decided during the tuning of the filter to reduce the uncertainty affecting δa. These considerations are reflected in the process noise setting depicted in Table 5.1. The other filter settings described in the table comprise the *a priori* covariance matrix, derived from typical TLEs accuracy, and the measurement noise, which assumes centroiding performance at subpixel level.

Table 5.1: Adopted filter settings for the AVANTI experiment.

Item	Value
A priori covariance	diag(10^2,100^2,100^2,100^2,100^2,500^2,10^{-8}) [m^2,m^2/s^2]
Process noise	(10^{-4},0.03,0.03,0.03,0.03,0.1,10^{-7}) [m,m/s]
Measurement noise	80 arcsec

5.4. Flight Results

5.4.1. System Commissioning

As already stated, the target identification task is expected to sometimes fail. This is typically not an issue (at least in case of sporadic occurrence) if a target visible in the image is simply not detected (for example because it is slightly outside the search area S or because the curve fitting residuals σ_B is too high). In this case, the filter propagates the relative state until a new measurement is provided. It becomes problematic, however, if a false positive is provided, that is, if the target identification algorithms provides a line-of-sight measurement to a wrong target. This problem was encountered early in the commissioning phase, as another target flying on a similar orbit was visible. Reducing the size of the search area (for example 0.8S instead of S) is a possibility to mitigate this issue but this is definitely not an easy task. The dilemma is the following: a too restricting measurement editing threshold can lead to reject all valid measurements, preventing the state estimate from being updated. On the contrary, if a bad measurement deviating too

much from the truth is introduced, this can heavily degrade the navigation solution or even lead to a filter divergence.

The original objective of the AVANTI experiment was to initialize the onboard filter with a reference solution derived from TLEs. This strategy has been deeply investigated during the two months of commissioning phase. It turned out that this goal was too ambitious. In fact, during the filter convergence, the covariance is very large in order to cope with the errors of the TLEs, resulting in a wide search area S, which in turn increases the probably of filter divergence in case of bad observations. Note that these are qualitative considerations. It is in fact extremely difficult to precisely define the error level above which an outlier will lead to a filter divergence. Nevertheless, one important lesson learned is that only a statistical approach based on a set of measurements (as done in Chapter 4) is able to reliably detect all the outliers.The proper tuning of the filter, done by means of simulation and later by replaying the flight data collected during the commissioning phase, was also shown to be difficult. The weak observability, the model deficiencies and the introduction of process noise make the filter prone to divergence.

Consequently, it has been decided to provide a better estimate of the *a priori* solution, based on the results from the onground angles-only relative orbit determination, to initialize the onboard relative navigation filter. In order to investigate the filter convergence, artificial errors have been afterwards introduced on top of the *a priori* solution, but without reaching the typical level of errors exhibited by TLEs. Thus the covariance described in Table 5.1 is not representative of the accuracy of TLEs, which can amount to several hundred meters in case of a CubeSat [102]. Using this workaround, it was possible to successfully conduct the fully autonomous rendezvous twice. Note that this additional aid does not reduce the value of onboard autonomy, since this preliminary activity could be done for example as part of the coarse orbit phasing.

5.4.2. Far- to Mid-Range Regime

The first autonomous approach represents the core of the AVANTI demonstration. As described in Section 2.1.4, this experiment was conducted between 19 and 23 November 2016, starting from a distance of 13 km down to 1 km. As already mentioned, the main difficulty at far-range lies in properly recognizing the target. The TLEs are of little help, since their large cross-track error (up to a few hundred meters) does not significantly reduce the target search area in the image, so that many candidate target objects can be simultaneously visible. The kinematic analysis of the trajectory is thus the preferred method for the target detection when initiating the approach. However, this is not a trivial activity considering the few available pictures. Figure 5.6 depicts the difficulty of this task by focusing on the first hours after the start of the autonomous rendezvous. In Fig. 5.6, the total number of centroids visible in the images are drawn in blue, while the centroids which have not been identified as stars are shown in red. Here again, the limited number of measurements is clearly visible: the gray areas represent the eclipse phases, during which the target is not visible, and the remaining areas without centroids correspond to the phases where the camera was blinded by the Sun.

As a result, only approximately 10 minutes of pictures are remaining every orbit, from which the target has to be identified. Figure 5.6 shows that the number of unrecognized objects is slightly greater than one with some unexpected peaks where the satellite on-
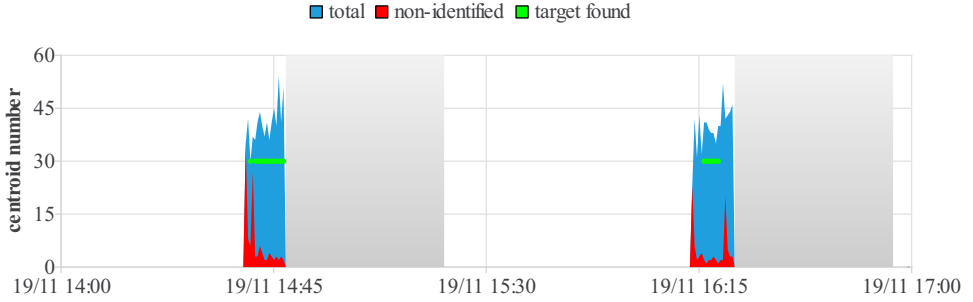
Figure 5.6: Centroids detected and identified at 13 km distance.

board attitude estimation is too degraded to allow for the proper detection of the stars. Nevertheless, despite these anomalies, the strategy adopted for target detection was robust enough to successfully detect the picosatellite (green dots in Fig. 5.6). Note that the detection is not immediate since the algorithm first needs to collect a sequence of images to be able to detect a candidate trajectory.

Once a few line-of-sight observations are successfully extracted from the images, the filter refines its coarse *a priori* knowledge of the relative state until it gains enough confidence about the validity of its solution. The filter is considered to have converged if the standard deviation of the solution decreases to below a user-defined threshold. From this moment, the filter state can be used to support the target detection, thus providing more measurements. This behavior is illustrated in Fig. 5.7, where the filter residuals are depicted during the complete approach. The residuals are evaluated by computing the angular deviation between modeled and measured line-of-sight unit vectors as in Eq. 3.32. The measurements obtained using the kinematic target detection are depicted in blue, and the new measurements gained with a dynamic detection are represented in green. These dynamically detected measurements appear once the standard devi-
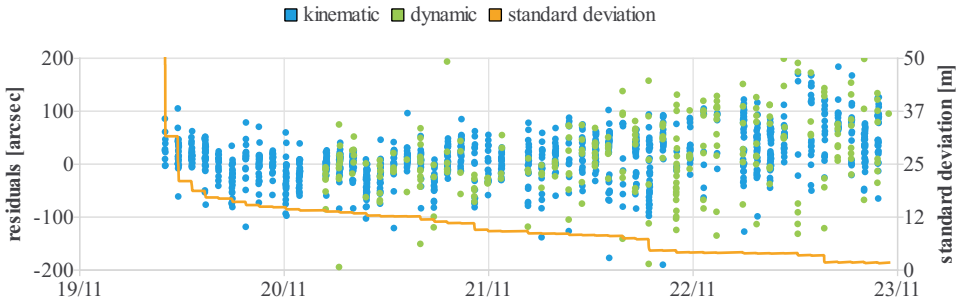

Figure 5.7: Filter residuals during the far- to mid-range autonomous approach. The main source of measurements comes from the kinematic target detection (in blue), complemented by additional measurements obtained using the filter solution (in green). This filter-based detection is enabled when the standard deviation of the solution (represented in orange) decreases below 13 m.

ation (in orange) decreases under 13 m. The standard deviation has been computed excluding $a\delta u$ to provide a measure of the lateral accuracy. A clear degradation of the residuals based on the distance can be observed while decreasing the intersatellite separation (corresponding to $a\delta u$ in Fig. 5.8). This aspect will be even more pronounced at close-range and will be treated in the next section.

The filter was initialized with an a priori state $\boldsymbol{x}_0$ with the following components: $a\delta a$=-50 m, $a\delta\boldsymbol{e}$=(0 250) m, $a\delta\boldsymbol{i}$=(0 300) m, $a\delta u$=10000 m and $a\delta\dot{a}$=0 m/s at epoch t_0= 2016/11/19 9:00 UTC. According to Fig. 5.8, this corresponds to an initial state error of a few tens of meters. As already mentioned in Section 5.4.1, this does not really reflect the uncertainties of the TLEs.

Overall, despite the sparse measurements, the filter convergence was achieved after
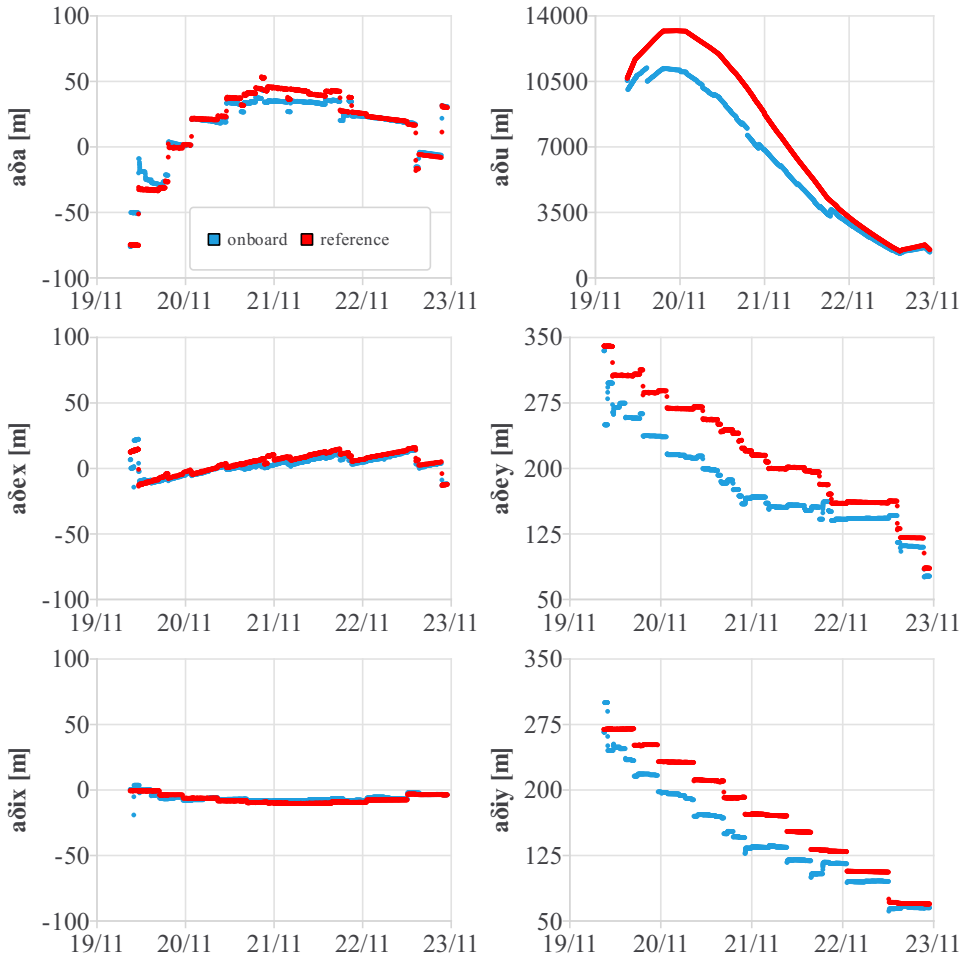

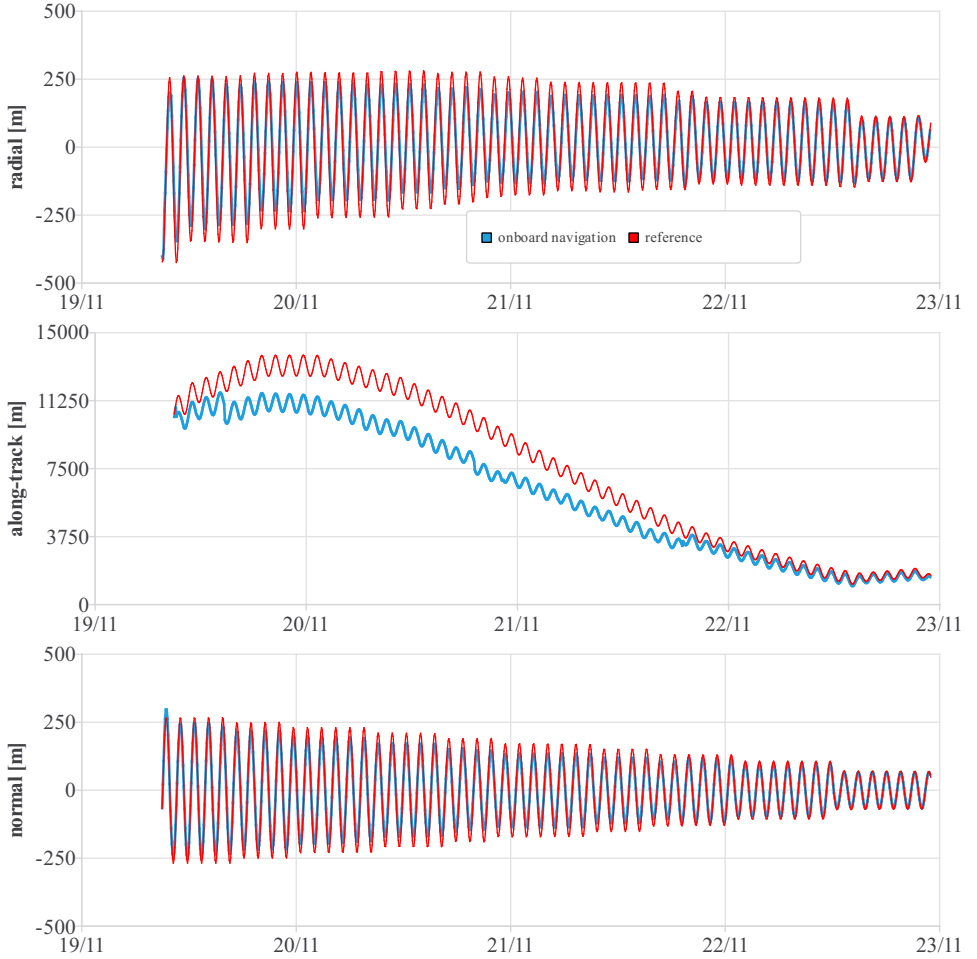Figure 5.8: Onboard navigation solution (blue) vs. reference (red).

Figure 5.9: Onboard navigation solution (blue) vs. reference (red) mapped in the local Cartesian frame $\mathcal{O}$.

a few orbits as depicted in Fig. 5.8. For completeness, the relative motion is also depicted in the Cartesian local orbital frame $\mathcal{O}$ in Fig. 5.9. The reference solution (in red in Figures 5.8 and 5.9) is the solution coming from the relative orbit determination done *a posteriori* on ground. Due to the anisotropy of the problem, the resulting accuracy differs greatly among the orbital elements, especially for $a\delta u$ whose error amounts to several hundred meters at 10 km distance and diminishes to a few tens of meters at the end of the approach. The lateral accuracy is instead much better: $a\delta a$ is accurate to the meter level (ensuring thus a smooth approach) while the relative eccentricity and inclination vectors are accurately known a few orbits after the start of the approach to about 10% of their size. As already explained in Chapter 4, the advantage of this concept lies in the fact that the shape of the apparent motion can be estimated accurately in the early stage of the rendezvous allowing the establishment of a passively safe approach based on the proper phasing of $\delta\boldsymbol{e}$ and $\delta\boldsymbol{i}$.
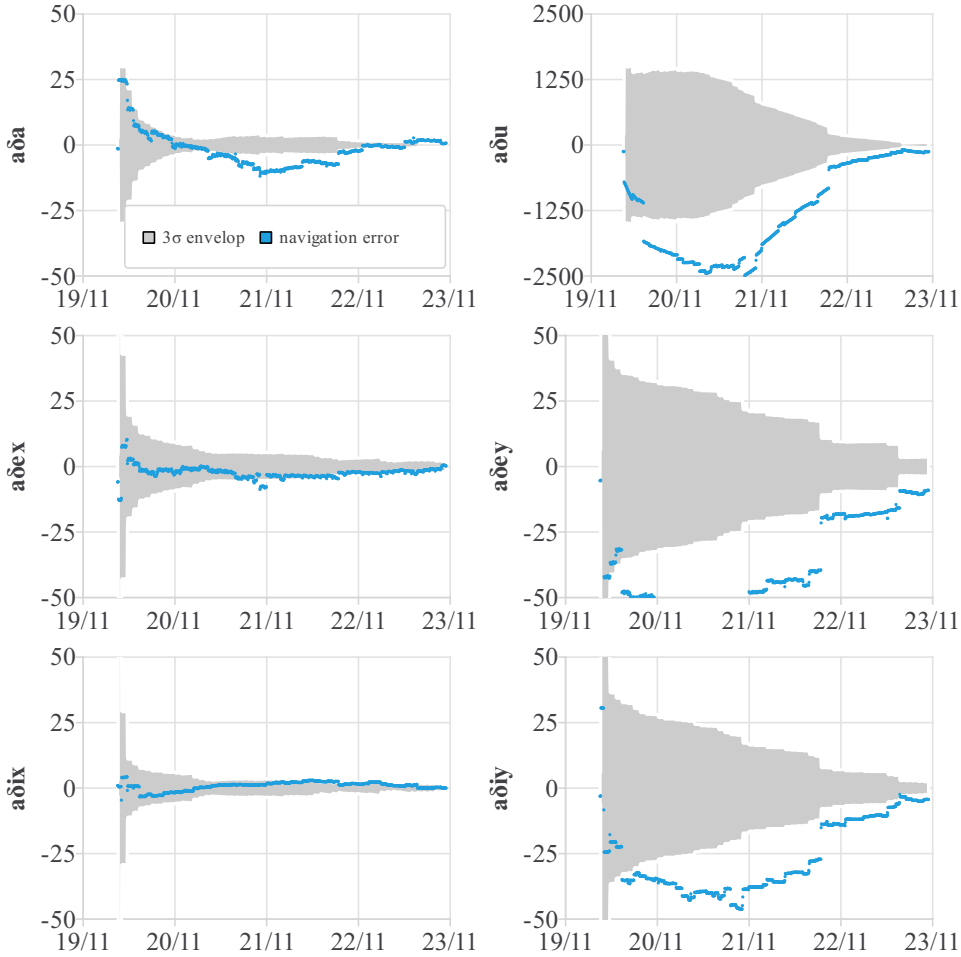
Figure 5.10: Onboard navigation errors with respect to the solution computed onground. The gray areas represent the σ envelop derived from the covariance matrix.

The navigation errors can be better investigated in Fig. 5.10, which depicts the difference between the onboard navigation and the reference solution. The 3σ envelop derived from the covariance matrix is represented in gray in the background. The improvement of observability due to the execution of maneuvers can be observed by sudden reductions of errors. Despite the good convergence of the navigation solution, the covariance matrix is not representative of the navigation errors, denoting an improper filter tuning. As already mentioned in Section 5.3.2, further investigations are obviously needed to improve the filter behavior. This will be part of future work.

Fig. 5.10 shows very different error levels between the elements $\{\delta a, \delta e_x, \delta i_x\}$ and the elements $\{\delta u, \delta e_y, \delta i_y\}$. This is caused by the poor estimation of δu due to the weak observability, and to the peculiar nominal values of δe and δi. As a matter of fact, a wrong

estimate of δu mainly affects the estimation of the "size" of the elliptic Radial-Normal lateral motion (*c.f.*, Fig. 3.4). On the contrary, the "shape" of the ellipse (orientation and eccentricity, which depends on the sizes and phases of δe and δi) is always accurately estimated. Mathematically, this means that the magnitudes of δe and δi are affected by large errors, proportional to the range estimation errors, while their phases are more accurately estimated. As a result, the errors of the components of δe and δi are proportional to their nominal value. Since these vectors have, per design, specific values with vanishing x-components, substantially smaller errors are achieved for δe_x and δi_x.
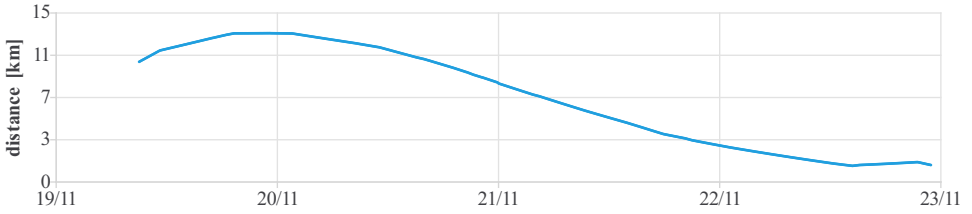
(a) Mean along-track distance during the rendezvous.
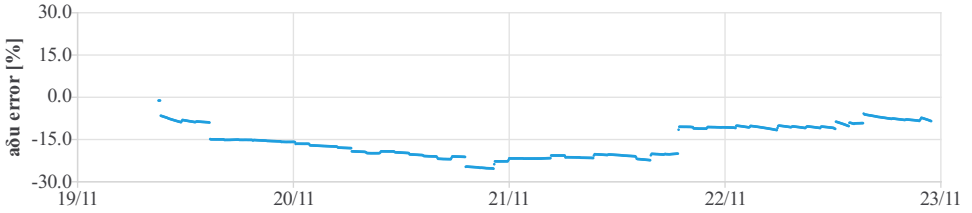
(b) Relative error of the estimated mean relative argument of attitude.
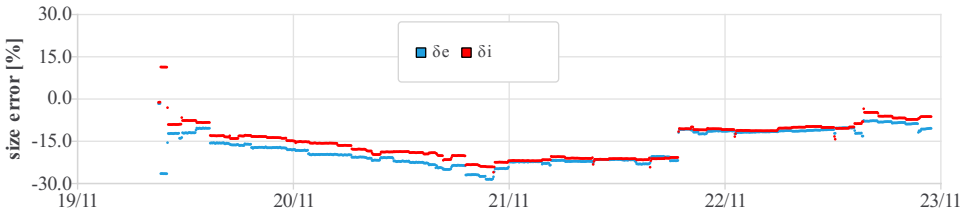
(c) Relative error of the estimated magnitudes of the relative eccentricity (in blue) and inclination vectors (in red).
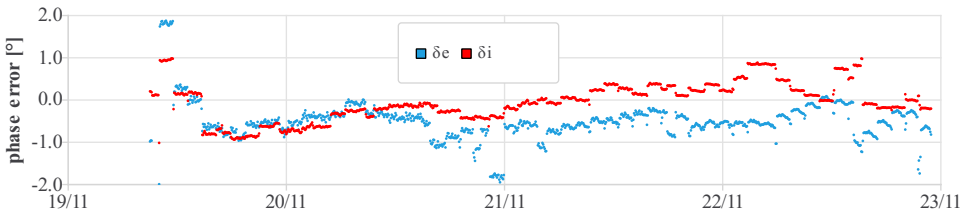

(d) Relative error of the estimated phases of the relative eccentricity (in blue) and inclination vectors (in red).

Figure 5.11: One month of relative orbit determination during the AVANTI campaign.

This phenomenon is more visible in Fig. 5.11, which depicts the intersatellite separation during the rendezvous (Fig. 5.11a) and the errors of the estimated δu, δe and δi. No clear correlation between the intersatellite distance and the errors can be recognized. The error of $a\delta u$, depicted in Fig. 5.11b, reaches a maximum of about 25% on 21 November 2016, and decreases to less than 10% at the end of the rendezvous. This behavior is more related to the convergence of the filter than to the actual intersatellite distance, and is similar to the convergence of the estimated δa shown in Fig. 5.10. A clear correlation between the relative error of δu and the relative error of the magnitude of δe and δi can, however, be observed (Fig. 5.11c). On the contrary, the error of the phase (Fig. 5.11d) does not depend on the distance and is almost always smaller than 1°.

The difficulty of the filter's task given the poor visibility and presence of significant errors in the dynamical model should again be emphasized. Figure 5.12 summarizes the main sources of errors.
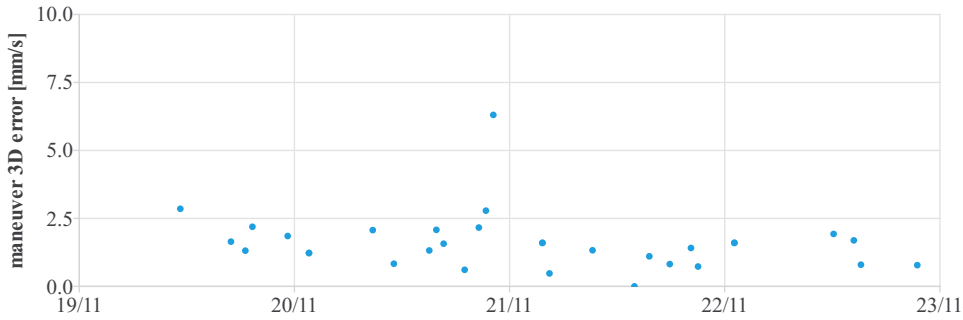
(a) Maneuver errors.
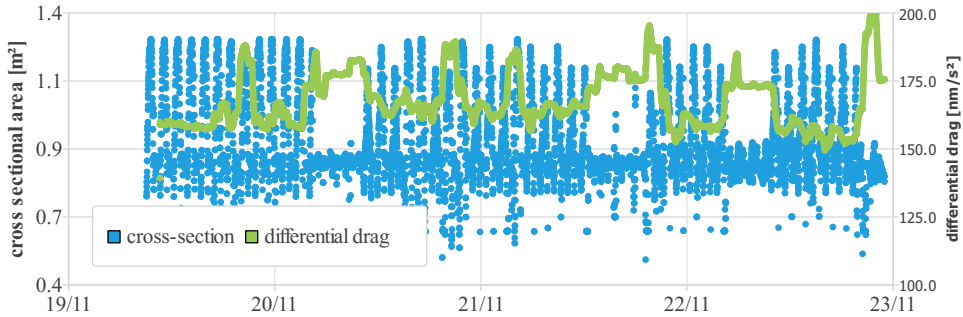
(b) Differential drag.

Figure 5.12: Main errors of the onboard dynamical model.

Figure 5.12a depicts the maneuver execution errors (assessed post-facto on-ground using precise GPS-based orbit determination). It can be observed that undesired maneuver errors up to 6 mm/s were encountered during the experiment, which is a large value while dealing with precise formation-flying (the typical maneuver size during the approach amounts to 1-2 cm/s). In fact, the maneuver errors might still be acceptable from a guidance and control point of view but are a real issue for the navigation, since the

improvement of the observability relies on well-known maneuvers. Figure 5.12b focuses instead on the unmodeled differential drag due to the variations of the cross-sectional area. This area has been reconstituted *post-facto* using attitude data and is associated with the left axis of the plot. Note how this value can vary as much as 100% during the cool-down phases corresponding to the noticeable blue peaks (*cf.* Fig. 4.18c). The cross-sectional area interacts with the atmosphere density, which varies substantially along the orbit (day-night variations), to create a differential drag force. The mean value (over one orbit) of the differential drag force - computed also *post facto* using a simple Harris-Priester model and assuming an identical drag coefficient for both spacecraft - is represented in green (associated to the right axis of Fig. 5.12b). In principle, the attitude of the target spacecraft also impacts the differential drag. This attitude is unknown, because the target is noncooperative. However, in the particular case of the AVANTI experiment, the variations of the cross-section of the target can be neglected in view of the symmetry of picosatellite.

The filter is designed to estimate $a\delta\dot{a}$, that is, the mean effect of this differential drag on the relative semi-major axis. This value is depicted in Fig. 5.13. Note that the decay of relative semi-major axis $a\delta\dot{a}$ can be linearly mapped into a differential drag ($a_d = na\delta\dot{a}/2$). Figure 5.13 depicts both values using two different vertical axes. Clearly, Fig. 5.12b and 5.13 show very different pictures. The estimated value for a_d depicted in Fig. 5.13 and the value reconstructed using an atmospheric density model in Fig. 5.12b do not match. Furthermore, the filter is not able to follow the unexpected rapid changes in differential drag depicted in Figure 5.12b, thus inducing errors in the dynamical model which have to be compensated with process noise. This constitutes an important lesson learned for future similar applications. In order to improve the response of the filter, a better onboard modeling of the attitude-dependent differential drag might be necessary.
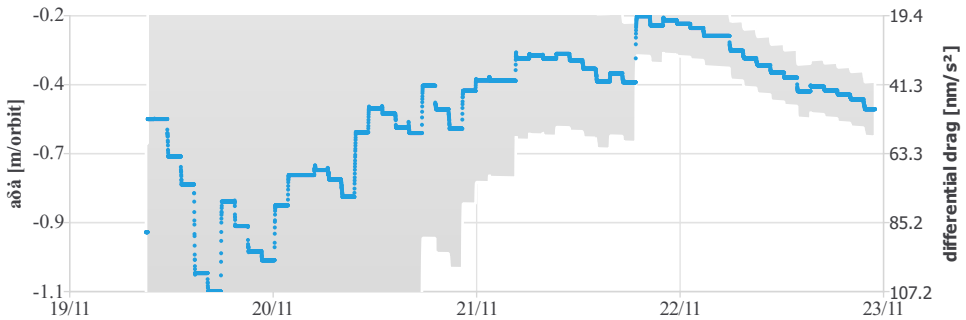
Figure 5.13: Estimated decay of relative semi-major axis. The right axis represents the equivalent differential drag necessary to produce such a decay. The gray area represents the 3σ envelop derived from the covariance matrix.

5.4.3. MID- TO CLOSE-RANGE REGIME

The second autonomous approach was intended to investigate the main difficulties encountered when the separation decreases. At close-range, the navigation task becomes much more challenging due to the following reasons:

- When the distance decreases, the errors of the centroids (which should correspond to the center of mass) increase because the target is not imaged as a point anymore (as seen in Fig. 5.14) so that the errors of the line-of-sight measurements are larger (as already observed in Fig. 5.7).
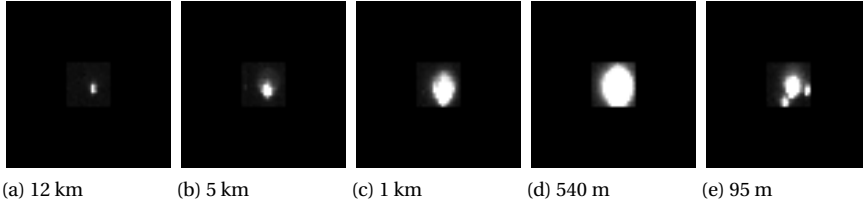

(a) 12 km   (b) 5 km   (c) 1 km   (d) 540 m   (e) 95 m

Figure 5.14: Target image at different distances.

- When further reducing the distance (*c.f* Fig. 5.15a), the increasing brightness of the target object makes the use of an electronic shutter mandatory, in order to limit the exposure time. The collateral damage is that the stars are not visible anymore in the background, making a precise measurement of the orientation of the camera impossible. Thus the onboard filter has to rely on the onboard attitude estimation to determine the direction of the camera. In the case of AVANTI, the onboard attitude estimation could not always rely on star trackers, since one head was already blinded by the target object and the other could not always be oriented to deep
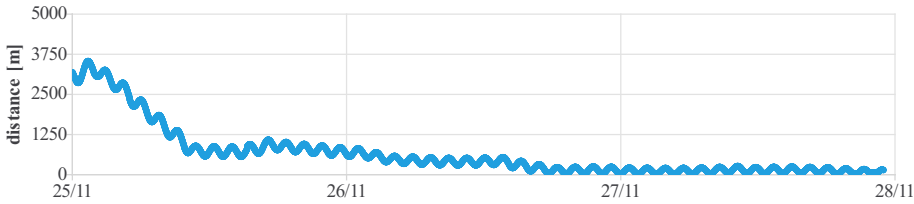
(a) Instantaneous intersatellite separation.
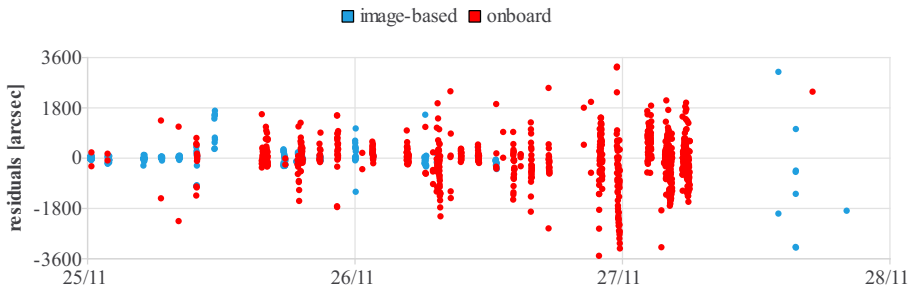
(b) Filter residuals using image-based vs. onboard attitude estimation.

Figure 5.15: Filter residuals and intersatellite distance.

sky. As a result, the onboard attitude error was sometimes affected by errors up to one degree (*cf.* Fig. 5.15b). This is another important lesson learned [49]: a similar mission dealing with close-proximity should ensure that at least one star tracker is always working, for example by using a third camera head (which was not available in AVANTI). However, it has to be kept in mind that one degree line-of-sight measurement error does not have the same impact at 100 m (1.7 m) as at 40 km (700 m). It is thus possible to cope with this error by tuning the filter measurement noise (*cf.* Table 5.1). In fact, during the close approach, this value was changed on 25 November 15:00 UTC from 80" (corresponding to 1 pixel) to 1000" in view of the poor onboard attitude estimation performance.

- At close-range, the cross-sectional area subject to the differential drag suffers from additional variations. This is due to the adopted passively safe approach, which requires non-zero cross-track and radial components of the relative motion. At small separations, large attitude variations of the spacecraft are needed to follow the target with the camera. For example, a cross-track offset of 30 m at 100 m distance requires a spacecraft slew of 17°. This effect was limited from far- to mid-range. At large separations, the apparent relative motion is small so that it is enough to point the camera in the flight direction to observe it entirely. However, when the distance decreases, the camera might need to point in radial or cross-track directions to follow the target. As depicted in Fig. 5.16, the differential drag becomes very different from the values previously observed in Fig. 5.12b.
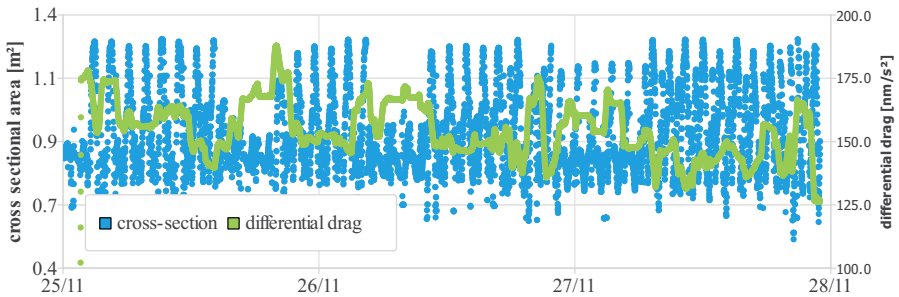
Figure 5.16: Cross-sectional area and differential drag at mid to close range.

- Given the limited field of view of the camera (14°x 18°), a precise real-time knowledge of the relative motion is necessary to point the camera in the proper direction. In view of the aforementioned difficulties (inaccurate measurements and large perturbations of the onboard relative motion model), it becomes a real challenge to properly point the camera towards the target. Fig. 5.17 depicts the real-time errors of the estimated direction to the target. From November 27th onwards, the errors become so large that the camera points in the wrong direction, making measurement updates impossible and eventually leading to a filter divergence. The fact that images are taken only every 30 seconds constitutes one of the major limitations of the navigation system. It would have probably been more robust (if the satellite would have allowed it) to work at a higher frequency (*e.g.* 1 Hz) and to implement a simple attitude feedback controller (or to use a gimbaled camera)

to always keep the bright object in the center of the field of view such that the navigation filter would have always been fed with measurements.
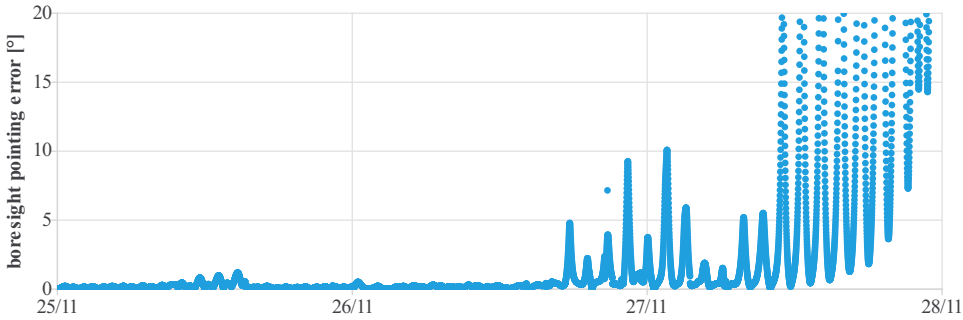

Figure 5.17: Onboard estimation errors of the direction to the target.

Further investigations will be needed to investigate the robustness of the filter. Preliminary analyses indicate that the filter is robust during the rendezvous, but becomes unstable when the chaser reaches its final destination. This is probably due to the fact that the large maneuvers (a few cm/s) executed during the rendezvous are frequently contributing to improve the observability. At the end of the rendezvous, only small maneuvers (a few mm/s) are required to maintain the formation. The resulting improvement of observability is not enough to compensate the uncertainties brought by the unknown differential drag. The AVANTI experiment was fortunately designed to be robust against such issues. To that end, a finite-time horizon controller was implemented onboard to perform the approach [49]. In this control scheme, an open-loop guidance plan is generated and updated autonomously at a low frequency (maximum a few times per day). Consequently, the relative navigation is used only to update the plan or generate a new one but, during the execution of the plan, the guidance and control work in open-loop. Since the filter divergence happened at the end of the guidance plan, no maneuver was foreseen anymore by the controller. Thanks to the passive safety ensured by the relative motion, no emergency action was required. After half a day, the strong differential drag made the target drift back to a few hundred meters separation. It was then sufficient to point the camera in the along-track direction to be able to see the target again and recover the formation.

Despite all these difficulties, the filter was able support the onboard guidance and control throughout the entire approach from 3 km to 50 m, and could deliver a reliable navigation solution during the approach. Figure 5.18 depicts the achieved intersatellite separation and the time at which measurements were available (red dots). The blue dots correspond to the time of the four images. Note how the rectangular shape and the antennas of the spacecraft become visible when the distance decreases below 100 m. In a mission dedicated to close-proximity operations, this corresponds exactly to the range where other kinds of metrology can be used (*e.g.* pose estimation, stereo vision, radar).
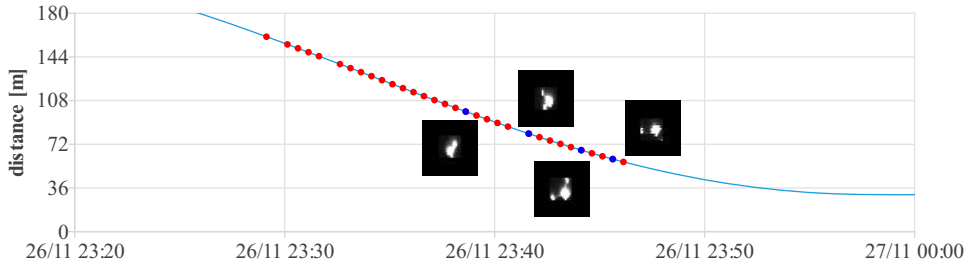
Figure 5.18: Measurements during the close range approach.

5.5. CONCLUSION AND LESSONS LEARNED

The AVANTI experiment demonstrated the capability to autonomously approach a truly noncooperative object in orbit using a single camera and showed the power of angles-only navigation. Despite its simplicity, a simple passive camera is able to support autonomous rendezvous from several dozen kilometers to only 50 m, paving the way to future close-proximity operations. This achievement was made possible thanks to the real-time angles-only relative navigation system embarked by the chaser satellite, which could successfully support the onboard guidance and control tasks to perform smooth and safe rendezvous.

Dealing with onboard autonomy, special attention has been paid to ensure the integrity of the real-time navigation solution, focusing in particular on the early stages of the process, that is, in the extraction of the line-of-sight measurements. For this purpose, a novel approach has been employed to decouple as much as possible the target recognition task from the navigation filter. Based on the kinematic analysis of visible relative trajectories of non-stellar objects, the target detection algorithm is able to recognize the desired target object when initiating the approach at far-range using only coarse relative state information. After the convergence of the filter, the onboard navigation solution is used as backup in case of failed kinematic detection, together with additional detection capability based on the obvious brightness of the target object at close-range.

The line-of-sight measurements are subsequently processed by a dynamical filter. In order to cope with the limited onboard resources, an extended Kalman filter has been implemented, based on an analytical model of the relative motion which takes into account the perturbations due to the Earth oblateness and due to the differential drag. During the experiment, the filter had to face severe navigation conditions. In fact only 10 minutes of observations could be collected every orbit. Furthermore, the onboard dynamical model was affected by strong unknown maneuver execution errors and unknown variations of differential drag.

Despite these difficulties, the relative navigation system was able to support two different autonomous approaches, first from 13 km to 1 km separation, then from 3 km to 50 m. At far-range, despite line-of-sight measurements accurate at the arcminute level, the poor observability is responsible for large longitudinal errors up to a few kilometers. This error steadily decreases during the rendezvous as the observability improves. A final longitudinal error of a few tens of meters is achieved when reaching the final desti-

nation at 1 km separation. At close-range, lateral navigation performance at meter level is achieved during the rendezvous.

Ensuring a robust implementation for onboard real-time application was shown to be much more challenging than the on-ground relative orbit determination task. This is mainly due to the sequential nature of the estimation process which cannot rely on the whole history of observations to improve the robustness. This limitation threatens the integrity of the relative navigation during the filter convergence phase, where a single bad observation can lead to a filter divergence. This issue disappears after the filter convergence, which allows for a more accurate and efficient data screening based on the relative state estimate, but is a real problem when initializing the filter. This weakness has been operationally mitigated by providing better initialization information to the filter, which had to be beforehand derived on ground and was thus not anymore representative of the accuracy of the TLEs. An elegant way to solve this problem could be the onboard combination of the batch-least squares approach described in Chapter 4 with an EKF. When initiating the rendezvous, the chaser could first spend several orbits observing the target and subsequently derive its first relative state estimate based on a least-squares approach (using an analytical model for the relative motion instead of a numerical integration and based on the optimizations and improvements done in Chapters 6 and 7). In this case, no real-time requirement would apply, so that this process could take dozens of minutes if needed, depending on the onboard resources. Once an accurate guess has been computed, the EKF would benefit from an efficient and reliable data screening. The batch-least squares processing could also always be active in the background as independent task with lower priority to monitor the behavior of the EKF and recover any filter anomaly.

The second main operational difficulty encountered during the conduction of the experiment was caused by the large and unpredictable perturbations affecting the relative dynamics, mainly due to the unknown varying differential drag and maneuver execution errors. The filter is, in principle, able to cope with such uncertainties thanks to the addition of process noise but this comes at the expense of a degradation of observability. This effect was fairly limited during the phases of rapid changes of the formation configuration due to frequent maneuvering, but became critical during the steady phases after the completion of the rendezvous. This is due to the fact that, at close-range, only small maneuvers are possible to finely control the rendezvous, which does not substantially improve the observability. In this case, the unpredictable varying differential drag alters the formation but the system is not able to properly estimate this effect anymore, which might eventually lead to a filter divergence. Several options might be considered to improve the system robustness. The first obvious measure would consist in a better comprehension and modeling of the differential drag. While this might be done for the AVANTI experiment, where the variation of the differential drag is mainly caused by the chaser itself, this approach would, however, not improve the accuracy of the relative motion model in case of a highly nonsymmetrical noncooperative tumbling object, whose attitude is unknown. Other improvements might be gained by better tuning the filter, using more robust filtering techniques such as the H_∞ filter [110], or employing the above-described hybrid approach. Since this difficulty is likely to arise in close-range after the conduction of the rendezvous, equipping the chaser with a small range-measurement

device reaching a distance of 100-200 m would also be extremely beneficial to the filter stability during subsequent station keeping. Taking measurements at a higher frequency in close-range, for example at 0.1 Hz, would also reduce the risk of loosing track of the target in case of growing navigation errors [111], because a simple independent feedback control loop could be implemented within the attitude guidance system to follow the target without relying too much on the onboard state estimate. In this case, the filter would have more chances to recover if measurements are still available despite a degraded onboard estimate. With this said, it should be noted that the high disturbance due to the drag is not a real practical issue for Active Debris Removal, which aims at capturing objects flying at higher altitude that cannot benefit from natural drag-based deorbiting.

5

6

THE PROBLEM OF INITIAL RELATIVE ORBIT DETERMINATION

The navigation algorithms described in the previous chapters are relying on the provision of an external coarse a priori solution derived from Two-Line Elements. This chapter demonstrates that, when initiating the rendezvous at a distance of several tens of kilometers, it is possible to directly compute this coarse solution from the line-of-sight observations, paving the way for a future simplification of the interfaces and for an improved autonomy of angles-only navigation systems.

6.1. INITIAL RELATIVE ORBIT DETERMINATION

6.1.1. OVERVIEW

Applied to the field of angles-only navigation, the problem of Initial Relative Orbit Determination (IROD) consists in deriving an estimate of the relative state of two spacecraft using solely line-of-sight measurements. This topic has recently attracted considerable attention in the space community. An overview of the current research directions in this domain is provided in the following section. These activities are of great relevance, since they provide the theoretical justification of possible approaches to improve the observability of the relative orbit determination problem.

This work intends to complement this fundamental research by providing a quantitative analysis based on flight data and experience collected during the ARGON and AVANTI experiments, which were both conducted in LEOs. The objective consists in determining the relative trajectory of objects flying in near-circular orbits, with applicability to areas such as in-space debris monitoring, active debris removal or on-orbit servicing activities. Note that these topics are currently of primary interest, given the density and natural evolution of the population of objects flying in LEOs [114, 4].

A second contribution regards the domain of applicability of the proposed solution in terms of relative range. From an operational point of view, in fact, IROD has to be performed when the spacecraft are separated by a few tens of kilometers, as it would be too dangerous to start estimating the relative state only at few kilometers of distance. On the other hand, working with too large separations, such as a few hundred kilometers, poses the problem of detectability of the target, a technological constraint driven by the sensor capabilities. As explained in more detail in the following section, these practical considerations limit the domain of applicability of some of the theoretical methods designed to perform at close or very large distances.

6.1.2. IMPROVING THE OBSERVABILITY

Section 3.3.2 introduced Woffinden's dilemma, which states that, if a linear relation exists between the initial relative state vector $\boldsymbol{x}(t_0)$ and the Cartesian relative position $\Delta\boldsymbol{r}(t)$, the angles-only relative navigation problem is not observable. As mentioned in Section 3.3.2, it is possible to reach observability by relaxing some of the assumptions made when demonstrating Woffinden's dilemma. A first possibility consists in executing maneuvers, so that the relative motion is no more homogeneous (*i.e.*, $\boldsymbol{x}(t) \neq \boldsymbol{\Phi}(t, t_0) \cdot \boldsymbol{x}(t_0)$). Examples are provided in [28, 29, 30, 31], where the focus is given on finding the optimal location and the direction of impulsive maneuvers to be performed during the rendezvous to improve the observability of the bearing-only relative navigation problem. In practice, this strategy has been used to enable the vision-based activities carried out within the PRISMA mission [46, 47, 48] as well as in AVANTI [49, 109]. A second option consists in introducing a camera offset with respect to the center of mass of the spacecraft [32, 33]. Since the angles-only relative navigation problem forms in reality a weakly observable system even in the absence of maneuvers, a third approach is to improve the modeling of the relative dynamics and/or the modeling of the measurement equations to enhance maneuver-free observability. In [34], for example, an observability criterion based on Lie derivatives for the nonlinear two-body relative problem is proposed. A ben-

eficial effect over time is achieved by including orbit perturbations (*i.e.*, the secular effect due to the J_2 term of the gravitational potential) in the relative motion modeling as discussed in [29] and [35]. This latter work also considers the eccentricity of the spacecraft orbit and nonlinearities in the measurement model. Note that these works exploit the parameterization in terms of relative orbital elements, as linearization with respect to mean orbital elements produces a better modeling of the orbit curvature compared to linearization in Cartesian coordinates.

Focusing on algorithms dedicated to IROD, Garg and Sinclair [36] use a second-order model of the relative dynamics combined with line-of-sight measurements modeled from the Cartesian relative state; whereas Geller and Lovell [37] alter the linear dependency of the measurement equation using cylindrical coordinates. Sullivan et al. [35] exploit the decoupling between the weakly observable range and the observable relative geometry (see also [29]) to define a reduced set of relative orbital elements normalized by the relative mean longitude. The resulting normalized state vector is then used to fit the observation batch, neglecting its dynamical evolution. In order to reduce the amount of required measurements, Sullivan and D'Amico [38] propose two variants to their original algorithm. The first, fully analytical, option consists in retaining the second-order expansion of the nonlinear transformation from the mean relative orbital elements to the local relative position to determine the predominant unknown scaling factor which approximates the null space of the observability matrix. The second option, which improves the performance of the analytical method in the presence of realistic noise, fits the scaled set of relative orbital elements accounting for J_2 (secular, long-period, and short-period effects) and starting from the *a priori* knowledge of the relative mean longitude derived from TLE products.

In view of the main characteristics of the scenario under considerations (*i.e.*, near-circular low Earth orbits with intersatellite distance of a few tens of kilometers), two of the aforementioned approaches are naturally excluded: improving the observability by considering the camera offset, for example, is rather intended for close-proximity regions (*i.e.,* up to a few tens of meters) and will be impracticable for far-range IROD. At the same time, the methods based on an analytical model which does not include at least J_2 introduce too large modeling errors in LEO. Although performing orbit corrections revealed a viable and practical solution for initializing angles-only relative navigation filters, this requires the estimation of additional parameters (*i.e.*, maneuver execution errors) and may lead to the expenditure of supplementary propellant during the rendezvous phase.

The IROD algorithm presented in this work belongs to the class of methods exploiting model nonlinearities within a maneuver-free observation arc to solve the range ambiguity. To that end, the decoupling between intersatellite range and geometry of the relative orbit is exploited to reduce the search space of the solution. As described in Section 3.3.2, there exists an infinity of collinear solutions, only differing by a scaling factor μ, to the linear angles-only navigation problem. However, in the presence of nonlinearities, there exists only one value $\hat{\mu}$ which best fits a set of angles-only measurements. The proposed method, described in more detail in the next sections, aims at numerically finding this value using a single-dimensional systematic search among all possible values for μ. Contrary to other works in the literature, this algorithm does not require any

external *a priori* information to resolve the scaling factor μ. Despite its apparent simplicity, the major challenges arise when dealing with real operational conditions: the ability for the camera to distinguish the small differences with respect to the linearized relative motion, given the sensor noise, the intersatellite separation and the visibility conditions.

6.1.3. Algorithm Description

As already stated, the linear assumptions leading to the Woffinden's dilemma result in an infinity of solutions matching a given measurement profile. In practice, these approximations translate into small discrepancies which will appear when trying to fit a solution from the linear theory with a set of real measurements. Intuitively, the smallest fitting errors will be obtained in the vicinity of the true solution, allowing for a discrimination between all the collinear candidate solutions. This statement sounds simple but is in fact not obvious. A formal demonstration is provided later in Section 6.4.1.

In order to accurately fit the measurements, a more advanced relative motion model is required, able to faithfully capture the effects neglected by the linear model. In this case, the state propagation becomes

$$x(t) = f(t, x(t_0), y_c(t_0)) \tag{6.1}$$

where f is a nonlinear function. Let $x_0 = x(t_0)$ denote the initial state vector at time t_0. The modeled relative position takes the general form

$$\Delta r(t, x_0) = g(x(t, x_0)), \tag{6.2}$$

g also being a nonlinear function. Following Eq. 3.24, the measurement model $h(t, x_0)$ is derived from the Cartesian relative position:

$$h(t, x_0) = \frac{\Delta r(t, x_0)}{\|\Delta r(t, x_0)\|}. \tag{6.3}$$

Note that h is a unit vector. According to Section 3.3.1, this representation is equivalent to a parameterization based on two angles.

Given a set $\{u_i\}$ of n line-of-sight observations, the problem of IROD consists in finding x_0 which minimizes the loss function

$$J = \sum_{i=1}^{n} \|h(t_i, x_0) \times u_i\|^2. \tag{6.4}$$

The difficulty here is to derive a method able to find in a reasonable time the global minimum of J. Due to the weak observability, a simple batch least-squares method may not converge to the global minimum. The proposed approach consists in aiding the least-squares method with the family of solutions coming from the linear theory to perform a systematic search of the best candidate within this family. For this purpose, it is first necessary to compute the linear solution. According to Eq. 3.31, a single measurement set u_i provides a set of three equations. By combining n measurement sets, a set of $3n$ equations can be derived and rearranged to form the following linear system:

$$A x_0 = 0, \tag{6.5}$$

where A is a $3n \times 6$ matrix of rank 5 because this system is not observable. Due to the rank deficiency of the matrix, a non-trivial solution $\hat{x}_0$ exists. This solution can be easily derived by computing the one-dimensional null-space of A.

A constrained (using an *a priori* covariance) batch least-squares adjustment is subsequently performed in the vicinity of this solution. Since $\hat{x}_0$ is a solution to the linear problem, the batch-least squares method will converge to a local solution x_0 in the vicinity of $\hat{x}_0$. This process can be repeated using a nonzero scaling factor μ to generate the solution $\mu\hat{x}_0$ (belonging as well to the null-space of A) which leads to a new local solution x_0^μ. Let $\sigma(\mu)$ denote the root mean square value of the measurement fitting residuals associated to x_0^μ:

$$\sigma(\mu) = \sqrt{\frac{1}{n}\sum_{i=1}^{n} \left\| h(t_i, x_0^\mu) \times u_i \right\|^2} = \sqrt{\frac{1}{n} J(x_0^\mu)} \tag{6.6}$$

where $h(t_i, x_0^\mu)$ stands for the modeled line-of-sight measurement at time t_i corresponding to the initial relative state x_0^μ. The numerical values for the lower and upper limits of μ are derived from the physical properties of the sensor and target spacecraft. For this task, it is advised to combine μ with a component of x_0 that best approximates the intersatellite distance. At far-range, the distance between the satellites mainly corresponds to the along-track relative position in case of a Cartesian representation of the state vector. When using relative orbital elements, this corresponds to $a\delta\lambda$. Let x_0^l denote this specific component of x_0. For a given measured quantity of light, it can, for example, be stated that the intersatellite distance must be comprised between 1 and 100 km. By varying the dimensioned scaling factor μx_0^l within this range, it becomes possible to derive the adimensional range for μ.

This process is depicted in Fig. 6.1, which represents the fitting residuals corresponding to a series of least-squares adjustments in the vicinity of the linear solutions $\mu\hat{x}_0$. These solutions correspond to relative elliptical motions of identical shape but different scaling factor, which are schematically represented by ellipses of growing size on top of the residual graph. In the linear formulation, this family of relative motions yields an identical measurement profile , represented by dashed lines. However, when performing a series of nonlinear estimations in the vicinity of the linear solutions, different residuals
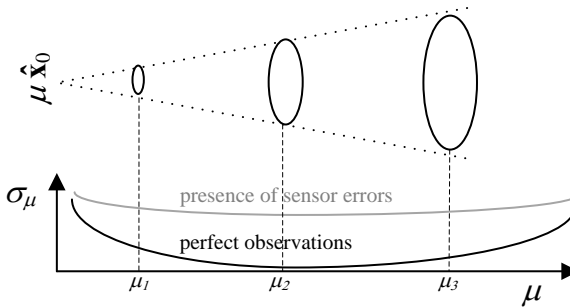

Figure 6.1: Schematic representation of the fitting residuals corresponding to a series of least-squares adjustments in the vicinity of the linear solutions $\mu\hat{x}_0$.

values σ_μ will be obtained for each run. The minimum value $\sigma_{\mu2}$ indicates that μ_2 is the scaling factor which best fits the set of observations. In the presence of sensor noise (in gray), the residual curve will be flatter and upshifted. Thanks to this approach, the search space has thus been reduced from six dimensions (x_0) to only one (μ).

The accuracy of the solution will depend on the flatness of the valley formed by the residuals. The flatter the curve, the less observable the minimum becomes. The steepness of the curve depends on several factors which are described in detail in Section 6.2. One of these factors is the noise of the sensor, which tends to fade the effects of the nonlinearity, as schematically depicted in Fig. 6.1.

6.2. Numerical Analysis

6.2.1. Relative Motion and Measurement Models

As already stated, accurate models for the relative motion and measurements are needed to enable the observation of small differences with respect to the linear motion model. Two options for accurate measurement and relative dynamics models are investigated:

- **Numerical propagation**. In this case, x is the Cartesian inertial relative state vector, g (*c.f.*, Eq. 6.2) is the identity matrix and f (*c.f.*, Eq. 6.1) corresponds to a numerical integration of the equations of motion described by Eq. 3.2 considering a gravity field which includes at least J_2. As the equations are numerically integrated, no linearization is performed and the overall accuracy depends on the order and degree of the considered terms of the gravitational potential, as well as on the additional perturbations included in the model (*e.g.*, aerodynamic drag, solar radiation pressure, third-body). This model is very accurate, provided that these perturbations can be precisely modeled, which is in reality often not the case, given the uncertainties associated to the atmospheric density and to the characteristics of a noncooperative target. The main drawback of this model lies in the high computational load.

- **Analytical propagation using mean relative orbital elements**. In this case, the relative motion model is parameterized using the mean relative orbital elements (*i.e.*, $x = \delta\alpha$) as introduced in Section 3.2.4, for which a linear motion model is available (*i.e.* $\delta\alpha(t) = \Phi(t, t_0) \cdot \delta\alpha(t_0)$). On the contrary, the model of the relative position g is not linear anymore. In order to reach sufficient accuracy, it is indeed necessary to use the nonlinear mapping described in Fig. 3.5 to retrieve the relative position from the relative state vector. This model does not include the higher terms of the gravity field nor non-gravitational perturbations (except for the mean effect of the drag) and is thus slightly less accurate than the numerical integration with a full model, but has the advantage of being computationally-light.

Practically, the proposed method will correctly perform if the measurement noise is similar to the errors of a given model but smaller than the discrepancies between this model and the linear motion model (otherwise they cannot be observed). This assessment can be done by evaluating the line-of-sight errors introduced by a given model, as done in Section 3.3.3. The camera [21] employed for ARGON and AVANTI exhibits

a line-of-sight noise of about 40" at far-range (corresponding to less than half-a-pixel). The differential drag is the second largest perturbation after J_2 in low Earth orbit. This perturbation can be helpful to accentuate the discrepancies with respect to the linear motion model but is extremely difficult to faithfully model, especially when dealing with a noncooperative target, with unknown geometry and attitude. Hence, in the case of IROD, it might be more judicious to reduce the observation time span as much as possible (a few orbits), in order to limit the effect of this mismodeled perturbation.

The performance comparison of different relative motion models was already presented in Section 3.3.3 and showed that both numerical integration and analytical model were well adapted to line-of-sight navigation. However, the results of Section 3.3.3 were derived over a large time scale representative of an orbit determination arc employed during operations (four days), while the IROD is restricted to a much shorter arc, typically a few orbits. Thus, Fig. 6.2 is introduced to depict in detail the line-of-sight errors resulting from the model deficiencies over five orbits. A real trajectory from the PRISMA mission (accurate at centimeter level) is used as reference. The model indexes in the legend correspond to the description in Table 3.2. As expected, Fig. 6.2 indicates that, for that limited time span, all model errors stay well below the sensor noise. At this altitude, the differential drag does not play any noticeable role over such a short time scale. Note that the model using the 20x20 gravity field slightly outperforms the J_2-numerical propagation and the analytical model, but these two models are still accurate to about five arcsec over the considered time span. As a result, it can be stated that both analytical and numerical models are well suited for IROD.
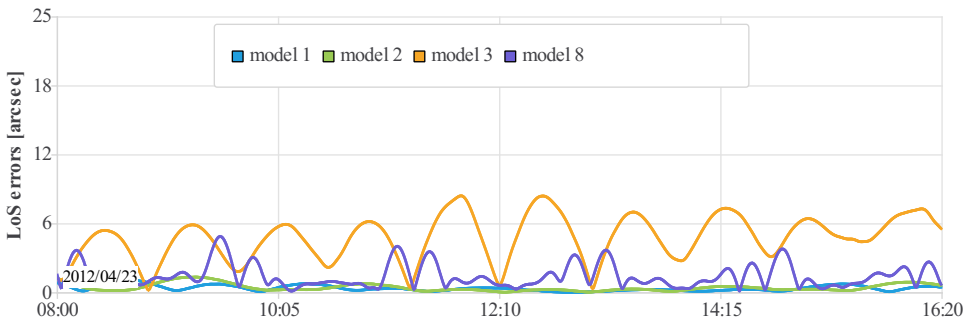
Figure 6.2: Line-of-sight (LoS) errors introduced by the model deficiencies.

6.2.2. SENSITIVITY ANALYSIS

As stated in Section 6.1.3, several effects influence the steepness of the valley of fitting residuals. This section intends to investigate the impact of four factors by means of simulations. The ultimate validation with flight data will follow in the next section. The scenario used for the simulations is directly inspired from the ARGON experiment. A chaser satellite is flying on a 750 km high, dusk-dawn, Sun-synchronous, near-circular orbit and observes a target satellite at 30 km distance. The different cases used for the sensitivity analysis are derived from this scenario, whose simulation parameters are summarized in Table 6.1. Single parameters are altered case-by-case to investigate their impact on the residual curve.

Table 6.1: Simulation parameters used to create the scenario.

Item	Value
t_0	2012/04/24 00:00:00 UTC
y_c^T	(2278.94, -6524.81, 1717.67, -1.625, 1.304, 7.193) (km,km/s)
Arc length	2 orbits
$a\delta\boldsymbol{\alpha}^T$	(-20 -30000 -50 -390 0 295) [m]
Maneuvers	None
Motion model	Numerical propagation using 20x20 gravity field, with third-body, solar radiation pressure and drag perturbations
Spacecraft properties	See Table 2.1
Measurements	One every 30 s, noiseless

The investigations are performed by the means of residuals plots (*cf.* Fig. 6.1) created according to the method described in Section 6.1.3. To that end, the linear solution is first derived by building the system $\boldsymbol{Ax}_0 = \boldsymbol{0}$ (*cf.* Eq. 3.31). Since relative orbital elements are used, the matrix $\boldsymbol{C}$, defined by Eq. 3.23, is used to map the relative orbital elements into a Cartesian relative position. Note that this linear measurement model is not very accurate but is sufficient to derive a coarse solution to initialize the relative orbit determination. Since $\delta\lambda$ is not observable [29], the linear solution corresponding to a specific value $a\delta\lambda = L$ in a least-squares sense can be derived as follows:

$$\tilde{\boldsymbol{A}} = \begin{pmatrix} \boldsymbol{A}_1 & \boldsymbol{A}_3 & \boldsymbol{A}_4 & \boldsymbol{A}_5 & \boldsymbol{A}_6 \end{pmatrix} \tag{6.7a}$$

$$\boldsymbol{b} = -L \cdot \boldsymbol{A}_2 \tag{6.7b}$$

$$\boldsymbol{\gamma} = (\tilde{\boldsymbol{A}}^T \cdot \tilde{\boldsymbol{A}})^{-1} \cdot \tilde{\boldsymbol{A}}^T \cdot \boldsymbol{b} = \tilde{\boldsymbol{A}}^+ \boldsymbol{b} \tag{6.7c}$$

where $\boldsymbol{A}_i$ corresponds to the ith column of $\boldsymbol{A}$ and $\tilde{\boldsymbol{A}}^+$ is the Moore–Penrose pseudoinverse introduced in Eq. 3.36. Finally, the linear solution $\hat{\boldsymbol{x}}_0^L$ corresponding to the relative motion at mean relative longitude L is reconstructed as

$$\hat{\boldsymbol{x}}_0^L = \begin{pmatrix} \gamma_1 & L & \gamma_2 & \gamma_3 & \gamma_4 & \gamma_5 \end{pmatrix}^T, \tag{6.8}$$

where γ_i represents the ith component of $\boldsymbol{\gamma}$.

In order to create the residual plots, a granularity of 1 km is employed, which means that the linear solution $\hat{\boldsymbol{x}}_0^L$ corresponding to the relative motion at discretized distance $L \in [5, 100]$ km is used to initialize the batch least-squares adjustments. This process is executed 95 times, starting with L=5 km. The analytical model based on relative orbital elements is used to perform the series of least-squares runs. The covariance matrix used to constrain the solution is set as $\boldsymbol{P} = \text{diag}(100^2, 1^2, 100^2, 100^2, 100^2, 100^2)$ m^2. These values are derived from the fact that the linear solution is inaccurate at far-range, resulting in errors of a few tens of meters for $a\delta a$, $a\delta e$ and $a\delta i$. For each least-squares run, the associated residual value σ is computed as in Eq. 6.6. The residual curve is finally created by collecting the residual values corresponding to the 95 runs. Based on the residual curve, the influence of several factors can be investigated:

- **Observation arc**. A longer observation time span increases the chance of having more informative measurements and thus plays a predominant role in the improvement of the solution accuracy. In order to investigate this effect, the arc length property of Table 6.1 is altered. Figure 6.3 shows that a significant steepness already appears by collecting observations over more than 2 orbits.
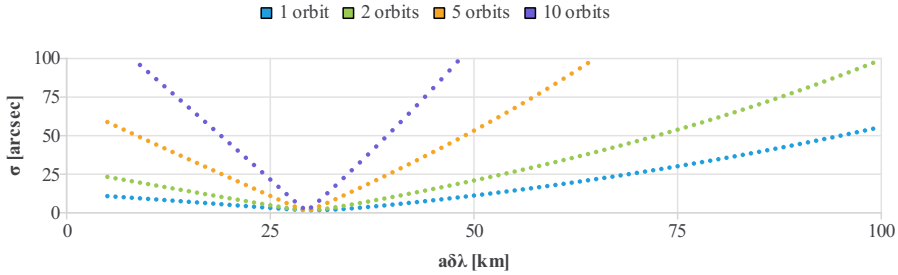

Figure 6.3: Improvement of observability due to increased number of measurements resulting from larger observation time spans.

On the contrary, a limited visibility of the relative motion dramatically reduces the number of available measurements. ARGON was a favorable case, because the relative motion was fully visible thanks to the dusk-dawn orbit of the PRISMA satellites. When flying on an arbitrary orbit in LEO, part of the motion may not be visible anymore, because the target may be eclipsed or because the camera may be blinded by the Sun. As shown in the previous chapters, as little as 10% of the relative motion was visible during the rendezvous of the AVANTI experiment. In order to simulate this effect, only the measurements taken at mean argument of latitude $u \in [0, 2\pi/10]$ are kept for the following analysis. Figure 6.4 shows a comparison for a two-orbit-long data arc with full (in green) and limited visibility (in blue). It can be seen that the residual curve corresponding to sparse measurements is almost flat, thus making the IROD process challenging. The small value of residuals at wrong separations (*e.g.*, at 100 km) can be explained by the fact that the least-squares process will find a wrong solution which will correspond to the very few available measurements, thus exhibiting good fitting residuals.
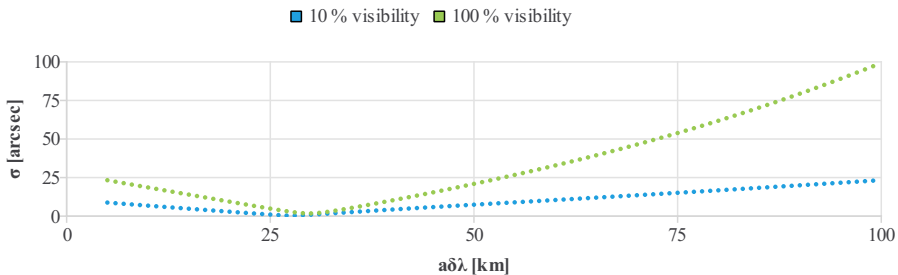

Figure 6.4: Degradation of observability due to reduced visibility.

- **Execution of maneuvers**. Maneuvers act as perturbations which introduce addi-

tional discrepancies with respect to the linear motion. To investigate their impact, a maneuver is introduced in the maneuver-free scenario described in Table 6.1. Even if any maneuver could in principle be used, the main drivers during a rendezvous concern the mission safety and propellant consumption. For IROD, it is tempting to seek for the smallest maneuver able to improve observability given the intersatellite satellite separation and the sensor noise. Since the drift of the formation is unknown at this stage, it is preferable to execute cross-track maneuvers which will not put the formation at a risk.
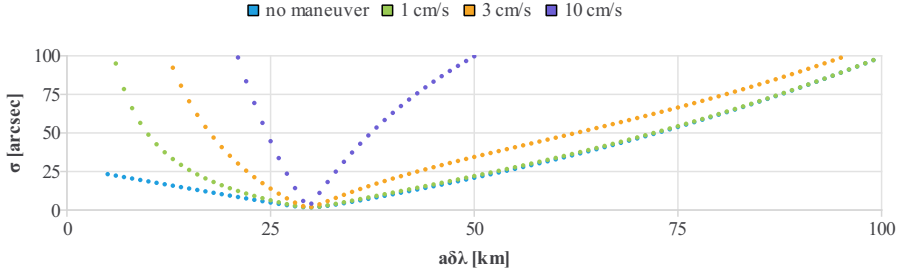
Figure 6.5: Improvement of observability due to the execution of cross-track maneuvers.

Cross-track maneuvers of different sizes are executed to analyze their effect on the IROD. Their locations do not influence the results, thus each maneuver has simply been executed 100 minutes after the simulation start. Their magnitude is instead of relevance, because this is directly related to the amount of nonhomogeneity introduced in the relative motion model. Figure 6.5 indicates that, at 30 km separation, a 3 cm/s maneuver can already greatly improve the steepness of the residual curve. Note that a known and predictable perturbation (for example solar radiation pressure or differential drag) will have a similar effect, as long as it can be accurately modeled.

• **Sensor noise**. Increasing noise of the line-of-sight measurements flattens the residual curve, and is thus the biggest challenge for the IROD. Figure 6.6 depicts the effect of measurement noise, obtained by introducing measurement noise in the scenario described in Table 6.1. It can be noticed that a small noise level of 15" already causes a significant flattening of the curve, thus diluting the accuracy of the solution.

Figure 6.6: Impact of sensor noise on the residual curve.

During a rendezvous, the noise will depend on the camera characteristics but also on the size of the imaged target (thus on the separation and target characteristics). As rule of thumb, the noise decreases when the image of the target increases, since the centroiding function in charge of 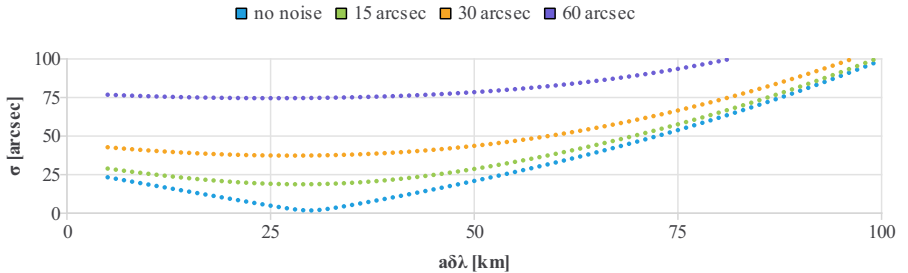measuring the position of the center of mass is more precise when the image is spread over more pixels (this is not true anymore at mid-range where the image of the target cannot be considered anymore as a Gaussian point spread function [109]). In case of larger measurement noise, it will be necessary to increase the observation time span to counterbalance the flattening effect introduced by the sensor noise. As depicted in Fig. 6.1, the presence of measurement noise not only flattens the residual curve but also upshifts it. This is due to the fact that, even when reaching the true scale factor μ_2, the residual value $\sigma_{\mu 2}$ cannot decrease below the standard deviation of the measurement noise.

- **Formation configuration**. The configuration of the formation also plays a role in the overall observability. It would be out of the scope of this research to investigate all the possible configurations. For the sake of this analysis, only $a\delta\lambda$ is changed, keeping the other relative orbital elements constant. Such assumption does not represent a limitation in the validity of the analysis, but rather reflects the fact that a slowly drifting (anti-)parallel $\delta e/\delta i$ configuration trajectory is the operationally safest way to rendezvous a noncooperative target. Figure 6.7 shows that, when staying in the same order of magnitude of several tens of kilometers, the increasing separation slightly flattens the curve, but this effect is not as pronounced as the ones described above.
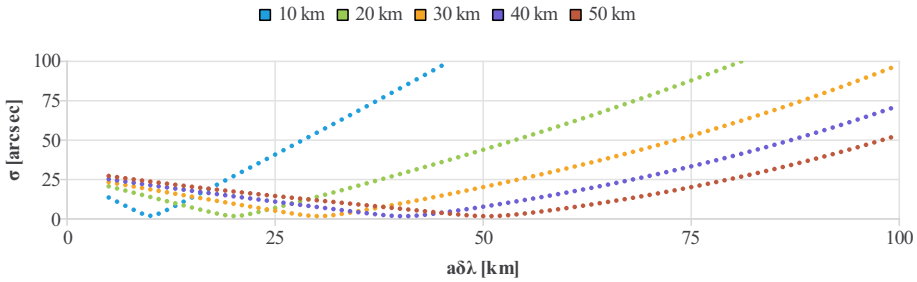
Figure 6.7: Impact of the intersatellite separation on the residual curve.

6.3. Demonstration using Flight Data

6.3.1. Selection of the Representative Cases

The demonstration cases presented in this section aim at validating the above-described method using flight data from the ARGON and AVANTI experiments. Unfortunately, very few data arcs could be exploited. The ARGON experiment was short (four days) with frequent maneuvers and several data outages due to the limited onboard data storage capability. As a result, only two representative maneuver-free data arcs could be extracted. The AVANTI experiment was much longer (more than two months of observations) and offers numerous interesting data arcs to exercise IROD. However, it suffers from the fact

that no reference exists for the relative state (since the Target spacecraft was fully nonco-operative) except for the one-day-long radar-based campaign (*c.f.*, Section 4.4.3). Consequently, it was possible to only extract one single demonstration case from the AVANTI experiment for which an external reference is available.

6.3.2. 5H-LONG ARC RECONSTRUCTION WITH FULL VISIBILITY (ARGON)

The IROD is performed using a 5h-long (or three orbits) maneuver-free data arc on April 24th, 2012. At that time the chaser and target are separated by about 30 km. The two models described in Section 6.2.1 are investigated to create the residuals plots in Fig. 6.8, represented by two different colors. The solution to the IROD corresponds to the measurement fitting which exhibits the smallest residuals. This global minimum is graphically identified by a large round marker of the same color as the corresponding curve.
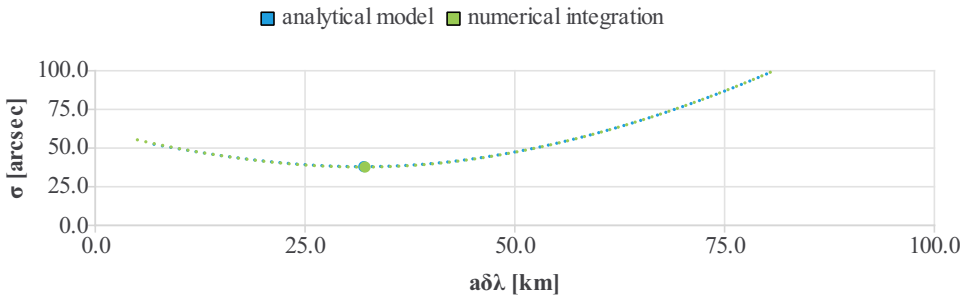
Figure 6.8: Solution for the 5h-long maneuver-free ARGON case.

Table 6.2 summarizes the solutions found using both models, as well as the reference relative state derived with relative GPS. Table 6.2 indicates that both models exhibit similar performance, accurate to less than 10 %. However, the numerical model comes at the cost of much larger computational time. On a desktop computer equipped with a Core i5 processor clocked at 2.6 GHz, a few dozen seconds are typically required to derive the solution based on the analytical model while the numerical integration can take more than one hour, depending on the number of measurements and iterations required for the least-squares adjustments.

Table 6.2: Solution $a\delta\boldsymbol{\alpha}$ for the 5h-long ARGON case.

Reference	[-21 -29568 -51 -395 -4 295] m
Analytical model	[-20 -32000 -55 -429 -4 317] m
Numerical propagation	[-21 -32146 -56 -430 -4 319] m

The similarity of the results can be explained by the fact that both models are more or less equivalent in this case. The differential drag at the altitude of PRISMA (750 km) is weak and the short observation time limits as well its effects. In both cases, the longitudinal (along-track) accuracy of the solution is equivalent to the one of TLEs (a few km). The lateral (radial + cross-track) accuracy outperforms the TLEs by one order of magni-

tude (it is indeed not uncommon for TLEs to exhibit cross-track errors of a few hundred meters [102]). For completeness, the observation residuals (parameterized in terms of right-ascension α and declination δ) corresponding the selected solution are depicted in Fig. 6.9. It can be seen that, thanks to the dusk-dawn orbit of the PRISMA satellites, the measurements are homogeneously distributed over time.

Figure 6.9: Residuals of the orbit determination corresponding to the solution for the 5h-long ARGON case.

6.3.3. 14H-LONG ARC RECONSTRUCTION WITH FULL VISIBILITY (ARGON)

If more time is available to collect measurements, it might be judicious to extend the observation arc to improve the observability (as depicted in Fig. 6.3). The second study case comes again from the PRISMA mission, but spans now 14 h or 9 orbits (April 25th 2012, from 2:00 to 14:00 UTC). At that time, the chaser and target are separated by 23.5 km. As expected, Figure 6.10 shows that the steepness of the residual curve is much more pronounced, leading to a more accurate solution.
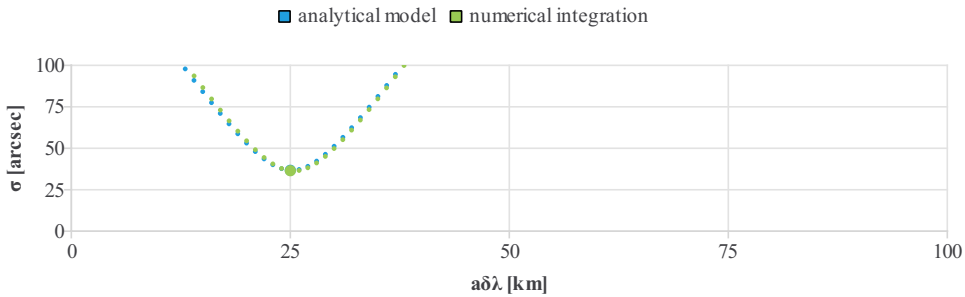
Figure 6.10: Solution for the 14h-long maneuver-free ARGON case.

The steepness of the curve is consistent with the one derived per simulation for a ten-orbit-long data arc in Fig. 6.3. An exact match is, however, not possible, since the shape of the curve depends on the number of measurements, on the formation configuration, and on the measurement noise, which all slightly differ from the simulation parameters described in Table 6.1.

Table 6.3 indicates that the range ambiguity can be determined with an error of less than 5%. In such a case, the result from the IROD clearly outperforms a solution derived from TLEs.

Table 6.3: Solution $a\delta\alpha$ for the 14h-long ARGON case.

Reference	[-131 -23650 -20 -303 -4 247] m
Analytical model	[-140 -25000 -21 -319 -5 261] m
Numerical propagation	[-139 -25002 -21 -319 -5 261] m

As depicted in Fig. 6.11, a large data gap (7 hours) affects the observations, but this is not an issue as long as the measurements are located at the beginning and at the end of the data arc.
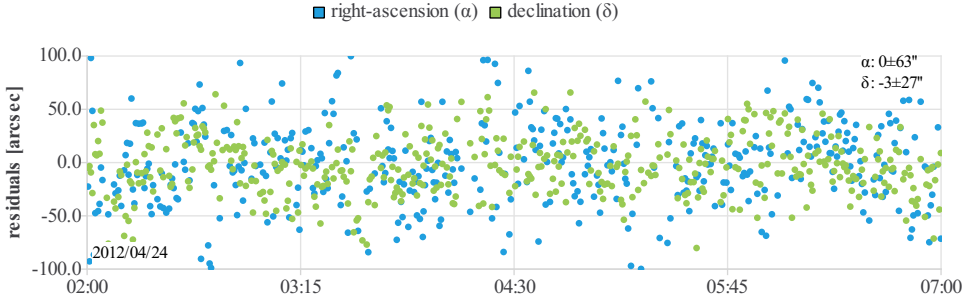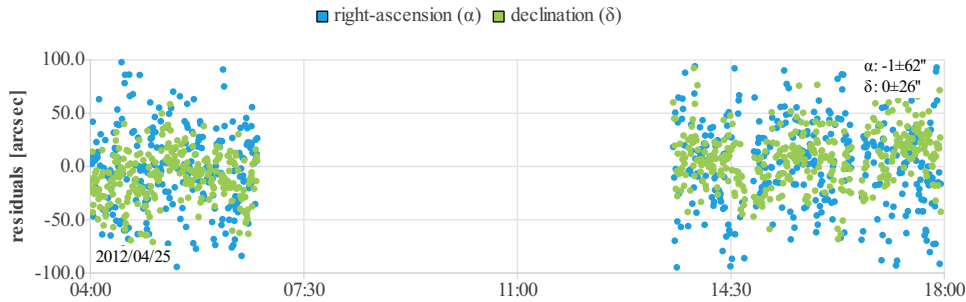

Figure 6.11: Residuals of the orbit determination corresponding to the solution for the 14h-long ARGON case.

6.3.4. 18H-Long Arc Reconstruction with Poor Visibility (AVANTI)

The same method is now applied to a data arc coming from the AVANTI experiment. The collection of observations starts on October 20th, 2016 22:00 UTC when the satellites are separated by 45 km. Due to the poor visibility conditions encountered during AVANTI, this case is much more challenging because only 10 minutes of observations are available every orbit. According to the preliminary investigations done in Section 6.2.2, the residual curve is expected to be extremely flat due to the limited visibility (*cf.* Fig. 6.4) and to the larger distance (*cf.* Fig. 6.7). In order to counterbalance this flatness, it is necessary to extend the observation time span: the data arc has thus been extended to span 18 h (11 orbits). Figure 6.12 depicts the residual plot obtained using the numerical and analytical models.
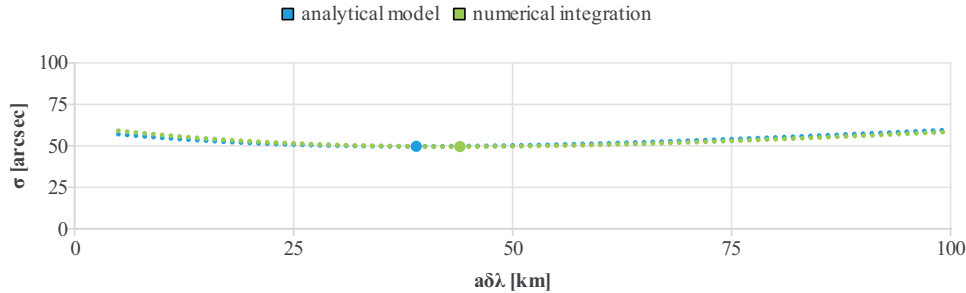
Figure 6.12: Solution for the 18h-long AVANTI case.

In view of the difficulty to estimate the drag of a noncooperative object, this perturbation has been first disabled in the numerical model. Both models exhibit a very similar residual curve. However, its extreme flatness makes an accurate determination of the global minimum very challenging: a difference of 10% can be observed in Table 6.4 between both solutions. The reference solution is derived from the ground-based radar observations and is expected to be accurate to 10 m. It can be tempting to include the perturbation due to the differential drag to improve the observability. Since a reference trajectory is available for the target, it is possible to estimate empirically the drag coefficient of the target.
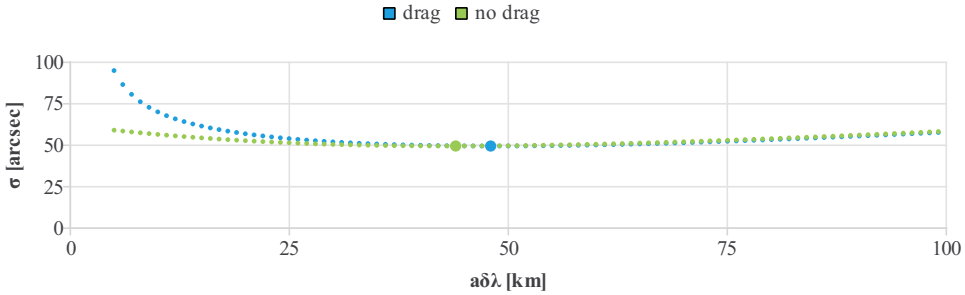
Figure 6.13: Solution found by enabling and disabling the drag.

Figure 6.13 depicts the results obtained by including the drag. As expected, the residual curve is steeper when considering this perturbation but the improvement is unfortunately too weak at this intersatellite distance to really enhance the accuracy of the solution. In fact, Table 6.4 indicates that the solution found by activating the differential drag is even less accurate. However, this does not allow drawing any conclusion, because the apparent better performance of the drag-free solution is probably due to the uncertainties in finding the minimum of a flat curve.

Table 6.4: Solution $a\delta\boldsymbol{\alpha}$ for the AVANTI case.

Reference	[84 44786 155 609 -8 714] m
Analytical model	[68 39000 137 533 -10 625] m
Numerical propagation (no drag)	[78 43953 152 614 -12 704] m
Numerical propagation (with drag)	[89 48947 164 696 -14 782] m

The orbit determination residuals are finally depicted in Fig. 6.14, highlighting the challenging sparsity of the measurement distribution.
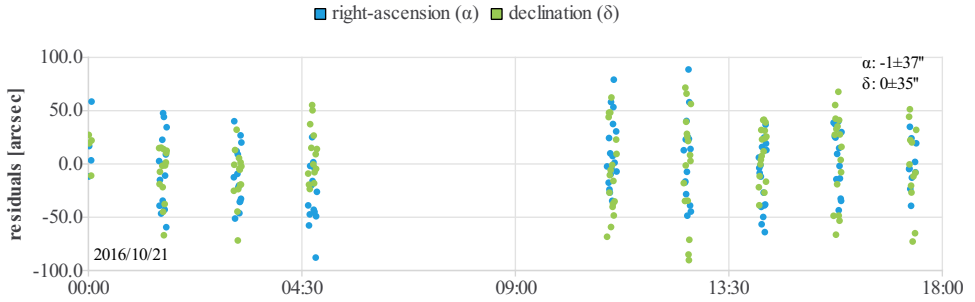
Figure 6.14: Residuals of the orbit determination corresponding to the solution for the AVANTI case.

6.4. FAST METHODS FOR ONBOARD IMPLEMENTATION

The method proposed so far is performing well. However, since it relies on a systematic search over a given range of the scaling factor μ (or for more convenience of the intersatellite separation), it might be too time-consuming for some onboard applications with limited computational resources. This section intends to explore possible faster alternatives. To that end, it is first necessary to first set up the mathematical foundations which will be used to derive faster IROD algorithms.

6.4.1. CONVEXITY OF THE RESIDUAL FUNCTION

CURVATURE OF THE ORBITAL PATH AS MAIN SOURCE OF NONLINEARITY

The algorithm described in Section 6.1.3 relies on the fact that the residual curve $\sigma(\mu)$ is convex and reaches its minimum for $\mu = \hat{\mu}$, where $\hat{\mu}$ is the value corresponding to the solution yielding the global minimum of the loss function J. Unfortunately this behavior is not always true for an arbitrary loss function $J(\boldsymbol{x})$ (for example if J were depending on $\cos^2 \mu$). Thus, the empirically observed convexity of the residual function has to be linked to the nature of the problem under consideration. For simplicity, the minimum $m(\mu)$ of the loss function J will be now investigated instead of the residual curve $\sigma(\mu)$. This is justified by the fact that m is convex if and only if σ is convex, *cf.* Eq. 6.6.

In order to analyze the behavior of this minimum, an analytical formulation of the problem is required. Unfortunately, the minimum $m(\mu)$ is the result of an iterative nonlinear least-squares estimation and cannot be analytically described. Thus the problem needs to be simplified and reshaped to reach a formulation for which an analytical expression of the minimum can be found.

The investigations done so far relied on the fact that the nonlinearities with respect to Eq. 3.31 were responsible for the weak observability. This section intends to focus more specifically on the main nonlinear contribution. In fact, it has to be distinguished if the nonlinearities are due to:

1. the first order linearization done when deriving the relative motion model;

2. the neglect of the curvature of the orbital path.

These effects can be isolated and thus individually quantified by adopting a specific parameterization of the relative state $\boldsymbol{x}$. In fact, the curvature of the orbital path can

be taken into account by using a set of relative orbital elements or a set of curvilinear Cartesian components to describe the vector $\boldsymbol{x}$. In this case, the relative motion model $\boldsymbol{f}$ describes the time evolution of the state vector (and thus deals with the possible approximations due to the linearization of the relative motion model) while the function $\boldsymbol{g}$ maps the relative state vector $\boldsymbol{x}$ into a rectilinear Cartesian relative position, thus capturing the effect of the curved orbital path.

A linear model describing the time evolution of the curvilinear Cartesian relative state vector is now adopted. As seen later, compared to a parameterization based on relative orbital elements such as the one described in Section 3.2.4, this choice is driven by the fact that a simpler $\boldsymbol{g}$ function is subsequently obtained. An alternative precise linear model using a curvilinear Cartesian state is thus needed for the sake of the demonstration. Two options are investigated: the curvilinear Hill-Clohessy-Wiltshire (HCW) [79] and Gim-Alfriend [81] models. The latter is in fact based on relative orbital elements but provides a linear mapping $\boldsymbol{T}$ to transform the orbital elements into a curvilinear Cartesian state representation:

$$\boldsymbol{x}(t) = \boldsymbol{T}(t)\boldsymbol{D}(t)\boldsymbol{\varphi}(t, t_0)\boldsymbol{D}^{-1}(t_0)\boldsymbol{T}^{-1}(t_0)\boldsymbol{x_0} = \boldsymbol{\Phi}(t, t_0)\boldsymbol{x_0}, \qquad (6.9)$$

where $\boldsymbol{\varphi}$ is the state transition matrix based on mean relative orbital elements and $\boldsymbol{D}$ the transformation matrix between mean and osculating elements. Note that, in near-circular orbits, $\boldsymbol{\varphi}$ is equivalent to the state transition matrix of the model described in Section 3.2.4. The benefits of the Gim-Alfriend formulation in terms of accuracy lie in the mapping matrix $\boldsymbol{T}$, which is more accurate than the matrix $\boldsymbol{C}$ described by Eq. 5.7.
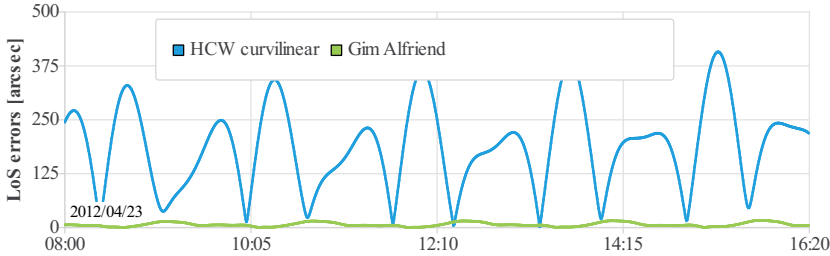
Figure 6.15: Line-of-sight (LoS) errors introduced by the model deficiencies.

In order to quantify the nonlinearities neglected by the linear motion models, the same approach used to create Fig. 6.2 is employed: both models are fitted against an accurate nonlinear reference model and the difference in terms of line-of-sight errors is analyzed. Figure 6.15 shows that the angular errors introduced by the curvilinear HCW model are large despite the modeling of the curvature of the orbital path. This is due to the fact that this simple model does not take the effect of J_2 into account, thus resulting in unacceptable errors. Obviously this model is not adapted to distinguish small differences at arcsecond level resulting from nonlinearities. On the contrary, the Gim-Alfriend model behaves much better, because it includes in the state transition matrix a linear model for the effect of J_2. Using this model, the line-of-sight errors introduced by the model deficiencies over several orbits are below the sensor noise and thus cannot be

observed. Therefore, it does not make any observable difference to use a state transition matrix $\boldsymbol{\Phi}$ instead of a nonlinear model $\boldsymbol{f}$ to describe the time evolution of the relative state vector $\boldsymbol{x}$. The Gim-Alfriend model deficiencies can thus be treated together with the sensor noise. Consequently, it can be assumed that it is mainly the curvature of the orbital path which introduces observability.

QUADRATIC REFORMULATION OF THE NONLINEAR ANGLES-ONLY NAVIGATION PROBLEM
Using a linear relative motion model, the general nonlinear measurement equation described by Eq. 3.30 for noiseless measurements:

$$\boldsymbol{u}_i \times \Delta \boldsymbol{r}(t_i) = \boldsymbol{u}_i \times \big(\boldsymbol{g}(t_i, \boldsymbol{f}(t_i, \boldsymbol{x}_0), \boldsymbol{y}_c(t_0)) \big) = \boldsymbol{0}, i \in [1, n] \tag{6.10}$$

can be simplified to:

$$\boldsymbol{u}_i \times \big(\boldsymbol{g}(t_i, \boldsymbol{\Phi}(t_i, t_0) \boldsymbol{x}_0) \big) = \boldsymbol{0}, i \in [1, n]. \tag{6.11}$$

In the sequel, it is now assumed that the curvilinear relative state is expressed in the orbital frame and that the components are ordered in the Radial-Tangential-Normal sequence. For the rendezvous problem under consideration (that is, the relative motion is mainly an along-track separation), the rectilinear relative position $\Delta \boldsymbol{r}$ can be approximated from the curvilinear relative position $\Delta \check{\boldsymbol{r}}$ as:

$$\Delta \boldsymbol{r} \approx \Delta \check{\boldsymbol{r}} + \begin{pmatrix} R - \sqrt{R^2 + \Delta \check{r}_2^2} \\ 0 \\ 0 \end{pmatrix}, \tag{6.12}$$

where R is the radius of the circular orbit and $\Delta \check{r}_2$ denotes the along-track component of the relative position. Noting that $R \gg \Delta \check{r}_2$, this simplifies to:

$$\Delta \boldsymbol{r} \approx \Delta \check{\boldsymbol{r}} + \begin{pmatrix} -\frac{\Delta \check{r}_2^2}{2R} \\ 0 \\ 0 \end{pmatrix}. \tag{6.13}$$

Let the state transition matrix be split into two blocks such as $\boldsymbol{\Phi} = \begin{pmatrix} \boldsymbol{\Phi}_{1\text{-}3,1\text{-}6} \\ \boldsymbol{\Phi}_{4\text{-}6,1\text{-}6} \end{pmatrix}$ and let $\boldsymbol{\Phi}_{2,1\text{-}6}$ denote the second row of the matrix $\boldsymbol{\Phi}$. Noting that $\Delta \check{\boldsymbol{r}} \approx \boldsymbol{g}(\boldsymbol{x}) = \boldsymbol{g}(\boldsymbol{\Phi} \boldsymbol{x}_0) = \boldsymbol{\Phi}_{1\text{-}3,1\text{-}6} \boldsymbol{x}_0$, Eq. 6.11 takes the form

$$\boldsymbol{u}_i \times \left(\boldsymbol{\Phi}_{1\text{-}3,1\text{-}6} \boldsymbol{x}_0 - \frac{1}{2R} \begin{pmatrix} 1 \\ 0 \\ 0 \end{pmatrix} \boldsymbol{x}_0^T \boldsymbol{\Phi}_{2,1\text{-}6}^T \boldsymbol{\Phi}_{2,1\text{-}6} \boldsymbol{x}_0 \right) = \boldsymbol{0}, i \in [1, n]. \tag{6.14}$$

Thus, with respect to the general nonlinear formulation of Eq. 6.10, the problem has been simplified to the minimization of a quadratic function. The quadratic part $\boldsymbol{q}$, corresponding to the model of the curvature of the orbital path, is now introduced for simplification:

$$\boldsymbol{q}(\boldsymbol{x}) = -\frac{1}{2R} \begin{pmatrix} 1 \\ 0 \\ 0 \end{pmatrix} \boldsymbol{x}^T \boldsymbol{\Phi}_{2,1\text{-}6}^T \boldsymbol{\Phi}_{2,1\text{-}6} \boldsymbol{x}. \tag{6.15}$$

Analytical Expression of the Minimum of the Loss Function

The quadratic formulation obtained in Eq. 6.15 is used in what follows to model the residual function depicted in Fig. 6.1. For this purpose, it is useful to recall that this residual function is obtained by performing nonlinear least-squares estimations around a series of linear solutions $\hat{x}_0^\mu$. Thus, a mathematical formulation of the linear solution $\hat{x}_0^\mu$ is first needed to derive an expression of the residual function. As explained in Section 6.1.3, the adimensional scale factor μ can equivalently be replaced by the dimensioned component μx_0^l of the state vector, for which a physical range can be more intuitively derived. Without loss of generality, this component of the state vector is arbitrarily chosen to be the last one in order to ease the following developments. In order to further simplify the notations, μ is used in the sequel for the dimensioned component μx_0^l. Using this convention, the initial state vector x_0 is parameterized as $x_0 = (\tilde{x}_0, \mu)$. Starting from Eq. 6.14 and neglecting the quadratic part, an approximate relation is obtained:

$$u_i \times \left(\Phi_{\text{1-3,1-6}} \cdot x_0 \right) = 0, \, i \in [1, n] \tag{6.16}$$

which expands to:

$$u_i \times \left(\Phi_{\text{1-3,1-5}} \cdot \tilde{x}_0 \right) = -\mu u_i \times \Phi_{\text{1-3,6}}, \, i \in [1, n] \tag{6.17}$$

where $\Phi_{\text{1-3,1-6}} = \left(\begin{matrix} \Phi_{\text{1-3,1-5}} & \Phi_{\text{1-3,6}} \end{matrix} \right)$ has been split into two blocks. After accumulating n measurements, a linear system is obtained, identified by the subscript L which denotes the linear problem:

$$A_{\text{L}} \tilde{x}_0 = \mu b_{\text{L}} \tag{6.18}$$

whose 5-dimensional solution is given in a least-squares sense by:

$$\hat{\tilde{x}}_0^\mu = \mu (A_{\text{L}}^T A_{\text{L}})^{-1} A_{\text{L}}^T b_{\text{L}} = \mu A_{\text{L}}^+ b_{\text{L}} \tag{6.19}$$

where A_{L}^+ is the Moore–Penrose pseudoinverse already introduced in Eq. 3.36. Thus, the 6-dimensional linear solution $\hat{x}_0^\mu$ is a function of μ.

Having derived the expression $\hat{x}_0^\mu$ of the linear solution, it becomes possible to compute the residuals obtained in the vicinity of a given solution $\hat{x}_0^\mu$ when μ differs from the true value. For this purpose, the nonlinear least-squares estimation is approximated with a linear system, for which an expression of the loss function can easily be derived. In fact, since the nonlinear least-squares estimation described in Section 6.1.3 is done in the vicinity of the linear solution $\hat{x}_0^\mu$, it is legitimate to assume that the nonlinear solution x_0^μ will be close to the linear solution $\hat{x}_0^\mu$. By linearizing Eq. 6.14 around this linear solution, the following relation is obtained:

$$u_i \times \left(\Phi_{\text{1-3,1-6}} x_0 + q(\hat{x}_0^\mu) + \frac{dq}{dx_0} \Big|_{x_0 = \hat{x}_0^\mu} (x_0 - \hat{x}_0^\mu) \right) = \tag{6.20}$$

$$u_i \times \left(\Phi_{\text{1-3,1-6}} x_0 - \frac{1}{2R} \begin{pmatrix} 1 \\ 0 \\ 0 \end{pmatrix} \hat{x}_0^{\mu T} \Phi_{\text{2,1-6}}^T \Phi_{\text{2,1-6}} (2x_0 - \hat{x}_0^\mu) \right) = 0, \, i \in [1, n]. \tag{6.21}$$

The same approach used for Eq. 6.17 is now used to restrict the problem in a 5-dimensional

space:

$$\boldsymbol{u}_i \times \left(\boldsymbol{\Phi}_{1\text{-}3,1\text{-}5} - \frac{1}{R} \begin{pmatrix} 1 \\ 0 \\ 0 \end{pmatrix} \hat{\boldsymbol{x}}_0^{\mu T} \boldsymbol{\Phi}_{2,1\text{-}6}^{T} \boldsymbol{\Phi}_{2,1\text{-}5} \right) \cdot \tilde{\boldsymbol{x}}_0 =$$

$$\boldsymbol{u}_i \times \left(\mu \left(-\boldsymbol{\Phi}_{1\text{-}3,6} + \frac{1}{R} \begin{pmatrix} 1 \\ 0 \\ 0 \end{pmatrix} \hat{\boldsymbol{x}}_0^{\mu T} \boldsymbol{\Phi}_{2,1\text{-}6}^{T} \boldsymbol{\Phi}_{2,6} \right) + \boldsymbol{q}(\hat{\boldsymbol{x}}_0^{\mu}) \right), i \in [1, n]. \quad (6.22)$$

Using this formulation, the loss function can be minimized using a linear least-squares method. However it has to be recalled that, following this strategy, the minimum of $\sum_{i=1}^{n} \| \boldsymbol{r}(t_i, \boldsymbol{x}_0) \times \boldsymbol{u}_i \|^2$ would then be obtained instead of the minimum of the loss function $J = \sum_{i=1}^{n} \| \boldsymbol{h}(t_i, \boldsymbol{x}_0) \times \boldsymbol{u}_i \|^2$. Thus, Eq. 6.22 has to be divided by the norm of the relative position, which can be approximated as

$$r^{\mu} \approx \left\| \boldsymbol{I}_\text{r} \hat{\boldsymbol{x}}_0^{\mu} \right\| = \left| \mu \right| \left\| \boldsymbol{I}_\text{r} \boldsymbol{A}_\text{L}^{+} \boldsymbol{b}_\text{L} \right\| \quad (6.23)$$

where $\boldsymbol{I}_\text{r} = (\boldsymbol{I}_{3\times3} \quad \boldsymbol{0}_{3\times3})$ is the identity matrix returning only the relative position. After accumulating n measurements, another linear system is obtained:

$$\boldsymbol{A}(\mu)\tilde{\boldsymbol{x}}_0 = \boldsymbol{b}(\mu) \quad (6.24)$$

for which the minimum can be analytically computed. It is noted that $\boldsymbol{A}$ and $\boldsymbol{b}$ depend on μ because they are function of $\hat{\boldsymbol{x}}_0^{\mu}$. The minimum $m(\mu)$ of $\left\| \boldsymbol{A}(\mu)\tilde{\boldsymbol{x}}_0 - \boldsymbol{b}(\mu) \right\|^2$ is finally obtained introducing the solution $\hat{\tilde{\boldsymbol{x}}}_0^{\mu}$ in the loss function:

$$m(\mu) = \left\| \boldsymbol{A}(\mu)\hat{\tilde{\boldsymbol{x}}}_0^{\mu} - \boldsymbol{b}(\mu) \right\|^2 \quad (6.25)$$

$$= \left(\boldsymbol{A}(\mu)\hat{\tilde{\boldsymbol{x}}}_0^{\mu} - \boldsymbol{b}(\mu) \right)^T \left(\boldsymbol{A}(\mu)\hat{\tilde{\boldsymbol{x}}}_0^{\mu} - \boldsymbol{b}(\mu) \right) \quad (6.26)$$

$$= \boldsymbol{b}(\mu)^T \left(\boldsymbol{P}(\mu) - \boldsymbol{I} \right)^2 \boldsymbol{b}(\mu) \quad (6.27)$$

$$= \boldsymbol{b}(\mu)^T \left(\boldsymbol{I} - \boldsymbol{P}(\mu) \right) \boldsymbol{b}(\mu) \quad (6.28)$$

where the projection matrix $\boldsymbol{P}(\mu) = \boldsymbol{A}(\mu) \left(\boldsymbol{A}(\mu)^T \boldsymbol{A}(\mu) \right)^{-1} \boldsymbol{A}(\mu)^T$ has been introduced for simplicity. Note that the last equality results from the fact that a projection matrix is idempotent (*i.e.*, $\boldsymbol{P}^2(\mu) = \boldsymbol{P}(\mu)$), and so is the matrix $(\boldsymbol{I} - \boldsymbol{P}(\mu))$.

Convexity of the Loss Function

An analytical formulation of the minimum in the least-squares sense of the loss function for a given μ has now been derived. Its convexity has still to be demonstrated though. Deriving the analytical formulation of $\boldsymbol{P}(\mu)$ would be extremely tedious. Fortunately, it is possible to simplify Eq. 6.22 in order to approximate $\boldsymbol{A}(\mu)$ by considering that :

$$\left\| \boldsymbol{\Phi}_{1,1\text{-}5} \right\| \gg \frac{1}{R} \left\| \hat{\boldsymbol{x}}_0^{\mu T} \boldsymbol{\Phi}_{2,1\text{-}6}^{T} \boldsymbol{\Phi}_{2,1\text{-}5} \right\|. \quad (6.29)$$

This assumption is easily justified as $\boldsymbol{\Phi}_{2,1\text{-}6} \hat{\boldsymbol{x}}_0^{\mu}$ is the along-track component of the propagated linear solution using a linear relative motion model, which amounts to a few tens

of kilometers in the problem under consideration. R is instead the orbit radius. Consequently, the left part of the inequality is two orders of magnitude larger than the right part. Recalling that Eq. 6.22 has been divided by r^μ, this allows us to assume that $A(\mu)$ is inversely proportional to $|\mu|$ (*i.e.*, $A(\mu) \approx A/|\mu|$) and that $P(\mu) \approx AA^+$, which does not depend on μ anymore. Let $P = AA^+$ denote the approximated constant value for $P(\mu)$. The expression of $b(\mu)$ can be more easily derived. Inserting Eq. 6.19 in Eq. 6.22, the contribution b_i of a single measurement to the vector b is:

$$b_i = \frac{1}{|\mu| \, \|I_r A_L^+ b_L\|} u_i \times \mu \left(-\Phi_{1\text{-}3,6} + \frac{1}{R} \begin{pmatrix} 1 \\ 0 \\ 0 \end{pmatrix} \mu \left(A_L^+ b_L \right)^T \Phi_{2,1\text{-}6}^T \Phi_{2,6} \right)$$

$$- \frac{1}{|\mu| \, \|I_r A_L^+ b_L\|} u_i \times \frac{1}{2R} \begin{pmatrix} 1 \\ 0 \\ 0 \end{pmatrix} \mu^2 \left(A_L^+ b_L \right)^T \Phi_{2,1\text{-}6}^T \Phi_{2,1\text{-}6} A_L^+ b_L, \, i \in [1, n]. \quad (6.30)$$

Thus, the vector b can be expressed in the form:

$$b = \text{sign}(\mu)(b_1 + \mu b_2) \qquad (6.31)$$

and, by introducing for simplicity $M = (I - P)$, the minimum becomes

$$m(\mu) = b_1^T M b_1 + \mu^2 b_2^T M b_2 + 2\mu b_1^T M b_2. \qquad (6.32)$$

The convexity of the function $m(\mu)$ is verified using the second order derivative, which is positive because M is semi-definite positive, yielding $d^2 m(\mu)/d\mu^2 = 2b_2^T M b_2 \geq 0$. Consequently, the minimum function is convex and reaches its minimum for

$$\hat{\mu} = -\frac{b_1^T M b_2}{b_2^T M b_2}. \qquad (6.33)$$

Interestingly, an approximate value for $\hat{\mu}$ is analytically provided as byproduct. As described in the following section, this paves the way for faster IROD algorithms in case of limited computational resources (typically for onboard implementation). In this case, it is sufficient to choose an arbitrary value for μ and to retrieve, after linearization around the associated linear solution, the approximate value of $\hat{\mu}$ from Eq. 6.33.

6.4.2. ALTERNATIVE IROD ALGORITHMS
BINARY SEARCH
The convexity of the residual function in Eq. 6.32 makes it possible to replace the systematic search by a faster algorithm, based on gradient descent or binary search. In view of the flatness of the curve, a binary search is considered more robust to find the minimum of the residual function. The algorithm is very simple: starting from an interval $I_0 = [\mu_A, \mu_B]$, the derivative $m'(\mu)$ is evaluated at the points μ_A and $\mu_k = \frac{1}{2}(\mu_A + \mu_B)$. The computation of $m'(\mu)$ is done numerically by evaluating the minimum at μ and $\mu + h$ with $h \ll \mu$. The objective is to find an interval over which the sign of the derivative changes. Thus, if $m'(\mu_A)m'(\mu_k) < 0$, the interval will be restricted in the next iteration

to $I_k = [\mu_A, \mu_k]$ otherwise to $I_k = [\mu_k, \mu_B]$. The iteration stops if the size of the interval becomes smaller than a user-defined threshold. Consequently, four evaluations of $m(\mu)$ are required at each step but, because a solution is expected to be found within few steps, a substantial reduction of the number of relative orbit determinations is still achieved compared to the systematic search. Obviously, a nonlinear least-squares estimation based on an analytical model of the relative motion is mandatory when evaluating $m(\mu)$ to reduce the computational efforts. In order to further optimize the computational load, the approximate solution for $m(\mu)$ provided by Eq. 6.32 can be used instead of the nonlinear least-squares estimate. The computational complexity of both methods is similar to retrieve the least-squares solution. However, the nonlinear approach will typically require several iterations to achieve the convergence while the analytical solution given by Eq. 6.32 will be faster.

Exploiting the Model of the Residual Curve

The mathematical framework developed in Section 6.4.1 may also be used to derive analytical methods faster than the binary search. The most obvious approach consists in using Eq. 6.33 in an iterative way. Starting from an arbitrary μ_1, a value for $\hat{\mu}$ is obtained. This value might not be accurate enough because of the linearizations and approximations assumed when deriving Eq. 6.33. Thus, an updated value for the global minimum can be obtained by starting with $\mu_2 = \hat{\mu}$. The iterative process stops at iteration i when the difference between μ_i and $\hat{\mu}$ drops below a user-defined threshold. This process is named Curve Modeling Method (CMM) in the sequel.

Linear Matrix Method

The third approach is taken from [115]. This method consists in creating a 27-dimensional vector χ comprising the state vector x augmented by all the possible quadratic combinations of its components. If x_i denotes the ith component of x, χ can be written in the form of:

$$\chi = \left(\begin{array}{ccccccc} x_1 & ... & x_6 & x_1 x_1 & x_1 x_2 & ... & x_6 x_6 \end{array}\right)^T. \tag{6.34}$$

Eq. 6.14 can be rewritten as:

$$a_{i,1} x_1 + ... + a_{i,6} x_6 + a_{i,7} x_1^2 + a_{i,8} x_1 x_2 + ... + a_{i,27} x_6^2 = 0, i \in [1, n] \tag{6.35}$$

where $a_{i,j}$ is a 3-dimensional column vector. By accumulating n measurements, a linear system is obtained:

$$A\chi = 0. \tag{6.36}$$

where A is a $3n \times 27$ matrix formed by n vertically concatenated 3×27 matrices $A_i = [a_{i,1} ... a_{i,27}]$. Thus the solution of this linear problem belongs to the null space of A. If $\hat{\chi}$ is a solution of A then $\alpha \hat{\chi}$ belongs as well to the null space. It is now possible to exploit the fact that the components of χ are not independent to solve for the scaling factor α. In fact, the 7th component of χ has to be the square of the 1st component, etc. Thus, a solution to the problem must have the form:

$$\chi = \left(\begin{array}{ccccccc} \alpha \hat{\chi}_1 & ... & \alpha \hat{\chi}_6 & \alpha^2 \hat{\chi}_1^2 & \alpha^2 \hat{\chi}_1 \hat{\chi}_2 & ... & \alpha^2 \hat{\chi}_6 \hat{\chi}_6 \end{array}\right)^T. \tag{6.37}$$

Using this formulation, Eq. 6.36 becomes

$$\alpha \boldsymbol{A}_{1-3n,1-6} \begin{pmatrix} \hat{\chi}_1 \\ \hat{\chi}_1 \\ \vdots \\ \hat{\chi}_6 \end{pmatrix} + \alpha^2 \boldsymbol{A}_{1-3n,7-27} \begin{pmatrix} \hat{\chi}_1 \hat{\chi}_1 \\ \hat{\chi}_1 \hat{\chi}_2 \\ \vdots \\ \hat{\chi}_6 \hat{\chi}_6 \end{pmatrix} = \boldsymbol{0}, \qquad (6.38)$$

which can be rewritten in the form:

$$\alpha \boldsymbol{q} + \alpha^2 \boldsymbol{p} = \boldsymbol{0}, \qquad (6.39)$$

where $\boldsymbol{p}$ and $\boldsymbol{q}$ are computed by first solving Eq. 6.36 and then introducing the resulting solution $\hat{\chi}$ in Eq. 6.38. Excluding the trivial solution, the value α can finally be solved in the least-squares sense with

$$\alpha = -\frac{\boldsymbol{p}^T \boldsymbol{q}}{\boldsymbol{p}^T \boldsymbol{p}}. \qquad (6.40)$$

Ideally, the null space corresponds to an eigenvalue equal to zero. As described in [115], values slightly different from zero might be obtained in the presence of sensor noise. Thus, [115] advises to use a Singular Value Decomposition and to systematically compute 27 values of α corresponding to the 27 eigenvectors, yielding 27 different solutions. The final solution is obtained by computing the measurement residuals associated to each solution and retaining the solution yielding the smallest residuals. This process is called Linear Matrix Method (LMM) in what follows.

6.4.3. PERFORMANCE ASSESSMENT

The performance of each method is investigated using the three scenarios presented in Section 6.3 and summarized in Table 6.5. For each scenario, the reference based on an external independent sensor as well as the solution found in Section 6.3 using the series of least-squares are recalled to ease the comparison. The binary search method is performed using the nonlinear least-squares estimation of $m(\mu)$ and with the approximate value of $m(\mu)$ obtained using the linear least-squares solution of Eq. 6.32. Finally, the Curve Modeling and Linear Matrix Methods are investigated. The computational time required by each method is coarsely evaluated from sample runs on a desktop equipped with a Core i5 processor and is only intended to provide an order of magnitude. Higher values will be obtained in case of spaceborne embedded applications due to the limited computational power of onboard computers.

Table 6.5 indicates that all methods yield similar solutions for the ARGON scenarios, except for the LMM which results in a degraded solution in the 5h-long case. The CMM and LMM are two orders of magnitude faster than the series of least-squares, but failed to find a solution in the AVANTI case. Being based on exactly the same model as the series of least-squares approach, the nonlinear binary search yields almost identical results but is about one order of magnitude faster. The linear binary search is even faster but provides a degraded solution for the AVANTI case.

Obviously, the AVANTI case is more challenging for the IROD methods. Two methods failed: the value for $\hat{\mu}$ obtained during the first iteration by the CMM approach was negative, leading to a divergence in the next iterations. The solution yielding the smallest

Table 6.5: Performance comparison of the different methods applied to real in-orbit scenarios. The computational time is evaluated using a desktop computer with a Core i5 processor.

	Method	Solution [m]	Time [s]
ARGON 5h	Reference	[-21 -29568 -51 -395 -4 295]	-
	Series of least-squares	[-20 -32000 -55 -429 -4 317]	51
	Binary search (nonlinear)	[-20 -32100 -55 -429 -5 318]	8
	Binary search (linear)	[-20 -32100 -53 -431 -6 325]	3
	Curve Modeling Method	[-23 -30000 -50 -401 -5 302]	0.6
	Linear Matrix method	[-26 -24000 -80 -311 -5 240]	0.4
ARGON 14h	Reference	[-131 -23650 -20 -303 -4 247]	-
	Series of least-squares	[-139 -25000 -21 -315 -5 257]	70
	Binary search (nonlinear)	[-139 -24800 -21 -316 -5 258]	10
	Binary search (linear)	[-138 -24800 -20 -318 -6 263]	7
	Curve Modeling Method	[-138 -24700 -20 -316 -6 261]	0.7
	Linear Matrix Method	[-133 -24700 -20 -316 -6 261]	0.6
AVANTI 18h	Reference	[84 44786 155 609 -8 714]	-
	Series of least-squares	[68 39000 137 533 -10 625]	11
	Binary search (nonlinear)	[65 38000 132 522 -6 604]	2
	Binary search (linear)	[56 31888 113 419 -3 500]	0.3
	Curve Modeling Method	failed	-
	Linear Matrix Method	failed	-

residuals computed with the LMM yields very high residuals, indicating that this was an unrealistic solution. With respect to the ARGON cases, two major differences are affecting this scenario: a large unknown differential drag which is not taken into account by the models and very sparse measurements. In order to better isolate the contribution of these effects, two additional scenarios are simulated in the sequel. The first one consists of the 14h-ARGON case, for which only 10 minutes of measurements per orbit have been retained to simulate poor visibility conditions. The second one consists of the AVANTI scenario completed with additional simulated measurements, as if a dusk-dawn orbit was used. Table 6.6 summarizes the IROD performance obtained using these simulated cases.

The simulated ARGON case with reduced visibility posed some difficulties to the LMM, and to a lesser extent, to the linear binary search. Reciprocally, all methods are properly working for the AVANTI case with full visibility, which tends to indicate that the limited visibility is the main reason for the degraded performance and failure of some methods rather than the unmodeled differential drag. There is no obvious explanation for the degraded behavior in case of poor visibility. One hypothesis is that the linear mapping between mean and osculating elements within the underlying Gim-Alfriend model introduces some errors, which compensate when observing the full relative motion but introduce nonrecoverable systematic errors when observing only a small part of the motion.

As a conclusion, despite their low resource consumption, the success and performance of the alternative methods is not always guaranteed. Some care has thus to be

Table 6.6: Performance comparison of the different methods applied to simulated scenarios. The computational time is evaluated using a desktop computer with a Core i5 processor.

	Method	Solution [m]	Time [s]
ARGON poor visibility	Reference	[-131 -23650 -20 -303 -4 247]	-
	Series of least-squares	[-139 -25000 -19 -320 -5 257]	6.4
	Binary search (nonlinear)	[-137 -24800 -19 -319 -5 256]	1.2
	Binary search (linear)	[-157 -27861 -21 -349 -6 290]	0.2
	Curve Modeling Method	[-143 -25617 -19 -326 -6 267]	0.04
	Linear Matrix Method	failed	-
AVANTI full visibility	Reference	[84 44786 155 609 -8 714]	-
	Series of least-squares	[72 43000 149 589 -7 692]	276
	Binary search (nonlinear)	[72 42900 149 589 -7 692]	60
	Binary search (linear)	[77 44473 157 607 -3 704]	40
	Curve Modeling Method	[77 44200 157 604 -3 701]	8
	Linear Matrix Method	[86 46400 161 620 -4 730]	1.9

taken when utilizing these fast methods. The binary search based on nonlinear least-squares estimation seems to be the best compromise for onboard applications, combining good performance and robustness.

6.5. CONCLUSION

Despite the weak observability of the angles-only relative navigation problem, it is possible to perform an initial relative orbit determination in low Earth near-circular orbit without executing any maneuver, by observing, during a few orbits, the apparent motion of a target with a camera.

The proposed approach aims at exploiting the small discrepancies which can be observed between a linear relative motion model and the reality. The method consists in performing a series of least-squares adjustments at varying distances in the vicinity of a family of collinear solutions stemming from the linear theory. The solution of the problem is found by selecting the distance corresponding to the global minimum of the fitting residuals. In order to correctly perform, this method relies on relative motion models which can effectively capture these small differences. Two models are considered: an analytical model based on relative orbital elements which considers only J_2 and a numerical propagation for which additional perturbations can be included. De facto the proposed method consists in an oriented search in the solution space, where the search direction is determined by varying the relative range, which corresponds to one component of the state expressed in terms of relative orbital elements (*i.e.*, the relative mean longitude). Accordingly, this method does not have the elegance of a direct analytical solution and is computationally intensive. However, as compared to a numerical propagation of the relative motion, the use of an analytical model can reduce the computational time by two orders of magnitude without significant degradation of performance, making this method eligible for onboard implementation. Several approaches can be used to further reduce the computational efforts. Some analytical solutions for the IROD

problem even allow for a dramatic reduction of the computational time but might not always be robust in case of poor visibility. A reasonable compromise for onboard application consists in accelerating the derivation of the global minimum using a binary search method.

Different factors influence the accuracy of the solution, such as observation time span, visibility conditions, formation configuration, presence of additional maneuvers, and sensor noise. Consequently, it is difficult to outline a general performance index of the proposed methodology. Nevertheless its effectiveness has been proven by processing two different real data sets coming from the ARGON and AVANTI experiments. The obtained results show that this approach can at least achieve the same accuracy as offered by Two-Line-Element products.

6

7

REVISITING THE RELATIVE ORBIT DETERMINATION TASK

This chapter tackles the operational limitations encountered while performing angles-only relative orbit determination during the AVANTI and ARGON experiments. Thanks to the introduction of new tools based on the linear theory, key functionalities such as data screening or provision of an a priori solution are greatly improved, making the system operationally more sound.

7.1. Preprocessing Based on the Linear Solution

As described in the previous chapters, the relative orbit determination task during the ARGON and AVANTI experiments relied on a nonlinear batch least-squares process. This choice was motivated by the desire to reach the best possible accuracy. However, the less accurate linear solution can sometimes be of great help to tackle specific problems for which ultimate accuracy is not required. This section intends to do justice to the linear framework by employing it in a preprocessing stage to solve two major operational issues encountered during the conduction of AVANTI: the derivation of an *a priori* solution to initialize the nonlinear batch least-squares adjustment and the reliable data screening.

7.1.1. Problem Statement

Deriving an *a priori* solution to support the nonlinear batch least-squares estimation was shown to be a real challenge during AVANTI. As described in Chapter 3, the nonlinear least-squares method requires a coarse approximation x_0^{apr} of the state vector around which a linearization is performed. Thus, if the *a priori* solution deviates too much from the truth, the least-squares process might not converge. It was often difficult during AVANTI to derive an *a priori* solution valid for a several-days-long data arc, mainly because of the unpredictable large differential drag acting on the formation at low altitude but also because a small error in the estimated value for δa translates into very large along-track errors after several days. Thus, it was often not enough to start from a very good estimate x_0 of the relative state (coming for example from a previous successful estimation of the relative motion or from an initial relative orbit determination) to guarantee the success of a subsequent relative orbit determination over a new arc. An additional difficulty makes the problem even more arduous: when dealing with line-of-sight measurements, the size of the measurement residuals depends on the intersatellite distance which is likely to considerably vary during a rendezvous. The measurement residuals are the difference between the observations $z(t)$ and the modeled observations $\tilde{h}\left(t, x_0^{apr}\right)$.

A simple fictive example is depicted in Fig. 7.1 to better highlight the contribution of these two aspects. Let us suppose that a formation is defined at time t_0 by the following configuration : $a\delta\boldsymbol{\alpha}_0 = (0\ 40000\ 0\ 200\ 0\ 300)$ m. A 5 cm/s maneuver is executed in along-track direction at time t_0+5h to initiate a rendezvous. It is assumed that a good estimate for $a\delta\boldsymbol{\alpha}$ exists at the initial epoch t_0: $a\delta\hat{\boldsymbol{\alpha}}_0 = (2\ 41000\ 10\ 220\ -5\ 310)$ m. Let us also assume that, during a previous orbit determination, a mean value of the change rate of the relative semi-major axis due to the differential drag has been derived: $a\delta\hat{\dot{a}} = -1 \times 10^{-4} \mathrm{ms}^{-1}$. Together, these variables constitute the *a priori* initial relative state vector $\boldsymbol{x}_0^{apr}$. Let us finally suppose that the next relative orbit determination is performed by processing 4 days of data. If, during this time, the perturbation due to the differential drag varies by 20% (for example, $a\delta\dot{a} = -1.2 \times 10^{-4} \mathrm{ms}^{-1}$), an additional growing error in along-track direction will appear with respect to the relative motion predicted by the *a priori* solution. At the first glance, the propagated *a priori* solution depicted in Fig. 7.1 is still very close to the true relative motion and seems to be a suitable approximate solution for the nonlinear least-squares estimation. However, measurement residuals are rapidly growing during the rendezvous because the distance is also decreasing. As depicted in Fig 7.2, the residual values, which are below 100" at 40 km distance (a lateral error of about 30 m translates into 15" error at this distance), are increased by four orders of magnitude dur-
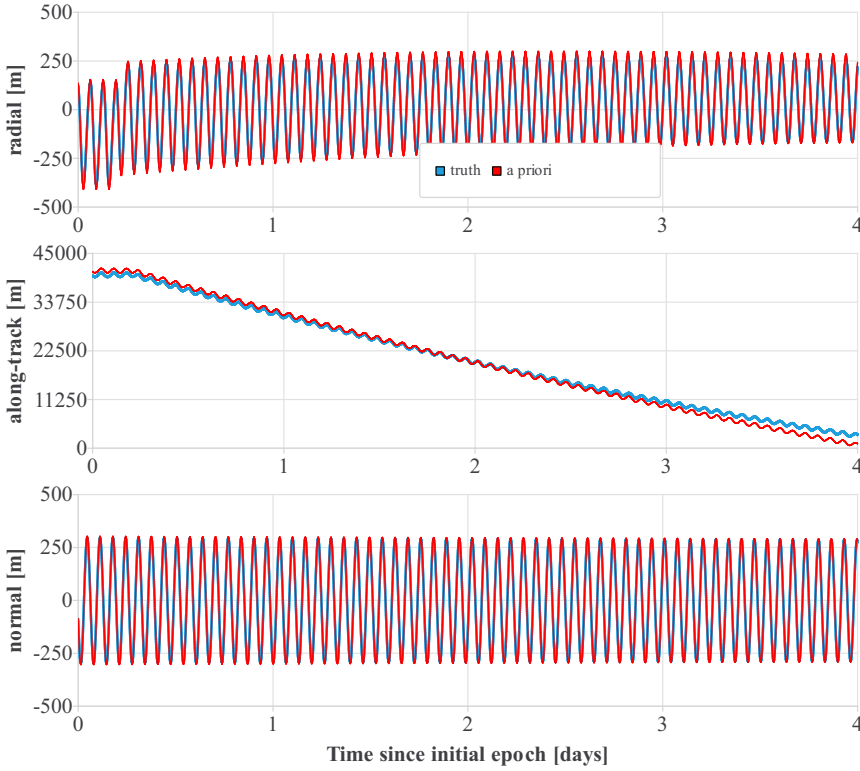
Figure 7.1: True vs. propagated *a priori* relative motion.

ing the rendezvous.

Even if the prediction of the relative motion is still accurate after four days (especially for the radial and cross-track components), the accumulated along-track error of about 2 km translates into very large line-of-sight errors because the final intersatellite separation (3 km) is of the same order of magnitude as the propagated errors. During AVANTI, the resulting very large discrepancy between modeled measurements derived from the *a priori* solution and observations often led to a filter divergence. The workaround used at that time was to manually refine by trial and error the *a priori* solution (and especially the predicted value for $a\delta\dot{a}$) to reduce this effect and finally reach the convergence.
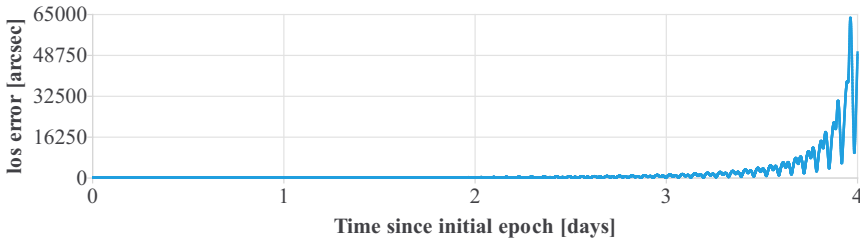

Figure 7.2: Measurement residuals obtained using the *a priori* solution x_0^{apr}.

7.1.2. SOLUTION FROM THE LINEAR THEORY

The aforedescribed problem can in fact be solved by deriving the *a priori* solution using the linear theory. As already mentioned, the execution of maneuvers is a simple means to improve observability. According to Eq. 3.22, the instantaneous change of relative orbital elements $\Delta\delta\boldsymbol{\alpha}$ due to an impulsive maneuver $\Delta\boldsymbol{V}$ executed at time t_M and argument of latitude u_M is described by the matrix $\boldsymbol{B}(u_M)$:

$$\Delta\delta\boldsymbol{\alpha} = \boldsymbol{B}(u_M)\cdot\Delta\boldsymbol{V}. \tag{7.1}$$

Thus, the augmented relative state vector $\boldsymbol{x}(t)^T = \left(\delta\boldsymbol{\alpha}(t)^T \quad \delta\dot{a}\right)$ is no more a linear function of $\boldsymbol{x}_0$ after the execution of the maneuver:

$$\boldsymbol{x}(t) = \boldsymbol{\Phi}(t,t_M)\left(\boldsymbol{\Phi}(t_M,t_0)\boldsymbol{x}_0 + \boldsymbol{B}_{\boldsymbol{x}}(u_M)\Delta\boldsymbol{V}\right), \tag{7.2}$$

where the matrix $\boldsymbol{B}_{\boldsymbol{x}}$ is directly derived from $\boldsymbol{B}$:

$$\boldsymbol{B}_{\boldsymbol{x}}(u_M) = \begin{pmatrix} \boldsymbol{B}(u_M) \\ \boldsymbol{0}_{1\times 3} \end{pmatrix}. \tag{7.3}$$

This can be generalized for the case of m maneuvers $\Delta\boldsymbol{V}_j$, $j \in [1,m]$, executed at mean argument of latitude $u_{M,j}$ and time $t_{M,j}$:

$$\boldsymbol{x}(t) = \boldsymbol{\Phi}(t,t_0)\boldsymbol{x}_0 + \sum_{i=j}^{m}\boldsymbol{\Phi}(t,t_{M,j})\boldsymbol{B}_{\boldsymbol{x}}(u_{M,j})\Delta\boldsymbol{V}_j. \tag{7.4}$$

Introducing this relation into Eq. 3.30 yields:

$$\boldsymbol{u}_i \times \boldsymbol{C}(t_i)\boldsymbol{\Phi}(t,t_0)\boldsymbol{x}_0 = -\boldsymbol{u}_i \times \boldsymbol{C}(t_i)\left(\sum_{j=1}^{m}\boldsymbol{\Phi}(t,t_{M,j})\boldsymbol{B}_{\boldsymbol{x}}(u_{M,j})\Delta\boldsymbol{V}_j\right), i \in [1,n]. \tag{7.5}$$

This solves the range ambiguity problem: if $\hat{\boldsymbol{x}}$ is solution of Eq. 7.5, $\mu\hat{\boldsymbol{x}}$ is not a solution anymore. By accumulating n measurements, a linear system of the form

$$\boldsymbol{A}\boldsymbol{x} = \boldsymbol{b} \tag{7.6}$$

can be built and a direct solution to the problem in the least-squares sense can be computed ($\hat{\boldsymbol{x}} = \boldsymbol{A}^+\boldsymbol{b}$, *cf.* Chapter 6). Note that this method was first formulated in [39] using the Hill-Clohessy-Wiltshire equations and was here adapted to relative orbital elements.

Obviously, this solution cannot compete in terms of accuracy with the result of a nonlinear estimation using more accurate models. In particular, the mapping matrix $\boldsymbol{C}$ is inaccurate and Eq. 7.5 does not take the curvature of the orbital path into account as seen in Chapter 6. Still, because the measurement residuals are minimized in a least-squares sense, this solution will prevent the advent of very large residuals depicted in Fig. 7.2 and can thus be used to improve the convergence of the nonlinear batch least-squares adjustment.

The scenario presented in Section 7.1.1 is now used as illustration. By collecting a set of error-free line-of-sight measurements every 30 s over four days, the following linear solution is obtained using Eq. 7.6: $a\delta\boldsymbol{\alpha}_0$ = (-71 8800 -52 53 1 88) m and $a\delta\dot{a}$ =

-1.3×10^{-6} m.s^{-1}. In this context, a linear solution means a solution derived from linear equations which neglect the curvature of the orbital path. This solution is far from accurate, mainly because the curvature of the orbital path is not taken into account, yielding a large offset in the relative semi-major axis. Still, as depicted in Fig. 7.3, it fulfills the primary objective of the preprocessing task by achieving a better conditioning of the residual vector. Note that, during this process, the measurement residuals at far-range are slightly degraded (to about 400") while the ones at close-range are dramatically reduced (to about 2500"), resulting in only one order of magnitude of difference.
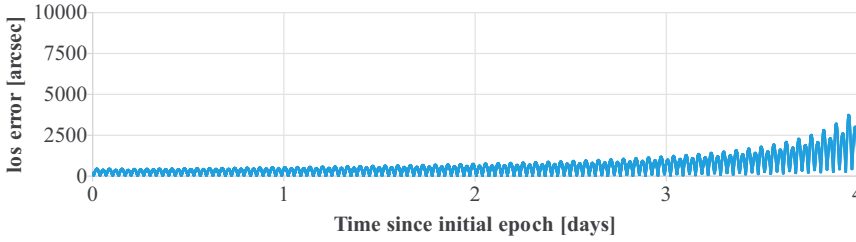

Figure 7.3: Measurement residuals obtained using the linear solution.

Note that this *a priori* solution has been derived without any additional *a priori* information. If a coarse knowledge of the intersatellite distance is available, either thanks to TLEs, or thanks to the IROD method described in Chapter 6, or thanks to a previous successful relative orbit determination, it is possible to further improve the quality of this *a priori* solution by introducing a coarse correction of curvature of the orbital path. Taking again as example the scenario of Section 7.1.1, it is possible to make use of the *a priori* solution depicted in Fig. 7.1 to obtain an estimate L of the intersatellite separation. Based on this coarse estimate, the curvature of the orbital path can be taken into account in the measurement equation. This can be done by introducing Eq. 6.13 into Eq. 7.5:

$$
\boldsymbol{u}_i \times \boldsymbol{C}(t_i)\boldsymbol{\Phi}(t,t_0)\boldsymbol{x}_0 = -\boldsymbol{u}_i \times \boldsymbol{C}(t_i)\left(\sum_{i=1}^{m} \boldsymbol{\Phi}(t,t_{\mathrm{M},i})\boldsymbol{B}_{\boldsymbol{x}}(u_{\mathrm{M},i})\Delta \boldsymbol{V}_i \right) + \boldsymbol{u}_i \times \begin{pmatrix} \frac{L^2}{2R} \\ 0 \\ 0 \end{pmatrix}, i \in [1,n].
$$

(7.7)

Here again, a linear system of the form $\boldsymbol{Ax} = \boldsymbol{b}$ is obtained that can be solved easily. Despite its simplicity, this small correction allows for a substantial improvement of the linear solution, especially for large intersatellite separations. The resulting linear solution becomes: $a\delta\boldsymbol{\alpha}_0 = $ (-4 39900 -24 235 2 304) m with $a\delta\dot{a} = -1.0 \times 10^{-4}$m.s^{-1}, which is much closer to the true formation configuration. The residual level is also further decreased as depicted in Fig. 7.4.

It has to be noted that the curvature of the orbital path mainly affects the far-range field (typically for intersatellite distances greater than 10 km). Operational experience (as described in the next sections) indicates, however, that for smaller separations this additional correction is not needed to ensure the convergence of the nonlinear least-squares method.
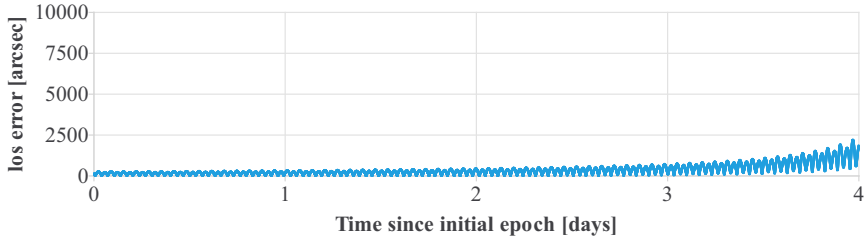
Figure 7.4: Measurement residuals obtained using the linear solution corrected for curved orbital path.

7.1.3. ROBUST DATA SCREENING

Relying on the linear solution can also be advantageous to filter out the outliers from a data set. The presence of bad data among a set of measurements is a common problem when dealing with estimation. Usually, this is mitigated in two ways: either one observation is obviously false, or it does not fit together with the other data. The outliers belonging to the first case can be simply discarded using an *a priori* solution. The corresponding rejection threshold depends on the uncertainties of this solution and on the expected measurement noise. The second case is more difficult and is often solved in an iterative way. In this case, all the measurements are apparently consistent with the *a priori* solution. In order to detect the bad observations, a solution more accurate than the *a priori* one is first computed using all the data. Then the standard deviation σ of the measurement residuals is evaluated and the observations whose residuals are larger than a threshold (typically σ or 3σ) are discarded.

This latter approach worked well for ARGON, because the number of healthy measurements greatly outnumbered the few outliers. For AVANTI instead, the very few observations collected every orbit made the solution very sensitive to any outlier. In fact, the above-described strategy can be applied in case of sporadic small outliers (for example if a star is almost collocated with the target and degrades the centroiding performance), but fails if another parasite object is simultaneously visible. This behavior can be better understood by simulating such an event using again the scenario of Section 7.1.1. In order to reproduce the poor visibility conditions of the AVANTI experiment, only the observations taken at a specific location of the orbit (at mean argument of latitude comprised in the interval [260° 300°]) are retained. A Gaussian noise (mean=0",standard deviation=30") is now applied to the measurements. In order to make the problem even more difficult, a larger data gap is introduced between 7 am and 3 pm during the first day. Figure 7.5 depicts the normalized coordinates of the measured target in the the virtual frame $\mathcal{V}$, as defined in Section 4.2.2. For clarity, only the measurements corresponding to the first 15 orbits have been depicted. Figure 7.5a depicts a scenario in which only the target is visible, that is, no outlier affects the data set. Figure 7.5b depicts the case in which a parasite object, flying on a similar orbit, crosses one time the field of view during the observation arc.

The detection of the parasite trajectory is trivial for a human being (the orientation of the arc is completely different from the orientation of the other trajectories), but is fairly difficult for an algorithm. A detection based on a coarse *a priori* solution is almost
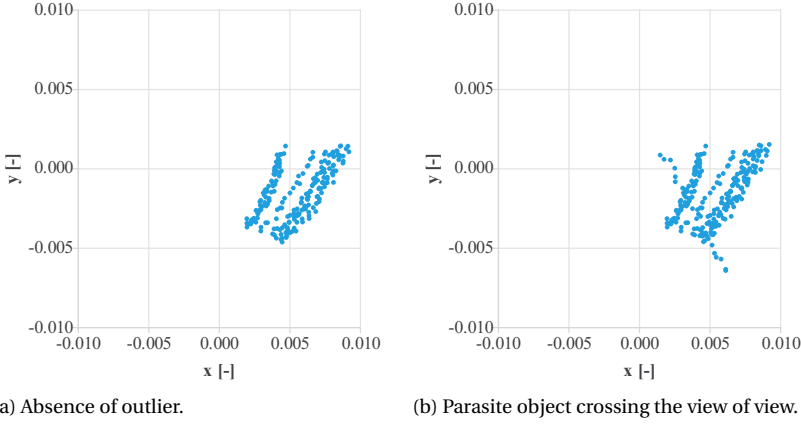
(a) Absence of outlier.   (b) Parasite object crossing the view of view.

Figure 7.5: Normalized coordinates of the target measured in the virtual frame $\mathcal{V}$.

impossible: the cross-track errors exhibited by TLEs can amount to 500 m. Reasoning in terms of normalized coordinates, this means that, at 40 km distance, a search area of radius $S = 500/40000 = 0.0125$ is used to discard the parasite trajectories, which exceeds the size of the plot. Thus, this parasite trajectory has to be discarded by recognizing that it is not compatible with the other measurements.

The experience collected during the AVANTI experiment shows that such an event does statistically not happen every orbit. Thus, one efficient data screening strategy consists in using several subarcs. In this case, it is possible to recognize that a data set is corrupted by the unusual high value of residuals compared to the other subarcs. Afterwards, the corrupted data set can be further either processed to exclude the outliers, or simply discarded. The main challenge of this strategy lies in the fact that a solution has to be computed for each subarc, in order to compute the measurement residuals and to be able to detect discrepancies between the subarcs. However, deriving a solution based on angles-only measurements requires a long data arc, possibly comprising several maneuvers, in order to reach enough observability.

In order to solve this dilemma, the approach adopted in this research consists in finding a solution in the 5 dimensional (5D) instead of the six dimensional (6D) space. The reason is simple: as depicted in Fig. 7.6a, when trying to solve the 6D problem using a corrupted data set, the least-squares estimation equally includes all observations, thus degrading the solution and enlarging the residual values of the good observation. As a result, it is not clear which observations are unhealthy from the values of the measurement residuals.

If the complete data arc is now subdivided into a series of small subarcs delimited by the execution of maneuvers, it becomes possible to make a series of least-squares adjustments without solving the range ambiguity over each subarc. To that end, it is only needed to arbitrarily set a value of the mean along-track separation (for example $a\delta\lambda = 1$ km), and estimate the other relative orbital elements using the method described by Eq. 6.8. No matter what is the actual intersatellite distance, the problem is

weakly observable, so that the measurement residuals will always stay very small. The residual budget is in fact composed of the sensor noise, the errors of the linear model, plus an additional contribution due to the unknown unmodeled curvature of the orbital path, which amounts to less than 50" for separations below 75 km. This approach makes the detection of outliers easier, as depicted in Fig. 7.6b, where the measurement residuals obtained using the 5D linear solution computed at fixed distance $a\delta\lambda = 1$ km are shown. Note that, in this example, only one maneuver is executed at time $t_0 + 5h$, resulting in two subarcs for the 5D data screening.
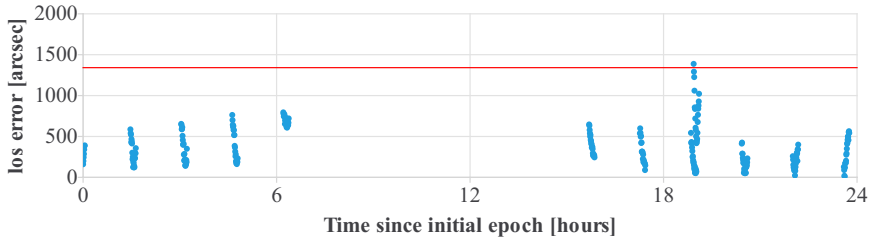
(a) 6D filtering.
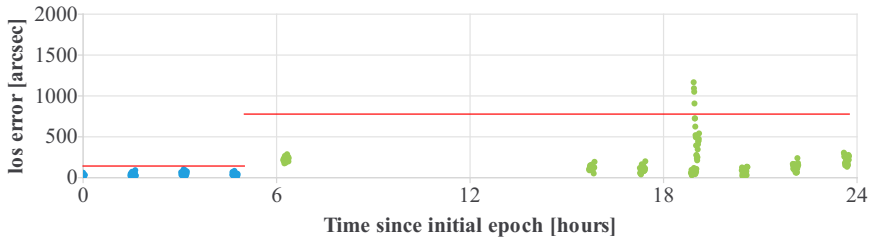
(b) 5D filtering.

Figure 7.6: Data screening based on measurement residuals. The horizontal red line corresponds to three times the standard deviation of the residuals.

In Fig. 7.6a and Fig. 7.6b, the horizontal red line corresponds to 3 times the standard deviation of the residuals. Thus, no outlier will be detected in the first case. On the contrary, when using several subarcs, it is easier to recognize that the first subarc is healthy and the second one not. Note that, since the standard deviation is computed at once using all data from a given data arc (*i.e*, over 5 h and 19 h in Fig. 7.6b), the data screening is independent from the history of the previous arc. Even more interesting: because shorter arcs are used, the residual value of the corrupted data arc is lower than when considering the whole data arc. Thus, it becomes possible to recover the healthy data from the corrupted data set: in a first iteration, the measurements above the red line are discarded, leading to a smaller value of the threshold for the second iteration, allowing for more rejections, until all the bad measurements are filtered out. Note that there is no guarantee that such a recovery works, but at least this task is made easier when using several subarcs. If the final residual level cannot allow for a clear statement regarding the success of the recovery action, it is advised to simply reject the whole subarc, thus

generating an additional data gap in the whole data set which is better than still using corrupted data.

Note that this approach also offers a simple strategy to delimit the subarcs for the data screening: the maneuvers done during the rendezvous constitute the boundaries of the subarcs. Thus, if n maneuvers are executed, $n + 1$ subarcs will be preprocessed as part of the data screening activities. Note that, at this point, the range ambiguity is not solved. Once the data screening has been done, a 6D solution can be computed using the method described in Section 7.1.2.

7.2. Fast and Robust Relative Orbit Determination

7.2.1. Improved Design

The tools and methods introduced in the previous Section can be used to greatly improve the relative orbit determination system presented in Chapter 4. A new design is proposed, aiming at reaching three objectives:

- **O1**: simplification of the interfaces;
- **O2**: improvement of robustness;
- **O3**: reduction of computational load.

Objective **O1** is realized by avoiding the usage of TLEs. In the previous design, TLEs were used to initialize the nonlinear batch least-squares method by providing an *a priori* solution. This coarse solution can now be derived either from the IROD strategy presented in Chapter 6 in case of maneuver-free data arc, or from the linear method presented in Section 7.1.2 if maneuvers are executed during the data arc under consideration. Objective **O2** takes advantage of the 5D data screening described in Section 7.1.3 and of the fact that a better *a priori* solution can now be derived beforehand, preventing the measurement residuals from reaching too high values during the orbit determination process. Finally, Objective **O3** is achieved by employing only analytical models instead of a numerical integration.

Figure 7.7 depicts the functional flow chart of the new angles-only relative orbit determination design, which now consists of an iterative preprocessing stage before nonlinear least-squares estimation. The kinematic target detection is identical to the one presented in Section 4.2.1. The only difficulty here is that this module better performs with some *a priori* guess of the relative motion in order to finely tune the parameter ϵ and to delimit the search radius S as defined in Section 4.2.1. An iterative process is the key to mitigate this issue. The arbitrary values $\epsilon = 10$ pixels and $S = 1000$ pixels are used for the first iteration. These settings are sub-optimal because they can lead to miss some target observations if the actual displacement is greater than ϵ (which might happen at close-range) and might lead to detect additional parasite objects because S is too high, thus endangering the integrity of the subsequent tasks. In the next iterations, once a solution has been derived, ϵ and S are refined to more efficiently search for the target based on its expected location. Since the kinematic target detection does not always perform well at close-range (due to the larger centroiding errors), an additional target detection based on evident brightness is made afterwards to find possible missing observations.

A robust 5D data screening is performed after the target detection for each maneuver-free subarc. Some of the data screenings will not be successful if too many parasite ob-
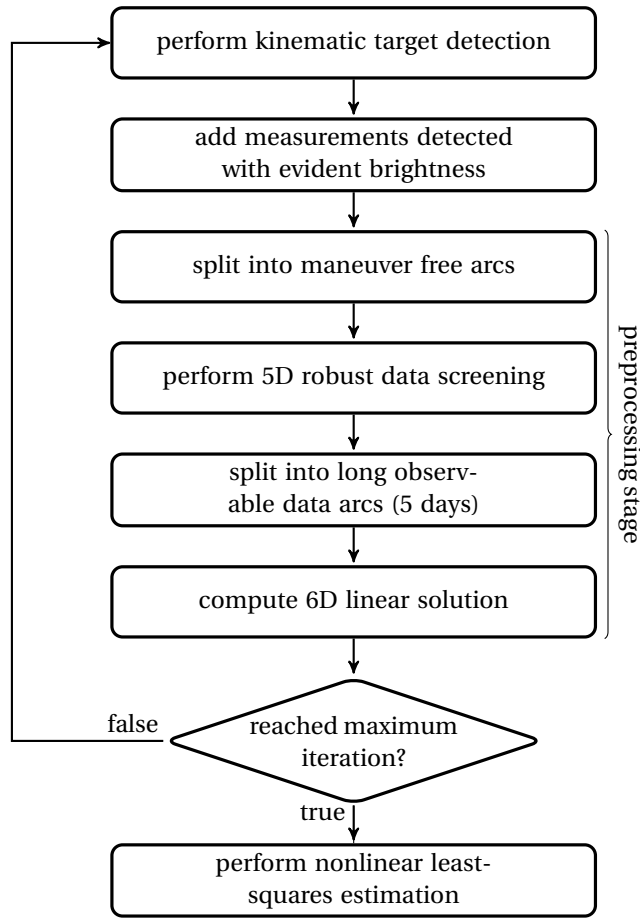
Figure 7.7: Design of fast and robust relative orbit determination.

jects are present in the data arc. In this case, no observation at all is delivered, so that the probability of healthy measurements stays very high.

From that point, a set of healthy but possibly sparse measurements is available. The next step consists in processing these observations over a longer data arc comprising maneuvers. Since this guarantees observability, a first 6D linear solution can be derived, which will be used for the next iteration. After some iterations, a set of healthy measurements together with a good reference solution are available. Note that, since the data screening and derivation of the *a priori* solution are based on analytical models, they are computationally-light and do not conflict with objective **O3**. Instead, they allow for the provision of a healthy data set and greatly increase the probability for a successful convergence of the nonlinear least-squares estimation, thus saving a considerable amount of time during the final step.

The final nonlinear least-squares estimation is now using the analytical relative motion model described in Section 3.2.4 to reduce the computational load. In order to fur-

ther improve the accuracy, the mean-to-osculating conversion required by the transformation chain depicted in Fig. 3.5 is done using the second-order theory for near-circular orbits of Ustinov with Eckstein corrections [116, 117], which is more precise than the Brouwer algorithm [84] used during AVANTI. An order of magnitude of the resulting reduction of the computational time can be obtained using a simple representative test: a relative motion is propagated during four days with a step of 30 seconds, corresponding to the frequency of observations using during the AVANTI experiment. This test is executed within about 20 s using a numerical integration of the relative equations of motion and relying on the numerical model described in Table 4.1. On the contrary, only 200 ms are necessary to propagate the relative motion and accurately model the measurements using the combination of the analytical model and of the nonlinear transformation depicted in Fig. 3.5. This test has been executed on a desktop computer with a Core i5 processor clocked at 2.6 GHz, and may yield slightly different results depending on the chosen integration method and accuracy settings. Still, it indicates that an improvement of two orders of magnitude is achieved.

Instead of estimating the inertial relative state vector and drag coefficient as described in Section 4.3.1, the state vector is now parameterized by means of relative orbital elements:

$$\boldsymbol{x}^T = \begin{pmatrix} \delta\boldsymbol{\alpha}^T & \delta\dot{a} \end{pmatrix}. \tag{7.8}$$

In fact, the estimation concept is similar to the onboard relative navigation filter, except that:

- a batch-least squares process is used instead of a sequential filter;
- the newest convention for the relative orbital elements $\delta\boldsymbol{\alpha}$ is used instead of $\delta\hat{\boldsymbol{\alpha}}$;
- the maneuvers are estimated beforehand;
- the transformation between mean and osculating elements is done using a more accurate algorithm.

Note that the IROD method developed in Chapter 6 has been kept as separated tool and is thus not included in the standard system design. Most of the time, observability is ensured thanks to the presence of maneuvers. Consequently, the IROD algorithm is in fact needed only once when initiating a rendezvous.

7.2.2. REPROCESSING THE AVANTI DATASET

The advantages of the improved design can be better demonstrated using the data from the AVANTI experiment, which was more affected by robustness issues than the ARGON experiment due to the already-mentioned unfavorable experimental conditions. The complete data set from the AVANTI experiment is now reprocessed, comprising 62542 images collected between 21 September and 28 November 2016. A total of 240 maneuvers have been executed during this time span. Table 7.1 illustrates how the target detection task is improved using an iterative process. For each iteration, the number of measurements successfully validated after 5D data screening is reported, followed by the total number of target detections. For clarity, the first 10 maneuver-free arcs are described in the table. Due to the high value of the search area S during the first iteration, some additional parasite objects are detected but could however be successfully discarded by the 5D data screening.

Table 7.1: Kinematic data detection and data screening. For each iteration, the number of measurements selected after 5D data screening is indicated, followed by the total number of measurements detected using the kinematic approach.

Data arc	Iteration 1	Iteration 2	Iteration 3
2016/9/21 14:33:26 - 2016/9/23 10:59:50	215/256	185/201	184/199
2016/9/23 10:59:50 - 2016/9/26 20:25:00	391/431	349/367	350/369
2016/9/26 20:25:00 - 2016/9/27 11:04:50	49/68	37/37	35/35
2016/9/27 11:04:50 - 2016/9/27 11:52:11	11/11	12/12	12/12
2016/9/27 11:52:11 - 2016/9/27 13:18:28	0/8	0/7	0/7
2016/9/27 13:18:28 - 2016/9/27 14:14:17	0/0	0/0	0/0
2016/9/27 14:14:17 - 2016/9/28 20:09:52	79/112	16/50	16/50
2016/9/28 20:09:52 - 2016/9/29 11:02:25	38/56	35/36	36/36
2016/9/29 11:02:25 - 2016/9/29 11:49:50	0/0	0/0	0/0
2016/9/29 11:49:50 - 2016/9/29 15:55:58	38/63	36/38	36/38

Figure 7.8 depicts the results of the preprocessing stage during the AVANTI campaign. Figure 7.8a shows the residuals of the Bezier curve fitting used for kinematic target detection. A value $\sigma = 0.5$ pixel has been used as threshold to consider the kinematic target detection valid. As this stage, the measurement set comprises all possible targets which have been kinematically detected (*i.e.*, mainly the desired target and some sporadic parasite objects).

Figure 7.8b depicts the residuals obtained after 5D filtering over all maneuver-free subarcs. The gray vertical lines represent the maneuvers which have been executed. Note that the measurement set slightly differs from the previous one: observations of parasite objects should have been removed by the data screening, and new observations detected using evident brightness have been added. These additional observations are depicted in green and appear when the intersatellite distance decreases.

Finally, Fig. 7.8c shows the measurement residuals obtained when computing the linear solution over five-day-long data arcs. These arcs are represented by gray areas. Note that the fourth data arc has been merged with the fifth one which was not observable (absence of maneuver) to form a ten-day-long data arc. The measurement set of Fig. 7.8c corresponds to the one of Fig. 7.8b, except that additional unprecise measurements have been added for completeness and are depicted in red. These measurements correspond to the case where the target has been detected based on its evident brightness but no star was visible in the background, so that the knowledge of the orientation of the camera is not precise, resulting in larger measurement errors.

As already stated, two products are generated out of the preprocessing stage: a healthy data set without large outliers and an associated coarse reference solution. These products finally feed the nonlinear batch least-squares estimation. Fig. 7.9 depicts in orange the solution computed using the new design of the relative orbit determination. The solution derived during the AVANTI campaign serves as reference and is depicted in blue. The coarse *a priori* solution computed with the linear method is depicted in green. Two conclusions can be drawn: first, the linear solution is similar to the nonlinear ones for intersatellites separation below 10 km, but exhibits unacceptable errors at larger distance. This is due to the fact that the linear solution does not take the curvature of the orbital path into account, as thoroughly explained in Chapter 6. This solution is accept-

able for data screening but cannot compete with the nonlinear solutions. Second, the nonlinear estimation using the new design is almost equivalent to the one based on the old design, except for the far-range field, where the weak observability introduces large uncertainties in line with the covariance analysis done in Chapter 4. In this case, small differences in the data set or measurement editing threshold might be the reason for different solutions. In the absence of an external reference, it is however impossible to state which solution is more accurate. This discussion is nevertheless of little relevance because the observed discrepancies amount to only a few percents of the separation at very far-range.

As a conclusion, it can be stated that the new design of the relative orbit determination offers similar accuracy while processing the data several orders of magnitude faster than the previous design: thanks to the robust data screening and computation of the
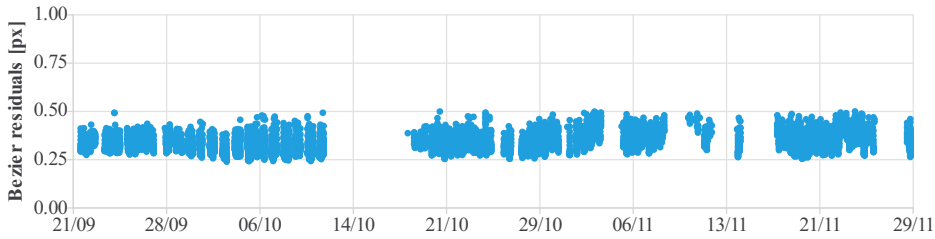
(a) Residuals of the Bezier curve fitting obtained during the kinematic target detection.
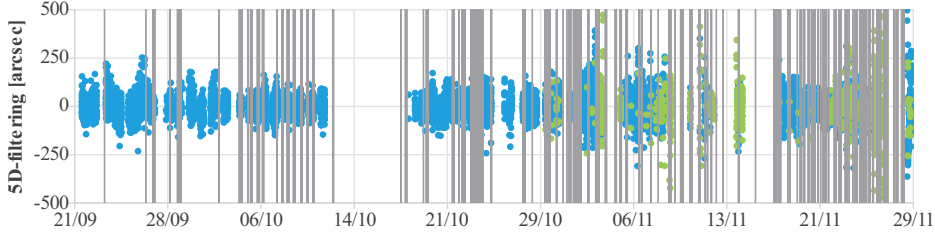
(b) Residuals of the 5D dynamical filtering. Maneuvers are represented by gray vertical lines. The majority of measurements has been kinematically detected (in blue). Additional measurements detected based on their brightness are depicted in green.
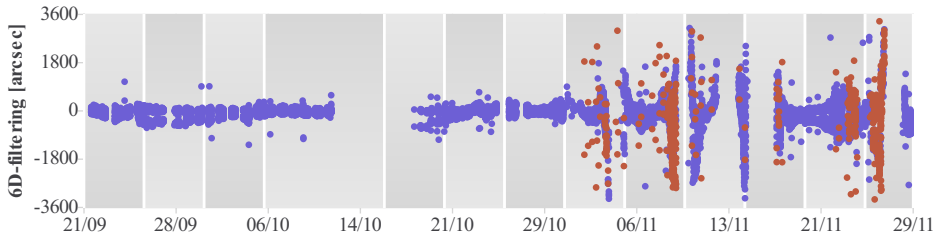
(c) Residuals of the 6D linear filtering over different data arcs represented by gray areas. Unprecise measurements due to coarse knowledge of the camera orientation are depicted in red.

Figure 7.8: Result of the preprocessing stage during AVANTI campaign.

reference solution, it is in fact not necessary anymore to spend hours refining the initial conditions and finely tuning the data editing thresholds to select healthy measurements. Furthermore, the analytical propagation of the relative motion adopted in the new design is shown to be at least one order of magnitude faster than the numerical one. Together, these aspects are responsible for a substantial reduction of computational effort: while several hours were dedicated every day during the AVANTI campaign to relative orbit determination activities, the whole AVANTI data set is now processed at once within a few dozen minutes.
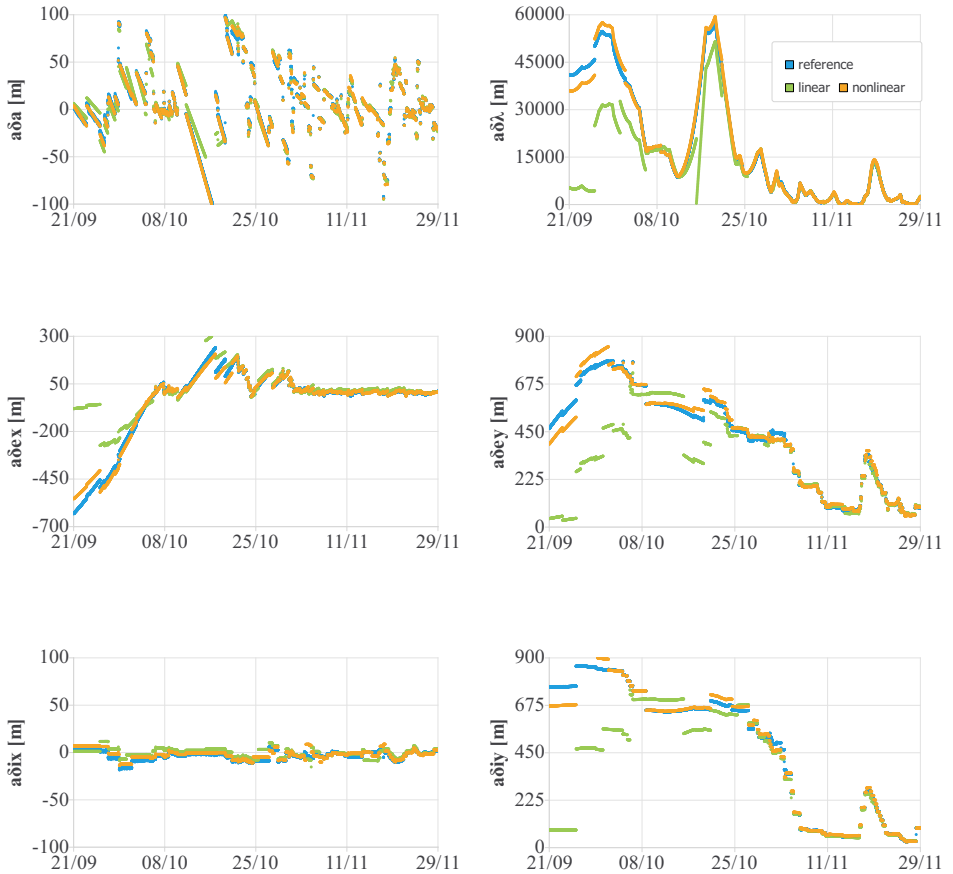

Figure 7.9: Comparison between reference solution derived during the AVANTI campaign (blue), linear solution from the preprocessing stage (green) and nonlinear solution (orange).

7.3. REALISTIC ERROR BUDGET

7.3.1. OVERVIEW

As pointed out in Section 4.4.3, one limitation of the relative orbit determination design presented in Chapter 4 was the unrealistic covariance which did not correspond to the real error of the solution. This discrepancy is caused by the errors of the dynamical model and systematic measurement biases. As already demonstrated in Section 4.4.3 using the ARGON data, the maneuver execution uncertainties are the main source of errors, followed by a bias in the angular measurements which appears at mid-range when the image of the target cannot be considered as a point source anymore. Until now, these errors have simply been neglected. Estimating them using additional dynamical and measurement parameters is one possible approach to improve the navigation accuracy. However, this is not advised for angles-only navigation because the observability is brought by the execution of maneuvers. Thus, estimating the maneuver errors as part of the state vector would degrade the observability. A more appropriate approach is to consider these errors in the estimation process as constant parameters whose uncertainties are known (by means of simulations or previous flight experience). Following [68], the general measurement equation described by Eq. 3.34 can be parameterized using a vector $\boldsymbol{c}$ of parameters

$$\boldsymbol{z} = \tilde{\boldsymbol{h}}(t, \boldsymbol{x}_0, \boldsymbol{c}) + \boldsymbol{\epsilon}, \tag{7.9}$$

so that, after linearization, Eq. 3.39 is complemented with a new term:

$$\Delta \boldsymbol{z} = \tilde{\boldsymbol{H}} \Delta \boldsymbol{x_0} + \tilde{\boldsymbol{H}}_c \boldsymbol{c}. \tag{7.10}$$

Here, $\tilde{\boldsymbol{H}}_c$ is the partial derivative of $\tilde{\boldsymbol{h}}$ with respect to $\boldsymbol{c}$. The parameters are chosen to be small values with expected value of zero which are added to the nominal values of the dynamic and measurements parameters. In what follows, they are assumed to be random quantities of covariance $\boldsymbol{C}$. They are also supposed to be uncorrelated with the measurement noise. Following [68], the consider covariance $\boldsymbol{P}^c$ which takes into account these uncertainties becomes:

$$\boldsymbol{P}^c = \boldsymbol{P} + (\boldsymbol{P}\tilde{\boldsymbol{H}}^T \boldsymbol{W})(\tilde{\boldsymbol{H}}_c \boldsymbol{C} \tilde{\boldsymbol{H}}_c^T)(\boldsymbol{P}\tilde{\boldsymbol{H}}^T \boldsymbol{W})^T, \tag{7.11}$$

where $\boldsymbol{P}$ is the covariance matrix described by Eq. 3.42. The simplicity of the analytical dynamical model allows for a straightforward derivation of $\tilde{\boldsymbol{H}}_c$. Let $\boldsymbol{c}$ be the set of parameters comprising the measurement biases $\Delta \tilde{\boldsymbol{h}}^T$ and the execution errors $\Delta \Delta \boldsymbol{V}_i, i \in [1, m]$ of the m maneuvers which are executed during the data arc under consideration:

$$\boldsymbol{c}^T = (\Delta \tilde{\boldsymbol{h}}^T, \Delta \Delta \boldsymbol{V}_1^T, ..., \Delta \Delta \boldsymbol{V}_m^T). \tag{7.12}$$

The partial derivatives with respect to the measurement biases are trivial:

$$\frac{\partial \tilde{\boldsymbol{h}}}{\partial \Delta \tilde{\boldsymbol{h}}} = \boldsymbol{I}. \tag{7.13}$$

According to Eq. 7.4, the partial derivatives with respect to the execution error of a maneuver executed at time $t_{\mathrm{M},i}$ is:

$$\frac{\partial \tilde{\boldsymbol{h}}}{\partial \Delta \Delta \boldsymbol{V}_i} = \frac{\partial \tilde{\boldsymbol{h}}}{\partial \boldsymbol{x}} \frac{\partial \boldsymbol{x}}{\partial \Delta \Delta \boldsymbol{V}_i} = \begin{cases} \frac{\partial \tilde{\boldsymbol{h}}}{\partial \boldsymbol{x}} \boldsymbol{\Phi}(t, t_{\mathrm{M},i}) \boldsymbol{B}_{\boldsymbol{x}}(u_{\mathrm{M},i}) & \text{if} \quad t > t_{\mathrm{M},i}, \\ 0 & \text{otherwise.} \end{cases} \tag{7.14}$$

7.3.2. CONSIDER COVARIANCE ANALYSIS USING THE ARGON DATASET

While the robustness and computational speed could be better assessed using the dataset from AVANTI, the PRISMA data set is more adapted for performance assessment thanks to the presence of an accurate external reference. This section intends to investigate and predict the contribution of maneuver execution errors and measurement biases to the error budget of the solution. For the sake of the analysis, three data set are generated:

- **Case 1 : error-free simulated dynamics and measurements**. The relative motion is propagated using a numerical model. Maneuvers are included as part of the guidance profile without execution errors. The measurement noise is purely Gaussian (mean=0", standard deviation=40").

- **Case 2 : real dynamics - simulated measurements**. The relative motion is extracted from GPS-based precise relative orbit determination accurate at subcentimeter level. The measurements are simulated using Gaussian noise (mean=0, standard deviation=40").

- **Case 3 : real dynamics and measurements**. The true trajectory and measurements from the ARGON experiment are used.

All scenarios share the same initial conditions: $a\delta\boldsymbol{\alpha}$ = (-2.5 -30437 -103 -396 -0.9 204) m at epoch t_0=2012/04/23 12:00:00 UTC and the same measurement distribution. For each case, a relative orbit determination is performed and the standard deviation of the solution $\sigma_{a\delta\alpha}$ predicted by the covariance matrix is retrieved. The real error of the solution is also retrieved by computing the root mean square (rms) value of the difference between predicted state from the solution and reference state over the whole estimation arc. For the cases 2 and 3, the maneuvers are either (precisely) estimated using differential GPS or (coarsely) estimated using absolute GPS (in this case, an asterisk is added to differentiate both cases). The results are summarized in Table 7.2. Note that the last component of the state vector $a\delta\dot{a}$ has been intentionally omitted in what follows for clarity. Its value is anyway negligible during ARGON.

Table 7.2: Covariance analysis for the ARGON case.)

Case	$\sigma_{a\delta\alpha}$ [m]	error (rms) [m]	$\sigma_{a\delta\alpha}^c$ [m]
1	[0.2 43 0.1 0.4 0.1 0.3]	[0.5 96 1.0 1.87 1.1 1.1]	-
2	[0.2 43 0.1 0.4 0.1 0.3]	[1.8 168 1.2 2.0 1.1 2.0]	[1.0 116 1.0 2.1 0.5 1.5]
2*	[0.2 43 0.1 0.4 0.1 0.3]	[2.8 320 1.7 5.0 1.1 4.4]	[2.9 325 3.1 6.3 1.4 4.4]
3	[0.2 45 0.1 0.4 0.1 0.4]	[2.0 226 1.6 2.1 1.4 3.5]	[1.0 215 1.2 3.1 2.4 4.1]
3*	[0.2 45 0.1 0.4 0.1 0.4]	[2.9 350 1.9 6.1 1.6 3.7]	[2.9 372 3.0 6.6 2.8 5.8]

Being a clean scenario without errors, the error of the solution estimated for Case 1 should be in line with the error predicted by $\sigma_{a\delta\alpha}$. This is almost the case, except for some small discrepancies which can be attributed to the deficiencies of the analytical model with respect to the numerical propagation and to the fact that the simulated noise might not be perfectly Gaussian. Case 2 shows a performance degradation due to the maneuver execution errors which is more pronounced for Case 2*. Case 3 shows that an additional contribution to the error budget is due to the real measurement noise.

During a rendezvous, it is desirable to better predict this error budget in order to increase the safety of the rendezvous. Hence the need for consider covariance analysis. However, only coarse values for the errors sources are available during operations. In particular, it is hard to precisely predict which errors will affect each component of a 3D maneuver vector. Thus, is has been assumed that all components of a maneuver are affected by 0.2 mm/s error when precisely estimated using differential GPS and 0.6 mm/s when estimated using absolute GPS. Cases 2 and 3 use identical settings for maneuver execution errors. The measurement biases are set to 2 pixels which corresponds to approximately 150" in both azimuth and elevation. Because the problem of measurement biases only appears at mid-range (when the image of the target is not a point source anymore), the biases are activated when the intersatellite distance decreases below 10 km. A consider covariance is now performed for the cases 2 and 3 and reported in the last column of Table 7.2. For the case 2, maneuver execution errors but no measurement bias are considered. For the case 3, both maneuver execution errors and measurement bias are considered. The resulting consider standard deviation $\sigma^c_{a\delta\alpha}$ is reported in the last column of Table 7.2.

A much better estimate of the real errors is clearly obtained using these simple considerations. Of course, some engineering judgment is required to introduce the typical values for the uncertainties of the key parameters. However, if this is properly done, a much more realistic error budget can be obtained.

7.4. TOWARDS AN ONBOARD IMPLEMENTATION

The robustness shown by the above-described algorithms is appealing for an onboard implementation. However, it is important to remember that this robustness is mainly achieved by processing batches of measurements in an iterative way over several-day-long arcs, which is not adapted for real-time applications. This section intends to lay the foundation for an hybrid approach, combining robustness of the batch least-squares method and real-time capability of sequential filtering.

This proposed hybrid approach is schematically depicted in Figure 7.10. It is primarily based on the same architecture as the onboard real-time navigation filter described in Chapter 5. The images are taken at fixed frequency (typically $T = 30$ s), and are processed as they arrive to extract the centroids, recognize the stars, and precisely estimate the orientation of the camera. The resulting list of unrecognized nonstellar objects feeds a real-time target detection module, whose output is used by an extended Kalman filter to estimate in real-time the relative motion. The hybrid approach foresees, in addition, a low-frequency task (for example, with a period $T_{\text{lsq}} = 12$ h), composed of robust target detection (based on an iterative preprocessing scheme) and batch least-squares estimation. Note that, contrary to the relative orbit determination scheme described in the previous sections, the non-calibrated maneuvers are used now in view of the desired onboard application.

The robust target detection reprocesses a circular buffer comprising the history of nonstellar objects over T_{lsq}, which is populated in real-time when a new image is processed onboard. As part of the preprocessing activities, the iterative data screening used for robust target detection relies on the 6D solution computed with the linear theory as depicted in Figure 7.7. This solution is derived based on the history of measurements,
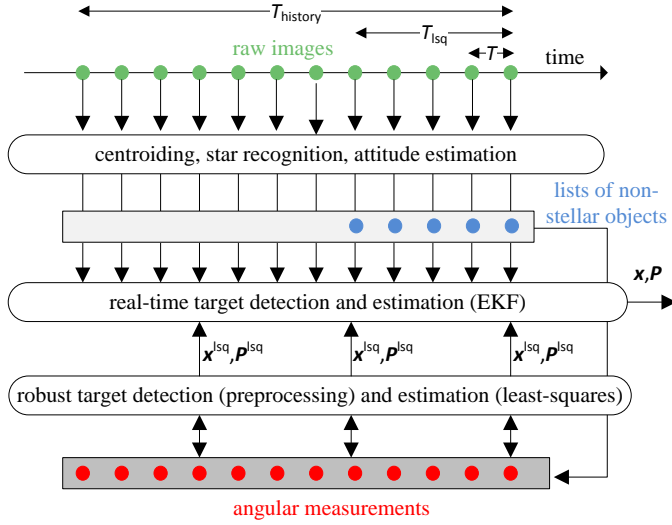
Figure 7.10: Architectural overview of the hybrid approach. The raw images (in green) are retrieved at high frequency and directly processed. The resulting unrecognized nonstellar objects (in blue) feed the real-time target detection and Extended Kalman Filter but are also stored into a circular buffer (light-gray rectangle) of limited length. A sliding robust target detection and least-squares filter runs in parallel at lower frequency, re-processing at each step the nonstellar objects and keeping a several-day long history of angular measurements (red) in another circular buffer (dark gray).

which has to be sufficiently long to bridge data gaps and to ensure enough observability (typically $T_{\text{history}} = 4$ days). This value is derived from the operational experience collected with the ARGON and AVANTI experiments, and takes into account the moderate pace of the rendezvous (conducted within a few days) adopted to conduct these in-orbit demonstrations. The data set is kept onboard by the means of a circular buffer comprising the history of the measurements over T_{history} and is updated after the execution of the robust target detection and data screening. Afterwards, a nonlinear batch least-squares estimation is finally performed over T_{history}.

The low-frequency task has no real-time requirement and can run as background activity with very low priority on an onboard computer. In view of the slow update rate, a processing time of several minutes or even several dozen minutes is acceptable. Once this task is done, the least-squares solution x^{lsq} and associated covariance P^{lsq} are used to initialize the EKF. Every time a new estimate from the batch least-squares process is available, the consistency of both solutions is evaluated and, in case of discrepancy, the EKF is reinitialized with the more robust least-squares solution. Note that this approach also improves the robustness of the EKF. As discussed in Chapter 5, it was often found too risky to initialize an EKF with a too large covariance (coming for example from TLEs), because this could lead to a filter divergence. Thus, the adopted workaround during AVANTI was to initialize the filter with an accurate solution which had been derived beforehand on ground based on optical measurements. The proposed hybrid concept is based on the same principle, except that this initialization process is now done onboard.

Such a hybrid implementation is made possible not only by the fact that the preprocessing and estimation algorithms solely rely on analytical models, but also considering the small amount of measurements collected in orbit. Based on the sampling rate of AVANTI (one image every 30 s), the limited visibility of the relative motion (about 10 minutes per orbit) generates about 20 measurements per orbit. These measurements have to be extracted from a series of images, but not all images need to be processed, because some are taken during eclipses or with the Sun in the field of view. Consequently, it can be conservatively assumed that images are available during 50% of the time, generating a maximum of about 100 images per orbit. Note that an image does not necessarily comprise a valid measurement (*e.g.*, if the target is not visible), which explains why only 20 measurements are collected each orbit. This results in about 750 new images which have to be processed every 12 h. As depicted in Figure 7.10, there is no need to store onboard the whole history of images in a raw format: it is enough to store the list of centroids detected in the image in the form of pixel positions with single precision. This can be further optimized by only storing the list of non-stellar objects detected in the image. Considering an average of 10 non-stellar objects per image, this corresponds to about 60 kB for 12 h. Once the measurements are extracted, it is enough to keep the list of measurements in the form of two angles (which are double-precision float values) after onboard processing. Thus, the history of measurements over 4 days approximately requires 20 kB of memory and the estimation algorithms need to process a maximum of 1200 measurements over four days.

In order to assess its feasibility, the complete AVANTI data set has been reprocessed using this hybrid approach. In this scenario, the first onboard least-squares relative orbit determination is performed on 29 September 2016 to ensure enough observability. At that time, the onboard circular buffer already comprises 4 days of measurements. Afterwards, the least-squares task is called every 12 h and is used to reinitialize the EFK. Note that this section only intends to demonstrate the viability of the concept. Thus the algorithms were implemented on a desktop computer with a Core i5 processor clocked at 2.6 GHz, which is not representative of an onboard computer. The computational time is related to the number of new images and to the total number of measurements in the circular buffer as depicted in Figure 7.11a. Figure 7.11b shows that the measured computational time of each call to the sliding least-squares task amounts to a few seconds. By using a conservative approach stating that a typical onboard computer might be two orders of magnitude slower than a desktop computer, a processing time of a few minutes seems possible on an onboard computer.

It is worth mentioning that there exists further room for optimization. In the current implementation, all measurements stored in the circular buffer undergo at each step a data screening. However, measurements already screened by a previous least-squares estimation do not need to be screened again at the next step. This will further reduce the computational load.

The uneven distribution of measurements over time is related to the pecularities of the AVANTI experiment. Since the chaser had to slew to execute maneuvers, the maximum number of measurements has been reached at far-range, when the chaser was not frequently maneuvering. Minor issues with the spacecraft during the commissioning phase have also resulted in data gaps, as already seen in Figure 7.8. In a mission
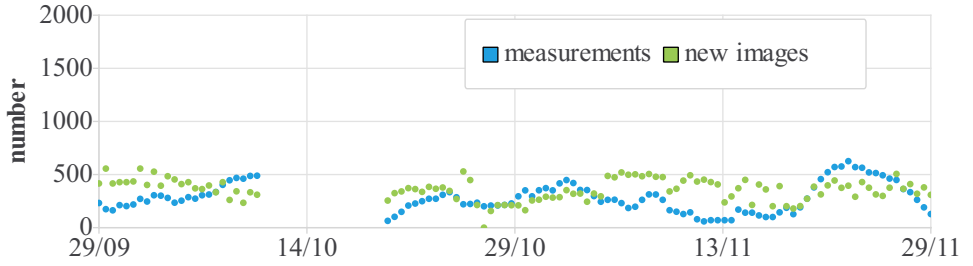
(a) Number of new images processed at every least-squares step (green) and total number of measurements stored in the circular buffer (blue).
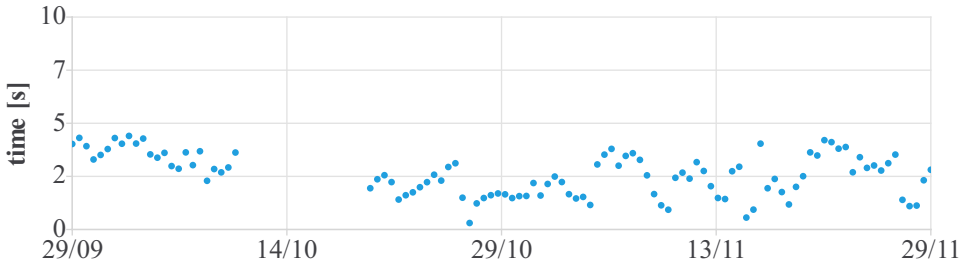
(b) Computational time needed to perform one least-squares step.

Figure 7.11: Data volume and computational time at each step.

7

specifically designed for rendezvous, a more uniform distribution of measurements and computational load is expected. As already stated, the reduced visibility of the relative motion due to the orbit characteristics and to the frequent slews of the chaser, the large data gaps due to minor spacecraft contingencies encountered during the commissioning phase, the unpredictable varying differential drag and large maneuver execution errors constitute the main challenges of this data set and are mainly specific to the AVANTI experiment. This tends to indicate that AVANTI is a worst scenario in terms of angles-only relative navigation: any algorithm reliably working with the AVANTI data set is likely to also properly perform with less challenging conditions.

Figure 7.12 depicts the relative navigation estimated with the hybrid approach and compared to the reference solution computed on ground during the experiment. The black dots represent the solution estimated every 12 h by the sliding least-squares task. The orange curve depicts the real-time solution provided by the EKF. It can been seen, in the presence of large data gaps such as between 15 and 20 October, that the EKF is not able to recover from such situations. On November 6 and 11, the EFK also starts to diverge because of lack of measurements. The situation is successfully recovered at the next call the least-squares task.

Overall, this hybrid approach shows a high level of robustness and greatly improves the weakness of the EFK implementation used during the AVANTI experiment.
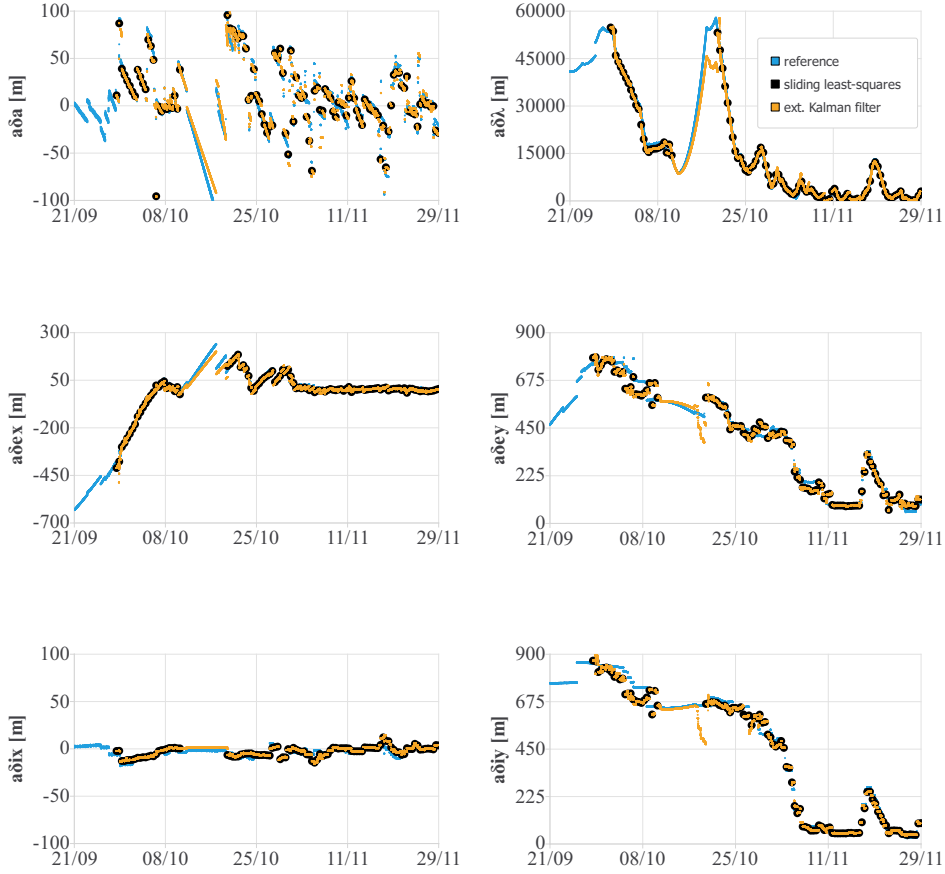
Figure 7.12: Comparison between reference solution derived during the AVANTI campaign and results from the sequential hybrid approach.

7.5. CONCLUSION

During the conduction of the AVANTI experiment, several robustness issues have been encountered when performing routine angles-only relative orbit determination, often preventing the convergence of the estimation process. More specifically, it was often difficult to properly reject all wrong target observations and to reliably supply the non-linear least-squares estimation with an appropriate *a priori* solution. These difficulties were mainly due to the poor visibility conditions and unpredictable orbital perturbations faced by AVANTI, which explains why they had not been discovered earlier during the preparation of the experiment. Even if they did not threaten the successful completion of the experiment, these limitations resulted in additional operational efforts to manually tune the data screening thresholds and refine the *a priori* solution until con-

vergence was achieved.

In order to remedy these issues, an additional preprocessing stage has been developed, able to deliver an outlier-free measurement set and an appropriate *a priori* solution to the subsequent nonlinear least-squares estimation. This achievement has been made possible by relying on a linear framework, which enables the direct and fast derivation of coarse solutions without the aid of any *a priori* information. Even if the resulting estimates are not as accurate as the nonlinear ones, this latter feature makes this framework well suited for preprocessing activities.

Two final additional improvements have been made to further enhance the relative orbit determination system. First, a more precise version of the mean to osculating conversion used during AVANTI has been introduced, making the analytical relative motion model more accurate. Based on this model, the angles-only relative orbit determination now shows similar performance as the one based on a numerical integration, but is at least one order of magnitude faster. The last improvement consists in the introduction of a consider covariance analysis, which is able to provide a more realistic error budget in the presence of maneuver errors and systematic measurement biases.

Since the aforedescribed algorithms rely on computationally-light analytical models, they are also suitable for an onboard implementation. However, their robustness is mainly achieved by the iterative processing of batches of measurements, which prevents a real-time implementation. The approach proposed to solve this dilemma is a hybrid concept with relative orbit determination and real-time navigation running onboard in parallel at different frequencies, combining the robustness of the least-squares estimation and real-time capability of the extended Kalman filter. A prototype of this hybrid-concept was successfully validated on a desktop computer using two months of flight data. However, further investigations are needed to verify its portability to a representative onboard computer.

8

CONCLUSIONS

The main objective of this research was the design, implementation and in-orbit validation of a spaceborne autonomous angles-only relative navigation system, demonstrating that line-of-sight navigation can be employed to conduct safe and reliable rendezvous with a noncooperative target up to the close-proximity domain. The following sections provide a concise summary of each chapter, followed by a conclusion gathering the results and findings of this work and aiming at thoroughly answering the Research Questions formulated in the introduction. The perspectives opened up by this research are finally sketched out in the final section.

8.1. SUMMARY

The first chapter justifies the need for this research and provides a description of its objectives and contributions. It is first recalled that, from a societal perspective, the evergrowing population of orbiting debris poses a major threat to space activities. Removing these debris objects at a large scale belongs to the possible mitigation strategies to keep a sustainable space environment, stressing the need for reliable and affordable rendezvous and capture capabilities. Most of the available expertise in this field regards the rendezvous and docking with a cooperative and well-controlled spacecraft. In order to enable the capture of noncooperative und uncontrolled tumbling objects, technological advances are needed. Among them, reliable and accurate relative navigation to a noncooperative object is a key capability to enable active debris removal. When initiating the rendezvous at a large intersatellite distance, this task can advantageously be performed using line-of-sight navigation and solely relying on a single space-based monocular camera. This choice contributes to a simplified design of the chaser satellite and to a reduction of costs. The research activities conducted so far on spaceborne angles-only relative navigation are, however, mainly theoretical and the real experience in orbit is rather limited. The PRISMA mission constitutes a notable exception, during which several in-orbit experiments dedicated to line-of-sight relative navigation have been conducted. However, these experimental activities were not fully representative of the challenging navigation conditions encountered by a debris removal mission

targeting an arbitrary object. Overall, missing expertise on how to design robust algorithms able to reliably function in real conditions and limited in-orbit experience have been identified as main gaps in the body of knowledge. In order to cover these gaps, this research focuses on the design and implementation of a spaceborne autonomous angles-only relative navigation system, and on the analysis of its behavior under real conditions. To that end, a peculiar iterative research roadmap has been used to conduct this work, composed of two on-orbit experiments with increasing complexity: ARGON, demonstrating ground-in-the-loop rendezvous with a noncooperative object, followed by AVANTI, demonstrating autonomous angles-only rendezvous under more challenging experimental and operational conditions.

These two experiments and their parent missions are described in more detail in the second chapter. ARGON was conducted in 2012 using the PRISMA formation-flying demonstration mission. The experiment could benefit from the advantages in terms of spacecraft capability and safety monitoring offered by a system dedicated to cooperative formation flight, and by the optimal visibility conditions guaranteed by the dawn-dusk orbit of the mission, creating a favorable framework for the angles-only relative navigation problem. Instead, AVANTI was implemented on BIROS, a German Earth observation satellite not primarily designed for vision-based rendezvous. It used a truly noncooperative target to demonstrate autonomous rendezvous based solely on angles-only measurements. Compared to ARGON, AVANTI had to cope with additional constraints such as frequent data gaps, limited onboard computational resources, poor visibility conditions and highly unpredictable perturbations of the relative motion. These difficulties did not prevent the successful completion of the experiment: after two months of commissioning, two autonomous rendezvous demonstrations could be executed. This achievement would not have been possible without the development of an advanced simulation and testing environment, which is also shortly described in this chapter.

The third chapter addresses the fundamentals of angles-only navigation. Relying on line-of-sight measurements to determine one's position and motion is an ancient technique, which has recently regained interest in view of its possible spaceborne applications. By accumulating angles-only measurements over time and using a dynamical motion model, it is possible to determine the relative motion of a noncooperative object from a chaser spacecraft during a rendezvous. This apparent simplicity comes, however, at the cost of a weak observability. Under the assumptions of a homogeneous linear relative motion and a linear relation between the Cartesian relative position and the relative state vector, the angles-only relative navigation problem is not observable. In reality, weak observability is realized if one of these assumptions is altered, paving the way to different strategies to reach observability: executing maneuvers or considering the nonlinearities of the relative motion or/and measurement models. The relative motion model plays a predominant role in the relative navigation process. As rule of thumb, the model accuracy shall be of the same order of magnitude as the measurement noise to support the relative navigation task. In view of the typical working distance of several tens of kilometers and time scale of several days during a rendezvous, a suitable model should at least consider J_2 and the curvature of the orbital path. At the low altitude of 550 km encountered by AVANTI, modeling the differential drag is also mandatory. The Hill-Clohessy-Wiltshire equations constitute the most famous relative

motion model. However, they are unable to satisfy the above-mentioned far-range accuracy requirements. Therefore, this research relies on an alternative analytical model, which uses a set of relative orbital elements to parameterize the relative motion. This model is more accurate thanks to its ability to take into account the mean effect of the main perturbations acting on a formation of spacecraft flying in low Earth orbit. Furthermore, the curvature of the orbital path is also intrinsically properly modeled thanks to the use of orbital elements. The numerical integration of the equations of motion is also a valid alternative model. This is even slightly more accurate than the analytical model but comes at the cost of much higher computational efforts. Two well-established estimation techniques were used in this work to determine the relative motion from a set of angles-only observations. The on-ground relative orbit determination supporting the ARGON and AVANTI experiments relied on a nonlinear batch least-squares estimation. This offers a high robustness but is not adapted for real-time application because it is computationally intensive and requires the history of measurements. On the contrary, the spaceborne real-time navigation filter employed to conduct the AVANTI experiment implemented an extended Kalman filter, which is suited for real-time application but is more prone to instability and thus has to be handled with care.

The fourth chapter addresses the design of the on-ground process for relative orbit determination and presents key results from both AVANTI and ARGON experiments. In order to improve the robustness of the target detection, a novel algorithm has been developed, which exploits the fact that chaser and target are flying on similar orbits to kinematically recognize the target trajectory over a sequence of images. This allows for a robust discrimination among all possible nonstellar objects that might be visible in the field of view of the camera. This detection strategy is complemented at close-range by an additional recognition based on the obvious brightness of the target. A nonlinear batch least-squares process is finally implemented to estimate the relative motion once the measurements are extracted from the images. The performance and behavior of the on-ground relative orbit determination are evaluated using flight data, collected when initiating the rendezvous at far-range, when performing the approach from far- to mid-range, and when reaching the close-range field. Overall, angles-only navigation has been found to be a powerful navigation method to rendezvous with a noncooperative target. Due to the weak observability, the solution of the orbit determination exhibits large along-track errors up to a few hundred meters at far-range, but is able to accurately estimate the shape of the elliptical relative motion, thus supporting a smooth and safe rendezvous at an early stage. At mid-range and in the presence of large variations of the relative motion, the observability improves, enabling successful and accurate determination of the relative trajectory. The achievable accuracy is shown to continuously improve throughout the entire rendezvous, promising relative navigation performance at (sub)meter level when reaching the close range field.

The fifth chapter addresses the design and flight results of the onboard real-time angles-only navigation system used to conduct the AVANTI experiment. The onboard implementation makes use of the target detection algorithm developed for the onground relative orbit determination. Minor adaptations are made to improve the autonomy. Since the onboard implementation does not have the possibility to iterate over the history of measurements to improve the robustness, additional measures, based on the on-

board navigation solution, are necessary to select the proper target and to reject wrong observations. The onboard navigation solution is estimated by means of an extended Kalman filter. Such a filter is suited for a real-time implementation, but was often found difficult to be properly tuned in the presence of high perturbations and poor visibility. Moreover, it was not always robust in the presence of outliers and perturbations, requiring additional support from ground for frequent monitoring and proper initialization. Despite these difficulties, the onboard relative navigation system was able to support two different autonomous approaches, first from 13 km to 1 km separation, then from 3 km to 50 m.

The sixth and seventh chapters result from additional analyses that have been performed after the conduction of the AVANTI experiment, following the desire to remedy some of the limitations discovered during the experiment. The sixth chapter intends to simplify the interfaces and to increase the level of autonomy by removing the dependency on TLEs. For this purpose, a novel algorithm has been designed, able to solve the problem of Initial Relative Orbit Determination (IROD) using a series of least-squares adjustments at varying distances. This algorithm exploits the nonlinearities of the models to solve the range ambiguity, and is successfully validated using real datasets from the ARGON and AVANTI experiments. Overall, this IROD method is robust and can compete with TLEs in terms of accuracy. However, it is computationally intensive. Consequently, alternative IROD methods are finally derived based on analytical models, aiming at reducing the computational load to enable an onboard implementation. Compared to the original IROD algorithm, they suffer, however, from degraded robustness, indicating that further research is needed in this field.

The seventh chapter revisits the relative orbit determination task, aiming at improving the robustness and making it operationally more sound. To that end, novel preprocessing techniques are introduced to perform a more robust data screening and to derive a more accurate *a priori* solution for the least-squares process using the linear theory. Based on these new algorithms, it is possible to greatly improve the robustness of the relative orbit determination process. By replacing the original numerical propagation of the relative motion with an accurate analytical model, it becomes possible to realize faster relative orbit determination. A final improvement is made by deriving a more realistic estimate of the error of the solution based on a consider covariance analysis. The resulting gain of speed and robustness makes such a system also appealing for embedded applications. Thus, a hybrid approach, suited for onboard implementation, is finally proposed, combining sliding relative orbit determination and extended Kalman filter, in order to pave the way for future robust, accurate and real-time spaceborne angles-only relative navigation systems.

8.2. CONCLUSIONS

The conclusions drawn from this research are based on the three Research Questions formulated in the introduction, which are recalled here for convenience. The main innovations brought by this research are highlighted by a tag written in bold in what follows.

Reliability, accuracy and real-time capability are three major interdependent challenges
for an onboard navigation system. In order to satisfy these requirements, the following
recommendations shall be followed during the system design:

- It is crucial to ensure that a healthy set of observations is provided to the estima-
  tion task, which might otherwise diverge. The kinematic target detection algo-
  rithm developed in this research (**Key Innovation 1**) improves the reliability of the
  target identification by only selecting objects flying on similar orbits. In order to
  further improve the quality of the measurement set, additional checks and aiding
  functions based on the object brightness and on the dynamical solution shall be
  implemented in the relative navigation system to better select the target and reject
  the wrong candidates.

- Measurement and model errors shall not be estimated as part of the state vector. It
  is tempting to estimate these errors to improve the navigation accuracy. However,
  the addition of too many parameters in the estimation process would weaken the
  robustness of the state estimation because of the weak observability. Thus, only
  the six elements of the relative state vector shall be estimated, augmented by a
  single parameter describing the mean effect of the differential drag when flying at
  altitudes below 800 km.

- In order to satisfy the real-time requirements, the onboard estimator shall rely on
  a nonlinear sequential filter which uses a computationally-light analytical model
  for the relative motion. This model shall include the perturbations due to J_2 and to
  differential drag. The curvature of the orbital path must be taken into account for
  a precise modeling of the line-of-sight measurements at intersatellite distances up
  to several tens of kilometers. Such a filter needs to be initialized using an *a priori*
  solution, which can be provided by means of TLEs.

- An additional ground-based verification layer is strongly advised to tune the on-
  board system and monitor its behavior. Since such a relative orbit determination
  process is less subject to resource limitation, alternative algorithms can be envi-
  sioned that are intrinsically more robust and more precise, because they can con-
  sider the complete history of data and process these data in an iterative scheme,
  refining the solution step-by-step. The precise knowledge of the maneuvers exe-
  cuted during the rendezvous is also a key to improve achievable accuracy. While it
  is difficult to estimate them onboard due to the limited available resources and to
  the real-time requirements, the ground implementation can greatly benefit from
  GPS-based *post facto* reconstruction of the executed maneuvers.

RQ2: How does an angles-only relative navigation system behave under real
conditions?
The main achievement of this research lies in the realization of two in-orbit demonstra-
tions, resulting in a unique mine of experience and lessons learned. This experience not

8

only concerns the behavior of the system, but also the environment itself, which could not be simulated with enough realism before the conduction of the experience.

- **Target visibility.** The sensor demonstrated a remarkable sensitivity, able to track a picosatellite with limited reflecting surface up to a distance of about 50 km. The visibility conditions were, instead, worse than expected. Prior to the conduction of the experiment, it was assumed that the object would not be visible during eclipse and camera blinding. However, there was the expectation that the CubeSat would at least be visible at two different locations of the orbit. Alas, during the experiment, the object could be seen only in one single location, when the Sun, chaser and target were aligned. Since the target was always actively orienting its solar panels towards the Sun, this might even represent a best case scenario, for which the reflecting surface is normal to the Sun direction and to the direction of the observer, thus maximizing the radiance.

- **Measurement errors.** At a certain threshold distance, the image of the target cannot be considered as Gaussian point spread function anymore. The resulting measurement biases can degrade the relative navigation. There is little that can be done to counteract that effect, except adapting the measurement noise level in the estimation process. If, in order to reduce the data link budget, only parts of the image are sent by the sensor to the onboard computer, this phenomenon may also be created by too small Regions of Interest (ROI), as experienced in the PRISMA mission. In this case, a too large target image may not fit into a fixed-sized ROI, creating a measurement bias.

- **Orbital perturbations.** Differential drag was unpredictable at the low altitude of 500 km for the AVANTI experiment. Both poor visibility conditions and high perturbation of the relative motion were shown to be extremely challenging for the relative navigation task, making it sometimes difficult to reach convergence of both the on-ground and onboard estimation processes.

8

- **System performance.** Despite these challenging conditions, the onboard relative navigation system was shown to be able to support the autonomous guidance and control in real-time. Line-of-sight navigation was shown to be a powerful tool, enabling autonomous rendezvous up to a distance of 50 m. At far-range, the longitudinal accuracy suffers from the weak observability and might exhibit errors up to 10% of the intersatellite distance. Instead, the lateral motion estimation benefits from the precision of angles-only navigation to reach an accuracy of about ten meters, allowing, at an early stage, for a precise estimation of the relative motion and for the establishment of passively safe relative motion. During the rendezvous, the relative navigation performance improves as the intersatellite distance decreases, finally reaching accuracy at the (sub) meter level at close-range. In the absence of an external reference orbit, it is hard to precisely assess the navigation performance reached during AVANTI. Thus, the relative navigation errors have been estimated based on a covariance analysis. It has to be noted that the error predicted by the covariance has been found much too optimistic when analyzing the ARGON results. Thus, a more realistic prediction of the error budget is advised to ensure

safer operations. The image processing, target detection and estimation algorithm could successfully run on a low-power onboard computer, giving confidence that such a relative navigation system can be implemented on a large variety of missions.

- **Reliability.** Despite the efforts made to properly recognize the target, wrong identifications occasionally occurred in few percent of cases. This is mainly due to the fact that BIROS was launched together with other satellites, and that these spacecraft were flying on similar orbits. In this case, their trajectories are also plausible for the target detection algorithm. This problem can be subsequently corrected using dynamical filtering, if healthy measurements greatly outnumber the wrong detections. Alas, the sparsity of measurements during AVANTI made this strategy risky, because even a single measurement outlier might lead to a filter divergence. A possible workaround (*i.e.*, which does not require deep modification of the detection algorithm) consists in restricting the search area around an expected position predicted using an *a priori* solution. However, this requires an accurate guess of the relative motion.

- **Initialization.** Deriving a precise *a priori* solution was often found to be a challenging task due to the unpredictable perturbations and the inaccuracies of the TLEs. Furthermore, an accurate *a priori* solution is not only needed to improve the robustness of the target detection, but also to favor the convergence of the nonlinear estimation techniques. In fact, if the *a priori* solution deviates too much from reality, the linearization assumptions are no longer valid, which often leads to divergence of the navigation filter. During the experiment, the proper functioning of the target detection and estimation algorithms has been achieved by manually refining the *a priori* solution on ground. To that end, it was necessary to spend time tuning the data editing thresholds and the length of the data arcs until the least-squares estimation converged. This accurate solution coming from ground processing was subsequently used to properly initialize and ensure the convergence of the onboard relative navigation.

- **Tuning.** It was found difficult to properly tune the onboard filter in the presence of high perturbations and few measurements, which leads to two contradicting challenges: reducing the process noise gives more weight to the dynamical model which might be wrong in case of rapid variations of the differential drag. Increasing the process noise gives more importance to the measurements which may be sparse.

- **Close-range behavior.** The relative navigation system was intended to cover the far- to mid- range field and, indeed, better performed at these regimes. At close-range, the stars in the image background were not visible anymore, making the precise estimation of the orientation of the camera impossible, and resulting in large line-of-sight errors. The other main difficulty of the close-range field regards the observability. At far-range, observability is improved by considering the non-linearity of the measurement model induced by the curvature of the orbital path.

8

During the rendezvous, this is ensured by the maneuvers executed during the approach. When reaching the close-range field, only small maneuvers can be used to perform station keeping, which might not be sufficient to solve the range ambiguity. In an ideal case, this range has already been determined during the rendezvous. However, in case of unpredictable varying differential drag such as encountered during AVANTI, this range cannot be accurately predicted based on a past solution. Thus, the range estimate needs to be updated using measurements, which is impossible at close-range in the absence of large maneuvers. As a result, the filter is prone to divergence during station keeping in the presence of unknown differential drag.

RQ3: How can future angles-only relative navigation systems be improved?

Several possible improvements have been identified based on the experience collected during the execution of the AVANTI experiment. Some of them regard the design of the chaser spacecraft, because this affects the performance of the angles-only relative navigation system. Others are related to the design of the algorithms and consist of improvements which could be validated in this thesis by reprocessing *a posteriori* the data collected during the experiments.

Regarding the design of the spacecraft, it is more efficient to specifically design the chaser for angles-only navigation than to cope with the limitations of a platform intended for Earth observation. To that end, it is preferable, as done in the PRISMA mission, to have a dedicated far-range camera, nominally pointing in along-track direction, to avoid thermal issues during the rendezvous, instead of using an existing star tracker as done in AVANTI. This eases the accommodation of a ground communication antenna, which can nominally point to the Earth, thus avoiding unnecessary attitude slew during ground contact. Implementing a 3D maneuver capability also leads to a more stable attitude profile, which in turns greatly reduces the data gaps. Another important advantage brought by a dedicated camera is the fact that, at close-range, its attitude can be better estimated using additional star trackers which are steadily pointing to deep sky. Finally, it is preferable to decouple the target tracking function from the onboard relative navigation to ensure a more reliable provision of measurements. By decoupling, it is meant that the camera direction shall be steered at close-range by tracking the brightest non-celestial object instead of relying on the onboard real-time estimate of the relative position. This latter concept was used during the AVANTI experiment. However, in case of large navigation errors, no measurement can be collected anymore, preventing any filter recovery. A simple attitude guidance could be envisioned, running at high frequency and always keeping the target in the center of the camera field of view. In this case, provision of measurements and relative state estimation is decoupled, which will improve the robustness of the relative navigation system.

This robustness can, however, be greatly improved at software level. This has been demonstrated in the last chapter of the thesis. By introducing a preprocessing step based on the linear theory (**Key Innovation 2**), a more robust data screening and a more accurate derivation of the *a priori* solution can be reached, entirely solving the issues encountered with the on-ground verification layer. By replacing the numerical integration of the relative motion by an analytical model, it becomes possible to obtain a robust relative orbit determination process, fast enough to be eligible for onboard application. This

task still needs to process the history of data to derive a robust solution and will always remain slower than a sequential implementation. However, it might advantageously be used as background activity for the initialization of the extended Kalman filter and to autonomously monitor its behavior at a low frequency. This hybrid approach (**Key Innovation 3**) is extremely appealing, since it combines the robustness of processing of a history of data and the real-time capability of a sequential filter.

By revisiting the design of the relative orbit determination process, this thesis has shown opportunities for improvements in operations. The use of Two-Line Elements can be avoided by relying on Initial Relative Orbit Determination algorithms (**Key Innovation 4**), delivering range estimation whose accuracy can compete with the one of TLEs. During this process, better lateral accuracy is also reached, outperforming the typical TLE accuracy by one order of magnitude. Such IROD algorithms could in principle also be used onboard. Finally, it has been shown that a consider covariance analysis provides much more realistic estimates of the errors affecting the solution.

8.3. OUTLOOK

The conduction of two in-orbit experiments under very different conditions gave the unique opportunity to perform thorough investigations and analyses on angles-only relative navigation in low Earth orbit. There remain a few topics which have not be covered by this research and deserve further investigations. The first one concerns the impact of large systematic measurement biases at close-range, which might greatly degrade the navigation solution. This aspect was not relevant for AVANTI because of the small symmetrical shape of the Cubesat. It was limited in ARGON, because the target also had a small size and the experiment ended at 3 km intersatellite separation. However, large systematic measurement errors might become a problem for larger space structures if, for example, only the extremity of a several-meter-long solar panel is illuminated, creating large line-of-sight errors which cannot be modeled by Gaussian noise.

Another aspect, specific to the AVANTI experiment, concerns the modeling of the differential drag. Unrealistic values of the drag coefficient observed during the conduction of AVANTI indicate that a better model of this perturbation could be reached. In the specific case of AVANTI, considering the fact that this was mainly caused by the attitude changes of the chaser, it is worth investigating if this perturbation can be estimated based on GPS data from the chaser, instead of modeling it. A better knowledge of the differential drag may also be used to improve the observability, since this contributes to the nonlinearity of the relative motion. Regarding the design of the onboard relative navigation system, there are possible improvements to develop faster and more reliable onboard Initial Relative Orbit Determination algorithms. A few promising ideas have been sketched in the thesis, such as directly solving the range ambiguity using an analytical method. However, further improvements of the analytical relative motion models might be necessary to reach better robustness and performance of the onboard IROD. Finally, it would also be worth investigating if more robust filtering techniques, such as H_∞-based filters, can be employed for the onboard real-time relative navigation task as computationally-lighter alternative for the hybrid architecture proposed in this thesis.

Overall, this work opens the doors to the widespread utilization of angles-only spaceborne rendezvous systems based on monocular cameras in future active debris removal

8

missions. Such systems enable the rendezvous to a noncooperative target in a safe and fully autonomous way, up to a distance of a few tens of meters. When reaching the close-range field, other techniques and sensors have to be employed for the relative navigation task. The simplest enhancement of the angle-only relative navigation system would consist in using additional range measurement, by means of low-power radars or lidars reaching a working distance of a few tens of meters. This would allow for the design of simple, computationally-light relative navigation systems fusing line-of-sight and range measurements, combining the accuracy at submeter level of line-of-sight navigation and preventing divergence due to the weak observability during station keeping. Such a computationally-light and low-complexity formation-keeping system would enable the design of fly-around close-range observation orbits, which could be autonomously maintained during a long period of time, and could serve as in-orbit testbed to gain experience, validate and qualify more advanced vision-based techniques such as pose estimation or stereo-vision.

8

BIBLIOGRAPHY

[1] U. N. O. for Outer Space Affairs (UNOOSA). *Online Index of Objects Launched into Outer Space*. http://www.unoosa.org/oosa/osoindex [Accessed 1 July 2019]. 2019.

[2] ESA. *Space Debris By the Numbers*. https://www.esa.int/Our_Activities/Space_Safety/Space_Debris/Space_debris_by_the_numbers [Accessed 1 July 2019]. 2019.

[3] D. J. Kessler and B. G. Cour-Palais. "Collision Frequency of Artificial Satellites: The Creation of a Debris Belt". In: *Journal of Geophysical Research* 83 (1978), pp. 2637–2646.
     DOI: 10.1029/JA083iA06p02637.

[4] J.-C. Liou. "An active debris removal parametric study for LEO environment remediation". In: *Advances in Space Research* 47 (2011), pp. 1865–1876.
     DOI: 10.1016/j.asr.2011.02.003.

[5] M. Shan, J. Guo, and E. Gill. "Review and comparison of active space debris capturing and removal methods". In: *Progress in Aerospace Sciences* 80 (2016), pp. 18–32.
     DOI: 10.1016/j.paerosci.2015.11.001.

[6] B. Aldrin. "Line-of-sight guidance techniques for manned orbital rendezvous". PhD thesis. U.S.A: Massachusetts Institute of Technology. Dept. of Aeronautics and Astronautics., 1963.

[7] O. Montenbruck. *Space Applications. In Springer Handbook of Global Navigation Satellite Systems (pp. 933-959)*. Basel: Springer International Publishing, 2017.
     DOI: 10.1007/978-3-319-42928-1.

[8] J.-S. Ardaens and S. D'Amico. "Spaceborne Autonomous Relative Control System for Dual Satellite Formations". In: *Journal of Guidance, Control, and Dynamics* 32.6 (2009), pp. 1859–1870.
     DOI: 10.2514/1.42855.

[9] J.-S. Ardaens, R. Kahle, and D. Schulze. "In-Flight Performance Validation of the TanDEM-X Autonomous Formation Flying System". In: *International Journal of Space Science and Engineering* 2.2 (2014), pp. 157–170.
     DOI: 10.1504/IJSPACESE.2014.060596.

[10] S. D'Amico. "Autonomous Formation Flying in Low Earth Orbit". PhD thesis. The Netherlands: Technical University of Delft, 2010.

[11] J.-S. Ardaens, S. D'Amico, and O. Montenbruck. "Final Commissioning of the PRISMA GPS Navigation System". In: *Journal of Aerospace Engineering, Sciences and Applications* 4.3 (2012), pp. 104–118.

[12] J. Llorente, A. Agenjo, C. Carrascosa, C. de Negueruela, A. Mestreau-Garreau, A. Cropp, and A. Santovincenzo. "PROBA-3: Precise formation flying demonstration mission". In: *Acta Astronautica* 82.1 (2013), pp. 38–46. ISSN: 0094-5765. DOI: 10.1016/j.actaastro.2012.05.029.

[13] B. D. Tapley, S. Bettadpur, M. Watkins, and C. Reigber. "The gravity recovery and climate experiment: Mission overview and early results". In: *Geophysical Research Letters* 31.9 (2004). DOI: 10.1029/2004GL019920.

[14] T. Grelier, P.-Y. Guidotti, M. Delpech, J. Harr, J.-B. Thevenet, and X. Leyre. "Formation Flying Radio Frequency Instrument: First Flight Results from the PRISMA Mission". In: *Proceedings of the 5rd ESA Workshop on Satellite Navigation User Equipment Technologies, NAVITEC*. Noordwijk, The Netherlands: IEEE, 2010.

[15] S. Roose, Y. Stockman, and Z. Sodnik. "A Lateral Sensor for the Alignment of two Formation-Flying Satellites". In: *Proceedings of the 5th International Conference on Spacecraft Formation Flying Missions & Technologies (SFFMT)*. Munich, Germany: DLR, German Space Operations Center, 2013.

[16] C. Dunn, W. Bertiger, Y. Bar-Sever, S. Desai, B. Haines, D. Kuang, G. Franklin, I. Harris, G. Kruizinga, T. Meehan, S. Nandi, D. Nguyen, T. Rogstad, J. Thomas, J. Tien, L. Romans, M. Watkins, S. Wu, S. Bettadpur, and J. Kim. "Instrument of Grace: GPS augments gravity measurements". In: *GPS World* 14 (2003). ISSN: 1048-5104.

[17] W. Fehse. *Automated Rendezvous and Docking of Spacecraft*. Cambridge: Cambridge University Press, 2003. DOI: 10.1017/CBO9780511543388.

[18] NASA. *About the Hubble Space Telescope*. https://www.nasa.gov/mission_pages/hubble/story/index.html [Accessed 1 July 2019]. 2019.

[19] ESA. *Sentinel 2*. https://earth.esa.int/web/guest/missions/esa-operational-eo-missions/sentinel-2 [Accessed 1 July 2019]. 2019.

[20] NASA. *Hubble Space Telescope – Advanced Camera for Surveys*. https://www.nasa.gov/content/hubble-space-telescope-advanced-camera-for-surveys [Accessed 1 July 2019]. 2019.

[21] J. Jørgensen, T. Denver, M. Betto, P. Jørgensen, H.-P. Röser, R. Sandau, and A. Valenzuela. "The Micro ASC, a Miniature Star Tracker". In: *Proceedings of the 4th International Symposium of the International Academy of Astronautics*. 2003, pp. 157–162.

[22] S. Micro. *5MP Space Camera Data Sheet*. https://www.spacemicro.com/assets/datasheets/guidance-and-nav/5MP_Space_Camera.pdf [Accessed 1 July 2019]. 2019.

[23] XCAM. *C3D CubeSat Camera Data Sheet*. http://www.xcam.co.uk/sites/default/files/MKPU-XCAM-MS-00011.pdf [Accessed 1 July 2019]. 2019.

[24]   S. C. Nardone and M. L. Graham. "A closed-form solution to bearings-only target motion analysis". In: *IEEE Journal of Oceanic Engineering* 22.1 (1997), pp. 168–178.
        DOI: 10.1109/48.557551.

[25]   C. Sabol and D. Vallado. "A Fresh Look at Angles-Only Orbit Determination". In: AAS/AIA Vol. AAS 99-363. AAS/AIAA Astrodynamics Specialist Conference. Girdwood, Alaska, 1999.

[26]   R. J. V. Chari. "Autonomous Orbital Rendezvous Using Angles-Only Navigation". PhD thesis. U.S.A: Massachusetts Institute of Technology. Dept. of Aeronautics and Astronautics., 2001.

[27]   D. C. Woffinden. "Angles-Only Navigation for Autonomous Orbital Rendezvous". PhD thesis. U.S.A: Utah State University, 2008.

[28]   D. C. Woffinden and D. K. Geller. "Optimal Orbital Rendezvous Maneuvering for Angles-Only Navigation". In: *Journal of Guidance, Control, and Dynamics* 32.4 (2009), pp. 1382–1387.
        DOI: 10.2514/1.45006.

[29]   G. Gaias, S. D'Amico, and J.-S. Ardaens. "Angles-Only Navigation to a Noncooperative Satellite Using Relative Orbital Elements". In: *Journal of Guidance, Control, and Dynamics* 37.2 (2014), pp. 439–451.
        DOI: 10.2514/1.61494.

[30]   J. Grzymisch and W. Fichter. "Analytic Optimal Observability Maneuvers for In-Orbit Bearings-Only Rendezvous". In: *Journal of Guidance, Control, and Dynamics* 37.5 (2014), pp. 1658–1664.
        DOI: 10.2514/1.G000612.

[31]   J. Grzymisch and W. Fichter. "Observability Criteria and Unobservable Maneuvers for In-Orbit Bearings-Only Navigation". In: *Journal of Guidance, Control, and Dynamics* 37.4 (2014), pp. 1250–1259.
        DOI: 10.2514/1.62476.

[32]   D. K. Geller and I. Klein. "Angles-Only Navigation State Observability During Orbital Proximity Operations". In: *Journal of Guidance, Control, and Dynamics* 37.6 (2014), pp. 1976–1983.
        DOI: 10.2514/1.G000133.

[33]   A. C. Perez. "Applications of Relative Motion Models Using Curvilinear Coordinate Frames". PhD thesis. U.S.A: Utah State University, 2017.

[34]   T. A. Lovell and S. G. Tragesser. "Guidance for Relative Motion of low Earth Orbit Spacecraft based on Relative Orbit Elements". In: 04-4988. AIAA Guidance, Navigation, Control Conference, and Exhibit. Providence, Rhode Island, USA, 2004.

[35]   J. Sullivan, A. Koenig, and S. D'Amico. "Improved Maneuver-Free Approach to Angles-Only Navigation for Space Rendezvous". In: 16-530. 26th AAS/AIAA Space Flight Mechanics Conference. Napa, California, 2016.

[36] S. Garg and A. Sinclair. "Initial Relative-Orbit Determination Using Second-Order Dynamics and Line-of-Sight Measurements". In: 25th AAS/AIAA Space Flight Mechanics Meeting. Williamsburg, Virginia, 2015.

[37] D. K. Geller and T. A. Lovell. "Angles-Only Initial Relative Orbit Determination Performance Analysis using Cylindrical Coordinates". English. In: *The Journal of the Astronautical Sciences* 64.1 (Sept. 2017), pp. 72–96.
DOI: 10.1007/s40295-016-0095-z.

[38] J. Sullivan and S. D'Amico. "Nonlinear Kalman Filtering for Improved Angles-Only Navigation Using Relative Orbital Elements". In: *Journal of Guidance, Control, and Dynamics* 40.9 (2017), pp. 2183–2200.
DOI: 10.2514/1.G002719.

[39] L. Hebert. "Angles-Only Initial Relative-Orbit Determination via Successive Maneuvers". MA thesis. U.S.A: Auburn University, 2016.

[40] A. Perez, D. Geller, and T. Lovell. "Non-iterative angles-only initial relative orbit determination with J2 perturbations". In: *Acta Astronautica* 151 (2018), pp. 146–159.
DOI: 10.1016/j.actaastro.2018.06.033.

[41] D. Rössler, D. A. K. Pedersen, M. Benn, and J. L. Jørgensen. "Optical Stimulator for Vision-Based Sensors". In: *Advanced Optical Technologies* 3.1 (2014), pp. 199–207.
DOI: 10.1515/aot-2013-0045.

[42] C. Beierle. "High Fidelity Validation of Vision-Based Sensors and Algorithms for Spaceborne Navigation". PhD thesis. U.S.A: Stanford University, 2019.

[43] *DARPA archive: Orbital Express.* https://www.darpa.mil/about-us/timeline/orbital-express, DARPA Tactical Technology Office. [Accessed 1 July 2019]. July 2007.

[44] S. Persson, B. Jakobsson, and E. Gill. "PRISMA - Demonstration Mission for Advanced Rendezvous and Formation Flying Technologies and Sensors". In: 05-B56B07. 56th International Astronautical Congress. Fukuoka, Japan, 2005.

[45] J. Jørgensen and M. Benn. "VBS - The Optical Rendezvous and Docking Sensor for PRISMA". In: *NordicSpace* (2010), pp. 16–19. ISSN: 0805-7397.

[46] R. Noteborn, P. Bodin, R. Larsson, and C. Chasset. "Flight Results from the PRISMA Optical Line of Sight Based Autonomous Rendezvous Experiment". In: *Proceedings of the 4th International Conference on Spacecraft Formation Flying Missions & Technologies (SFFMT)*. St-Hubert, Quebec: Canadian Space Agency, 2011.

[47] M. Delpech, J.-C. Berges, S. Djalal, and J. Christy. "Vision Based Rendezvous Experiment performed during the PRISMA Extended Mission". In: *Proceedings of the 23rd International Symposium on Space Flight Dynamics*. Pasadena, California, USA: Jet Propulsion Laboratory, 2012.

[48]   S. D'Amico, J.-S. Ardaens, G. Gaias, H. Benninghoff, B. Schlepp, and J. L. Jørgensen. "Noncooperative Rendezvous Using Angles-Only Optical Navigation: System Design and Flight Results". In: *Journal of Guidance, Control, and Dynamics* 36.6 (2013), pp. 1576–1595.
DOI: 10.2514/1.59236.

[49]   G. Gaias and J.-S. Ardaens. "Flight Demonstration of Autonomous Noncooperative Rendezvous in Low Earth Orbit". In: *Journal of Guidance, Control, and Dynamics* 41.6 (2018), pp. 1137–1354.
DOI: 10.2514/1.G003239.

[50]   W. Halle, W. Bärwald, T. Terzibaschian, M. Schlicker, and K. Westerdorf. "The DLR -Satellite BIROS in the Fire-Bird Mission". In: *Proceedings of the 4S Symposium: Small Satellites, Systems and Services*. 26 - 30 May 2014, Majorca, Spain. Noordwijk, The Netherlands: European Space Agency, 2014.

[51]   J.-S. Ardaens and G. Gaias. "Angles-Only Relative Orbit Determination in Low Earth Orbit". In: *Advances in Space Research* 31.11 (2018), pp. 2740–2760.
DOI: 10.1016/j.asr.2018.03.016.

[52]   J.-S. Ardaens, G. Gaias, and R. Kahle. "From GRACE to AVANTI: 15 years of Formation-Flying Experience at DLR". In: *Proceedings of the 69th International Astronautical Congress (IAC)*. D1.2.3. International Astronautical Federation. Bremen, Germany, 2018.

[53]   J.-S. Ardaens and G. Gaias. "Integrated Solution for Rapid Development of Complex GNC Software". In: *Proceedings of the Workshop on Simulation for European Space Programmes (SESP)*. ESTEC, Noordwijk, The Netherland: European Space Agency, 2015.

[54]   P. Bodin, R. Noteborn, R. Larsson, T. Karlsson, S. D'Amico, J.-S. Ardaens, M. Delpech, and J.-C. Berges. "PRISMA Formation Flying Demonstrator: Overview and Conclusions from the Nominal Mission". In: *Proceedings of the 35th Annual AAS Guidance and Control Conference*. 12-072. Breckenridge, Colorado, USA, 2012.

[55]   S. D'Amico, E. Gill, M. F. Garcia, and O. Montenbruck. " GPS-Based Real-Time Navigation for the PRISMA Formation Flying Mission". In: *Proceedings of the 3rd ESA Workshop on Satellite Navigation User Equipment Technologies, NAVITEC*. Noordwijk, The Netherlands: ESA, 2006.

[56]   O. Montenbruck, B. Nortier, and S. Mostert. "A Miniature GPS Receiver for Precise Orbit Determination of the SUNSAT2004 Micro-Satellite". In: ION National Technical Meeting. San Diego, California, USA, 2004.

[57]   S. D'Amico, J.-S. Ardaens, and R. Larsson. "Spaceborne Autonomous Formation-Flying Experiment on the PRISMA Mission". In: *Journal of Guidance, Control, and Dynamics* 35.3 (2012), pp. 834–850.
DOI: 10.2514/1.55638.

[58]   S. D. Florio, S. D'Amico, and G. Radice. "Virtual Formation Method for Precise Autonomous Absolute Orbit Control". In: *Journal of Guidance, Control, and Dynamics* 37.2 (2014), pp. 425–438.
DOI: 10.2514/1.61575.

[59]   T. Karlsson, N. Ahlgren, R. Faller, and B. Schlepp. "PRISMA Mission Control: Trans-
       ferring Satellite Control between Organisations". In: *SpaceOps 2012*. Stockholm,
       Sweden. American Institute of Aeronautics and Astronautics, 2012.
       DOI: 10.2514/6.2012-1287645.

[60]   F. Baumann, S. Trowitzsch, and K. Brieß. "BEESAT - A CubeSat Series Demon-
       strates Novel Picosatellite Technologies". In: *Proceedings of the 4th European Cube-
       Sat Symposium*. Brussels, Belgium, 2012.

[61]   S. Roemer and S. Stoltz. "SPL – Light Weight Deployment Mechanism for Single
       CubeSats and DPL for Double CubeSats". In: Symposium on Small Satellite Sys-
       tems and Services (4S). Funchal, Madeira, Portugal, 2010.

[62]   G. Gaias, J.-S. Ardaens, and C. Schultz. "The AVANTI experiment: flight results".
       In: *Proceedings of the 10th International ESA Conference on Guidance, Navigation
       & Control Systems*. ESTEC, Noordwijk, The Netherlands: European Space Agency,
       2017.

[63]   S. Montenegro. *RODOS, DLR-Network Centric Core Avionics*. DLR-RY TN 05-08.
       Bremen, Germany: Deutsches Zentrum für Luft- und Raumfahrt, Nov. 2008.

[64]   G. Gaias, J.-S. Ardaens, and T. Terzibaschian. "Paving the Way for Future On-
       Orbit-Servicing Missions: the AVANTI Experiment". In: *Proceedings of the 25th
       International Symposium on Space Flight Dynamics ISSFD*. Munich, Germany:
       DLR, German Space Operations Center, 2015.

[65]   S. Montenegro and W. Bärwald. "PowerBIRD - Modern Spacecraft Bus Controller".
       In: *Acta Astronautica* 52.9-12 (2003), pp. 957–963.
       DOI: 10.1016/S0094-5765(03)00077-8.

[66]   G. Gaias and J.-S. Ardaens. "Design challenges and safety concept for the AVANTI
       experiment". In: *Acta Astronautica* 123 (2016), pp. 409–419.
       DOI: 10.1016/j.actaastro.2015.12.034.

[67]   G. Gaias, J.-S. Ardaens, and S. D'Amico. "Formation Flying Testbed at DLR's Ger-
       man Space Operations Center". In: *Proceedings of the 8th International ESA Con-
       ference on Guidance, Navigation & Control Systems*. ESTEC, Noordwijk, The Nether-
       land: European Space Agency, 2011.

[68]   O. Montenbruck and E. Gill. *Satellite Orbits - Models, Methods, and Applications*.
       Heidelberg: Springer Verlag, 2001.

[69]   Microsoft. *Component Object Model (COM)*. https://docs.microsoft.com/
       en-us/windows/desktop/com/component-object-model--com--portal
       [Accessed 1 May 2019]. 2019.

[70]   H. Benninghoff, F. Rems, E.-A. Risse, and C. Mietner. "European Proximity Oper-
       ations Simulator 2.0 (EPOS) - A Robotic-Based Rendezvous and Docking Simula-
       tor". In: *Journal of Large-Scale Research Facilities* (2017).
       DOI: 10.17815/jlsrf-3-155.

[71]   T. Delabie, T. Durt, and J. Vandersteen. "Highly Robust Lost-in-Space Algorithm Based on the Shortest Distance Transform". In: *Journal of Guidance, Control, and Dynamics* 36.2 (2013), pp. 476–484.
DOI: 10.2514/1.56860.

[72]   G. Brat. "Reducing V & V Cost of Flight Critical Systems: Myth or Reality". In: *IAA Information Systems-AIAA Infotech @Aerospace, AIAA SciTech Forum, (AIAA 2017-0563)*. 2017.

[73]   J. Coulton. *The Dioptra of Hero of Alexandria. In Science and Mathematics in Ancient Greek Culture, edited by C. J. Tuplin, and T. E. Rihll.* Oxford, U.K.: Oxford University Press, 2002.

[74]   C. F. Gauss. *Theory of the Motion of the Heavenly Bodies Moving about the Sun in Conic Sections: a translation of Gauss's "Theoria motus.".* Boston: (English translation, Little, Brown and company), 1809.

[75]   L. P. Cassinis, R. Fonod, and E. Gill. "Review of the robustness and applicability of monocular pose estimation systems for relative navigation with an uncooperative spacecraft". In: *Progress in Aerospace Sciences* 110 (2019), p. 100548.
DOI: 10.1016/j.paerosci.2019.05.008.

[76]   G. W. Hill. "Researches in the Lunar Theory". In: *American Journal of Mathematics* 23.1 (1878), pp. 5–26.
DOI: 10.2307/2369430.

[77]   D. A. Vallado. *Fundamentals of Astrodynamics and Applications.* New York City: McGraw-Hill, 1997.

[78]   W. H. Clohessy and R. S. Wiltshire. "Terminal Guidance System for Satellite Rendezvous". In: *Journal of the Aerospace Sciences* 27.9 (1960), pp. 653–658.
DOI: 10.2514/8.8704.

[79]   F. de Bruijn, E. Gill, and J. H. How. "Comparative analysis of Cartesian and curvilinear Clohessy-Wiltshire equations". In: *Journal of Aerospace Engineering, Sciences and Applications* 3.2 (2011).
DOI: 10.7446/jaesa.0302.01.

[80]   H. Schaub, S. R. Vadali, and K. T. Alfriend. "Spacecraft Formation Flying Control Using Mean Orbit Elements". In: *Journal of the Astronautical Sciences* 48.1 (2000), pp. 69–87.

[81]   D.-W. Gim and K. T. Alfriend. "State Transition Matrix of Relative Motion for the Perturbed Noncircular Reference Orbit". In: *Journal of Guidance, Control and Dynamics* 26.6 (2003), pp. 956–971.
DOI: 10.2514/2.6924.

[82]   J. Tschauner and P. Hempel. "Rendezvous zu einem in Elliptischer Bahn Umlaufenden Ziel". In: *Acta Astronautica* 11 (1965), pp. 104–109.

[83]   K. Yamanaka and F. Ankersen. "New State Transition Matrix for Relative Motion on an Arbitrary Elliptical Orbit". In: *Journal of Guidance, Control and Dynamics* 25.1 (2002), pp. 60–66.
DOI: 10.2514/2.4875.

[84] D. Brouwer. "Solution of the problem of artificial satellite theory without drag". In: *Astronomical Journal* 64.1274 (1959), pp. 378–397. DOI: 10.1086/107958.

[85] H. G. Walter. "Conversion of osculating orbital elements into mean elements". In: *Astronomical Journal* 72 (1967), p. 994. DOI: 10.1086/110374.

[86] R. Burkard. *Geodesy for the Layman*. St Louis, MO:USAF Aeronautical Chart and Information Center, 1964.

[87] S. A. Schweighart and R. J. Sedwick. "High-Fidelity Linearized J2 Model for Satellite Formation Flight". In: *Journal of Guidance, Control and Dynamics* 25.6 (2002), pp. 1073–1080. DOI: 10.2514/2.4986.

[88] G. Gaias, J.-S. Ardaens, and O. Montenbruck. "Model of J2 Perturbed Satellite Relative Motion with Time-Varying Differential Drag". In: *Celestial Mechanics and Dynamical Astronomy* 123.4 (2015), pp. 411–433. DOI: 10.1007/s10569-015-9643-2.

[89] J. Sullivan, S. Grimberg, and S. D'Amico. "Comprehensive Survey and Assessment of Spacecraft Relative Motion Dynamics Models". In: *Journal of Guidance, Control, and Dynamics* 40.8 (2017), pp. 1837–1859. DOI: 10.2514/1.G002309.

[90] G. Gaias and C. Colombo. "Semi-Analytical Framework for Precise Relative Motion in Low Earth Orbits". In: 7$^\text{th}$ International Conference of Astrodynamics Tools and Techniques ICATT. Oberpfaffenhofen, Germany, 2018.

[91] O. Montenbruck, M. Kirschner, S. D'Amico, and S. Bettadpur. "E/I-Vector Separation for Safe Switching of the GRACE Formation". In: *Aerospace Science and Technology* 10.7 (2006), pp. 628–635. DOI: 10.1016/j.ast.2006.04.001.

[92] A. W. Koenig, T. Guffanti, and S. D'Amico. "New State Transition Matrices for Spacecraft Relative Motion in Perturbed Orbits". In: *Journal of Guidance, Control, and Dynamics* 40.7 (2017), pp. 1749–1768. DOI: 10.2514/1.G002409.

[93] D. Maessen. "Autonomous Relative Navigation for Small Spacecraft". PhD thesis. The Netherlands: Technical University of Delft, 2011.

[94] S. E. Hammel and V. J. Aidala. "Observability Requirements for Three-Dimensional Tracking via Angle Measurements". In: *IEEE Transactions on Aerospace and Electronic Systems* 21.2 (1985), pp. 200–207. DOI: 10.1109/TAES.1985.310617.

[95] D. C. Woffinden and D. K. Geller. "Observability Criteria for Angles-Only Navigation". In: *IEEE Transactions on Aerospace and Electronic Systems* 45.3 (2009), pp. 1194–1208. DOI: 10.1109/TAES.2009.5259193.

[96]   I. Harris and W. Priester. "Time-Dependent Structure of the Upper Atmosphere". In: *Journal of the Atmospheric Sciences* 19.4 (1962), pp. 286–301. DOI: 10.1175/1520-0469(1962)019<0286:TDSOTU>2.0.CO;2.

[97]   R. Kalman. "A New Approach to Linear Filtering and Prediction Problems". In: *Journal of Basic Engineering* 82.1 (1960), pp. 35–45. DOI: 10.1115/1.3662552.

[98]   P. D. Moral. "Non Linear Filtering: Interacting Particle Solution". In: *Markov Processes and Related Fields* 2.4 (1996), pp. 555–580.

[99]   M. Benn and J. L. Jørgensen. "Autonomous Vision Based Detection of Non-stellar Objects Flying in Formation with Camera Point of View". In: *Proceedings of the 5th International Conference on Spacecraft Formation Flying Missions & Technologies (SFFMT)*. Munich, Germany: DLR, German Space Operations Center, 2013.

[100]   H. Benninghoff, T. Tzschichholz, T. Boge, and G. Gaias. "A Far Range Image Processing Method for Autonomous Tracking of an Uncooperative Target". In: *Proceedings of the 12th Symposium on Advanced Space Technologies in Robotics and Automation*. Noordwijk, The Netherlands: ESA, 2013.

[101]   O. Montenbruck, T. van Helleputte, R. Kroes, and E. Gill. "Reduced Dynamic Orbit Determination using GPS Code and Carrier Measurements". In: *Aerospace Science and Technology* 9.3 (2005), pp. 261–271. DOI: 10.1016/j.ast.2005.01.003.

[102]   E. Kahr, S. Skone, and K. O'Keefe. "Orbit Determination for the Canx-2 Nanosatellite Using Intermittent GPS Data". In: Proceedings of the ION GNSS 2010. Portland, Oregon, USA, 2010.

[103]   M. Ester, H.-P. Kriegel, J. Sander, and X. Xu. "A Density-Based Algorithm for Discovering Clusters in Large Spatial Databases with Noise". In: *Proceedings of the 2nd International Conference on Knowledge Discovery and Data mining*. 1996, pp. 226–231.

[104]   J.-Y. Bouguet. *Camera Calibration Toolbox for Matlab*. http://www.vision.caltech.edu/bouguetj/calib_doc/ [Accessed 1 July 2019]. 2004.

[105]   J. Heikkila and O. Silven. "A Four-step Camera Calibration Procedure with Implicit Image Correction". In: *Proceedings of the 1997 Conference on Computer Vision and Pattern Recognition (CVPR '97)*. CVPR '97. Washington, DC, USA: IEEE Computer Society, 1997. ISBN: 0-8186-7822-4.

[106]   P. B. Davenport. *A Vector Approach to the Algebra of Rotations with Applications*. NASA X-546-65-437. NASA, Nov. 1965.

[107]   G. Allende-Alba, O. Montenbruck, J.-S. Ardaens, M. Wermuth, and U. Hugentobler. "Estimating maneuvers for precise relative orbit determination using GPS". In: *Advances in Space Research* 59.1 (2017), pp. 45–62. DOI: 10.1016/j.asr.2016.08.039.

[108]   R. Kahle, M. Weigel, M. Kirschner, S. Spiridonova, E. Kahr, and K. Letsch. "Relative
        Navigation to Non-cooperative Targets in LEO: Achievable Accuracy from Radar
        Tracking Measurements". In: *Int. J. Space Science and Engineering* 2.1 (2014), pp. 81–
        95.
        DOI: 10.1504/IJSPACESE.2014.060112.

[109]   J.-S. Ardaens and G. Gaias. "Flight Demonstration of Spaceborne Real-Time Angles-
        Only Navigation to a Noncooperative Target in Low Earth Orbit". In: *Acta Astro-
        nautica* 153 (2018), pp. 367–382.
        DOI: 10.1016/j.actaastro.2018.01.044.

[110]   J. B. Burl. *Linear Optimal Control: H2 and H∞ Methods.* Boston, MA, United
        States: Addison-Wesley Longman Publishing Co., Inc., 1998.

[111]   G. Gaias and J.-S. Ardaens. "In-orbit experience and lessons learned from the
        AVANTI experiment". In: *Acta Astronautica* (2017).
        DOI: 10.1016/j.actaastro.2018.01.042.

[112]   J.-S. Ardaens and G. Gaias. "A Numerical Approach to the Problem of Angles-Only
        Initial Relative Orbit Determination in Low Earth Orbit". In: *Advances in Space
        Research* 63.12 (2019), pp. 3884–3899.
        DOI: 10.1016/j.asr.2019.03.001.

[113]   J.-S. Ardaens and G. Gaias. "Fast Angles-Only Initial Relative Orbit Determination
        for Onboard Application". In: *Proceedings of the 10th International Workshop on
        Satellite Constellations and Formation Flying.* Glasgow, United Kingdom, 2019.

[114]   J.-C. Liou and N. Johnson. "Instability of the present LEO satellite populations".
        In: *Advances in Space Research* 41.7 (2008), pp. 1046–1053.
        DOI: 10.1016/j.asr.2007.04.081.

[115]   D. A. Cicci. *Spacecraft Formation Control and Estimation via Improved Relative-
        Motion Dynamics.* Final Report AFRL-RV-PS-TR-2017-0052, Auburn University,
        Auburn, AL. 2017.

[116]   B. Ustinov. "Motion of satellites along low-eccentricity orbits in a noncentral ter-
        restrial gravitational field". In: *Cosmic research* 5 (1967), p. 159.

[117]   M. C. Eckstein and H. Hechler. *A reliable derivation of the perturbations due to
        any zonal and tesseral harmonics of the geopotential for nearly-circular satellite
        orbits.* ESRO SR-13. Darmstadt, Germany: ESOC, Nov. 1970.

CURRICULUM VITÆ

Jean-Sébastien Ardaens was born in Lille, France on July 1st, 1982. After obtaining his Baccalauréat in 2000, he undertook intensive courses preparing for the entrance examination of the *Grandes Ecoles* at Lycée Faidherbe, Lille. He succeeded in entering the Ecole Centrale Paris in 2002, where he followed a multidisciplinary generalist curriculum in engineering and science. As part of a double degree program, he specialized in aerospace by studying at the Technical University of Munich between 2004 and 2006. In 2006 he graduated with a Master thesis in the field of precise orbit determination of spacecraft using Satellite Laser Ranging measurements, for which he spent nine months at the German Space Operations Center (GSOC) of DLR in Oberpfaffenhofen, Germany.

After his graduation, he took a position in 2006 as young research scientist at the Space Flight Technology Department of DLR/GSOC. His first task was the design, implementation and in-orbit evaluation of the TanDEM-X Autonomous Formation Flying System. This experimental onboard add-on software was successfully used in orbit for several weeks, demonstrating the ability to routinely control a close formation of Earth observation satellites in a fully autonomous way using relative GPS. In 2009, he was responsible for the conception and operations of the ground facility for precise GPS-based relative orbit determination for the PRISMA mission, which served as reference to monitor the formation safety and to calibrate other relative navigation sensors. After the completion of the main mission phase, he focused on relative navigation to noncooperative objects by designing the on-ground angles-only relative orbit determination for the AR-GON experiment during the PRISMA extended mission phase. From 2013 on, he was co-responsible for the design, implementation and conduction of the AVANTI experiment, which was successfully executed in 2016. He joined the Swiss start-up ClearSpace in 2020 to contribute to building up the first European active debris removal mission.

LIST OF PUBLICATIONS

J.-S. Ardaens and G. Gaias. "A Numerical Approach to the Problem of Angles-Only Initial Relative Orbit Determination in Low Earth Orbit". In: *Advances in Space Research* 63.12 (2019), pp. 3884–3899.
DOI: 10.1016/j.asr.2019.03.001.

J.-S. Ardaens and G. Gaias. "Angles-Only Relative Orbit Determination in Low Earth Orbit". In: *Advances in Space Research* 31.11 (2018), pp. 2740–2760.
DOI: 10.1016/j.asr.2018.03.016.

J.-S. Ardaens and G. Gaias. "Flight Demonstration of Spaceborne Real-Time Angles-Only Navigation to a Noncooperative Target in Low Earth Orbit". In: *Acta Astronautica* 153 (2018), pp. 367–382.
DOI: 10.1016/j.actaastro.2018.01.044.

J.-S. Ardaens, R. Kahle, and D. Schulze. "In-Flight Performance Validation of the TanDEM-X Autonomous Formation Flying System". In: *International Journal of Space Science and Engineering* 2.2 (2014), pp. 157–170.
DOI: 10.1504/IJSPACESE.2014.060596.

J.-S. Ardaens, S. D'Amico, and A. Cropp. "GPS-Based Relative Navigation for the Proba-3 Formation Flying Mission". In: *Acta Astronautica* 91 (2013), pp. 341–355.
DOI: 10.1016/j.actaastro.2013.06.025.

J.-S. Ardaens, S. D'Amico, and O. Montenbruck. "Final Commissioning of the PRISMA GPS Navigation System". In: *Journal of Aerospace Engineering, Sciences and Applications* 4.3 (2012), pp. 104–118.

J.-S. Ardaens and D. Fischer. "TanDEM-X Autonomous Formation Flying System: Flight Results". In: *Journal of Mechanics Engineering and Automation* 2.5 (2012), pp. 332–340.
DOI: 10.17265/2159-5275/2012.05.009.

J.-S. Ardaens and S. D'Amico. "Spaceborne Autonomous Relative Control System for Dual Satellite Formations". In: *Journal of Guidance, Control, and Dynamics* 32.6 (2009), pp. 1859–1870.
DOI: 10.2514/1.42855.